Oscillatory transcription factors and stochastic gene expression

From pulsatile p53 dynamics to bursty transcription in the DNA damage response to ionizing radiation.

DISSERTATION

zur Erlangung des akademischen Grades

doctor rerum naturalium

(Dr. rer. nat.)

im Fach Biophysik

eingereicht an der Lebenswissenschaftlichen Fakultät
der Humboldt Universität zu Berlin

von

Dipl. Biochem. Dhana Friedrich

Präsidentin der Humboldt Universität:	Prof. Dr.-Ing. Dr. Sabine Kunst
Dekan der Lebenswissenschaftlichen Fakultät:	Prof. Dr. Bernhard Grimm

Gutachter:
1. Prof. Dr. Alexander Löwer
2. Prof. Dr. Andreas Herrmann
3. Prof. Dr. Markus Landthaler

Tag der mündlichen Prüfung: 27.11.2019

"Somewhere between the bottom of the climb and the summit is the answer to the mystery why we climb."

Greg Child

CONTENT

ABSTRACT

Transcription factors (TFs) are receiver and compiler of cell signaling, transmitting incoming input information into cellular responses. They enable an individual cell and, on a larger scale, an organ or organism to respond and adapt to a changing environment. In the past, it has been shown that many TFs show oscillations of nuclear abundance over time when activated by upstream signaling. One of these TFs is the tumor suppressor p53. P53 is a central hub in the signaling network regulating the cellular stress response, orchestrating the conversion of input signals to control cell fate decisions by changing the expression of hundreds of target genes. Aberrations in p53's activity are related to severe human malignancies such as cancer. The dynamics of p53's nuclear accumulation are stimulus-dependent and enable the p53 pathway to mediate distinct responses to cellular stress. However, the molecular mechanisms translating dynamics to altered gene expression remain elusive.

In this thesis, I address the question how oscillations of p53 in the nucleus affect the transcriptional regulation of target genes in single-cells and at individual promoters. Therefore, I chose a panel of seven target genes and employed a combinatorial approach of single-molecule fluorescence in-situ hybridization (smFISH) and mathematical analyses. First, I present the experimental and computational set-up and provide suggestions for selection criteria that can be used for studying other signaling pathways in the future. Based on this, I performed quantitative, time-resolved measurements of target gene mRNA expression and transcriptional bursting activity with single-cell and single-molecule resolution to inform a mathematical model of promoter activity. I provide evidence that p53 activation changes stochastic bursting in response to DNA damage. The absolute numbers of mRNA molecules and transcription properties of target genes are highly heterogeneous. My data show characteristic principles how p53 nuclear accumulation increases transcriptional bursting upon stimulation and reveal gene-specific modulations on longer time-scales, after several hours. I find that p53 target promoters are regulated by changing the fraction of active promoters, indicating burst frequency regulation. Based on this, they can be grouped along with three archetypes of activity: *sustained, transient* and *pulsatile*. The occurrence of these archetypes cannot solely be explained by nuclear p53 levels or promoter binding of total p53. Instead, I show that the time-varying acetylation state of p53's C-terminal lysine residues is critical for this gene-specific regulation. Lastly, to transfer these findings to a more time-resolved understanding of p53-mediated gene expression, I present pilot experiments employing live-cell RNA imaging by the MS2 system. In the future, this approach will allow performing mechanistic studies of stochastic bursting with high temporal resolution, to infer transcriptional activity before and after DNA damage in the exact same cells on long time scales.

In summary, I present a first quantitative analysis of p53 dependent gene expression in single cells and at individual promoters. The obtained results extend the current knowledge of p53 dependent transcription and may help to decipher the regulatory principles of cell fate regulation in health and disease.

ZUSAMMENFASSUNG

Transkriptionsfaktoren empfangen die eingehenden Signale zellulärer Signaltransduktionskaskaden, leiten diese weiter und übersetzen die darin enthaltenen Informationen in eine zelluläre Antwort. Dadurch ermöglichen sie es einer Zelle, einem Organ und dem Organismus sich an sich verändernde Umgebungsbedingungen anzupassen. Im Rahmen vorhergehender Studien konnte gezeigt werden, dass viele Transkriptionsfaktoren nach der Aktivierung durch einen Signalweg Oszillationen ihrer Lokalisation und Akkumulation im Zellkern aufweisen. Ein Beispiel dafür ist der Tumorsuppressor und Transkriptionsfaktor p53. P53 ist ein zentrales Protein innerhalb des Signaltransduktionsnetzwerks, welches die zelluläre Stressantwort reguliert. Dabei wandelt es die eingehenden Signale um, steuert die spezifische Expression hunderter Zielgene und somit das Zellschicksal. Anomalien in der Aktivität von p53 konnten im Zusammenhang mit schwerwiegenden Erkrankungen nachgewiesen werden, beispielsweise im Kontext der Krebsentstehung. Die Dynamiken der Akkumulation von p53 im Zellkern sind abhängig von externen Stimuli und bilden die Grundlage für die Zelle auf Stress, wie beispielsweise DNA Schäden, angemessen zu reagieren. Obwohl dieser Zusammenhang in verschiedenen Studien gezeigt wurde, sind die molekularen Mechanismen, die diese Dynamiken in eine Veränderung der Genexpression übersetzen, bisher weitgehend unerforscht.

Mit der vorliegenden Arbeit soll ein Beitrag zum Verständnis dazu geleistet werden, wie diese Oszillationen von p53 die transkriptionelle Regulation von Zielgenen in einzelnen Zellen an spezifischen Promotoren beeinflussen. Dazu wurden sieben Zielgene ausgewählt und mit Hilfe eines kombinatorischen Ansatzes von Einzelmolekül-Fluoreszenz in situ Hybridisierung und mathematischer Analyse charakterisiert. Im ersten Teil stelle ich das experimentelle und computergestützte Konzept vor und definiere Kriterien zur Auswahl des methodischen Ansatzes, was in zukünftigen Studien anderer Signalwege von Nutzen sein kann. Im Folgenden werden die Ergebnisse der quantitativen, zeitaufgelösten Messungen der mRNA Expression und der *bursting* Aktivität von Zielgenpromotoren mit Einzelzell- und Einzelmolekülauflösung dargestellt. Auf Grundlage dieser Ergebnisse wird dann ein mathematisches Modell der Promotoraktivität etabliert und angewendet. Dadurch werden Belege geliefert, dass die Aktivierung von p53 das stochastische *bursting* einzelner Promotoren als Antwort auf DNA Schäden ändert. Die absolute Zahl der mRNA Moleküle in einzelnen Zellen und die Transkriptionseigenschaften der Zielgene sind stark heterogen. Die präsentierten Daten offenbaren somit charakteristische Prinzipien wie durch die Akkumulation von p53 im Zellkern das transkriptionelle *bursting* nach Stimulation erhöht wird und decken zudem genspezifische Modulationen auf einer längeren Zeitskala auf. Im Rahmen dieser Arbeit wird gezeigt, dass die gewählten Zielgenpromotoren von p53 durch die Veränderung der Frequenz des stochastischen *bursting* reguliert werden. Basierend darauf werden diese in drei verschiedene Archetypen anhand ihrer Promotoraktivität eingeteilt: *anhaltend*, *transient* und *pulsierend*. Das Auftreten dieser Archetypen kann nicht

ausschließlich durch die nukleäre p53 Menge oder die Bindung von p53 an die untersuchten Promotoren erklärt werden. Stattdessen werden im Rahmen dieser Arbeit Belege dafür geliefert, dass der über die Zeit veränderliche Acetylierungszustand der C-terminalen Lysinreste von p53 entscheidend für die Gen-spezifische Regulation ist. Um zukünftige Zeit-aufgelöste Studien von p53-vermittelter Genexpression zu erleichtern, präsentiere ich schließlich Pilotexperimente von RNA Bildgebung in lebenden Zellen mit Hilfe des MS2 Systems. Die dabei etablierten Zelllinien werden mechanistische Untersuchungen von stochastischem *bursting* mit hoher zeitlicher Auflösung und Schlussfolgerungen auf die transkriptionelle Aktivität vor und nach DNA Schäden auf längeren Zeitskalen erlauben.

Zusammenfassend lässt sich sagen, dass in dieser Dissertation die erste quantitative Analyse von p53-abhängiger Genexpression in Einzelzellen an ausgewählten Promotoren vorgestellt wird. Die erzielten Ergebnisse erweitern das bisherige Wissen von p53-gesteuerter Transkription und werden zukünftig dabei helfen die Prinzipien der Regulation des Zellschicksals, sowohl in gesunden als auch in erkrankten Zellen, deren Fehlfunktion mit Veränderungen des p53 Signalwegs im Zusammenhang stehen, zu entschlüsseln.

CONTRIBUTIONS

The presented research in this dissertation was conducted from March 2014 to August 2019 in the research group of Prof. Dr. Alexander Löwer at the Max Delbrück Center for Molecular Medicine Berlin and at the Technical University Darmstadt. From January 2015 to December 2018 experiments were performed in the research groups of Prof. Dr. Andreas Herrmann at the Institute for Biophysics, Humboldt Universität zu Berlin as well as of Dr. Stephan Preibisch at the Max Delbrück Center for Molecular Medicine.

Scientific research is a joint effort aiming to expand our current state of knowledge to better understand the world around us. Going from the known to the unknown is an exciting journey and always based on previous work of fellow scientists as well as collaborations with the surrounding scientific community. Contributions from colleagues to the experiment presented in this thesis are mentioned in the respective paragraphs and figure captions. These include Chromatin Immuno-precipitation (ChIP), selected Western Blots and RNA sequencing experiments. While I contributed to the experimental design and performed data analysis, the optimization of protocols for ChIP experiments and raw data were generated by Laura Friedel (TU Darmstadt). For technical reasons, also replicates of the K383ac/K370ac Western blots were performed in collaboration with Laura Friedel and Petra Snyder (TU Darmstadt). The MCF10A RNA sequencing dataset used for literature comparison to select p53 target genes was generated by Ana Finzel in the context of a previous project (Finzel, 2016a). Last but not least, excellent technical staff members at the MDC Berlin and the TU Darmstadt instructed by Alexander Loewer and myself assisted the effort to generate fluorescent reporter cell lines: Andrea Grybowski, Petra Snyder and Ulrike Burk.

Individual sections in this dissertation are based on a research study that has been uploaded to the bioRxiv server for scientific preprints (now published in *Molecular Systems Biology* (Friedrich et al., 2019)). In this publication, I am the single first author, wrote the manuscript, designed experiments and performed the computational analysis as well as the majority of experiments. Alexander Loewer supervised this study, contributed to the design and gave feedback to results and the manuscript. Also, Andreas Herrmann and Stephan Preibisch helped interpreting results. While most sections are novel as they are presented in this thesis, individual paragraphs and figures panels were freely edited based on an earlier version of the mentioned manuscript.

CHAPTER 1 INTRODUCTION

1.1. TRANSCRIPTION, A FUNDAMENTAL PROCESS OF LIFE

1.1

Transcription, the process of copying specific genomic information from DNA to RNA, is one of the most fundamental processes in a cell. The proper regulation of transcription in space and time plays a crucial role in cellular homeostasis and allows responses to intrinsic and extrinsic signals in the context of development and disease. In this initial step of gene expression, RNA polymerase reads the genomic sequence and generates a complementary nucleic acid strand (Figure 1.1.1). Eukaryotes have three forms of DNA dependent RNA polymerases (RNAP1/2/3) to transcribe DNA into RNA (Roeder and Rutter, 1969). RNAP2 is the most abundant of these enzymes, transcribing protein-coding genes, most microRNAs, small interfering RNAs and small nuclear RNAs (Kornberg, 1999; Sims et al., 2004).

IN THIS CHAPTER

1.1.1. EUKARYOTIC GENE EXPRESSION

The eukaryotic transcription cycle consists of three main regulatory steps: initiation, elongation and termination (Figure 1.1.1). During initiation, transcription factors (TFs) bind to defined DNA sequences close to the transcriptional start site (TSS) in the promoter region. The core promoter contains gene-specific functional elements, which can be categorized in different classes depending on their genomic architecture and function (Gagniuc and Ionescu-Tirgoviste, 2012). Initiation involves the assembly of six general transcription factors (GTFs) (Matsui et al., 1980) that bind to these functional elements, accompanied by association with the Mediator multi-protein complex to recruit RNAP2 resulting in the formation of the Pre-Initiation Complex (PIC) (Allen and Taatjes, 2015). To start transcription, the DNA double strand is melted and complementary nucleotides are polymerized at the active site of RNAP2, building a duplex with the DNA antisense strand. After polymerization of the first ten nucleotides, the PIC dissociates and RNAP2 looses connection to the core promoter and regulatory proteins that are dispensable for further elongation (Jonkers and Lis, 2015). While moving along the coding sequence (CDS), RNAP2 unwinds the DNA double-strand and continuously synthesizes the nascent RNA transcript to generate a growing antisense copy that is released through RNAP2's exit channel. During this process, different classes of elongation factors (EFs) are recruited, and RNAP2 is associated with varying proteins that co-transcriptionally process the nascent transcript (Saunders et al., 2006). At the end of the CDS, the poly-Adenine (poly-A) signal is recognized by co-regulatory proteins that are bound to the polymerase's C-terminal domain (CTD). These proteins cleave the nascent transcript, add a 3' poly-A tail of approximately 200 adenines and terminate transcription resulting in the release of the transcript and dissociation of RNAP2 from the DNA (Figure 1.1.1) (Richard and Manley, 2009). Different processes can affect gene expression output and transcription efficiency: re-current initiation,

PIC
Pre-initiation complex, a regulatory multiprotein complex that consists of >100 proteins and mediates the positioning of RNAP2 at the transcription site to initiate transcription.

PIC stability, as well as abortive initiation and elongation. Besides, the three phases of the transcription cycle can be regulated individually (Fuda et al., 2009). In general, transcription is a complex, multi-layer process that, at the level of a single gene, involves numerous molecular mechanisms. For example, gene-specific co-transcriptional RNA processing affects transcription. Also, the kinetics of TF binding to *cis*-regulatory elements vary and TFs interact in *trans* with co-regulatory factors, distal enhancer regions, or the surrounding chromatin in promoter proximal regions, leading to gene-specific regulation (Reiter et al., 2017).

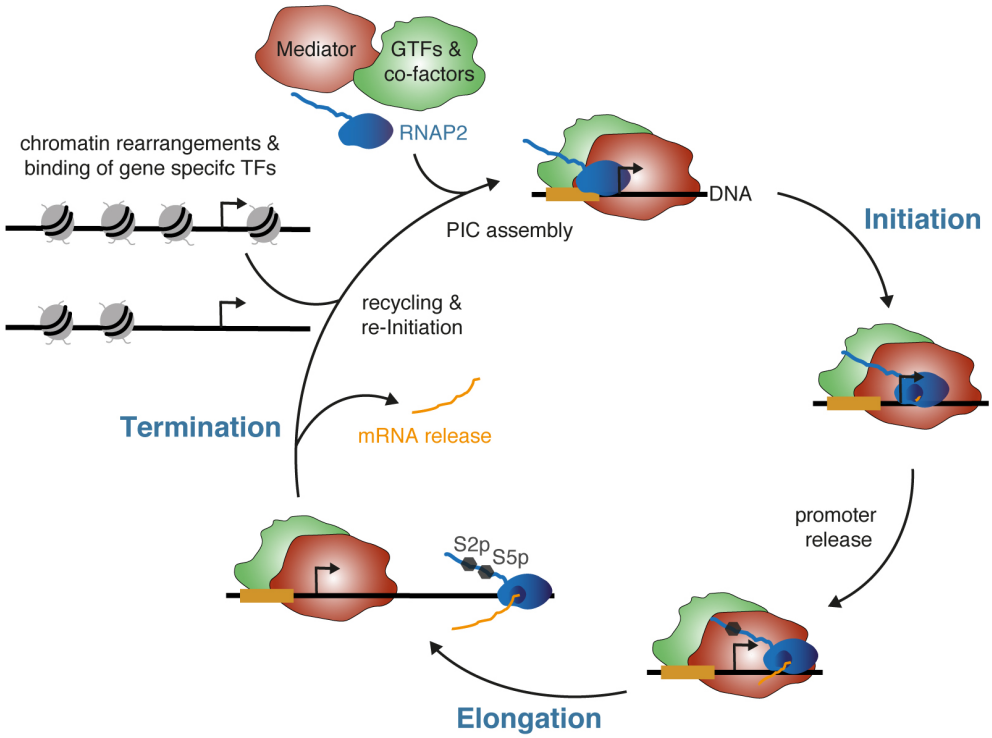

Figure 1.1.1 The transcription cycle, from initiation to elongation and termination.

Transcription is a tightly regulated process to copy RNA from DNA, involving several layers of regulation and numerous molecular processes. This allows a precise modulation of gene expression dependent on the context of cellular signaling and development. The transcription cycle consist of three phases: Initiation, Termination and Elongation.
Initiation starts through rearrangement of chromatin proximal to the transcription site (TSS, black arrow) and binding of gene-specific transcription factors inducing the assembly of General transcription factors (GTFs), the Mediator complex and RNA Polymerase 2 (RNAP2) to the Pre-Initiation Complex (PIC). In the Elongation phase, RNAP2 leaves the promoter generating the nascent transcript from the DNA template. When the poly-A signal is reached at the end of the coding sequence, Termination is induced and the mRNA is released. These phases differ in the phosphorylation state of Serine residues in the C-terminal domain of RNAP2 (indicated by S2p/S5p hexagons). As long as the promoter is in an open conformation, RNAP2 can be recycled and re-initiated to re-start another round of transcription. (Illustration freely adapted based on Fuda et al., 2009; Scholes et al., 2017)

1.1.2. TRANSCRIPTION FACTORS, RECEIVER AND COMPILER OF CELLULAR SIGNALING

Cells regularly respond to a variety of extrinsic and intrinsic stimuli, evaluate their current state and adapt to local and global changes of their environment. To retain cellular integrity, they mediate distinct signaling responses on the level of an individual cell but also in more sophisticated cellular systems such as tissues and whole organisms. In a changing environment, it is a fundamental challenge for each cell to filter important information from noise and react to incoming signals with adequate cellular responses at the right time to ensure survival and enable adaption. This task is inherited by a complex interplay of signaling molecules that sense and transmit stimuli inside cellular signaling cascades, translating them into distinct molecular reactions.

One key-regulatory mechanism of these cascades is to modulate the transcription cycle of specific genes and thus control mRNA and protein levels (Figure 1.1.1). Gene-specific transcription factors are a class of DNA binding proteins that function as central hubs of intracellular signaling. They encode upstream signals and decode their information into cell responses by DNA binding and regulation of gene expression (Figure 1.1.2). Eukaryotic cells have two major classes of transcription factors. The first are GTFs, which recruit the basal transcription machinery. These act in concert with the Mediator complex, chromatin remodelers, and RNAP2 to assemble the PIC as described in Chapter 1.1.1. In contrast, gene-specific TFs differentially regulate gene expression by sequence-specific binding to response elements (REs) in *cis*-regulatory DNA regions after activation by upstream signaling. They thus allow distinct regulation of transcription in development, differentiation and proliferation, but also in cell cycle progression, the immune response and when reacting to other environmental changes (Figure 1.1.2).

DBD
DNA binding domain, characteristic protein domain of transcription factors to bind to their recognized sequence motives.

TFs exhibit a broad structural and mechanistic variety of how, where and when DNA binding occurs. This includes individual functions such as binding of pioneer factors to closed chromatin, as well as complex interactions in concert with other TFs or co-factors. A unifying characteristic feature of TFs is the DNA binding domain (DBD) that interacts with the promoter or enhancer region of target genes, which is a fundamental difference to other regulators of transcription such as chromatin modifiers or methylases that lack direct sequence specific DNA binding. TFs are often classified by their recognized DNA motif and the structure of their DBD (Vaquerizas et al., 2009; Fulton et al., 2009; Wingender et al., 2015). Besides, they act in concert with other regulatory factors by protein-protein interactions through their trans-activation domains (TADs) leading to changes in gene expression. Furthermore, looping of the DNA allows TFs bound to enhancers, *cis*-regulatory genomic regions that can be several kilobases upstream of the TSS, to interact with a promoter and thereby regulate transcription.

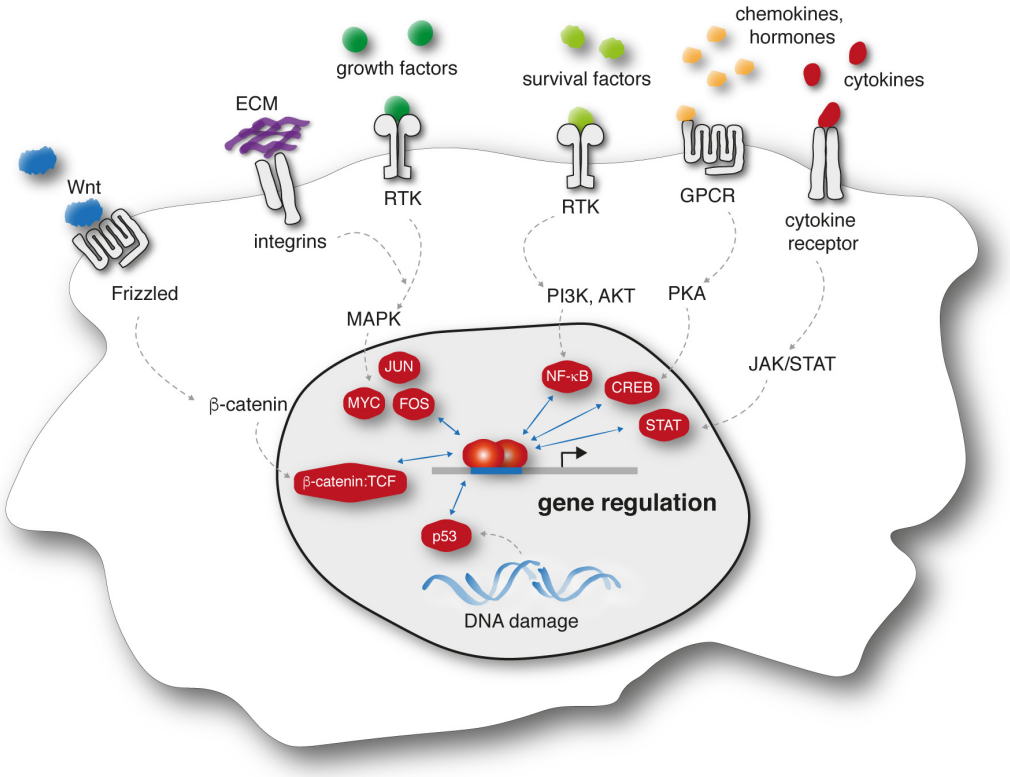

Figure 1.1.2 Transcription factors, receiver and compiler of cellular signaling.

Transcription factors (TFs) are an essential class of signaling molecules that serve as receiver and compiler of cell signaling to regulate gene expression in a changing environment. This figure presents a schematic illustration of a cell with examples of the different layers of cellular signaling cascades leading to TF activation mediating gene expression.
At the cell membrane, different receptor classes can be activated by specific extracellular stimuli. From receptors that build the input layer, signals are transmitted to the inner cell through the cytoplasm and further downstream in signaling cascades that can involve multiple proteins and chemical reactions (not shown, dashed lines indicate several steps). Inside the nucleus (dark grey), TFs (red) (some examples displayed) decode the information from upstream signaling into gene expression by direct regulation of target gene expression. Therefore, they recognize and bind response elements (RE) in the DNA in a sequence-specific manner. To regulate gene expression, TFs can bind in a solitary fashion or in concert with other TFs and additional proteins. P53 is a different case, as it is not activated through a signaling cascade by receptors, but by DNA damage that is sensed by PI3K-like kinases in the nucleus itself. These then directly activate p53 as well as other factors of the signaling network leading to an increase in p53 dependent gene expression (Chapter 1.2).
RTK: receptor tyrosine kinase; GPCR: G-protein coupled receptor; ECM: extracellular matrix; MAPK: Mitogen-Activated-Protein-Kinase; PI3K: phosphatidylinositol 3-kinases; AKT1: protein kinase B/AKT1; PKA: protein kinase A; JAK: Janus kinase; STAT: signal transducer and activator of transcription protein; CREB: cAMP response element-binding protein; NF-κB: nuclear factor kappa-light-chain-enhancer of activated B cells.

1.1.3. GENE-SPECIFIC TRANSCRIPTIONAL REGULATION

The spatiotemporal regulation of transcription orchestrates the life of every cell by controlling its cell fate. Gene expression is driven by TFs that bind to specific sequences in *cis*-regulatory DNA elements, such as enhancers, promoters and insulators (Long et al., 2016). Enhancers are gene-regulatory genomic regions that modulate transcription from core promoters of target genes. They harbor sequence motifs that are bound by TFs (*cis*-regulatory elements), then interacting in *trans* with co-factors such as the Mediator or histone

modifying enzymes. This co-factor interaction induces activation or repression of transcription. The Mediator consists of about 20 subunits and coordinates interactions between gene-specific regulators such as TFs and the general transcription machinery (Allen and Taatjes, 2015). Furthermore, many co-factors as the cyclin-dependent kinases of the GTFs or the CBP/p300 histone acetyl transferase (HAT) are enzymes regulating post-transcriptional modifications. Additionally, to initiate eukaryotic transcription, the general transcription factors TFIIB, D, E, F, and H, as well as the TATA-box binding protein (TBP), are necessary cofactors to establish the PIC at the promoter (Lue and Kornberg, 1987). However, to date it is mechanistically widely unexplored how the binding of TFs to enhancers and the resulting interaction with co-factors leads to distinct regulation of RNAP2, initiating transcription and modulating the transcription cycle (Reiter et al., 2017). In eukaryotes, it has been shown that the chromatin environment plays a significant role in mediating transcription. To enable transcription, chromatin has to be in a conformationally open, acetylated state, while transcription is reduced in closed chromatin (Li et al., 2007). The regulation of this transition to induce the expression of a specific gene requires nucleosome remodeling and a change in the chromatin state, mediated by enzymes as HATs (Weake and Workman, 2010). Additionally, TF mediated gene expression is often tightly controlled by their binding in distinct context specific combinations. In this regard, gene-specific transcription factors play a crucial role through the plethora of their co-regulatory interactions mediating differential gene expression. Regulation of TFs can be achieved through the DNA sequence, mediating cooperativity of TFs (Deplancke et al., 2016). This collaborative binding can be fostered by protein-protein interactions (TF-TF/ TF & co-factor) which have been hypothesized to induce nucleosome remodeling and promote interactions between TFs and co-factors (Spitz and Furlong, 2012). Also, sequential binding of TFs, in which a pioneer TF that binds to closed chromatin initiates the subsequent interactions of other factors, has been shown (Zaret and Carroll, 2011).

Even though a transition from an inactive to a transcribing promoter is often defined as an active state, it is still unknown how these differential promoter states can be described mechanistically. It yet remains unsolved what defines these states on the molecular level and if intermediate steps exist. One reason is that the transcription machinery is considerably sophisticated regarding the number of molecules and reactions involved. It is therefore also possible that a promoter can transition between a series of states or that the number of states varies depending on the cellular context (Corrigan et al., 2016; Fritzsch and Baumgärtner et al., 2018; Li et al., 2018). Previously, it has been suggested that transcription initiation is the rate-limiting factor for PIC formation and subsequent transcription of protein-coding genes (Hahn, 1998). Based on this, an active promoter state would be a promoter that (re-)initiates transcription.

1.2. P53, THE GUARDIAN OF THE GENOME

1.2

IN THIS CHAPTER

The tumor suppressor p53 is a transcription factor and central hub in the signaling network regulating the DNA damage response. Its primary function is to retain genetic integrity and inhibit uncontrolled cell proliferation. P53 regulates cell cycle arrest and induces cell death in the context of DNA damage. It is therefore often called *the guardian of the genome* or *cellular gatekeeper*. P53 is activated in response to different stimuli, including genotoxic stress, hypoxia and nutrient deprivation (Hafner et al., 2019). A loss of its cellular activity is tightly connected with the development of cancer, leading to uncontrolled tumor growth (Vousden and Lu, 2002). About 50% of all human cancers involve point mutations in the TP53 gene, altering either p53's protein-protein interactions or its transcription factor activity (Hainaut and Hollstein, 1999; Bykov and Wiman, 2003). The highly abundant p53 protein in cells, with estimated 70.000 - 200.000 protein molecules per cell (Schwanhäusser et al., 2011), undergoes a rapid turnover of about 15 min in unstressed cells (Weinberg, 1995).

1.2.1. THE TUMOR SUPPRESSOR P53 AND ITS RESPONSE TO CELL STRESS

MDM2
Ubiquitine-ligase for p53 and also a p53 target gene.

In the absence of cellular stress, the ubiquitin ligase MDM2 continuously ubiquitinylates p53, targeting it for rapid degradation in the proteasome (Haupt et al., 1997; Kubbutat et al., 1997). In response to cellular stress, however, p53 accumulates in the nucleus. This accumulation is due to phosphorylation in its N-terminus by upstream kinases of the PI3K-like kinase family. These post-translational modifications (PTMs) inhibit the interaction with MDM2. Furthermore, the p300/CBP (CREB-binding protein) acetyltransferase acetylates p53 in its C-terminal domain and thereby prevents MDM2 dependent ubiquitination (Haupt et al., 1997; Grossman et.al., 2001; Li et al., 2002). Subsequently, also nuclear import via importin-α3 increases (Marchenko et al., 2010), and p53 shows reduced nuclear export as a change in the C-terminal acetylation induces p53 tetramerization leading to a masking of its nuclear export sequence (NES) (Stommel et al., 1999). This rise in nuclear p53 controls cell fate decisions (Figure 1.2.2.B) by changing the expression of target genes (Horn and Vousden, 2007; Vogelstein et al., 2000; Vousden and Prives, 2009). More specifically, three kinases of the PI3K-like family are activated in the DNA damage response: ataxia telangiectasia mutated (ATM) (Harper and Elledge, 2007), ataxia telangiectasia and Rad3-related (ATR) (Cimprich and Cortez, 2008) and DNA dependent protein kinase (DNA-PKcs) (Chiruvella et al., 2013). All three kinases modify site-specifically amino acids of the p53 protein, leading to functionally different regulation of

the DNA damage response (Figure 1.2.2.A). The kind of DNA damage, for example double or single strand DNA breaks (DSB and SSB, respectively), and the connected repair pathways are tightly linked with the activity of the upstream kinases (Ciccia and Elledge, 2010). On the one hand, ATM is activated in response to DSBs and regulates two pathways of DNA repair: non-homologous end joining (NHEJ) and homologous recombination (HR) (Lavin et al., 2006). On the other hand, ATR is induced only during HR (Yazinski and Zou, 2016), while activation of DNA-PKcs is necessary for NHEJ (Davis et al., 2014). These upstream kinases in turn phosphorylate not only p53 at specific sites, but also the downstream checkpoint kinases CHEK1/CHEK2 (Chk1/Chk2) that themselves modify p53, leading to cell cycle arrest at G1/S and G2/M transitions in the cell cycle prohibiting replication in the context of DNA damage (Smith et al., 2010).

1.2.2. STIMULUS SPECIFIC DYNAMICS OF P53

In the past, live-cell time-lapse imaging showed that information in a signaling pathway is not only encoded in the abundance or current state of a signaling molecule but also in the time-dependent changes of the localization, amount or activation state of a signaling component (Purvis and Lahav, 2013). These dynamic patterns are frequently masked in methods that average over a population of cells, as even genetically identical cells inherit substantial heterogeneity due to stochastic fluctuations (Eldar and Elowitz, 2010; Loewer and Lahav, 2011). Such dynamics can be described as a trajectory, a curve over time that encodes information in its features, such as amplitude, duration, or frequency (Purvis and Lahav, 2013). Many molecules in cellular signaling cascades encounter intricate, stimulus-specific dynamic patterns that affect gene expression and control cell fate. One class of signaling molecules for which this plays an important role are transcription factors. They show stimulus specific dynamic patterns of nuclear abundance and mediate cell fate programs by regulating gene expression (Cai et al., 2008; Hao and O'Shea, 2011; Hoffmann et al., 2002; Murphy et al., 2002; Nelson et al., 2004; Santos et al., 2007; Süel et al., 2007; Tay et al., 2010; Batchelor et al., 2011; Purvis et al., 2012). The complex interplay of dynamics and post-translational modifications enables a cellular signaling pathway to mediate concerted responses to different forms of stimuli, provides robustness and increases information transmission possibilities (Purvis and Lahav, 2013). For example, NF-κB oscillates after TNFα stimulation followed by nuclear export and leads to an inflammatory response, while delayed sustained dynamics after activation by lipopolysaccharides (LPS) induce an adaptive immune response (Covert et al., 2005; Werner et al., 2005; Tay et al., 2010). Another example is Erk in the MAP-Kinase pathway, which responds with one pulse to EGF stimulation inducing cell proliferation, while NGF stimulation leads to sustained high nuclear Erk levels and induces cell differentiation (Marshall, 1995; Nguyen et al. 1993). Initially, it was hypothesized that p53 shows damped oscillations after induction of DSBs by γ-irradiation (Lev Bar-Or et al., 2000). However, single-cell measurements by fluorescence microscopy showed that p53 accumulates in repeated pulses of uniform amplitude and duration upon DSBs (Figure 1.2.2.B) (Lahav et al., 2004; Batchelor et al., 2008). P53 pulses

DYNAMICS
Trajectory, a curve over time that can encode information in its features as amplitude or frequency.

DSB
DNA double strand breaks, induced for example by γ-irradiation leading to an activation of the p53 pathway by phosphorylation through the kinases ATM and DNA-PKcs.

are regulated through negative feedbacks by MDM2 and the PPM1D (WIP1) phosphatase, which are both p53 target genes themselves. After γ-irradiation (inducing DSBs), the amplitude and duration of p53 pulses remain constrained, while the number of pulses correlates with the amount of damage. It therefore has been suggested that p53 pulses depend on the persistence of DNA damage and the time until DSB repair (Batchelor et al., 2008). In contrast, SSBs, e.g. induced by UV radiation, lead to a sustained increase in p53 with comparably higher amplitude and longer duration that correlates with the amount of applied damage (Batchelor et al., 2011).

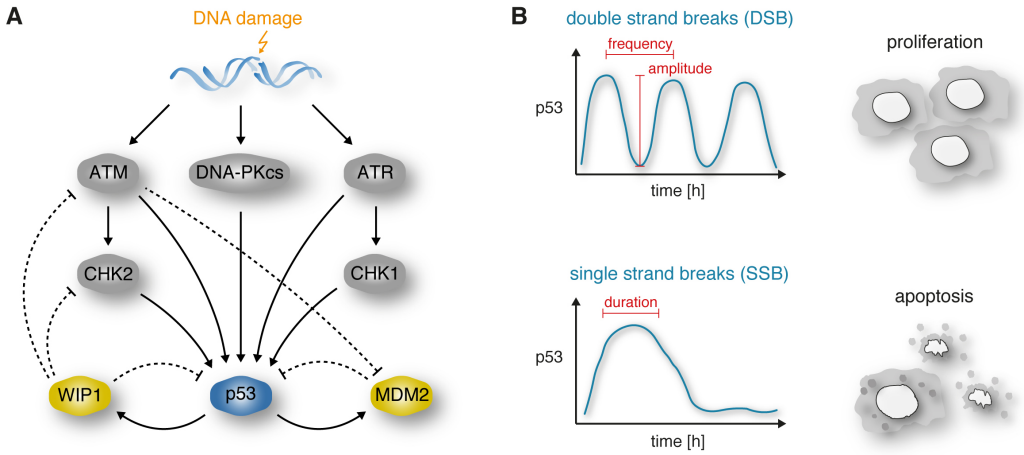

Figure 1.2.2 Stimulus specific p53 signaling dynamics in response to DNA damage mediate distinct cell fate decisions.

(A) The p53 signaling network exhibits different layers of regulation. Dependent on the kind of DNA breaks, different kinases are activated. In response to DNA double strand breaks (DSBs), ATM is recruited to damaged DNA sites by the MRN complex (complex of MRE11, RAD50 and NBS1 proteins), where it binds to DSBs and changes its conformation, leading to interaction and regulation of other proteins downstream. ATM is a Serine/Threonine kinase that autophosphorylates at S1918 upon damage and phosphorylates Chk2 as well as MDM2 and p53. ATR on the other hand is a Serine/Threonine kinase activated in response to single strand breaks (SSBs). In complex with its interaction partner ATRIP, it binds to SSBs when these are bound by replication protein A (RPA). ATR further phosphorylates Chk1 as well as p53 at different sites than ATM. The third kinase is DNA-PKcs. It is recruited to SSBs and DSBs through the protein Ku and activates p53. It has further been shown that DNA-PKcs can phosphorylate Chk1 and Chk2. While the different damage pathways have been studied separately for many years, it became more clear recently that the ATM-Chk2 and ATR-Chk1 pathways are not completely separate. When p53 is activated through site-specific phosphorylation, its direct interaction with the MDM2 protein and proteasomal degradation is prohibited. This increase in nuclear p53 levels leads to a rise in p53-dependent transcription of target genes. Two of these targets are MDM2 and PPM1D (WIP1). Both of these proteins build the core negative feedbacks of the dynamic p53 network. PPM1D is a phosphatase and not only a negative regulator of p53, but can also dephosphorylate the upstream kinases Chk2 and ATM leading to a reduction in their activity.
(B) The accumulation of p53 in the nucleus over time has been described by single-cell trajectories from live-cell time-lapse microscopy imaging. Induced by DSBs, p53 shows repeated pulses with an approximated pulse width of 6 h (depending on the cell line). These pulses of p53 do not change regarding their amplitude and width with an increase in the amount of damage (number of DSBs). In contrast, an increase in DNA damage has been shown to lead to more pulses of similar shape. Furthermore, this dynamics have been correlated with transient cell fate decisions as cell cycle arrest and DNA repair. SSBs on the other hand induce sustained high levels of p53 that correlate in duration and amplitude with the applied damage. Therefore, distinct pulse features, whether as a single long pulse that can be >12 h duration or a sustained increase cannot be defined for the p53 response to SSBs. However, this dynamic pattern has been shown to lead to terminal cell fates as apoptosis or senescence. The different dynamics are thought to result from a dominant upstream activation by ATM and ATR, and ATM specific dephosphorylarion by PPM1D (leading to pulses).

As suggested by mathematical modeling, the difference in dynamics is due to a lack of negative feedback regulation between PPM1D (WIP1) and the upstream kinase ATR in the DNA damage response to SSBs (Figure 1.2.2.B) (Batchelor et al., 2011). While pulsatile dynamics lead to transient cellular phenotypes such as cell cycle arrest, sustained p53 levels induce terminal cell states such as apoptosis or senescence (Purvis et al., 2012) (Figure 1.2.2.B). However, it is unclear how genetic circuits decode information from pulses and sustained dynamics mechanistically. More precisely, it remains unknown how transcription factors transmit this information at specific promoters into gene expression profiles that mediate cell fate decisions. Potential mechanisms include TF abundance, DNA binding affinity, post-translational modifications and interaction with co-factors, suggesting a complex interplay between upstream and downstream components.

1.2.3. DOMAIN STRUCTURE AND POST-TRANSLATIONAL MODIFICATIONS OF THE P53 PROTEIN

P53 has several functional domains that play critical roles in transcriptional regulation (Figure 1.2.3.A) (recently reviewed in Hafner et al., 2019; Sullivan et al., 2018). At the N-terminus, it contains two transactivation domains (TAD1, amino acids 20-40, and TAD2, amino acids 40-60) (Candau et al., 1997; Fields and Jang, 1990; Raycroft et al., 1990). Upstream kinases of the PI3K-like family phosphorylate the TADs in response to DNA damage, where they play an essential role in gene regulation (Brady et al., 2011). The TADs are followed by a proline-rich domain (PRD, amino acids 63-97) that promotes the interaction with RNAP2 and the TFIID complex during transcription initiation (Toledo and Wahl, 2006) and may regulate cell growth (Walker and Levine, 1996). The DNA binding domain (DBD, amino acids 100-300) recognizes promoter sites at the DNA (Pavletich et al., 1993; Cho et al., 1994; Kitayner et al., 2006; Kitayner et al., 2010). The interaction of cysteine residues (C176/238/242) in the DBD with one Zn^{2+} ion is fundamental for RE binding (Hainaut and Milner, 1993). The DBD is evolutionary conserved and exhibits mutations in 80% of p53 related cancers (Olivier et al., 2002; Pavletich et al., 1993). Next, p53 has a tetramerization/oligomerization domain (OD, amino acids 324-355) that is necessary for cooperative binding of p53 as a tetramer, as it oligomerizes as a dimer of dimers at target gene promoters (Wang et al., 1995; McLure and Lee, 1998; Kitayner et al., 2006). This process is promoted by the OD (Clore et al., 1995). However, in-vitro studies showed that the isolated DBD can also assemble tetramers (Veprintsev et al., 2006). Mutations in the OD lead to a loss of p53 binding to DNA and reduced expression of target genes (Davison et al., 1998; Imagawa et al., 2009; Kawaguchi et al., 2005). While the DBD regulates sequence-specific interactions to DNA, the intrinsically disordered C-terminal domain (CTD, amino acids 360-393) contributes to sequence-independent DNA recognition. Its secondary structure changes depending on interaction with different binding partners (Oldfield et al., 2008). For example, it forms an α-helix when interacting with calcium-binding protein S100($\beta\beta$) (Rust et al., 2000) or 53BP1 (Joo et al., 2002; Tong et al., 2015), while a β-strand

TAD1/2
N-terminal domains of p53, phosphorylated after γ-IR by upstream PI3K-like kinases, summarized as TAD in ***Figure 1.2.3.A.***

CTD
C-terminal domain of p53, intrinsically disordered and highly post translationally modified after DNA damage. ***Figure 1.2.3.A***

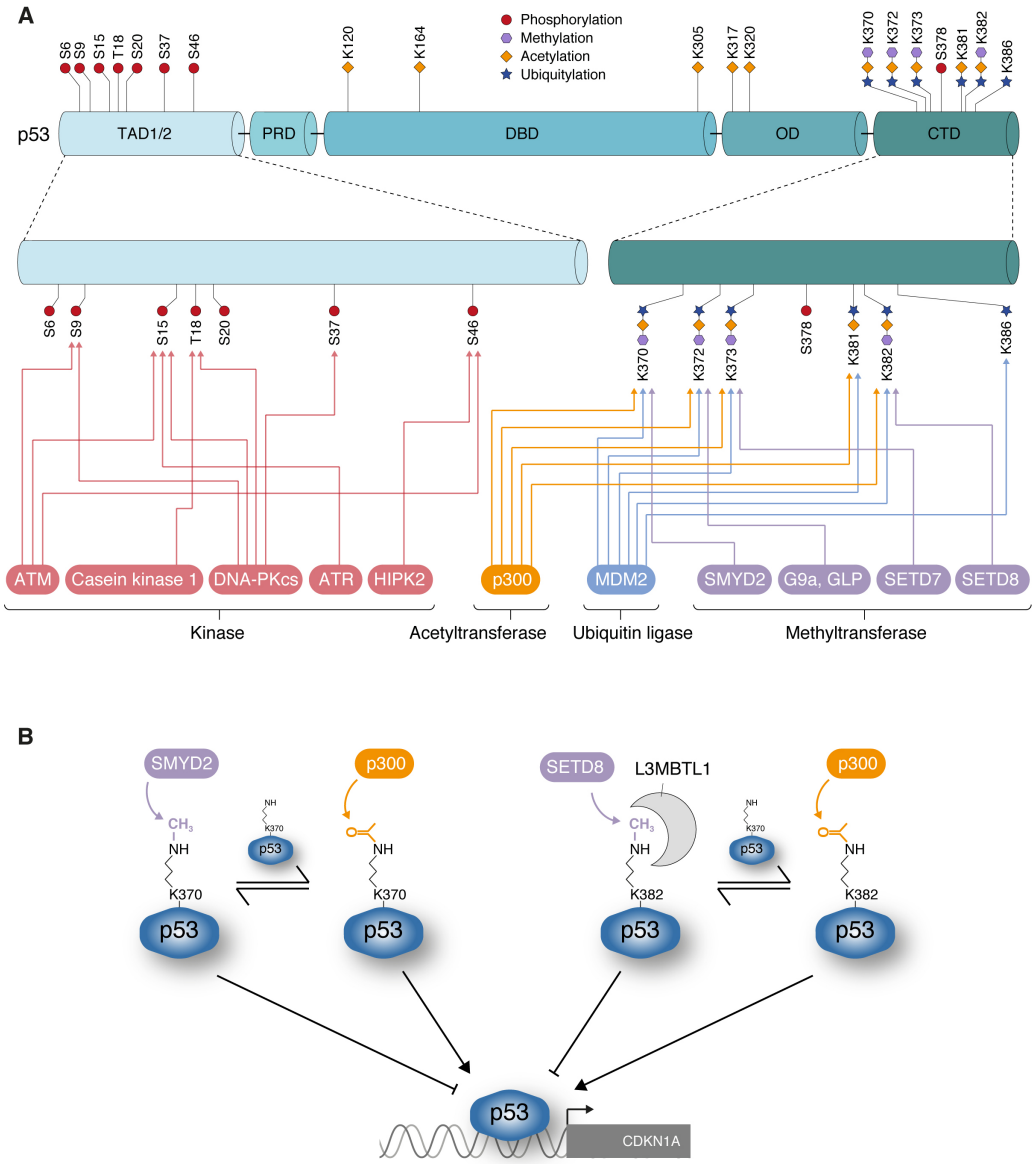

Figure 1.2.3 The p53 protein domains and selected post-translational modifications.

The p53 protein consists of several regulatory domains that play a key-role in p53's transcription factor activity and are highly post-translationally modified. A residue can be modified by different enzymes (mutually exclusive), key enzymes are displayed for N-terminal and C-terminal domains (enlargements).
(A) From N-terminus to C-terminus: TAD: transactivation domains (TAD1 amino acids 20-40, TAD2 amino acids 40-60), both depicted together as one domain; PRD: proline rich domain (amino acids 63-97); DBD: DNA binding domain (amino acids 100-300); OD: oligomerization/tetramerization domain (amino acids 324-355); CTD: C-terminal domain (amino acids 360-393); Enlargement left: Transactivation domains and post-translational regulation by upstream kinase signaling. Enlargement right: C-terminal domain and post-translational regulations. Modifying enzymes are only indicated for TADs and CTD.
(B) Lysine residues K370 and K382 in p53's C-terminal domain can be either acetylated or methylated with opposing effects on transcription. K370 is acetylated by p300 promoting transcription, while SMYD2 dependent mono-methylation of K370 has been shown to inhibit CDKN1A transcription. In the case of K382, also p300/CBP dependent acetylation leads to an increase in transcription. SETD8 dependent K382 mono-methylation, on the other hand, induces transcriptional repression of the CDKN1A promoter through binding of L3MBTL1 that keeps p53 bound in an inactive state at the promoter.
(Illustration freely adapted based on Hafner et al., 2019*)*

is established when in contact with Sirtuin 2 (Avalos et al., 2002). The before mentioned studies also showed that PTMs of the CTD affect its structure and thus the interaction with other proteins. In general, it has been shown that the CTD has an impact on gene expression, while the underlying mechanistic background is discussed controversially (Hafner et al., 2019; Sullivan et al., 2018). One suggested function is that it contributes to diffusion along the DNA and binding of the DBD at promoters through an induced fit (Oldfield et al., 2008) while PTMs further fine-tune co-regulatory interactions.

More than 300 combinations of PTMs regulate p53's activity, including phosphorylation, neddylation, sumoylation, methylation and ubiquitination (Gu and Zhu, 2012; Brooks and Gu, 2003; Bode and Dong, 2004). Many residues are modified by different enzymes introducing mutually exclusive modifications that have key-regulatory functions. Interestingly, p53 PTM regulation has been frequently found to be embedded with redundancy. Presumably, this serves as a safeguarding mechanism in case of loss of function mutations that affect individual components of the pathway (Toledo and Wahl, 2006; Bode and Dong, 2004) (Figure 1.2.2.A). One example is S15 in the TADs that is phosphorylated by eight different kinases and Chk2, which phosphorylates at least seven of p53's residues (Toledo and Wahl, 2006; Bode and Dong, 2004). The two most strongly modified regions are the TADs and the CTD. In response to DNA damage, PI3K-like kinases upstream of p53 phosphorylate the serine and threonine residues S6, S9, S15, T18, S20, S37 and S46, which inhibit the p53:MDM2 interaction and reduce MDM2 dependent ubiquitination of p53 (Toledo and Wahl, 2006) (Figure 1.2.3.A, enlargement left). These phosphorylations depend on the kind of the applied DNA damage, affect gene expression and subsequently cell fate (Lu et al., 1997; Sakaguchi et al., 1998; Kapoor and Lozano, 1998; Appella and Anderson, 2001). Furthermore, phosphorylation in threonine-proline motifs in the PRD induces a structural change that fosters binding of PIN1 (Peptidyl-prolyl *cis-trans* isomerase NIMA-interacting 1) and leads to proline *cis-trans* isomerization reducing MDM2's affinity to p53 (Toledo and Wahl, 2006). The CTD harbors several lysine residues (Figure 1.2.3.A, enlargement right) that can be acetylated, methylated or ubiquitinated. While ubiquitination flags p53 for degradation, the equilibrium between methylation and acetylation of specific lysine residues (K370, K372/73, and K382) affects gene expression output. In experimental studies, C-terminally acetylated p53 has been shown to be enriched at promoter sites (Luo et al., 2004) and the acetylation state of the CTD has been correlated to an increase of gene expression of p53 targets (Tafvizi et al., 2008; Tang et al., 2008; Hupp and Lane, 1994; Gu et al., 1997b; Liu et al., 1999). Furthermore, live-cell single-molecule measurements of p53 transcription showed that the p53 residence time at a response element is longer for CTD-acetylated p53 (Loffreda et al., 2017). On the other hand, mono-methylation of K370 by SMYD2 reduces gene expression and K382 mono-methylation by SetD8 decreases CDKN1A expression (Figure 1.2.3.B) (Huang et al., 2006; Shi et al., 2007). This effect is thought to be mediated by binding of the chromatin compaction factor Lethal(3)malignant brain tumor-like protein (L3MBTL1) that keeps p53 bound to the promoter in an inactive form as illustrated in Figure 1.2.3.B (West et al., 2010).

SETD8/ SMYD2

Methylases acting at specific lysine residues in p53's C-terminal domain leading to transcriptional repression. Smyd2 mono-methylates K370 and SetD8 mono-methylates K382.
Figure 1.2.3.B

1.2.4. P53 DEPENDENT TARGET GENE EXPRESSION

P53 nuclear accumulation in response to cellular stress leads to expression of over 300 protein-coding genes and noncoding RNAs that mediate cell fate decisions such as cell cycle arrest (p21, 14-3-3), apoptosis (PIG, BAX, PUMA, NOXA), senescence (PAI-1) or autophagy (DRAM) (Beckerman and Prives, 2010). Among p53 targets are also negative regulators of the p53 network, e.g. MDM2 and PPM1D (Beckerman and Prives, 2010; Fischer, 2017). P53's transcription factor activity is modulated through many factors to enable a concerted regulation of stimulus and gene-specific transcription: Sequence-specific response element binding, organization, and localization of binding motifs, as well as levels and modifications of the p53 protein itself. Co-regulatory mechanisms, e.g. chromatin modifications, long-range enhancer contacts and gene-specific protein-protein interactions, influence p53's activity as a transcription factor additionally.

P53 RE
Response element, gene-specific DNA sequence bound by p53 to regulate transcription. Consensus motif RRRCWWGYYY as depicted in ***Figure 1.2.4.***

P53 REs are gene-specific *cis*-regulatory sites in the DNA, fostering target gene transcription upon p53 activation and binding. They consist of two decamers separated by spacers of 0-21 bp that can be described with the sequence-motif RRRCWWGYYY, in which R is A/T, W a purine base and Y a pyrimidine base (Figure 1.2.4) (El-Deiry et al., 1992; Funk et al. 1992; Riley et al., 2008; Fischer, 2017). However, the described REs interestingly do not consist of two identical half-sites, and functional p53 binding sites can include elements that do not match this motif (Göhler et al., 2002). In general, p53's REs cluster in noncoding regions and are mostly found upstream of the TSS while also binding inside the first exon has been reported, as described for miR-34a (Riley et al., 2008). Some REs are within 300 bp to the TSS (e.g. MDM2, PCNA), but they can also be located inside the first intron as shown for MDM2, PUMA and PIG3 (Beckerman and Prives, 2010), suggesting a regulation of alternative transcription initiation by p53 (Fischer, 2017).

AFFINITY MODEL
The model suggests that p53's affinity to REs is correlated with cell fate specific gene expression. Cell cycle modulating genes have higher binding affinities than targets inducing apoptosis.

The affinity of a response element correlates with gene expression and is therefore essential to understand transcriptional output. It is defined by the sequence of the central core motif, with CATG having the highest affinity (Riley et al., 2008). Furthermore, the length of the spacer, the configuration of the half-sites and, to a lesser extent, the sequence of the remaining decamer contribute to the overall affinity (Riley et al., 2008; Verfaillie et al., 2016). Target genes involved in aligned response pathways often contain bindings sites with similar affinities. For example, it has been shown that REs of cell cycle arrest genes have high-affinities, whereas pro-apoptotic genes contain low-affinity sites (Inga et al., 2002; Qian et al., 2002; Hafner et al., 2019). Along these lines, the affinity-model suggests that p53 binding to promoters of apoptotic genes is of lower affinity than at genes regulating the cell-cycle. These differences in affinity lead to the expression of apoptotic genes only in response to high nuclear p53 levels (Weinberg et al., 2005; Qian et al., 2002; Kracikova et al., 2013; Murray-Zmijewski et al., 2008). In genome-wide ChIP-Seq studies, transcriptional activity correlates with p53 binding, independent of the kind of activation of the p53 pathway (Nikulenkov et al., 2012; Verfaillie et al., 2016). Despite low total levels, p53 can also be found at binding sites of target genes under basal conditions (Espinosa et al., 2003; Shaked et al., 2008) and it has been shown that solely an increase in p53 abundance is

insufficient to induce transcription, but that p53 needs to be C-terminally acetylated to activate transcription (Loewer et al., 2010; Berger et al., 2010). In line with this, biochemical studies connected post-translational modifications of p53 with the affinity of RE binding (Gu and Roeder, 1997). However, ChIP-Seq experiments addressing this question yielded controversial results. Barlev et al. showed that CTD-acetylated p53 clusters at TSSs to the same extent as CTD mutants that cannot be acetylated (Barlev et al., 2001), and p53 acetylation does not increase response element binding either (Laptenko et al., 2015). On the other hand, live-cell measurements indicate that TFs as p53 bind to REs transiently, while the residence binding time modulates transcription (Mueller et al., 2008; Hager et al., 2009; Lickwar et al., 2012; Loffreda et al., 2017).

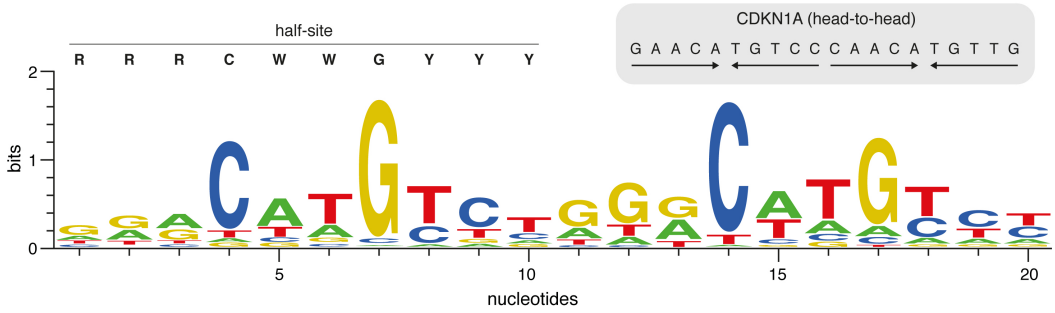

Figure 1.2.4 The consensus p53 binding motif.

Illustration of the p53 response element consisting of two decamers of the RRRCWWGYYY sequence in the *head-to-head* orientation. R stands for purine base (A/G) and Y for pyrimidine base (C/T), while W can be A or T. Between both decamers, some REs contain a short spacer of up to 13 bp. The orientation of p53 binding sites is described based on the orientation of the decamers to each other, which can be *head-to-head*, *head-to-tail*, or *tail-to-tail*. As an example, highlighted in grey, the genomic sequence of the CDKN1A (p21) RE is depicted, oriented in the *head-to-head* conformation without a spacer. (Figure adapted from Riley et al., 2008; Hafner et al., 2019)

An increase in p53 levels upon stimulation may lead to enhanced gene expression based on higher binding frequencies to REs (Coulon et al., 2013; Larson et al., 2009; Larson et al., 2011; Loffreda et al., 2017). For p53, live-cell fluorescence microscopy measurements showed that interactions of p53 with DNA are transient at the time-scale of seconds, both at specific and nonspecific targets (Hinow et al., 2006; Mueller et al., 2008; Mazza et al., 2012; Morisaki et al., 2014; Loffreda et al., 2017). Though, for many genes, including CDKN1A (p21), the abundance of p53 does not correlate with gene expression (Espinosa et al., 2003; Donner et al., 2007; Mattia et al., 2007; Hill et al., 2008). Instead, it has been shown that similar p53 levels lead to differential PIC assembly (Espinosa, 2008), indicating regulation of transcription through other co-regulatory factors at individual genes.

In addition to binding site architecture and position, one of such factors may be the DNA topology as the binding of the p53 tetramer introduces substantial changes to the DNA. It has been hypothesized that REs in flexible DNA conformational states are preferably bound by p53 (Nagaich et al., 1997a,b; Nagaich et al., 1999; Beckerman and Prives, 2010). Also, interactions of p53 with other regulatory co-factors have been suggested to orchestrate context specific promoter binding and transcriptional activation (Flores et al. 2002; Samuels-Lev et al., 2001; Sykes et al., 2006; Oda et al., 2000; Smeenk et al., 2011).

Directly at the promoters of its target genes, p53 interacts with co-factors and transcriptional regulators upon binding (Murray-Zmijewski et al., 2008). Examples are the histone modifiers p300/CBP, PRMT1, CARM1 or TIP60, leading to an increase in acetylation close to p53 REs (Beckerman and Prives, 2010) as well as of p53's CTD (p300/CBP). These proteins are involved in stimulus-specific gene regulation, e.g. GADD45 expression in response to SSBs (An et al., 2004) or PIN1 and ASSP1/2 related expression of targets that induce apoptosis (Follis et al., 2015; Aylon et al., 2010). Besides, interactions with other TFs have also been described. In response to DNA damage, NF-κB, estrogen receptor, MYC and SP1 are activated, leading to interactions with p53, modulating the transcriptional landscape and cell fate (Menendez et al., 2009; Beckerman and Prives, 2010). However, p53 binding does not exclusively correlate with an increase in gene expression. MDM2 and MDMX can bind to p53 at REs resulting in a repression of transcription (Pei et al.2012; Wade et al., 2013). This function is independent of their p53 specific ubiquitin ligase function. It is antagonized by competitive binding of MDM2 to p300, reducing gene expression of p53 targets (Grossman et al., 1998; Wadgaonkar and Collins, 1999). Downstream of p53 binding, additional factors may regulate target gene expression as well. RNA expression patterns of p53 targets depend on their RNA and protein half-lives (Hafner et al., 2017; Porter et al., 2016; Melanson et al., 2011; Hanson et al., 2019). Similar findings have been shown for the NF-κB pathway, highlighting that mRNA half-lives modulate gene expression downstream of NF-κB oscillations (Zambrano et al., 2016; Hao and Baltimore, 2009).

1.3. CHARACTERIZING STOCHASTIC GENE EXPRESSION

1.3

The classical view of eukaryotic transcription is based on the sequential binding of the associated proteins starting from TF recruitment to promoters leading to PIC assembly. According to this, binding of activators to regulatory sequences induces the sequential, step-wise assembly of the general transcription machinery and RNAP2 forming the PIC (Figure 1.3.1.A) (Orphanides and Reinberg, 2002; Fuda et al., 2009) (Figure 1.3.1.A). In this model, the rate of initiation is thought to be the limiting step of RNA production, as after the first initiation some factors remain at the TSS and can be re-initiated (Yudkovsky et al., 2000), leading to continuous transcriptional output featuring a Poisson-like distribution of RNA molecules in a population of cells (Ko et al., 1990) (Figure 1.3.1.A/1.3.2.B).

IN THIS CHAPTER

1.3.1. TRANSCRIPTION IS AN INHERENTLY STOCHASTIC PROCESS

In the past two decades it became clear that mRNA levels are highly heterogeneous in genetically identical cells, suggesting discontinuous instead of continuous transcription (Figure 1.3.1.B) (Suter et al., 2011b). In general, this gene expression noise can result from different sources. Intrinsic sources of noise are stochastic fluctuations of molecules and reactions involved in transcription, translation and degradation, which are the core processes of the RNA life-cycle. Extrinsic noise sources are changes in cell state, e.g. cell cycle, overall gene expression levels or the mitochondrial content (Elowitz et al., 2002; Swain et al. 2002; Kaufmann and van Oudenaarden, 2007; das Neves et al., 2010; Snijder and Pelkmans, 2011; Sherman et al., 2015). While all these factors increase the variability of cellular RNA levels, transcriptional noise has been identified as the main reason for heterogenous gene expression in isogenic cells (Raj and van Oudenaarden, 2008; Eldar and Elowitz, 2010, Suter et al., 2011b; Sanchez and Golding, 2013). In this regard, it has been shown for different organisms, including *Dictyostelium*, yeast, bacteria, *Drosophila* embryos and mammalian cell lines, that gene expression is primarily discontinuous, leading to episodic bursts of transcribed RNA, thereby increasing the cell-to-cell variability of RNA levels (Bar-Even et al., 2006; Raj et al., 2006; Paré et al., 2009; Yunger et al., 2010; Muramoto et al., 2012; Chong et al., 2014). This stochastic bursting was discovered already in 1979 by electron microscopy of chromosomes isolated from *Drosophila* embryos (McKnight and Miller Jr., 1979). In this study, nascent RNAs were detected only at defined genomic segments. These fluctuations are hypothesized to result from switching of promoter states between an active and an inactive period. Subsequently, RNA production is enhanced or attenuated respective to the state of the promoter leading to a broad heterogeneity in RNA counts between genetically identical cells in a population (Suter et al., 2011a; Blake et al., 2003; Kaern et al., 2005; Raj et al., 2006; Raj and van Oudenaarden, 2008; Sanchez and Golding, 2013). During a burst of

STOCHASTIC BURSTING
Discontinuous transcription at individual promoters that leads to heterogenous RNA expression. The molecular interactions leading to stochasticity are illustrated in ***Figure 1.3.1.B.***

transcription, trains of RNAP2 produce many nascent RNA molecules, while a promoter is in the transcriptionally active state (Lionnet and Singer, 2012). The characteristic traits of these bursts can be major regulating factors of the transcriptional response, with each gene operating in its specific range of kinetic parameters of stochastic transcription (Suter et al., 2011a; Molina et al., 2013). Single-cell fluorescence imaging has shown that this bursty transcription induces prominent temporal fluctuations in RNA levels (Chong et al., 2014; Suter et al., 2011a; Bahar Halpern et al., 2015b; Harper et al., 2011).

BURST SIZE
RNAs produced in an active promoter period. Includes the duration and amplitude of a burst.

BURST FREQUENCY
On:off rate of stochastic bursting, the frequency of transcription initiation.

Two features characterize bursting at a specific promoter over time: The number of RNAs transcribed in an active period (burst size) and the number of transcription periods over time (burst frequency) (Golding et al., 2005; Raj et al., 2006; Suter et al., 2011b). The burst frequency has been shown to increase gene expression noise during the cell cycle (Skinner et al., 2016), while cellular RNA levels were found to correlate with cellular volume mediated by the burst size (Kempe et al., 2015; Padovan-Mehar et al., 2015). Transcriptional output at the promoter can rise by faster switching between active and inactive states (increase in burst frequency), or by a stabilization of the active state (increase in burst size) (Figure 1.3.2.D). On the molecular level, an increase in the burst size reflects the duration of

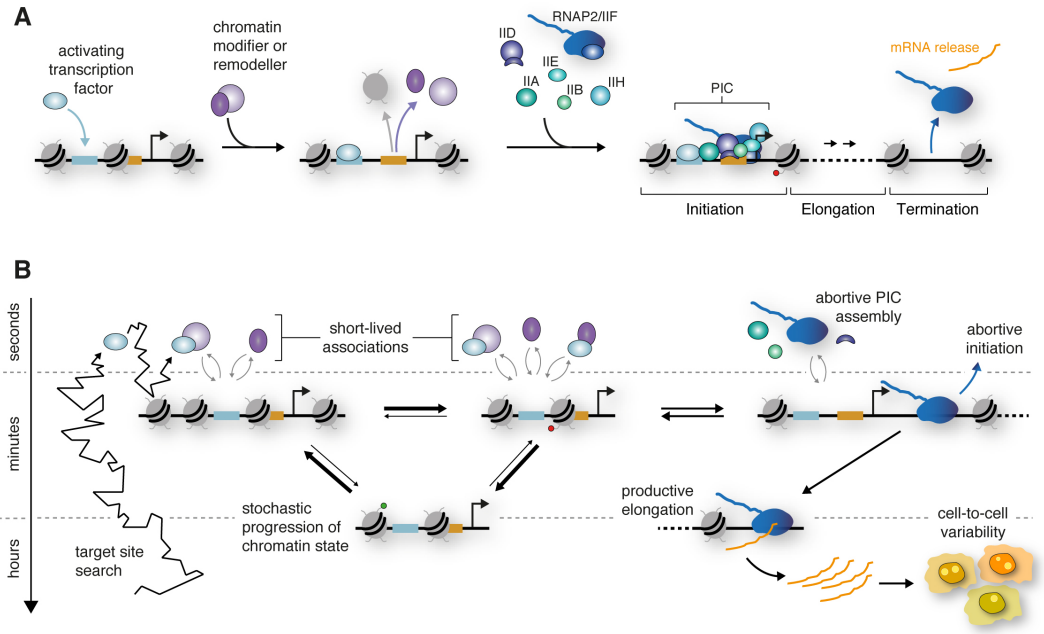

Figure 1.3.1 Transcription is rather a stochastic process including molecular interactions at different time scales than a continuous assembly.

(A) The initial model of transcription was the continuous assembly of molecules on different levels of gene regulation. Starting with binding of activators that interact with the *cis*-regulatory region, chromatin modifying enzymes and remodelers that lead to a rearrangement of the promoter proximal chromatin. According to this sequential recruitment model, this is followed by the assembly of RNAP2 and GTFs (TFIIA, IIB, IID, IID, IIH) forming the PIC and initiating the transcription cycle from initiation to elongation and termination.
(B) Recent work has shown that transcription is rather a stochastic than a continuous process including long- and short-lived associations that can range from seconds and minutes to hours. These differences in the time-scales and the low number of molecules involved in some of these processes affect the progression of different regulatory states of transcription as many steps become stochastic. Also, on the level of PIC assembly and transcription, disassembly and abortive transcription can occur, while only in the case of a productive transcription cycle RNAs are transcribed. These stochastic fluctuations throughout transcriptional activation and regulation introduce a distinct cell-to-cell variability.
(Illustration freely adapted based on Coulon et al., 2013)

RNAP2/IC re-initiation, while the burst frequency is the rate of initiation to establish the PIC (Yudkovsky et al., 2000; Hahn, 1998).

In both processes, several co-regulatory factors play a crucial role through promoter binding and recruitment of transcription machinery subunits (Figure 1.3.1.B) (Fuda et al., 2009). Though, the molecular mechanisms underlying transcriptional bursting kinetics remain elusive, both globally and on the level of specific genes (Larson et al., 2011; Suter et al., 2011b). Suggested effectors include TF binding, chromatin state, DNA topology, chromatin remodeling, enhancer looping, the stability of PIC and RNAP2 pausing that act on different time-scales and probabilities of interaction (Figure 1.3.1.B). Besides, burst size and frequency have been suggested to depend on the genomic context (Dar et al., 2012; Hocine et al. 2015). In this regard, it has been shown that while burst frequency often modulates transcription at weaker expression loci, genes with higher expression tend to be modulated by burst size (Dar et al., 2012). In contrast, spatially neighboring genomic loci were found to have similar kinetics, indicating a role of upstream effectors (Kaufmann and van Oudenaarden, 2007). Additionally, chromatin modifications and TF binding have been suggested to modulate bursting (Sanchez and Golding, 2013). Examples are H3K27 acetylation at the Bmal-1 promoter (Nicolas et al., 2018) as well as c-Fos nuclear accumulation (Senecal et al., 2014) that were both shown to correlate with burst frequency. Likewise, TATA-box and TF binding are related with gene expression noise (Blake et al., 2006; Murphy et al., 2007). Though, despite individual examples, global influences of chromatin remodeling on stochastic bursting are unclear (Raser and O'Shea, 2004). Also, bursting kinetics are potentially affected by modulation of the basal transcription machinery, RNAP2 recruitment, re-initiation, pausing and processivity through co-regulation by secondary factors and their interactions with RNAP2's CTD (Allen and Taatjes, 2015; Porrua and Libri, 2015; Jonkers and Lis, 2015; Margaritis and Holstege, 2008).

1.3.2. MATHEMATICAL MODELS TO QUANTIFY GENE EXPRESSION

Mathematical models allow to quantify and characterize cellular processes and enable to assess parameters that are not, or only inefficiently, measurable by experimental approaches. Models have been employed to characterize multiple layers of gene regulation from chromatin dynamics to TF binding kinetics and RNA expression. In the classical description of the gene regulatory function, TF occupancy at *cis*-regulatory elements can serve as an estimate for transcriptional output (Ptashne and Gann, 2002; Setty et al., 2002; Rosenfeld et al., 2005). However, transcription is a multi-layer process that is regulated on numerous levels (Figure 1.3.1). Beyond binding of TFs to their response elements and recruitment of the general transcription machinery, TFs can modulate transcription through the interaction with co-factors, e.g. chromatin modifying enzymes in *trans* (Figure 1.3.2.A) (Coulon et al., 2013; Voss and Hager, 2014) as described in the preceding chapters. Transcription is often characterized by stochastic models. In the simplest description, a one-state promoter model, transcription is continuously active and therefore leads to a low dispersion in total transcribed RNAs per cell in a population of cells for both moderate and

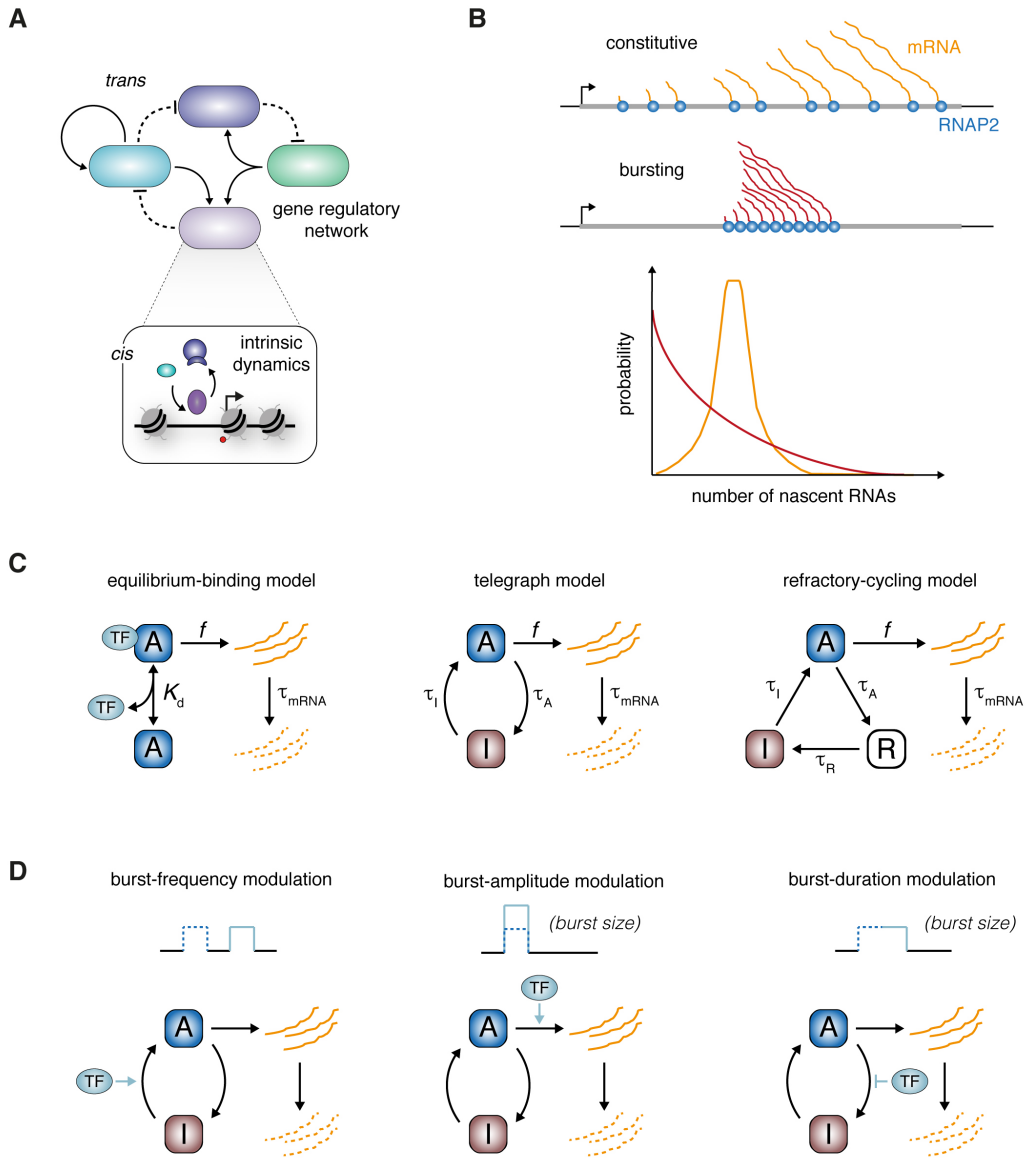

Figure 1.3.2 Mathematical modeling of transcriptional networks.

(A) Schematic illustration of interactions in a gene regulatory network. Transcription factors bind in *cis* to response elements following intrinsic binding kinetics and dynamic interactions with chromatin and co-factors. On the other hand, TFs are embedded in *trans* into dynamic networks with additional interaction factors, catalyzing for example enzymatic reactions.

(B) Transcription can be either constitutive with constant trains of RNAP2 transcribing nascent RNA or a bursty process with intermitted phases of active and inactive transcription. Dependent on the kind of the transcriptional process, the probability of a nascent RNA is similar to a Poisson (orange curve) or Non-Poisson (red curve) distribution.

(C) Mathematical models describing transcription. In the one-state equilibrium binding model (left panel), a gene is always in the active state (A) and TF binding to regulatory elements leads to RNAP2 recruitment and transcription initiation *(f)*. Stochastic bursting is represented by the two-state random telegraph model (center). Therein, a promoter can switch between an active (A) and an inactive (I) state with a lifetime τ_I/τ_A for both states, while only in the active state, transcription initiation *(f)* occurs. The refractory cycling model (right panel) describes a more complex scenario of an additional refractory state (R, lifetime τ_R) that is transcriptionally inactive, but cannot directly convert into the active state. τ_{mRNA} is the RNA lifetime.

(D) Illustration of different options how TF binding at the promoter may affect the rate of transcription *(f)* in the two-state random telegraph model, and changing burst size and frequency (Li et al., 2018).
(Illustration freely adapted based on Coulon et al., 2013 (A), Lenstra et al., 2016 (B), Li et al., 2018 (C/D))

strongly transcribed genes (Figure 1.3.1.A, 1.3.2.B). Steady-state mRNA levels in the population of cells can thus be described by a Poisson distribution (Figure 1.3.2.B). Examples for this are different yeast mRNAs, for which the dispersions of RNAs per cell as shown by single-molecule fluorescence in-situ hybridization (smFISH) fit a one state promoter model with a Poisson distribution (Femino et al., 1998; Zenklusen et al., 2008; Mueller et al., 2013; Zechner et al., 2014). On the other hand, stochastic gene expression from bursty transcription is commonly described using the *random telegraph* model. This includes the switching between two states, the active (A) and the inactive (I) state of a promoter (Figure 1.3.2.C) (Peccoud and Ycart, 1995; Kepler and Elston, 2001; Paulsson, 2004; Friedman et al., 2006). In the active state, transcription occurs with a constant probability over time, while there is no RNA transcription in the inactive phase. The distribution and variability of bursty transcription are not Poissonian with a broad heterogeneity in the population (Fano factor >1). TF binding to *cis*-regulatory elements in this framework leads to a modulation of burst-amplitude, burst-frequency or burst-duration (Figure 1.3.2.D). Many studies to date challenge the view of the two-state model, as transcription is a multi-state process and changes in different cellular contexts. The simplest example is a third refractory state before transcription (re-)initiation, as included in the refractory-cycling model (Figure 1.3.2.C) (Li et al., 2018). Due to the high complexity of the molecular processes and numerous interactions involved in transcription, recent studies point towards multi-state descriptions (Zoller et al., 2015; Fritzsch and Baumgaertner et al., 2018; Corrigan et al., 2016).

RANDOM TELEGRAPH
Two-state model describing stochastic bursting.

FANO FACTOR
Measure for the dispersion of a probability distribution. Calculated as:
$f = v^2/m$
v: variance
m: mean

1.3.3. EXPERIMENTAL APPROACHES TO STUDY RNA EXPRESSION BASED ON SINGLE-CELL IMAGING DATA

Studies of gene expression circuits have employed biochemical assays in the past, e.g. Northern Blotting and quantitative real-time PCR (qRT-PCR). These methods characterize average properties of gene expression over time in response to different stimuli and lead to a characterization of the relative changes of expression in the population allowing to compare different states. Though, due to cell lysis, pooling and amplification steps, these techniques only indirectly measure total RNA abundance and both localization and single-cell resolution are lost. Therefore, to quantitatively characterize small changes in abundance, RNA expression, transcription properties and localization of RNAs over time, these technologies are limited. Furthermore, recent developments in single-cell technologies have shown that observations in the population do not necessarily reflect the identity and molecular mechanisms in individual cells due to cellular heterogeneity even in genetically identical cells (Raj and Oudenaarden, 2008). In more sophisticated cellular systems, such as tissues or organisms, cell-type specific effects and low abundant or transition cell states can be overseen. Significant technological advances have been achieved by newly developed single-cell RNA sequencing approaches and corresponding computational analysis that can be broadly applied to study RNA expression kinetics transcriptome-wide (Tanay and Regev, 2017; Ziegenhain et al., 2018). Additionally, fluorescence imaging-based techniques allow to localize individual RNA molecules with sub-cellular localization of nanometer precision in single cells (Vera et

SMFISH
single molecule fluorescence in situ hybridization
Figure 1.3.3.A.

al., 2016). From such data, it is possible to measure the noise in a population of cells and transcription kinetics even for low abundant RNAs. SmFISH techniques that hybridize fluorescent-labeled oligonucleotide probes in fixed, permeabilized cells (Femino et al., 1998; Raj et al., 2008) have been applied and further developed in this context (Figure 1.3.3.A). The general principle of all these techniques is the hybridization of a critical amount of fluorescence-labeled DNA oligonucleotides with high sequence-specificity to an RNA of interest with a low binding rate to off-targets. SmFISH approaches are based on placing as many 50mer (Femino et al., 1998) or 20mer labeled oligonucleotides as possible on the target RNA (Raj et al., 2008) (usually >40) (Figure 1.3.3.A). After hybridization of samples with these probes and potential co-labelling of other cellular structures as the nucleus and cytoplasm, acquisition of 3-dimensional microscopy images (60x/100x objective) allows to visualize individual RNAs. These images can then be used to perform quantitative analyses of the number of RNAs, their localizations and fluorescence intensity, allowing to extract information of transcriptional activity and the dispersion in the population. Either custom scripts or available software tools as *FISH-Quant* (Mueller et al., 2013) are applied for quantitative image analysis (Figure 1.3.3.B). In *FISH-Quant,* images are loaded as 3D tiff-stacks and experimental parameters as the wavelength of the fluorescent dye and the pixel size are defined. Outlines of the nucleus, cytoplasm and transcription sites are then generated based on additional staining, either manually or automatically through additional software tools. To quantify RNA spots, images are filtered in a two-step process. Therefore, the background fluorescence is approximated by smoothing with a large Gaussian Kernel and then subtracted from the raw image. Then, the signal-to-noise ratio (SNR) is enhanced by smoothing with a small Gaussian Kernel (Figure 1.3.3.B) (Mueller et al., 2013). In the next step, RNA spots are pre-detected from filtered images either by identifying local maxima of the fluorescence intensity (3D local maximum detection), or by identifying connected components from a generated binary image after thresholding. For both approaches, the minimum intensity of a fluorescent spot needs to be defined by a manual threshold. For this, the number of detected spots is plotted as a function of the fluorescence intensity threshold, leading to a plateau of a range of intensities with similar resulting spot counts when analyzing high-quality images (Figure 1.3.3.B) (Mueller et al., 2013). Additionally, a quality score based on the intensity distribution around a spot can be applied. After this pre-detection of spot-candidates, RNA counts are quantified by fitting a 3D Gaussian at the pre-detected sites in the raw image for correct extraction of intensity values and locations (Figure 1.3.3.B) (Mueller et al., 2013). As false positive identifications of RNA spots show a broad width of the fitted Gaussian, detected RNA spots can be selected by thresholding the width of the Gaussian in x,y,z, as well as its amplitude and the background of the image (Figure 1.3.3.B). The remaining spots represent the single-cell RNA count, including spot intensity and sub-cellular localization. When images were acquired with identical conditions (same day experiments), the before mentioned settings can be applied to a batch of image stacks (Figure 1.3.3.B) (Mueller et al., 2013).

FISH-QUANT
Software for the quantitative analysis of RNAs from smFISH images
Figure 1.3.3.B.

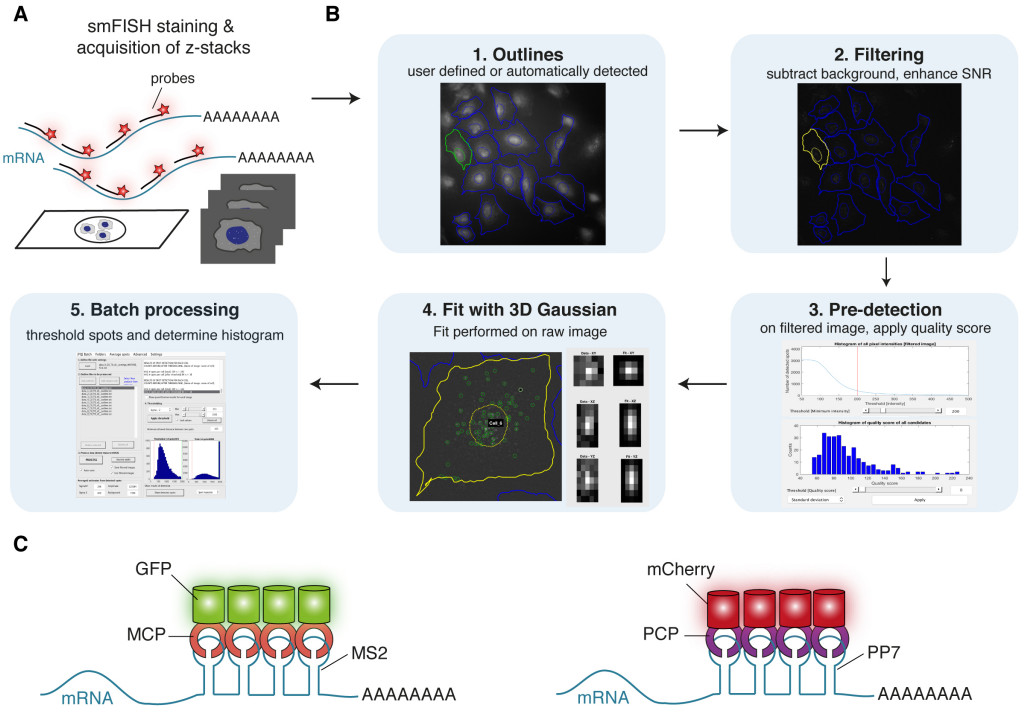

Figure 1.3.3 Imaging based quantification of RNA counts using *FISH-Quant*.

(A) Illustration of the traditional smFISH strategy, hybridizing fluorescence labeled, sequence specific oligonucleotides to a target RNA of interest after fixing and permeabilizing samples.
(B) Workflow of the *FISH-Quant* based analysis of RNA counts from smFISH images from outline generation (1), pre-processing steps as filtering (2) and pre-detection in filtered images (3) to the actual detection of spots by 3D Gauss fitting (4). Detection settings can be used for batch analysis of multiple images and the detected RNA counts can be further thresholded. (Flow chart freely adapted from Mueller et al., 2013)
(C) Repeats of RNA hairpins (e.g. MS2 or PP7) can be integrated into the mRNA (e.g. into 5' or 3' UTR), which are then specifically bound by a coat protein (MCP for MS2, PCP for PP7) that is co-expressed as a fluorescent protein fusion (Buxbaum et al., 2015).

While smFISH is based on staining fixed samples, techniques to label RNA in living cells exist as well. The most widely used technique is the MS2/PP7 based RNA imaging system. It employs repeats of cognate RNA hairpins integrated in the RNA of interest, usually at the 3' or 5' UTR (Figure 1.3.3.C). The specific co-expressed coat-proteins MCP or PCP (MS2-coat protein, PP7-coat protein) that can be fluorescently tagged (e.g. by GFP-fusion), bind to these hairpins and thereby allow to visualize individual RNAs and transcription sites inside cells (Bertrand et al., 1998; Chao et al., 2008). The MS2 and PP7 systems differ in their sequence, 3D structure of the hairpin and thus the specific coat protein. For both, multiple versions have been generated and both have been used in parallel to identify RNAs (Figure 1.3.3.C) (Hocine et al., 2013). These techniques now allow to quantitatively characterize stochastic transcription in single cells and at individual promoters.

In summary, these technologies pave the way for a better mechanistic understanding of transcriptional regulation in different cellular contexts as p53-mediated gene expression in response to distinct dynamics after DNA damage.

MS2/PP7
Hairpin repeats that can be genetically integrated into the RNA and are specifically bound by MCP/PCP.

MCP/PCP
MS2/PP7 binding proteins that can be conjugated with fluorescence proteins as GFP for live-cell RNA imaging ***Figure 1.3.3.C.***

CHAPTER 2 SCOPE

2.1. AIM OF THIS THESIS & LEADING QUESTIONS

The scope of this thesis is to understand how oscillations of transcription factors affect transcriptional regulation of their target genes in single cells and at individual promoters. To approach this question, I chose the tumor suppressor p53 as a paradigm. P53 responds with repeated nuclear pulses to ionizing radiation. These stimulus-specific dynamic features affect cell fate decisions through distinct expression of target genes. However, it is yet unknown how p53 oscillations are decoded into RNAP2 recruitment and transcriptional output on the level of an individual promoter and gene-specific differences have not been characterized yet. To approach this systematically, I addressed three aims and key-questions:

Aim 1: Characterizing p53 target gene expression in single cells by smFISH.
To understand gene regulation through TF dynamics, it is necessary to quantitatively characterize mRNA expression and transcription site activity in a high number of individual cells. Therefore, I aimed to set-up an imaging and computational analysis pipeline that allows to robustly characterize mRNA expression. As >300 genes have been shown to be regulated by p53, a higher number than quantifiable by smFISH, it is important to select a representative panel of target genes. The leading question of this first aim is: How can experimental and computational tools be employed to robustly characterize gene expression from single-cell imaging data?

Aim 2: Characterization of mRNA expression and stochastic bursting of target genes in the p53-mediated response to DNA damage by ionizing radiation (IR).
To characterize how p53 pulsing upon DNA damage affects the stochastic expression of its targets, single-cell mRNA levels, gene expression noise and promoter activity must be analyzed. To approach this question and derive changes in promoter activity upon p53 activation, I focused on differences in transcriptional activity and RNA counts in the context of p53 pulses induced by ionizing radiation, following two main questions: (1)What are the numbers and variability of target gene RNAs in single cells and how does p53 activation change dispersion and expression patterns? (2) Does p53 activation induce common mechanistic changes of promoter activity or are the effects gene-specific?

Aim 3: A mechanistic analysis of p53-mediated stochastic bursting.
Oscillations of transcription factors are a prominent feature in cell signaling. However, it has been previously shown that the dynamics of TFs are correlated with differential gene expression and cell fate. Hence, it is critical to understand how stochastic gene expression of target genes changes when p53 oscillations are tuned to other dynamic features. But, how does p53 activation modulate the transcription cycle mechanistically? To approach this, I aimed to analyze stochastic bursting in the context of targeted perturbations of the dynamic p53 response.

CHAPTER 3 RESULTS

3.1. SMFISH BASED ANALYSIS OF P53 DEPENDENT TRANSCRIPTION IN SINGLE CELLS

3.1

IN THIS CHAPTER

P53 dependent transcription has been studied extensively in the past decades. However, earlier work focused mainly on analyzing individual target gene promoters. With advances in next-generation sequencing, genome-wide and transcriptome-wide studies suggested more and more genes that are transcriptionally regulated by p53 (Riley et al., 2008; Beckerman and Prives, 2010; Sullivan et al., 2018; Fischer, 2017). Newly developed techniques that allow to infer RNA expression kinetics transcriptome-wide from single-cell RNA sequencing remain to proof their potential in the context of cell signaling and for studying low abundant RNAs (Herzog et al., 2017; Schofield et al., 2018; Erhard et al., 2019, Jürges et al., 2018). Therefore, smFISH (Raj et al., 2008) was chosen to characterize a subset of target genes as a paradigm to contribute to a better understanding of p53-mediated transcription after DNA damage.

3.1.1. SELECTION OF P53 TARGET GENES

To select p53 targets, I performed a meta-analysis of available RNA-Seq and ChIP datasets (Hafner et al., 2017; Fischer, 2017) and compared these to an unpublished RNA-Seq dataset of MCF10A cells in the context of stable p53 shRNA knock-down generated previously (Finzel, 2016a). Using available pre-processed read count data, I compiled a list of fold-changes of up- and down-regulated target genes based on their expression levels in basal state and 4 h after 10 Gy γ-IR. I applied a threshold of a minimum fold change of induction by 1.5 and a dependency on p53 by comparing MCF10A wild-type to cells expressing p53-shRNA as described in Chapter 5.3.4. Based on these parameters, 71 genes were found to be down-regulated 4 h post γ-IR, whereas 184 were up-regulated. The complete list of p53 dependent, up-regulated target genes in the MCF10A dataset can be found in Chapter 8.3.1 (Table 8.3.1). In a recent review, a list of 399 p53 target genes from 319 individual studies performed between 1992 and 2016 has been documented (Fischer, 2017). 349 of these were human target genes. This list includes 16 genome-wide datasets from different cell lines and treatments. P53 target gene expression was re-analyzed and evaluated with a summed regulation score (-16 to +16) based on their expression levels (Fischer, 2017). Remarkably, only CDKN1A and RRM2B were detected as target genes in all datasets. This may point towards cell line and stimulus-specific differences (Stewart-Ornstein et al., 2017) and highlights challenges regarding reproducibility. Based on the available data, 127 p53 targets were up-regulated in more than six genome-wide datasets (expression score >6) (Fischer, 2017). However, only one of the reviewed datasets was generated upon γ-IR treatment (5 Gy,

DATASETS

Fischer, 2017:
349 human targets, 127 up-regulated in >6 genome-wide datasets, multiple cell lines & damages

Finzel, 2016a:
144 targets, 105 up-regulated in MCF10A, 10 Gy 4 h

Hafner et al., 2017:
229 targets, 183 up-regulated in MCF7, 10 Gy 4 h

Figure 3.1.1.A, Table 3.3.1

CAL51 breast cancer cell line) (Rashi-Elkeles et al., 2014). Therefore, I compared this dataset with the MCF10A data and a time-course experiment in MCF7 cells (10 Gy γ-IR) that identified 229 differentially expressed targets with a fold change of >2.0 by RNA-Seq, of which 183 were up-regulated (Hafner et al., 2017). The comparison of all three datasets led to a candidate list of 17 genes that were consistently up-regulated across cell lines, with different p53 stimuli as measured by RNA-Seq and ChIP experiments (Table 3.1.1, Figure 3.1.1.A). Besides, additional genes were only found in both 10 Gy RNA-Seq datasets (Table 8.3.1). Differences in RPKM/FPKM counts between datasets may be due to cell line specific or technical aspects. Though, despite for CDKN1A and BTG2, the fold change of induction was surprisingly robust when comparing 4 h to basal levels in MCF7 and MCF10A cells (Table 3.1.1). A robust quantification of RNA molecules from smFISH is only possible when RNA counts do not exceed a concentration leading to an accumulation of fluorescent signal in one pixel. However, for most p53 targets no quantitative data on the exact numbers of mRNA molecules are available. Therefore, RPKM/FPKM read counts were used to approximate the order of magnitude of expression levels. In summary, criteria to select candidates for smFISH were defined as:

I. A fold change of mRNA levels by >1.5 in the early response (3-4 h)
II. A minimal gene length of 5000 bp to hybridize a sufficient number of fluorescent probes (>20) to exons and introns
III. RPKM/FPKM read counts of <100 in basal state

Seven protein coding p53 target genes were selected based on these criteria (Table 3.1.1, grey). These include MDM2 and PPM1D, the two proteins that build the core negative feedback loops of the p53 network. Both have been shown to shape the stimulus specificity of p53 dynamics (Lu et al., 2005; Pant et al., 2013; Batchelor et al., 2011). Additionally, BAX (BCL2 Associated X Protein) and CDKN1A, both regulating cell fate, were selected. BAX forms homo- or heterodimers with other members of the Bcl-2 protein family inducing apoptosis by interaction with the voltage-dependent anion channel (VDAC) in mitochondria. CDKN1A inhibits all cyclin/CDK complexes leading to cell cycle arrest in G1- and S-Phase of the cell cycle. Besides, DDB2 (Damage Specific DNA Binding Protein 2) and RRM2B (Ribonucleotide Reductase Regulatory TP53 Inducible Subunit M2B) were chosen as proteins involved in DNA damage sensing and DNA repair. DDB2 forms a heterodimer with DDB1 binding to damaged DNA sites, while RRM2B ist the R2 subunit of the ribonucleotide reductase enzyme that processes nucleotide precursors for DNA replication and DNA repair. Lastly, SESN1 (Sestrin1), a protein that activates AMPK (AMP-activated protein kinase) and inhibits the mTOR pathway and cell proliferation, was selected. All of these genes have been described in >10 genome-wide ChIP studies and show an increase in mRNA levels in both RNA-Seq datasets when cells were irradiated (Fischer, 2017; Hafner et al., 2017; Finzel, 2016a). Additionally, the selected genes are involved in different downstream response pathways (Figure 3.1.1.B), their expression is clearly p53 dependent and their fold change of induction after γ-IR is in the same order of magnitude (Figure 3.1.1.C). However, the number and position of p53 binding sites among these targets differs,

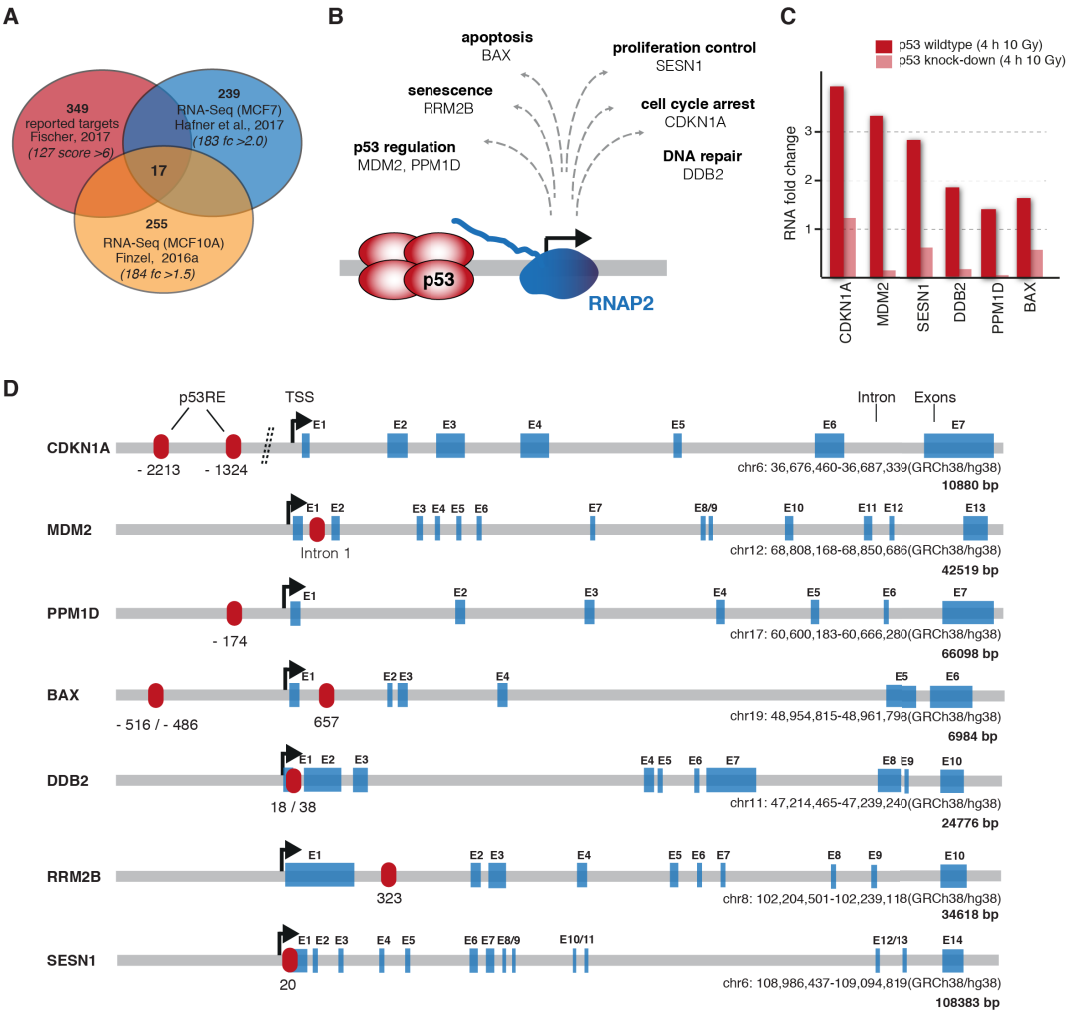

Figure 3.1.1 Selection of p53 target genes to study p53 dependent transcription.

(A) Venn diagram schematically illustrating the overlap of identified p53 target genes based on a meta-analysis of available datasets. This leads to the candidate list in Table 3.1.1. The analysis was generated based on datasets by Fischer, 2017, a recently published RNA-Seq time course data treating MCF7 cells with 10 Gy γ-IR (Hafner et al. 2017) and a dataset of MCF10A cells irradiated with 10 Gy γ-IR (Finzel, 2016a).

(B) Target genes that were selected for smFISH based, single-cell characterization of stochastic transcription, are involved in different cell fate programs as schematically indicated. CDKN1A (Cyclin Dependent Kinase Inhibitor 1A), MDM2 (Mouse Double Minute 2), PPM1D (Protein Phosphatase Mg^{2+}/MN^{2+} Dependent 1D), BAX (BCL2 Associated X Protein), DDB2 (Damage Specific DNA Binding Protein 2), RRM2B (Ribonucleotide Reductase Regulatory TP53 Inducible Subunit M2B), SESN1 (Sestrin1).

(C) All target genes selected for the course of this study, show a fold change in the same order of magnitude 4 h post 10 Gy γ-IR (red), while their expression level are strongly reduced in the context of stable p53 shRNA knock down (light red).

(D) Schematic representation of the genomic structure of selected p53 targets including Transcription Start Site (TSS), exons (blue) and non-coding/intronic regions (grey). Predicted positions of p53 response elements p53RE are shown in red with their respective position. When the exact position is unclear, multiple options or regions are depicted (Fischer, 2017; Riley et al., 2008; Tanaka et al., 2000; Ma et al., 2007). Illustration of genes is based on ensembl (Hubbard et al., 2002)/genome browser (Tyner et al., 2017) entries and only schematically represent the structure of the coding sequence. Distances and sizes are not to scale.

Table 3.1.1 Candidate list of p53 target genes.

Candidate list of 17 p53 target genes generated from a meta-analysis of available literature data. The compared datasets are named by the first author of the corresponding publication (Fischer, 2017; Finzel, 2016a and Hafner et al., 2017). The table provides an overview of the parameters for each target gene (gene symbol), its localization on the DNA strand and the documented gene length from genome browser/ensembl entries (Hubbard et al., 2002; Tyner et al., 2017). The regulation score as displayed for the reviewed p53 datasets from Fischer, 2017 represents the number of datasets in which a target appeared as p53 up-regulated (here min. 6, max. 17). The fold change of induction (fc) as displayed for the MCF10A (Finzel, 2016a) and MCF7 (Hafner et al., 2017) datasets, was calculated from the change in read counts measured before and 4 h post DNA damage. Genes that have a high regulation and expression score of at least 6, reviewed by Fischer, 2017 are up-regulated in MCF7 and MCF10A cells. To better approximate the expression strength, read counts from RNA-Seq are listed for both **γ**-IR treated cell lines as well. Gy: Gray; RPKM: reads per kilo base per million mapped reads; FPKM: fragments per kilo base per million reads. Selected p53 targets for subsequents experiments are highlighted in grey.

gene symbol	strand	gene length	regulation score (6-17)	fc MCF10A 4 h 10 Gy	fc MCF7 4 h 10 Gy	RPKM MCF10A 0 h (basal)	RPKM MCF10A 4 h 10 Gy	FPKM MCF7 0 h (basal)	FPKM MCF7 4 h 10 Gy
	+/-	[bases]	*Fischer, 2017*	*Finzel, 2016a*	*Hafner et al., 20 17*	*Finzel, 2016a*	*Finzel, 2016a*	*Hafner et al., 2017*	*Hafner et al., 2017*
ANKRA2	-	13506	10	2.2	3.0	1.8	4.0	4.4	13.3
BAX	+	6984	12	1.8	2.2	50.6	89.0	103.7	224.8
BTG2	+	4112	14	2.3	7.5	16.5	38.0	8.3	62.5
CDKN1A	+	10880	17	3.9	14.4	62.5	246.2	35.6	514.2
DDB2	+	24776	14	1.9	3.6	24.8	47.6	34.2	123.6
FAM212B	-	33762	8	3.8	4.2	1.2	4.7	3.0	12.3
GLS2	-	17471	6	2.1	3.2	2.0	4.1	1.8	5.9
MDM2	+	42519	16	3.3	3.4	15.7	51.6	38.1	127.9
ORAI3	+	7386	8	1.6	2.5	2.6	4.2	5.5	13.6
PPM1D	+	66098	12	1.9	2.0	2.1	4.1	56.3	110.8
RPS27L	-	32150	13	1.5	1.5	31.9	48.8	114.8	177.5
RRM2B	-	34618	17	2.7	2.4	8.1	21.9	25.0	59.0
SESN1	-	108383	11	3.0	5.9	5.2	15.6	11.5	67.8
SESN2	+	23040	8	2.4	3.7	4.3	10.5	6.9	25.7
TP53INP1	-	23440	11	3.9	5.2	2.1	8.0	9.3	48.5
XPC	-	33637	12	1.8	3.5	12.0	22.2	15.0	53.2
ZNF337	-	23710	7	1.5	2.1	19.8	30.1	11.0	22.9
ZNF79	+	22591	8	2.3	2.3	1.7	3.9	2.4	5.6

as does the architecture of their *cis*-regulatory regions and coding sequences (Figure 3.1.1.D). In summary, they can be considered as well studied, representing conditional p53 target genes that have core functions in the response to DNA damage including the p53 network, DNA repair, cell cycle arrest, apoptosis and proliferation upon DNA damage.

3.1.2. EVALUATION OF CONTROL GENES FOR SMFISH

Common house-keeping genes that are used as controls for quantitative real-time PCR (qRT-PCR), e.g. GAPDH and β-Actin, are not ideal for smFISH based analyses due to their high copy numbers, leading to more than one mRNA per pixel. Furthermore, it has been shown that DNA damage can affect the transcription of some housekeeping genes (Sharungbam et al., 2012; Iyer et al., 2017; Nielson et al., 2018). To test control genes, I performed a qRT-PCR based screen at 3 h and 6 h after 10 Gray (Gy) γ-IR in MCF10A and A549 cells (Figure 3.1.2.A/B). To this end, the mean relative quantification (RQ) RNA expression fold change of the following described house-keeping genes with reasonable gene length for smFISH was measured after γ-IR: HMBS (Hydroxy-methylbilane synthase), HPRT (Hypoxanthine Phosphoribosyl-transferase 1), PUM1 (Pumilio RNA Binding Family Member 1), SDHA (Succinate Dehydrogenase Complex Flavoprotein Subunit1) and HER2/ERBB2 (Erb-B2 Receptor Tyrosine Kinase 2) (Figure 3.1.2). The change in expression levels ranges from 0.5 (6 h 10 Gy HPRT, MCF10A) to 2.1 fold (6 h 10 Gy HER2, MCF10A) compared to basal expression. However, also cell line specific differences were observed as, for example, HER2, HRPT and SDHA showed differential effects increasing or decreasing after γ-IR in both cell lines (Figure 3.1.2). A minimum change in expression upon DNA damage was found for HMBS for both cell lines comparing the basal state to time-points after γ-IR treatment. HMBS was therefore selected as reference gene for smFISH.

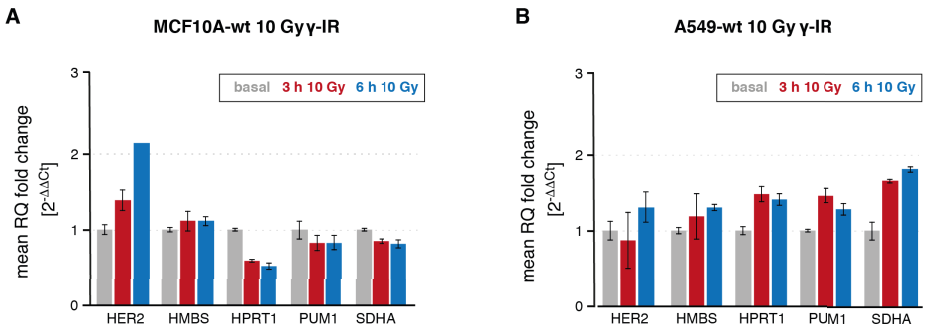

Figure 3.1.2 Selection of p53 independent control genes for smFISH experiments.

(A) QRT-PCR screen of MCF10A wild-type cells was performed, represented as mean relative fold change of mRNA expression 3 h and 6 h after 10 Gy γ-IR DNA damage for different potential control genes has been performed, with β-actin expression was used as a reference gene at time-point t=0 h (basal, no γ-IR). Error bars represent standard deviation of Ct values (CtSD); RQ: relative quantification, HMBS: Hydroxy-methylbilanesynthase; HPRT: Hypoxanthine Phospho-ribosyltransferase 1; PUM1: Pumilio RNA Binding Family Member 1; SDHA: Succinate Dehydrogenase Complex Flavoprotein Subunit1; HER2: Erb-B2 Receptor Tyrosine Kinase 2.
(B) Parallel screen to (A) with identical conditions, but in A549 wild-type cells.

3.1.3. SMFISH TO CHARACTERIZE P53 DEPENDENT TRANSCRIPTION IN SINGLE CELLS

To establish smFISH, MDM2 mRNA staining and analysis were optimized. First, existing hybridization, imaging and computational analysis protocols were extended and improved to increase the signal-to-noise ratio (SNR, S/N) and ensure technical and biological reproducibility. Therefore, a set of 48 fluorescent (CAL Fluor Red 610) labeled oligonucleotide probes targeting MDM2 RNA at different exons was designed (Figure 3.1.3.A, Chapter 5.1.1). Optimization of fixation and staining procedures led to a robust, high-quality staining protocol that allowed quantitive imaging and downstream analyses. To improve the SNR, a staining protocol with 0,5% (v/v) sodium dodecyl sulfate (SDS) and 5% (w/v) ethylene carbonate (EC) in the hybridization buffer for additional reduction of background fluorescence was implemented (relative SNR increase of 1.6) (Figure 3.1.3.C/E). The use of 10% EC has been suggested to completely replace toxic formamide in buffers in other studies (Moffit et al., 2016; Matthiesen and Hansen, 2012). Full substitution of formamide has not been established in this study but could be tested in future applications. The SNR quantification was performed using the FIJI plug-in SNR.jar (Sage and Unser, 2003; Schindelin et al., 2012). The SNR is expressed in decibel (dB) and measured as described in equation [1], where n is the pixelsize per image, r is the reference image, t is the tested image and x, y are positions of pixels in images. To determine the SNR, the plug-in requires a reference image that is compared to the test image(s).

SNR.JAR
Software for measurements of signal to noise ratio, FIJI plug-in. Allows to measure SNR, PSNR, RMSE, MAE from microscopy images (Daniel Sage, EPFL)

$$SNR = 10 \cdot log_{10}\left[\frac{\sum_{0}^{n_{x-1}}\sum_{0}^{n_{x-1}}[\,r(x,y)\,]^2}{\sum_{0}^{n_x}\sum_{0}^{n_{x-1}}[\,r(x,y)-t(x,y)\,]^2}\right] \qquad [1]$$

The optimization of buffer conditions led to an increase in SNR to 1.6 dB compared to 1.0 dB for the standard manufacturers protocol used as a reference as shown for an example experiment (Figure 3.1.3.E). Three different cell lines that have been used in representative, p53 related studies and express the selected target genes were stained: MCF10A, A549, and MCF7 (Figure 3.1.3.D) (Stewart-Ornstein and Lahav, 2017; Hafner et al., 2017; Finzel, 2016a, Finzel et al., 2016b, Chapter 3.1.1). Despite identical staining procedures, the direct comparison revealed differences in image quality and in the absolute number of mRNA spots. MCF7 cells showed elevated MDM2 expression under basal conditions, compared to both other cells lines (Figure 3.1.3.D). These higher levels may result from p53 independent MDM2 over-expression in MCF7 cells that has been reported previously for estrogen receptor α (ERα) positive breast cancer cell lines and tissue samples (Saji et al., 1999; Swetzig et al., 2016). A549 cells had quantitatively higher SNR ratios compared to MCF7 and MCF10A (SNR: 1.0_{MCF10A} dB < 2.3_{MCF7} dB < 7.03_{A549} dB) (Figure 3.1.3.E). While all three cell lines led to quantifiable smFISH staining after hybridization, A549 cells were therefore chosen as a model system for further analysis.

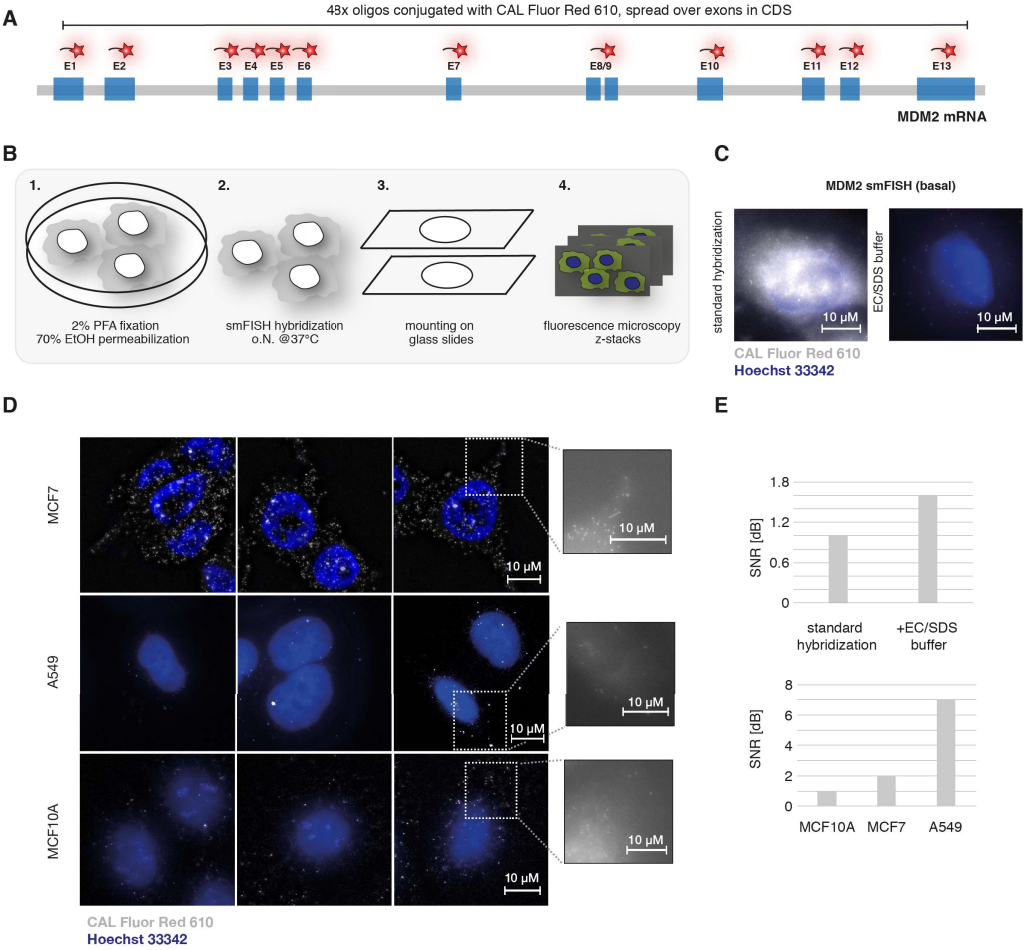

Figure 3.1.3 SmFISH to quantify p53 dependent transcription in single cells.

(A) Schematic outline of MDM2 RNA and positioning of smFISH probes conjugated with CAL Fluor Red 610 along the transcript. CDS: coding sequence; E: exon

(B) Overview of the manufacturers protocol for smFISH staining that was optimized to gain optimal fluorescent staining and imaging of fluorescence images. PFA: Para-form-aldehyde, EtOH: Ethanol, o.N.: over night.

(C) To reduce background fluorescence in smFISH images and gain additional background quenching, a novel hybridization buffer composition was established. EC: ethylene carbonate, SDS: sodium dodecyl sulfate. Different buffer compositions were screened to find optimal conditions. Two example images (A549 cells, 60x) of maximum projected and merged z-stacks (otherwise unprocessed) of MDM2 smFISH and Hoechst 33342 staining in presence and absence of EC/SDS buffer condition are displayed. The scale bar corresponds to 10 µM.

(D) Microscopy images (60x) of smFISH staining in three different cell lines (MCF7, A549, MCF10A). Images show different single cells under basal conditions of one image as composite representation of maximum intensity projection from z-stacks (Hoechst 33342 (405 nm) nuclear stain and CAL Fluor Red 610 smFISH probe). For better visualization, median filtered background subtraction (20 pixel) has been applied and LUTs have been optimized (only in print, not for analysis). The scale bars correspond to 10 µM for all images per row.

(E) Bargraphs of mean measured SNR in different images for MCF7, MCF10A and A549 cells under basal conditions from unprocessed example images shown in (D) (lower panel) as well as in two different hybridization buffer conditions (standard hybridization vs. EC/SDS buffer) (upper panel). The SNR is measured in dB.

3.1.4. HIGH THROUGHPUT ANALYSIS OF RNA EXPRESSION BASED ON SMFISH

Single-cell studies have shown that cell-to-cell heterogeneity leads to substantial differences in RNA expression levels (Raj et al., 2008). Sources of variability can be intrinsic or extrinsic and affect gene expression (Chapter 1.3.1) (Raj and van Oudenaarden, 2008). Also, p53 dynamics vary in single cells (Lahav et al., 2004), introducing a potential source of heterogeneity on the level of TF regulation. To obtain a representative picture of the transcriptional state, it is necessary to assess how many cells need to be quantified. To this end, I performed a quantitative analysis of three biological replicates of MDM2 mRNA staining under basal conditions and 3 h after 10 Gy (Figure 3.1.4.A). While mean levels were similar, indicating a high level of reproducibility, both the median and the coefficient of variation (CV) as a measure of variability changed significantly when the number of quantified cells was low (Figure 3.1.4.A). To estimate the optimal sample size (quantified cells), effect sizes employing bootstrap confidence intervals (CIs) were computed using the *MATLAB*-based *DABEST* packages (Ho et al., 2019). These datasets were then compared in two steps. First, effect sizes were computed as median differences based on 95% CIs for each pair of quantified MDM2 expression data (Figure 3.1.4.B). Second, all basal and induced (3 h 10 Gy) datasets were batch-analzyed (Figure 3.1.4.C). The computed effect sizes from the different datasets showed a correlation between CIs and sample size (comparison of datasets of one condition in Figure 8.3.1). Although this analysis was not performed systematically for more datasets and targets, the measured replicates of MDM2 expression had narrower CIs when increasing the sample size from <50 (set2) to 50-100 cells (set1). A further increase in sample size to >150 cells (set3) had only a lower effect. Therefore, about 100 cells per condition were considered as a robust cell number in the following experiments. However, CIs may differ for targets with expression noise distinct from MDM2's gene expression noise.

DABEST
MATLAB/ Python/R based packages by Ho et al., 2019; Estimation graphic as a method to measure effect sizes and display full statistical information of a dataset.

A comparison of fold changes from available RNA-Seq data in MCF7 and MCF10A cells (Chapter 3.1.1) with the quantified mRNA levels from smFISH showed a similar fold change of induction (Figure 3.1.4.D) at 3 h or 4 h post 10 Gy γ-IR. As bootstrapping data revealed the necessity to gain a high number of cells for reproducible quantitative data, the staining protocol and computational analysis pipeline were optimized to allow for quantification of a high number of cells. Staining of cells with NHS-succinimidylester conjugated with AlexaFluor-488 fluorescence dye and Hoechst 33342 DNA staining were employed to enable segmentation of the nucleus and cytoplasm. NHS is an amine-reactive cross-linker that non-specifically reacts with primary amines (R-NH_2) in proteins. This combination allowed for semi-automatic analysis using custom pipelines in *CellProfiler* (Carpenter et al., 2006) and *FISH-Quant* (Mueller et al., 2013) to generate cellular and nuclear outlines (Figure 3.1.4.E).

NHS-AF488
Succinimidylester conjugated with AlexaFluor 488 nm dye, amine reactive cross-linker, used for ubiquitous cytoplasmic staining and segmentation.

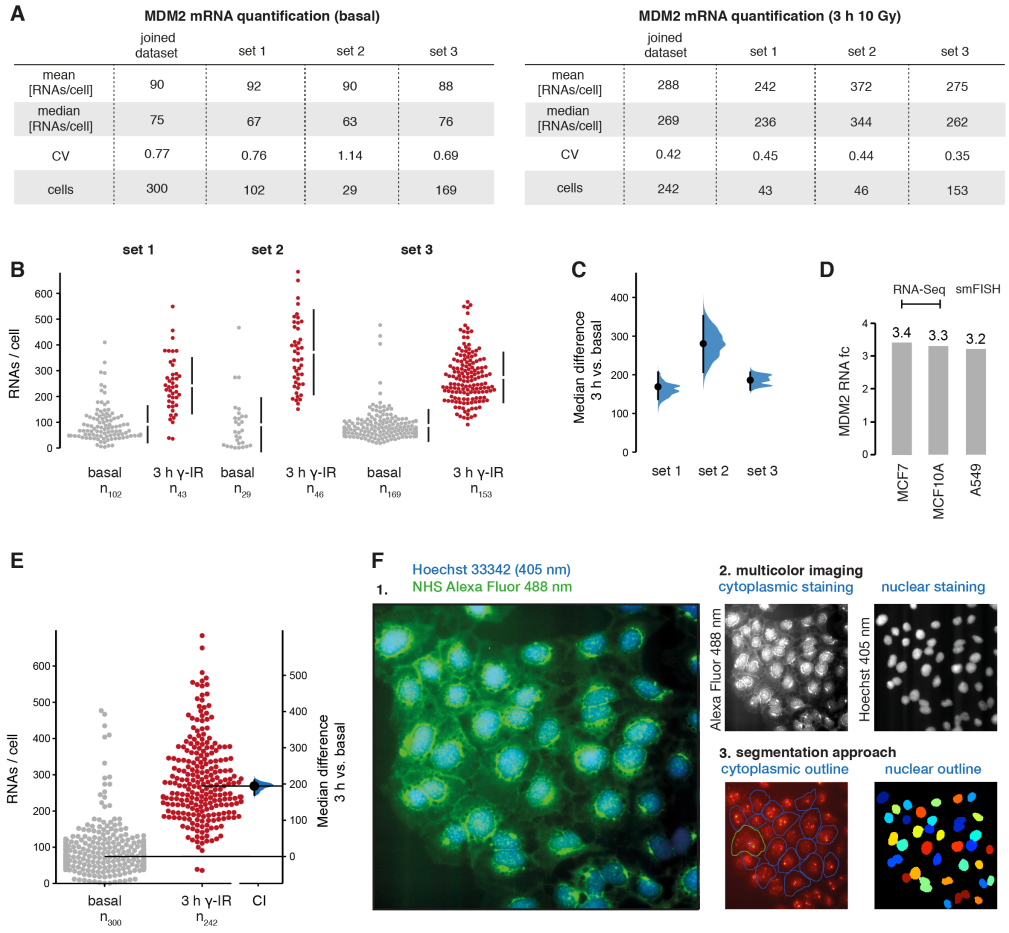

Figure 3.1.4 Reproducibility of smFISH quantifications and measurement sample size.

(A) Overview of mean and median quantified mRNA measurements from *FISH-Quant* from three biological replicates of independent experiments with different numbers of quantified cells in basal state (left panel) and 3 h post 10 Gy **γ**-IR DNA damage (right panel). CV: coefficient of variation used as a measure of variability in the population.

(B) Statistical comparison based on effect size measurement of the three paired sets of distributions.The median difference between control and 3 h 10 Gy is shown in the Gardner-Altman estimation plot (Ho et al., 2019).

(C) The median difference is plotted on a floating axes on the right as a bootstrap sampling distribution. The median difference is depicted as a dot while the 95% confidence interval (CI) is indicated by the ends of the vertical error bar. The unpaired median difference between Set1 basal 3 h 10 Gy is 1.69e+02 [95.0% CI 1.37e +02, 2.06e+02]. The two-sided p-value of the Kruskal test is 2.31e-13. The median difference for Set2 is 2.8e +02 [95.0% CI 2.07e+02, 3.52e+02] with a p-value of 5.36e-11, and for Set3 1.86e+02 [95.0% CI 1.61e+02, 2.06e+02] with a p-value of 5.51e-48. 5000 bootstrap samples were taken; the CI is bias-corrected and accelerated (Ho et al., 2019).

(D) A comparison of the median fold change of MDM2 mRNA expression after 10 Gy in MCF7, MCF10A and A549 cells is shown in bargraphs. MCF7 (3 h) and MCF10A data (4 h) are based on RNA-Seq experiments (Hafner et al., 2017; Finzel, 2016a), and A549 (3 h) data are quantified from smFISH. fc: fold change

(E) The median difference between basal and 3 h 10 Gy (summed as described in B/C) is displayed. The unpaired median difference is 1.94e+02 [95.0% CI 1.7e+02, 2.1e+02] with a p-value of 8.35e-73.

(F) A schematic overview of the experimental pipeline employing multicolor imaging and semi-automatic segmentation based on *FISH-Quant* (Mueller et al., 2013) and a custom cell profiler pipeline (Carpenter et al., 2006) is provided.

3.2. SINGLE-CELL RNA EXPRESSION LEVELS OF P53 TARGETS AFTER DNA DAMAGE

3.2

IN THIS CHAPTER

For characterizing p53 dependent gene expression of the selected target genes upon DNA damage it is crucial to compare RNA counts in the context of different p53 nuclear levels. Therefore, RNA expression levels for the selected genes and their distributions in single cells at defined time-points need to be compared. Furthermore, previous studies suggested correlations between the cell cycle state and cellular volume with RNA expression (Padovan-Merhar et al., 2015; Battich et al., 2013), as well as a passive noise filter through compartmentalization (Bahar Halpern, 2015a; Stoeger et al., 2016). Therefore, it may be informative to analyze the effect of these parameters on p53 target gene expression.

3.2.1. LIVE-CELL IMAGING TO DEFINE TIME-POINTS OF CHANGING P53 NUCLEAR LEVELS AFTER γ-IR

P53 responds with a series of undamped pulses to DNA damage by γ-IR (Lahav et al., 2004) while its dynamics can be highly heterogeneous in single cells (Geva-Zatorsky et al., 2006). Also, the timing of p53 pulses varies in cell lines due to distinct ATM states (Stewart-Ornstein and Lahav, 2017). To verify pulsatile dynamics in A549 cells, I generated a stable clonal fluorescent reporter cell line by lentivirus transduction and limited dilution cloning, employing screening based on antibiotic resistance. In line with previous work (Strasen et al., 2018), a histone 2B (H2B) reporter, fused to an enhanced cyan fluorescent protein (eCFP) (Heim and Tsien, 1996) at the C-terminus was constitutively expressed from a human Ubiquitin C promoter (UbCp). This leads to a homogeneously distributed nuclear fluorescence signal in most cell cycle phases (except mitosis) and allows for automated tracking of nuclei. To quantify p53 over time (Figure 3.2.1.A, B), cells were then transduced with a p53 reporter construct with a mVenus fluorescent protein at the C-terminus (Kremers et al., 2006), constitutively expressed from an EF1α promoter (Chapter 5.2). The use of transgenic cell lines is feasible in this context as nuclear p53 levels rise through stabilization of the p53 protein, but not via transcriptional up-regulation in response to γ-IR (Lakin and Jackson, 1999). Additional attempts to gain a p53-mVenus A549 reporter cell line based on Cas9-mediated knock-in remained ambiguous. Using available constructs (Sheng et al., 2019), a high number of resistant clones (>50) after selection for Neomycin resistance was reached, while genetic screening by direct PCR did not reveal results matching a successful knock-in. One explanation could be mutations due to imperfect homology-

REPORTER CELLS (*A549*)

UbCp-H2B-eCFP-Hygromycin

EF1αp-p53-mVenus Neomycin

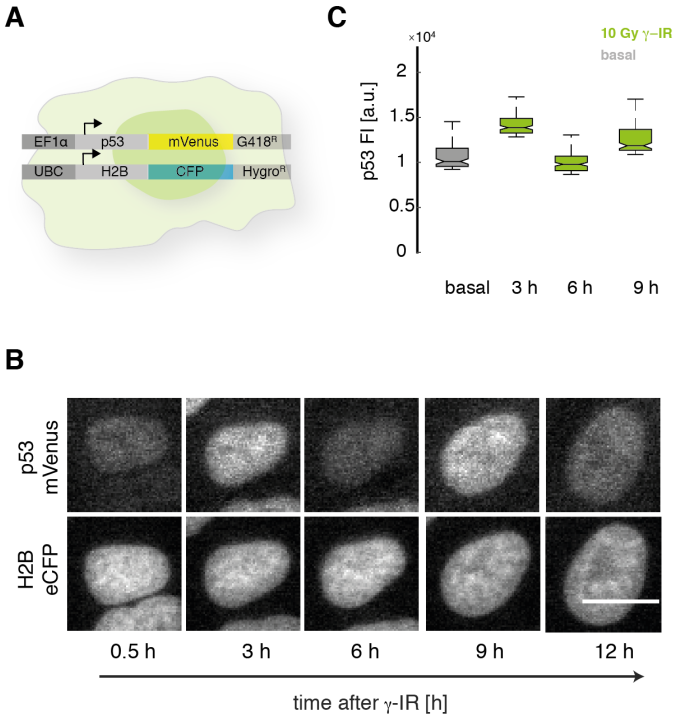

Figure 3.2.1 P53 dynamics in A549 reporter cells to define distinct time-points after γ-IR.

(A) Schematic representation of the stable clonal A549-p53-mVenus-H2B-eCFP reporter cell line that has been generated by lentivirus transduction. H2B-eCFP is expressed from a constitutive Ubiquitine C promoter (UbCp) and selected for antibiotic resistance using Hygromycin B. P53-mVenus is constitutively expressed from a human EF1α promoter and selected for antibiotic resistance based on Neomycin.
(B) Example images from live-cell time-lapse microscopy imaging of p53-mVenus and H2B-eCFP nuclear marker after 10 Gy **γ**-IR. Cells were imaged every 10 min for 24 h under stable temperature (37°C) and CO_2 (5%) conditions. P53 levels are clearly increased at 3 h and 9 h compared to basal, 6 h and 12 h time-points, while the H2B-eCFP nuclear signal remains similar at all time-points. Scale bar corresponds to 10 µm.
(C) P53 Immunofluorescence in A549 wild-type cells, quantified as integrated intensity levels. Boxplots represents the quantification at the defined time-points (basal, 3 h, 6 h and 9 h) of integrated intensity in cells with the highest 10% of signal. Whisker represent 25th to 75th percentile. Notches display interval endpoints. If notches do not overlap, they represent a significance at the 5% confidence level. Outliers are not shown. Sample size of the total dataset is 4839 cells (quantified nuclei), the upper 10th percentile of each condition is represented by 482 cells in total with similar sample sizes of n >100 for each conditions.

directed repair (HDR) after Cas9 cleavage. A recent genome-wide study also showed that genetic and transcriptional evolution induces substantial differences in response to chemotherapeutic drug treatment, which also activates the p53 pathway and DNA repair (Ben-David et al., 2018). However, these hypotheses were not approached in this thesis and it remains unclear if an increase in knock-in efficiency for example by using inhibitors such as XL413 (CDC7 kinase inhibitor) could be applied (Wienert et al., 2018). To extract p53 dynamics, transgenic A549-p53-mVenus-H2B-eCFP reporter cells were imaged every 10 min for 24 h after 10 Gy **γ**-IR for characterizing p53 nuclear accumulation over time (Figure 3.2.1.B). Trajectories of integrated fluorescence intensity (FI) of mVenus in the nucleus were extracted using custom-written *MATLAB* scripts in combination with previously described code from the research group of Uri Alon and the *CellProfiler* project (Carpenter et al., 2006; Cohen et al., 2009; Strasen et al., 2018) (Chapter 5.2.2). Median quantitative analyses of single-cell trajectories show p53-mVenus accumulation in repeated pulses after **γ**-IR, which

were on average similar to previously observed dynamics for A549-p53YFP reporter cells (Chen et al., 2013; Finzel et al., 2016b). While the first measurement time-point was defined as the non-irradiated condition (basal), further time-points were identified based on the shape of the median p53 curve: The average time of the first peak (3 h), the trough after the first peak (6 h) and the time of the second peak (9 h). P53's dynamics were strongly synchronous until the last selected time-point, which was further validated by quantitative analysis of p53 specific immunofluorescence (IF) staining in A549 wild-type cells that were used for subsequent smFISH experiments (Figure 3.1.2.C) (Chapter 5.1.2).

Previously, features of the nuclear dynamics of other transcription factors have been correlated with gene expression. For example, it has been shown for NF-κB that gene expression is closely connected to a fold change regulation of a nuclear NF-κB pulse upon activation of the pathway (Covert et al., 2005; Werner et al., 2005; Tay et al., 2010; Lee et al., 2014; Wong, et al., 2019). However, for p53, these measurements remain elusive. To correlate p53 dynamics directly in the same cell with RNA expression, I set up an imaging and analysis pipeline to first perform live-cell time-lapse imaging and then smFISH in the same cells. This set-up allowed to quantitatively analyze features of a p53 pulse in response to DNA damage and correlating these with cellular RNA abundance. However, while a p53 pulse was necessary for target gene transcription and p53 pulsing at higher **γ**-IR dose led to an increase in RNA levels (Figure 8.3.2/1), specific features as the amplitude or pulse-width were not found correlated with RNA expression levels upon the analyzed conditions and time-points.

3.2.2. RNA EXPRESSION OF P53 TARGET GENES IN THE DNA DAMAGE RESPONSE

P53 target genes showed distinct patterns of gene expression in response to DNA damage as measured in time-course experiments by RNA-Seq and qRT-PCR (Hafner et al., 2017; Porter et al., 2016). Based on different mathematical modeling approaches, these specific patterns have been hypothesized to originate from changes in RNA and protein stability (Porter et al., 2016; Hafner et al., 2017; Hanson et al., 2019). However, the mentioned studies did not provide substantial experimental and mechanistic evidence, and did not resolve single-cell RNA counts or promoter activity. To this end, I characterized the distribution of RNA counts by smFISH at the defined time-points after DNA damage: basal, 3 h, 6 h and 9 h post 10 Gy. Optimized protocols and analyses as described in Chapter 3.1.3/4 allowed the quantification of approximately 100 cells per condition using *FISH-Quant* (Mueller et al., 2013). Biological replicates were analyzed to compare RNA abundance in two experiments and validate the results. Representative replicates are displayed in Figure 8.3.2/2. Additionally, Table 3.1.1 provides an overview of average quantified parameters of one complete dataset, including all studied p53 targets. In total, 673015 spots in 3679 cells were analyzed for this dataset. Remarkably, all p53 targets are expressed in considerable numbers in the absence of DNA damage (Figure 3.2.2.A), even targets that correlate with strong terminal cell fate regulation such as BAX (Figure 3.2.2.A). At the same

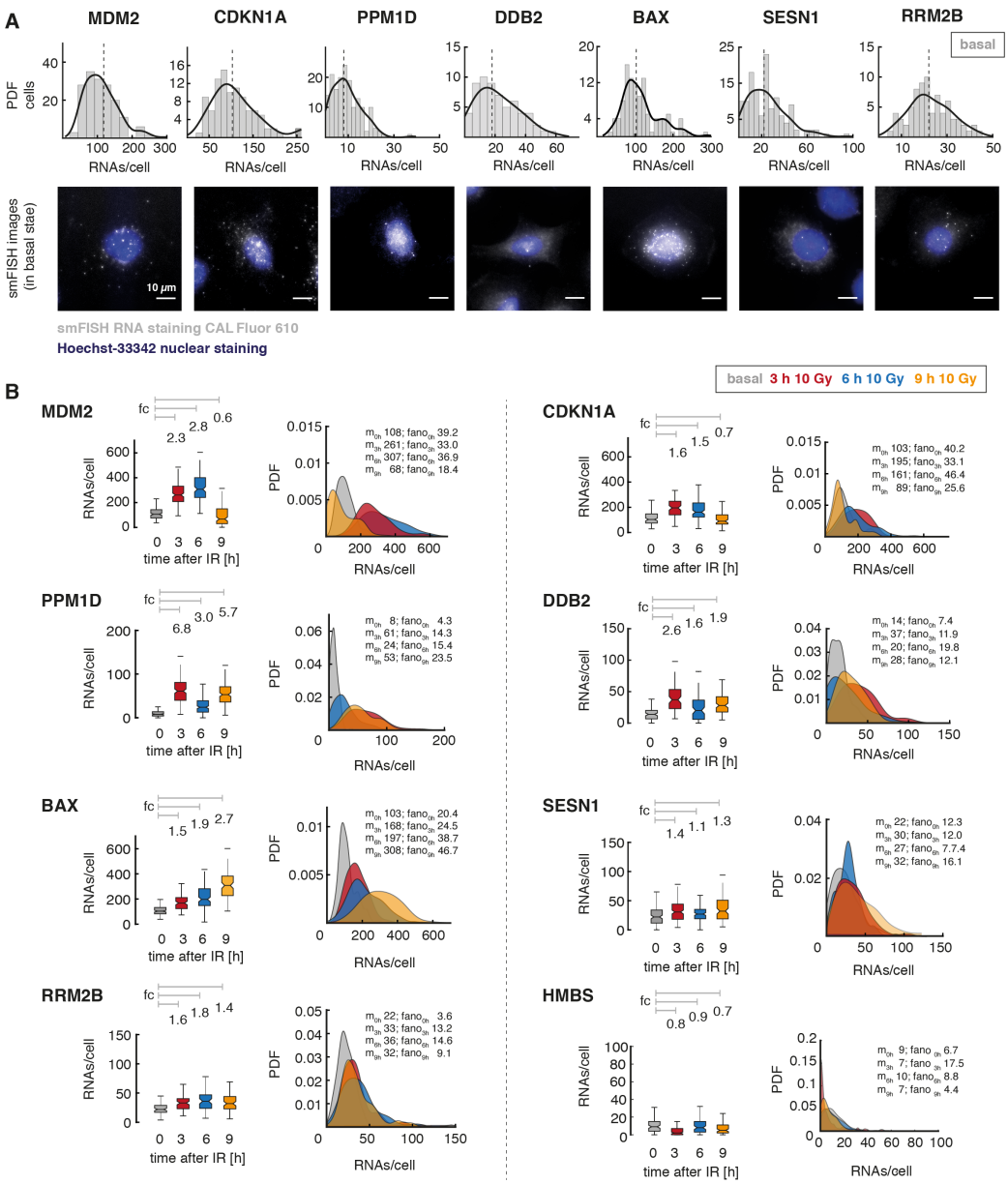

Figure 3.2.2 SmFISH analyses show distinct patterns of gene expression for p53 targets.

(A) All p53 targets are transcribed in absence of γ-IR (basal state) to a considerable extent. RNA counts range from median (dashed line) of a few molecules for some targets as PPM1D, DDB2, SESN1 and RRM2B to >100 as detected for BAX, CDKN1A and MDM2. Upper panel: Histograms of RNAs/cell in basal state, including an overlay of the density function illustrating the dispersion in the population (solid line). The dashed line highlights the median RNA count. The x-axis represents the number of cells, while the y-axis show RNAs per cell. A minimum of 75 (RRM2B) to a maximum of 169 (MDM2) cells per condition have been quantified. Lower panel: Representative images of RNA exon staining using the respective smFISH probe-sets (CAL Fluor Red 610 dye) and Hoechst 33342 for nuclear DNA staining. Images show brightness and contrast enhanced maximum projections of z-planes in focus. The scale bar (white) corresponds to 10 µm.
(B) The quantitative analysis of smFISH data shows distinct patterns of gene expression for p53 target genes upon 10 Gy γ-IR at the four defined time-points (boxplots, left panel) and a fundamental overlap of the distribution in single cells with strong heterogeneity (density plots, right panel). RNA counts increase for all targets with the peak of the first p53 pulse (3 h post 10 Gy, red). However, expression levels are gene-specific at later time-points of the trough (6 h post 10 Gy, blue) and the peak of the second p53 pulse (9 h post 10 Gy, orange). Left panel: Boxplots of RNAs/cell of all p53 target genes and the HMBS control gene. Whiskers represent 25th to 75th percentile; fc: fold change, average fold of induction relative to non-irradiated cells (basal state). Right panel: Distribution of RNAs per cell displayed as density functions $m_{0\ h\ -\ 9\ h}$: median RNA levels; $Fano_{0\ h\ -\ 9\ h}$: Fano factor used as a measure of heterogeneity in the population. For a summary of the number of quantified cells and average parameters, see Table 3.2.2.

Table 3.2.2 Overview of the smFISH based quantification of RNA abundance and variability of p53 target genes.

All quantified parameters are summarized for each target gene. From left to right columns show the name of the target gene, the condition and the time-point after **γ**-IR treatment, the number of analyzed cells (n) and RNA spots, median RNA spots in whole cells (RNAs/cell), nuclei (nuclear RNAs) and cytoplasm (cytoplasmic RNAs) and the average fold change of induction relative to the basal state (fc: fold change). Next, measures of cell-to-cell variability providing an overview of the heterogeneity in the population: MAD: mean absolute deviation; CV: coefficient of variation (root square difference); Fano factor: Fano noise factor. In total 3679 cells and 673015 spots have been quantified in one dataset. Selected replicates can be found in Figure 8.3.2/2.

gene symbol	condition	# cells (n)	# spots	median RNAs/cell	nuclear RNAs	cytoplasmic RNAs	average fold change	MAD	CV (RSD)	Fano factor
smFISH staining after γ-IR				*RNA quantification (median)*				*measures of variability*		
BAX	*basal*	111	12841	103	24	79	1.0	37	0.42	20.4
	3 h 10 Gy	99	17038	168	33	129	1.5	48	0.4	24.5
	6 h 10 Gy	128	27690	197	37	160	1.9	74	0.4	38.7
	9 h 10 Gy	104	31897	308	51	249	2.7	83	0.3	46.7
CDKN1A	*basal*	107	12972	103	36	62	1.0	52	0.58	40.2
	3 h 10 Gy	86	16763	195	54	128	1.6	63	0.4	33.1
	6 h 10 Gy	121	22167	161	52	108	1.5	73	0.5	46.4
	9 h 10 Gy	75	8227	89	41	48	0.7	52	0.6	25.6
DDB2	*basal*	101	1523	14	2	11	1.0	8	0.7	7.4
	3 h 10 Gy	80	3195	37	18	20	2.6	17	0.5	11.9
	6 h 10 Gy	84	2045	20	5	10	1.6	17	0.9	19.8
	9 h 10 Gy	117	3614	28	13	15	1.9	14	0.5	12.1
MDM2	*basal*	169	20024	108	50	55	1.0	44	0.6	39.2
	3 h 10 Gy	166	46157	261	115	147	2.3	74	0.3	33
	6 h 10 Gy	139	45415	307	98	206	2.8	91	0.3	36.9
	9 h 10 Gy	132	11090	68	9	54	0.6	64	0.8	18.4
PPM1D	*basal*	166	1550	8	3	5	1.0	5	0.7	4.3
	3 h 10 Gy	175	11116	61	15	44	6.8	24	0.5	14.3
	6 h 10 Gy	188	5307	24	6	18	3.0	16	0.7	15.4
	9 h 10 Gy	150	8304	53	11	39	5.7	21	0.5	23.5
RRM2B	*basal*	75	1698	22	6	16	1.0	7	0.4	3.6
	3 h 10 Gy	83	3076	33	9	24	1.6	15	0.6	13.2
	6 h 10 Gy	63	2524	36	8	28	1.8	17	0.6	14.6
	9 h 10 Gy	78	2818	32	6	24	1.4	14	0.5	9.1
SESN1	*basal*	128	3187	22	8	13	1.0	13	0.7	12.3
	3 h 10 Gy	158	5315	30	11	19	1.4	16	0.6	12
	6 h 10 Gy	119	3343	27	8	18	1.1	11	0.5	7.7
	9 h 10 Gy	101	3619	32	7	24	1.3	18	0.6	16.1
HMBS	*basal*	81	1341	9	4	7.0	1.0	6	0.8	6.7
	3 h 10 Gy	126	891	7	3.0	1.0	0.8	7	1.6	17.5
	6 h 10 Gy	82	959	10	3.0	4.0	0.9	7	0.9	8.8
	9 h 10 Gy	87	795	6	2.0	2.0	0.7	5	0.9	4.4
	sum	3679	673016							

time, average expression levels strongly varied from only a few (<10) RNAs/cell for PPM1D and SESN1 to several hundreds for CDKN1A, MDM2 and BAX (Figure 3.2.2.A, dashed lines). When comparing the dispersion of RNA counts per cell for one target gene in the basal state, expression levels in the population of cells showed a substantial heterogeneity as visible in histograms and fitted density functions (Figure 3.2.2.A, solid lines).

With the first p53 peak (3 h), all targets are induced compared to the basal state (Figure 3.2.2.B, red boxplots). The average fold change (fc) increase of target gene RNA levels range from 1.4 (SESN1) to 6.8 (PPM1D) (Figure 3.2.3.B). These fold changes are in a similar order of magnitude as measured by RNA-Seq for other cell lines under similar conditions (Chapter 3.1.1). After this rise in RNA abundance, a gene-specific regulation appears at the 6 h and 9 h time-points (Figure 3.2.2.B, blue/orange boxplots), which correspond to the trough and peak of the second p53 pulse. On the contrary, expression of the housekeeping gene HMBS remains on a similar level as in basal state when p53 is activated (Figure 3.2.2.B). The average fold induction and the distinct different median levels show the changes in RNA expression after **γ**-IR as described before. However, the detected single-cell dispersion highlights a severe overlap at the different time-points (Figure 3.2.2.B, distribution plots) with a trend towards a broader dispersion upon p53 activation, e.g. as observed for PPM1D (Figure 3.2.2.B, density plot grey/red). For later time-points RNA distributions remain gene-specific and strongly overlapping. However, measures of gene expression noise such as the Fano factor show gene-specific trends (Figure 3.2.2.B).

3.2.3. SUB-CELLULAR LOCALIZATION OF P53 TARGET GENE MRNAS

MRNAs in large, polarized cells such as neurons or during early embryonic development show distinct subcellular localization. Thoroughly studied examples are bicoid and oskar RNA accumulation to the anterior and posterior poles in *Drosophila* oocytes, β-actin at lamellipodia in fibroblasts and the transcriptional repressor ASH1 in budding yeast (Blower, 2007; Chartrand and Singer, 2001; Johnstone and Lasko, 2001; Condeelis and Singer, 2005; Blower, 2013). RNA localization, local translation, and protein function have been suggested to be closely connected (Martin and Ephrussi, 2009; Holt and Bullock, 2009). In addition, multiple studies indicate that the RNA distribution in a cell is generally not random, and a defined subcellular localization of RNAs is not a phenotype of specialized cell types or developmental stages (Blower, 2007; Lécuyer et al., 2007; Holt and Bullock, 2009; Sharp et al., 2011; Blower, 2013).

While on the protein level all p53 target proteins reside in the nucleus, also other distinct sub-cellular localization can be found (Figure 3.2.3.A). Some proteins are additionally localized in the cytoplasm (RRM2B and MDM2) or at distinct sub-cellular structures, e.g. at the endoplasmatic reticulum (ER) (PPM1D, BAX). Also, p53 target proteins are associated with cell junctions (DDB2), the plasma membrane (BAX, DDB2), mitochondria, or the Golgi apparatus (BAX) (Fazal et al., 2019; target gene data: v19.proteinatlas.org; Uhlén et al., 2010; Thul et al., 2017) (Figure 3.2.3.A).

However, the current literature of p53 research does not provide evidence for specific

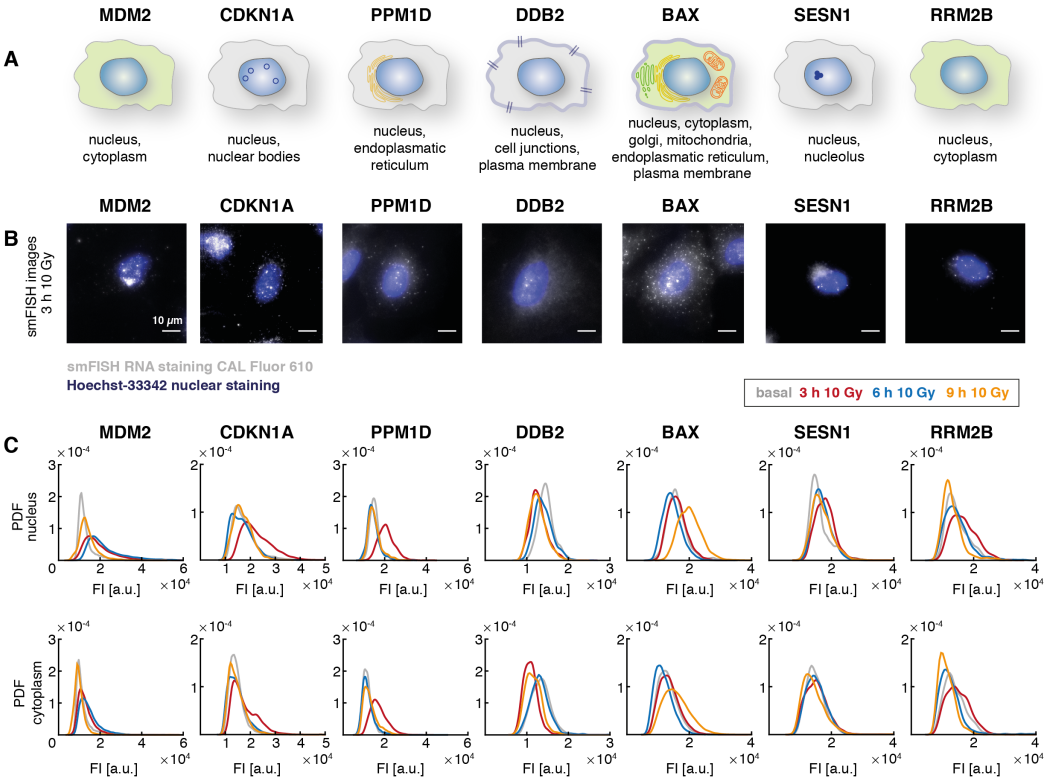

Figure 3.2.3 Localization and aggregation of p53 target gene mRNAs upon DNA damage.

(**A**) Schematic representation of expected protein location of p53 targets insides cells. For all selected target genes, the corresponding proteins have been described to be localized in the nucleus. However, some are also found in the cytoplasm (RRM2B and MDM2) or at distinct sub-cellular structures as in the endoplasmatic reticulum (ER) (PPM1D, BAX), at cell junctions (DDB2), at the plasma membrane (BAX, DDB2), in mitochondria or in the Golgi apparatus (BAX).
(**B**) Representative images of smFISH staining of target gene RNAs 3 h post 10 Gy DNA damage. As for target gene RNAs in basal state (Figure 3.2.2.A), upon DNA damage p53 targets do not resemble defined nuclear or cytoplasmic localizations upon DNA damage. Images show RNA exon staining using the respective smFISH probe-sets (CAL Fluor Red 610 dye) and Hoechst 33342 for nuclear DNA staining. Images are brightness and contrast enhanced maximum projections of z-planes in focus. The scale bar (white) corresponds to 10 µm.
(**C**) Fluorescence intensity (FI: fluorescence intensity) of detected smFISH spots of RNAs in nucleus (upper panel) and cytoplasm (lower panel) as measured by *FISH-Quant*. Histograms show the density function of the distribution of measured spot intensities in nucleus and cytoplasm in all cells per target gene for the different time-points before (grey) and after DNA damage (color-coded according to the time-points). Transcriptional start sites (TSS) in the nucleus were excluded. The sum of quantified spots per target (nucleus and cytoplasm) can be found in Table 3.2.2 (# spots) and ranges depending on the expression level from 2045 (DDB2, 6 h) to 46157 (MDM2, 3 h).

RNA localization patterns of targets under basal or DNA damage conditions. Until recently, techniques to study RNA localization in single cells were limited. Therefore, single-cell localization and aggregation of p53 target RNAs, including functional changes in response to intracellular signaling, remain ambiguous. Therefore, RNA spot distributions in smFISH images in the basal state and 3 h after DNA damage (Figure 3.2.2.A, 3.2.3.B) do not show a specific localization in cells. Also, the distance to the plasma membrane and nucleus based on

FISH-Quant segmentation did not suggest localized RNAs at the observed time-points after γ-irradiation.

The intensity distribution of RNA spots in the nucleus and cytoplasm may be indicative of RNA accumulation, as a rise in fluorescence intensity correlates with more bound smFISH probes that can result from a co-appearance of RNAs in one pixel. Therefore, the fluorescence intensities (FI) of detected spots outside the TSS in the nucleus and the cytoplasm were compared (Figure 3.2.3.C). No multi-modal distributions that would indicate RNA aggregates were seen and, in general, nuclear and cytoplasmic RNA spots had similar FIs (Figure 3.2.3.C). However, gene- and time-point-specific changes of the FI distribution are visible. The FI distributions of CDKN1A and PPM1D RNAs shift towards higher levels at 3 h after 10 Gy. This effect is more pronounced for nuclear RNAs (Figure 3.2.3.C). Furthermore, nuclear RNAs of BAX at 9 h showed higher intensities as well. As the size of a fitted spot does not include multiple pixels, a change in FI distribution of less than 2-fold and co-appearance with signals of lower intensity are difficult to interpret without additional measurements. However, the actual sterically required space of an individual RNA molecule and thus of potential aggregates remains speculative. The molecular 3D structure inside cells cannot be inferred from RNA length, and may change upon contact with RNA binding proteins and the subcellular microenvironment. In smFISH staining both are not necessarily preserved. Therefore, it is likely that the observed changes are due to enhanced accessibility of RNAs for labeled smFISH probes, e.g. through a lower amount of RNA bound proteins or variation in RNA 3D-structure.

3.2.4. NUCLEAR AND CYTOPLASMIC RNA ABUNDANCE AND GENE EXPRESSION NOISE AFTER γ-IR

The life-cycle of an mRNA includes transcription, splicing and processing in the nucleus, resulting in translation and degradation in the cytoplasm. In these processes, compartmentalization between the nucleus and cytoplasm has recently been suggested to fulfill a passive buffering role to reduce gene expression noise through retention of nuclear RNAs (Bahar Halpern et al., 2015a; Stoeger et al., 2016). However, in response to cellular signaling and an increase in transcription, it remains unknown if the RNA fractions in the nucleus and cytoplasm are proportional to each other, and if gene expression noise is buffered. Furthermore, it is unclear if the observed compartmentalization and resulting buffering effect is only a property of specific genes due to distinct cellular conditions (Hansen et al., 2018), or also applicable for p53 target gene expression.

To analyze this further, I characterized the ratio of p53 target gene RNAs in the nucleus (blue) and cytoplasm (green) (Figure 3.2.4.A). Target gene RNAs are mainly cytoplasmic under basal and induced conditions, reflected by a mean cytoplasmic abundance of up to 83% (BAX, 6 h 10 Gy) with differences in the relative percentages (Figure 3.2.4.A). Upon DNA damage, the ratio in the nucleus and cytoplasm remains similar for most targets, despite a change in the number of RNAs (Figure 3.2.2.B). Notably, the variability of the nuclear to cytoplasmic ratio in the population was generally small and did not change when

RNA counts increased (Figure 3.2.4.A). Next, I compared the dynamics of both RNA fractions to evaluate if both sub-cellular regions undergo different regulation (Figure 3.2.4.B). For all p53 targets, nuclear and cytoplasmic RNA counts follow similar dynamics, only differing in their levels (Figure 3.2.4.B). In conclusion, this indicates that nuclear export (time-scale about 10-30 min, de Leon et al., 2009) and RNA degradation are not rate-limiting factors with a strong influence on target gene patterns at the observed time scales. However, for some target genes as CDKN1A, DDB2 and SESN1, a slight shift in their expression patterns between nuclear and cytoplasmic regions can be found.

One example is MDM2 at 6 h, where the distribution of nuclear RNAs is similar to 3 h, while cytoplasmic levels still rise (Figure 3.2.4.B). This delay could be indicative of a change in transcriptional activity around this time-point. A direct comparison of the dispersions of total (black line), nuclear (blue) and cytoplasmic (green) RNAs, as displayed in fitted density functions, clearly shows a trend towards broader distributions in the cytoplasm compared to the nucleus, particularly after DNA damage (Figure 3.2.4.C). In contrast to previous studies that suggested a passive noise buffering of the nucleus through passive compartmentalization (Bahar Halpern et al., 2015a; Stoeger et al., 2016), this suggests an amplification rather than the attenuation of gene expression noise for p53 targets in the cytoplasm (Figure 3.2.4.C). This effect is even more dominant after p53 dependent transcriptional activation upon DNA damage.

As a quantitative measure of gene expression noise in the nucleus and cytoplasm, the ratio of the Fano factor was calculated ($Fano_{nuc}/Fano_{cyt}$) (Figure 3.2.4.D). Total mean RNA counts for p53 targets as well as in both sub-cellular locations differ strongly. Therefore the Fano factor allows a more direct noise comparison than the coefficient of variation (CV), which scales with mean RNA levels (Hansen et al., 2018, Chapter 4.1.5). For all p53 targets and time-points, the Fano noise in the cytoplasm was higher than in the nucleus. A recent study also showed a general trend of amplification from transcriptional noise in the nucleus to cytoplasmic fractions instead of attenuation or buffering (Hansen et al., 2018) (Figure 3.2.4.D). Target genes with higher expression levels exhibit higher cytoplasmic Fano factors (e.g. CDKN1A, BAX, MDM2) in contrast to targets with a moderate expression that had lower cytoplasmic Fano factors for most time-points (e.g. DDB2, SESN1, PPM1D). With one exception (9 h PPM1D), all other quantified Fano factors for nuclear RNA distributions were in a similar range (Figure 3.2.4.D). As under basal conditions the differences in gene expression noise are not as prominent for p53 targets either, suggesting a cell-type-specific behavior or pre-starvation of cells applied for synchronizing cell populations could explain the previously observed noise buffering effects (Bahar Halpern et al., 2015a; Stoeger et al., 2016). On the other hand, active signaling in the cellular responses to DNA damage may increase noise levels in the cytoplasm, potentially through additional regulatory factors that affect translation or RNA stability. Over time, Fano factors in the nucleus and cytoplasm change gene-specifically, but do not show a universal trend for all p53 targets (Figure 3.2.4.E). This suggests that, on the level of a single target, different noise sources are relevant. These are rather intrinsic and not exclusively correlated with p53, as a dominant pattern from p53 peak times is lacking.

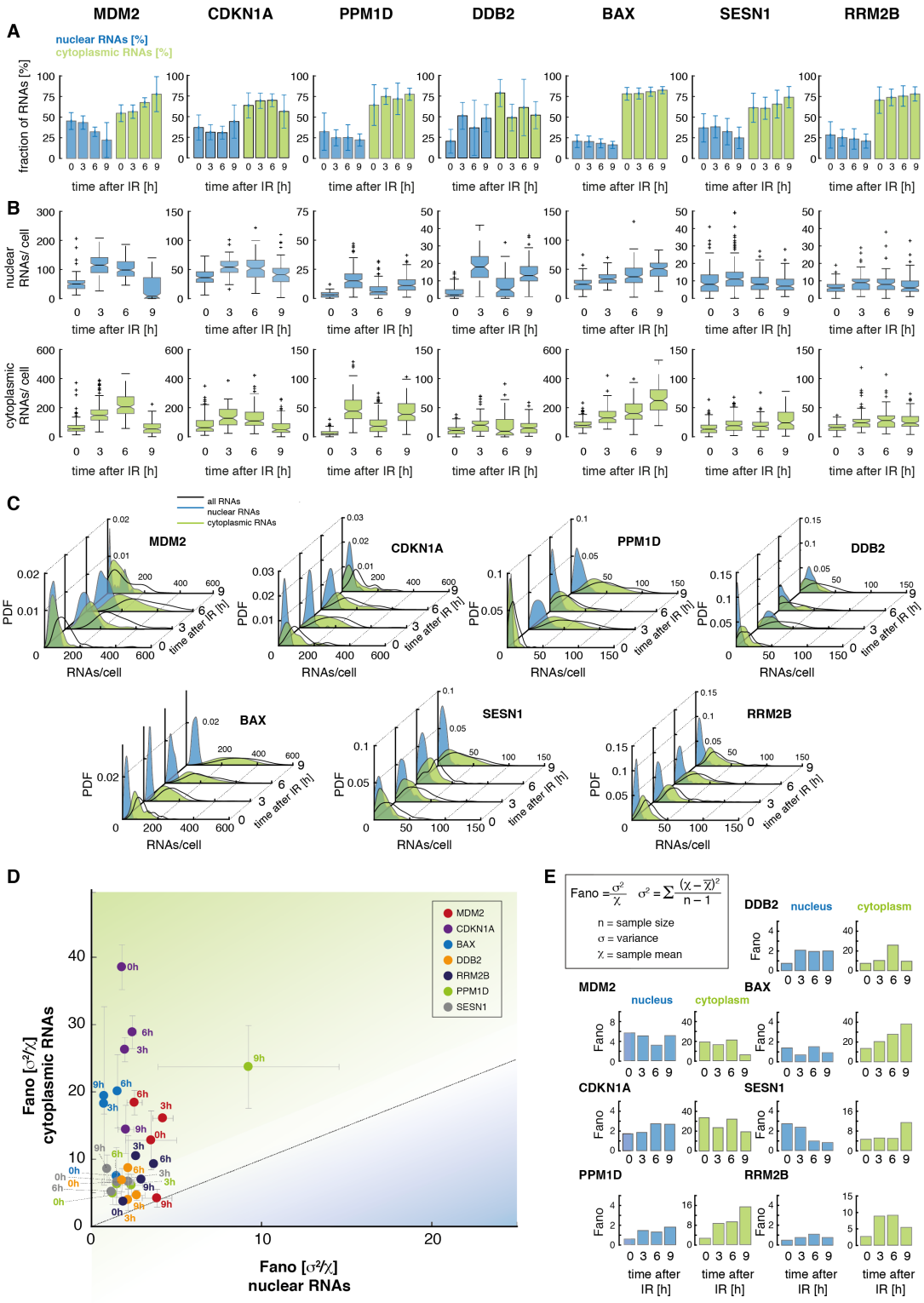

Figure 3.2.4 P53 target RNAs show similar nuclear and cytoplasmic expression patterns and an amplification of gene expression noise from nucleus to cytoplasm.

(A) Relative fraction of nuclear (blue) and cytoplasmic (green) RNAs in [%] over time after 10 Gy γ-IR. The percentage of nuclear vs. cytoplasmic RNAs was quantified from RNA counts of single-cell measurements and then averaged over the population. Error bars show the standard deviation at each time-point and sub-cellular region (STD). The number of quantified cells corresponds to the datasets from Table 3.2.2.

(B) Boxplots show dynamic changes of RNA counts over time after γ-IR in the nucleus (upper panel, blue) and cytoplasm (lower panel, green) for each target gene. Expression patterns are similar in both sub-cellular regions, but on different scales.

Figure description continues on the next page.

Figure 3.2.4 P53 target RNAs show similar nuclear and cytoplasmic expression patterns and an amplification of gene expression noise from nucleus to cytoplasm. ***(continued)***

(C) Dispersions of RNAs are shown as density functions of nuclear (blue) and cytoplasmic (green) RNA levels as well as of total RNA counts (solid black line) per target gene and time-point. Time-points are displayed in z-direction starting from basal state. A broader distribution in the cytoplasmic fraction of RNAs compared to nuclear RNAs can be found across all conditions, with an increase upon γ-IR. This suggests noise amplification rather than attenuation between nucleus and cytoplasm.
(D) The ratio of the Fano factor of nuclear and cytoplasmic RNA counts is displayed, showing a trend towards higher cytoplasmic gene expression noise for all targets, specifically for highly expressed genes (e.g. MDM2, CDKN1A and BAX). The cytoplasmic Fano factor is shown on the y-axis and the nuclear Fano factor on the x-axis. Measured values display the mean Fano factor of two independent datasets for all targets except RRM2B. Error bars indicate the standard error of the mean (S.E.) in both dimensions.
(**E)** Bargraphs show the Fano factor for each target gene at four time-points after γ-IR for nuclear (blue, left) and cytoplasmic (green, right) RNAs. While no general trends can be observed for all targets, gene-specific effects trends can be seen that differ between nucleus and cytoplasm.

3.2.5. TARGET GENE MRNAS AND THEIR CORRELATION TO CELL CYCLE AND CELLULAR VOLUME

The gene expression noise of p53 targets in the nucleus or cytoplasm was not strongly dependent on different p53 nuclear levels at the measured time-points (Figure 3.2.4.D/E). However, in addition to p53 induced heterogeneity, recent literature suggests a correlation between mRNA expression levels and other extrinsic noise sources such as cell cycle state and cellular volume (Padovan-Merhar et al., 2015; Battich et al., 2015; Bahar Halpern et al., 2015a; Stoeger et al., 2016). For example, the cell cycle state affects cellular RNA levels due to an increase in transcription levels after DNA replication (Buettner et al., 2015; Padovan-Merhar et al., 2015; Yunger et al., 2010). In zebrafish, the nuclear size has also been hypothesized to be correlated to transcription factor binding, thus influencing promoter activity of downstream targets (Reisser et al., 2018). To estimate the effect of the cell cycle phase and cellular volume on p53 target gene expression, the nuclear and cytoplasmic area was measured. Therefore, single-cell segmentation outlines from Hoechst 33342 (nuclei) and NHS-AlexaFluor-488 (cytoplasm) staining were used and the respective areas were determined from *FISH-Quant* software (Mueller et al., 2013). A comparison of both factors indicated that neither the nuclear nor the cytoplasmic area changed substantially after DNA damage by γ-IR as depicted for MDM2 (Figure 3.2.5.A, other targets: Figure 8.3.2/5). Along the lines of the nucleoskeletal theory, the cell cycle state was estimated based on the nuclear size (Gregory, 2001; Cavalier-Smith, 1980). According to this theory, the nuclear size scales with DNA content and subsequently also affects the cellular volume. A549 cell nuclei are mainly of ellipsoidal shape. As smFISH images from wide-field microscopy do not allow a precise measurement of the height of nuclei, the ellipsoidal area of the nuclear segmentation was used as a proxy for the size of each nucleus.

NUCLEO-SKELETAL THEORY
Assumes that cell cycle state determines nuclear size (Gregory, 2001; Cavalier-Smith, 1980).

When RNA counts per cell are plotted relative to the measured nuclear (Figure 3.2.5.B, upper row) or cell area (Figure 3.2.5.B, lower row), most p53 target genes display a trend towards higher RNA expression levels (total) in bigger cells. However, the strength of the correlation and its change in the p53 response differs. For example, upon DNA damage BAX RNA levels constantly rise in their correlation to the nuclear area and cell cycle from

R^2 0.47 (basal) to R^2 0.69 (9 h 10 Gy) (Figure, 3.2.5.B, Figure 8.3.2/4). PPM1D RNA counts are generally correlated to a lesser extent to the cell cycle (R^2 = 0.07, basal), with a stronger correlation at time-points of high p53 levels and stronger expression (3 h R^2 = 0.29, 6 h R^2 = 0.20, 9 h R^2 = 0.40) (Figure 3.2.5.B, Figure 8.3.2/3). These examples highlight that RNA counts are more correlated to the cell cycle after DNA damage, which could be an effect of cell cycle arrest at the G1-S checkpoint after DNA damage. However, as shown for MDM2, the nuclear area did not change significantly upon DNA damage and also the coefficient of variation of the nuclear area did not change strongly, indicating a more homogenous dispersion in the population (Figure 3.2.5.A). Together with the time-dependent change in the correlation as seen for BAX and PPM1D, this suggests that higher RNA expression levels are stronger correlated with the nuclear area. As A549 cells are flat regarding their shape, the cellular area was used to approximate the cell volume. When correlating the cell area from *FISH-Quant* with RNA counts, similar trends as for the correlation to the nucleus are found, while in general the correlation of the cell area was less than observed for the nucleus (Figure 3.2.5.B). For a better comparison of the impact of cell cycle and cell volume on RNA expression, the CV was quantified for each target gene dataset after applying a correction factor. For each cell, a correction factor was calculated, determining the difference to the average measured cell or nuclear size for one target gene dataset (all time-points individually), to exclude a bias from technical factors such as differences in cell density. Next, the CV was calculated based on the dispersion of RNA counts corrected by the cell specific divergence from the median. However, both normalizations only slightly reduced the CV, while also no significant differences were found for specific target genes (Figure 3.2.5.C).

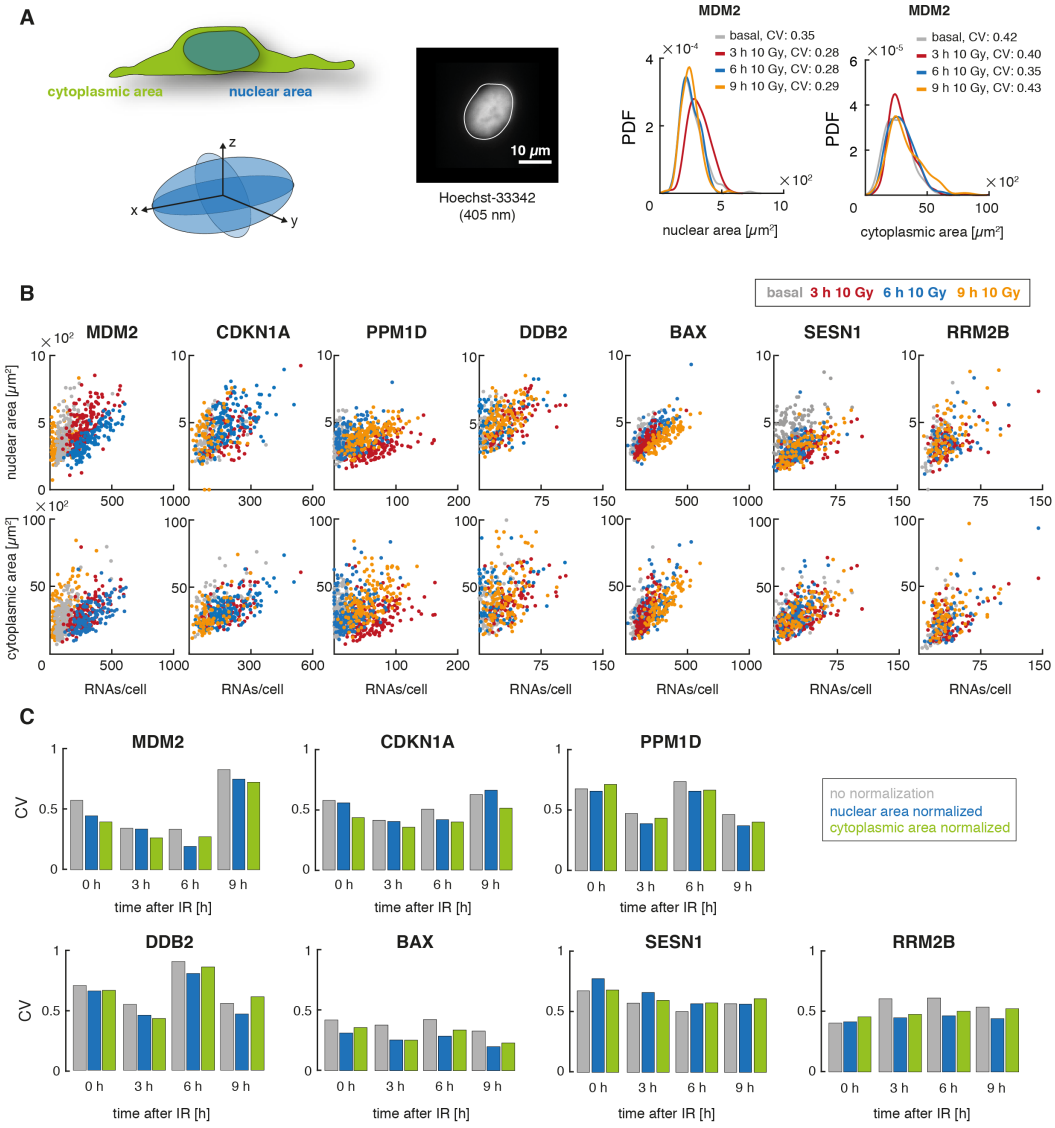

Figure 3.2.5 Target gene RNA abundances and their correlation to cell cycle phase and volume.

(A) The effect of cell cycle phase and cellular volume on RNA counts per cells and the applied approach to estimate cell cycle and cellular volume are schematically represented. Left panel: Schematic cell image, indicating ellipsoid nucleus and flat cell shapes. Middle panel: Segmentation example of a Hoechst 33342 nuclear staining and the automatic nuclear outline detection from *FISH-Quant*. Right panels: Density functions of the dispersion of measured nuclear and cytoplasmic area from segmented images stained by smFISH for MDM2 as an example.

(B) The correlation of RNA counts per cell with measured nuclear areas (upper row) as a proxy for the cell cycle state and cytoplasmic areas (lower row) to estimate the cell volume, is shown. The area was determined based on segmentation images from Hoechst 33342 and NHS-AF-405 staining using *FISH-Quant*.

(C) Coefficient of variation (CV) of RNA counts per cell before (grey) and after normalization for nuclear area (blue) as a proxy for the cell cycle and cytoplasmic area (green) as an estimate for the cellular volume. For normalization, a correction factor based on the divergence from the median cell size was calculated for each target gene dataset individually. The CV was then calculated for corrected dispersions of RNA counts. A general trend toward lower dispersion after correction can be found. However, the reduction in heterogeneity is small for most targets and time-points, with some gene- and time-point specific effects.

3.3. STOCHASTIC BURSTING OF P53 TARGET GENES IN RESPONSE TO γ-IRRADIATION

3.3

IN THIS CHAPTER

Gene expression of p53 target genes is heterogeneous between genetically identical cells for the same target, and the distribution in the population changes upon DNA damage. Transcription can either be constitutive (Poisson-like) or bursty (stochastic) with episodic periods of active transcription and silent promoter states. For many eukaryotic genes, it has been shown that the substantial variability in expression levels among cells can result from discontinuous transcription that is intrinsically stochastic (Raj et al., 2006; Singh et al., 2010; Zenklusen et al., 2008; Suter et al., 2011a; Dar et al., 2012; Golding et al., 2005, Coulon et al., 2013).

3.3.1. THE DISPERSION OF MRNA EXPRESSION INDICATES STOCHASTIC BURSTING

One approach for estimating the mode of transcription is to measure gene expression noise. The distribution of RNA abundance and the specific noise levels indicate the mode of gene expression when comparing different datasets or conditions (Singh et al., 2010; Dar et al., 2012; Dar et al., 2016). The inverse correlation between noise levels and RNA expression has been previously explained based on the two-state (random telegraph) model. An increase in burst frequency at a fixed burst size decreases the expression noise (Dar et al., 2016; Singh and Bokes, 2012). An increase in mean mRNA (<RNA>) expression is inversely correlated with gene expression noise: A rise of the burst size leads to an increase in noise, whereas an increase in burst frequency reduces noise levels (Peccoud and Ycart, 1995; Kepler and Elston, 2001).

P53 targets were expressed with a broad heterogeneity of the dispersion of RNA counts in the population (Figure 3.2.2.B, Table 3.2.2), with Fano factors >1 of the dispersion, deviating from Poisson distribution (Fano poisson=1) (Figure 3.2.2.B). Gene expression of p53 targets is thus rather of stochastic than of constitutive nature. I analyzed the CV^2 versus mean RNA relation for all targets and correlated expression levels with hyperbolic functions indicating a change of individual burst size (Figure 3.3.1.B) as previously described (Singh et al., 2010; Dar et al., 2012). Herein the burst size is:

$$\mu = (CV^2 \cdot \langle RNA \rangle) \qquad [2]$$

From this, a trend to similar or reduced noise levels with increasing mean RNA counts at 3 h after 10 Gy can be found (Figure 3.3.1.B). However, at later time-points, more gene-specific correlations are observed as well. These findings confirm a stabilization or even reduction of

variability as measured by a reduced or similar Fano factors after γ-IR (Chapter 3.2.4). According to this, the burst size remains similar with p53 activation (3 h 10 Gy), indicating a change in burst frequency rather than in burst size and suggests promoter-specific regulation at later time-points.

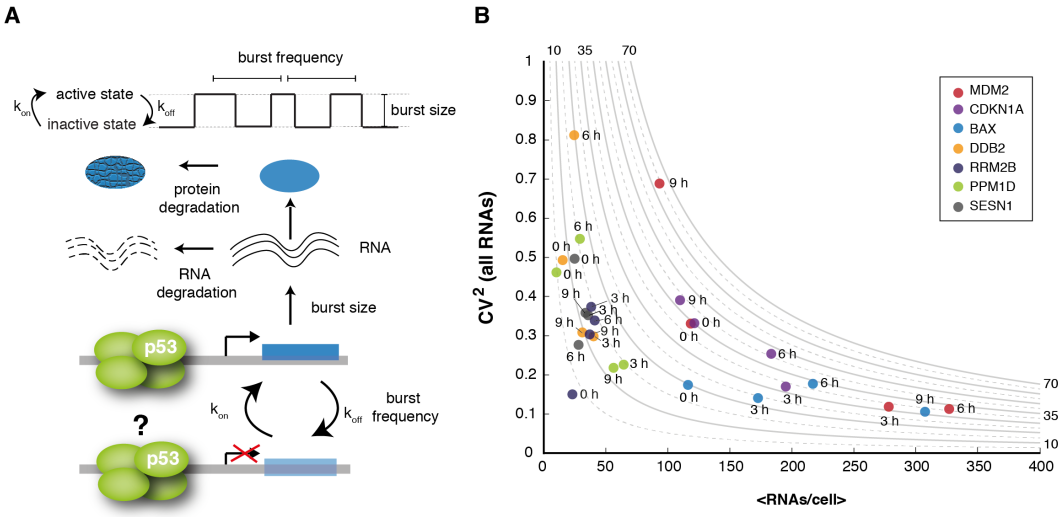

Figure 3.3.1 The variability of gene expression indicates stochastic bursting and a change of burst frequency upon DNA damage.

(A) Schematic representation of the random telegraph model and the representation of the description of how the different bursting parameters impact the life-cycle of an RNA from transcription at active promoters to RNA degradation (modified based on Zoller et al., 2015).
(B) The coefficient of variation (CV^2) as measured for RNA counts of each p53 target at the four different time-points after 10 Gy γ-IR plotted relative to the mean number of RNAs per cell (<RNAs/cell>). Hyperbolic lines represent the size of bursts, estimated from the simple gene expression model assuming that the burst size (μ) is: $\mu=(CV^2*<RNAs>)$ as previously described by Dar et al., 2016.

3.3.2. ANALYZING TRANSCRIPTION PARAMETERS IN SINGLE CELLS

Combinatorial smFISH imaging and mathematical modeling allow to directly characterize transcriptional bursting in single cells (Bahar Halpern et al., 2015b; Bahar Halpern and Itzkovitz, 2016). Following this approach, co-staining of introns and exons is used in this thesis to identify active sites of transcription and infer changes in transcription kinetics from smFISH staining of TSSs. The number of nascent RNAs is inferred from fluorescence intensities (FIs) at a TSS relative to the intensity of an average RNA spot, to estimate nascent RNAs and burst size as well as transcription rates (Figure 3.3.2.A, B). Two software tools support the analysis of transcription site FIs, enabling simultaneous analyses of TSS parameters and RNA counts from smFISH images: *FISH-Quant* (Mueller et al., 2013) and *TransQuant* (Bahar Halpern and Itzkovitz, 2016). A combination of both was used to characterize the activity of p53 target promoters. A second smFISH probe set, labeled with Quasar 670 was designed, targeting intronic RNA regions (Chapter 5.1.1). Through co-

staining for exons and introns, actively transcribing promoters were identified by co-localized nuclear fluorescence signals (Figure 3.3.2.C). Based on the exon staining, each TSS was segmented for further analyses. The fraction of active promoters f was used to approximate burst frequency, as both are correlated. It was calculated as described by equation [3], where f is the ratio of the number of TSS identified from co-stained nuclear dots per cell and the number of genetic loci (n):

$$f = \frac{TSS}{n} \quad [3]$$

The transcription rate at active sites (μ) can then be inferred from summed FIs of nascent RNAs at the TSS. For this approach, the FI of an average cytoplasmic mRNA spot is calculated from the median FI of all mature RNA spots per experiment ($mInt_{mRNA}$), and from the relative comparison to the measured TSS intensity (Int_{TSS}). Based on the summed TSS intensity values (Int_{TSS}), the occupancy of RNAP2 (M) is calculated [4] as the quotient of the TSS intensity and the median intensity of a cytoplasmic mRNA spot ($mInt_{mRNA}$), including correction factors for the probe position (η) and inferred RNAP2 occupancies ($\varkappa$) as described previously (Bahar Halpern et al., 2015b; Bahar Halpern and Itzkovitz, 2016). The correction factor η for the probe position was calculated based on the positioning of probes in the mRNA sequence using *TransQuant* (Figure 8.3.3/1).

$$M = \frac{Int_{TSS}}{\eta \cdot \varkappa \cdot mInt_{mRNA}} \quad [4]$$

In line with previous work, a fixed value of 1.5 was used to correct for RNAP2 occupancies ($\varkappa$) (Bahar Halpern et al., 2015b). The transcription rate per hour (μ) was then calculated from the RNAP2 occupancy (M), the estimated RNAP2 elongation speed (v) and the gene length of each target (l) to estimate changes in burst size. Depending on the cell line and treatment, the speed of RNAP2 elongation (v) in human cells has been suggested to range between 2 kb/min and 6 kb/min in HeLa cells (Fuchs et al., 2014), while 3.8 kb/min is considered as the general average (Singh and Padgett, 2009; Ardehali and Lis, 2009). At the same time, 1.75 kb/min in MCF-7 cells and 1.25 kb/min in K562 cells have been proposed as well (Veloso et al., 2014). A speed of v = 3 kb/min was therefore used for all calculations in this thesis. Worth to note is that the elongation speed strongly affects the calculation of the burst size (μ) (Figure 8.3.3/2). This approach assumes an equal probability for each nucleotide position and neglects erratic transcription due to pausing or co-transcriptional processing. The rate of transcribed RNAs per hour (μ) for each cell is used in this approach to infer changes in burst size. It is calculated as the number of transcribed RNAs per hour, based on the RNAP2 occupancy (M_{sum}) from all active TSS per cell. The relative transcription rate per TSS (μ_{TSS}) thus is the ratio of the cellular burst rate to the number of active TSS under the assumption that all TSS contribute equally to the pool of present RNAs, neglecting potential allele-specific factors.

$$\mu = M_{sum} \cdot \frac{v}{l} \quad [5]$$

As described previously (Raj et al., 2008; Bahar Halpern et al., 2015b; Bahar Halpern and Itzkovitz, 2016), the number of RNAs per cell can be derived from the burst size, the burst

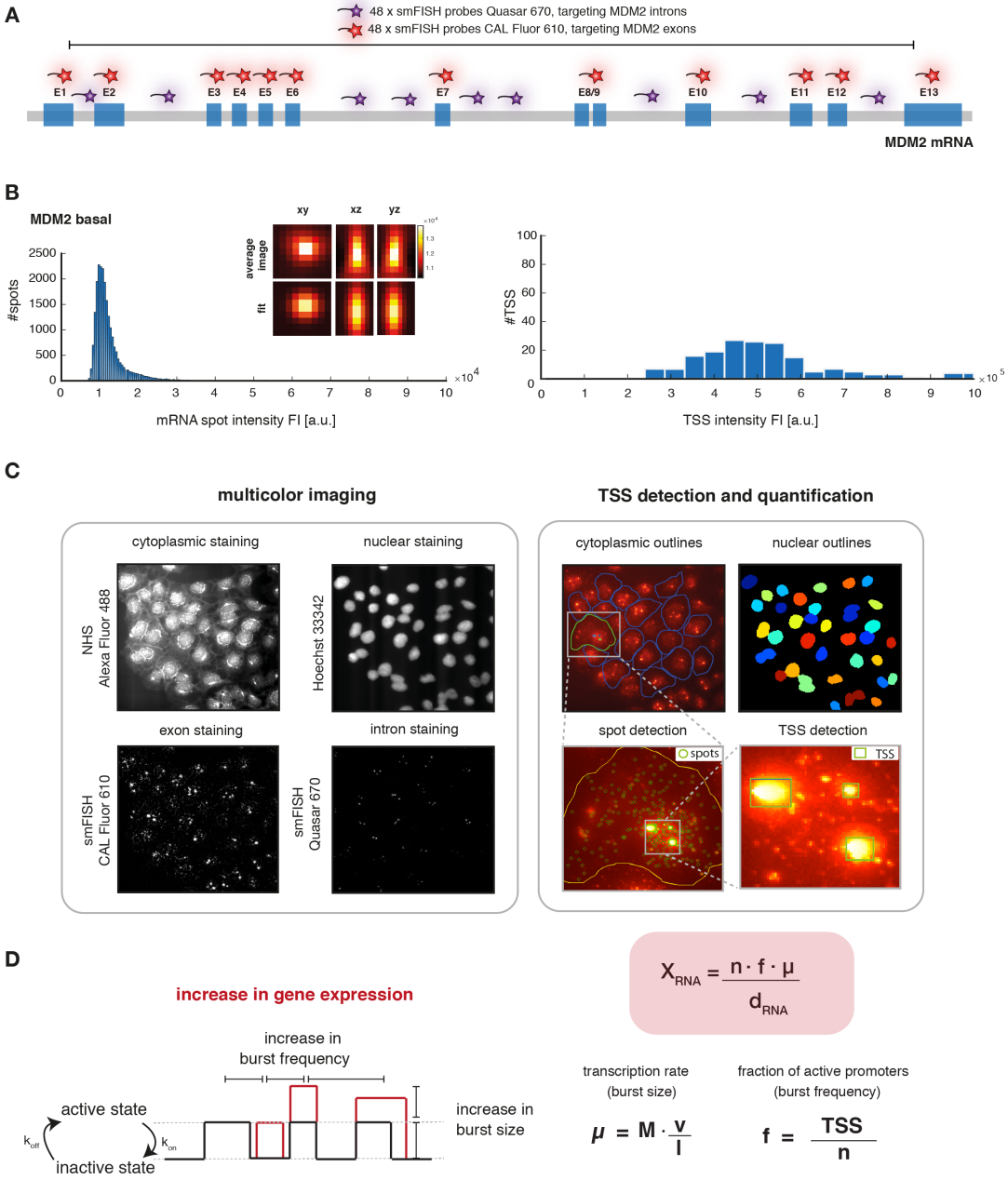

$$X_{RNA} = \frac{n \cdot f \cdot \mu}{d_{RNA}}$$

$$\mu = M \cdot \frac{v}{l} \qquad f = \frac{TSS}{n}$$

Figure 3.3.2 Quantification of bursting promoters of p53 target genes based on smFISH.

(A) Schematic representation of smFISH co-staining to identify TSS. Exon probes are labelled with CAL Fluor Red 610 and intron probes with Quasar 670. The latter probes are spread over several introns.
(B) Left panel: Histogram of the fluorescence intensity (FI) distribution for MDM2 RNA spots in basal state as an example. Calculated images in xy, xz and yz dimensions of the average MDM2 RNA spot (upper row) are depicted, that originate from the dataset shown in the histogram, generated by *FISH-Quant* and the corresponding fits (lower row). The FI intensity is indicated by a heat map. Right panel: Histogram showing the distribution of the FI for identified TSS transcribing MDM2 RNAs in basal state as an example.
(C) In addition to nuclear and cytoplasmic staining, TSS are identified by co-staining of introns and exons in the nucleus in a multicolor imaging approach (left panel). Using *FISH-Quant,* TSS in each nucleus are identified based on co-staining and each TSS is segmented for further analysis of fluorescence intensities.
(D) Two-state random telegraph burst model of promoter activity in the context of p53 activation. An increase in RNAs/cell on the promoter level may be achieved by either an increase in burst size or frequency (left panel). Characteristics of stochastic bursting (burst size and burst frequency) can be defined based on previously published models (Bahar-Halpern and Itzkovitz, 2016; Raj et al., 2008). X_{RNA} = RNA counts/cell, n = number of genomic loci, f = burst frequency, μ = burst size, d_{RNA}= RNA degradation rate, M= RNAP2 occupancy, v = speed of transcription, l = gene length, TSS = number of enumerated TSS/cell.

frequency and the RNA degradation rate (d_{RNA}) according to the following equation:

$$X_{RNA} = \frac{n \cdot f \cdot \mu}{d_{RNA}} \quad [6]$$

Except for the RNA degradation rate (d_{RNA}), all parameters were extracted from smFISH images. Therefore, d_{RNA} was validated for a selected target gene dataset, measuring the decrease in RNA abundance after inhibitor induced transcription shutdown. Actinomycin D (Sobell, 1985), a widely used drug to inhibit transcription (Lai et al., 2019), increases p53 abundance and activates the DNA damage response independent of **γ**-IR (Chen et al., 2014). Therefore, transcriptional inhibition by 100 µM DRB treatment for up to 3 h was used (Bensaude et al., 2011). The RNA decay rate was then obtained from the slope of a linear regression fit to the decreasing mean mRNA levels over time (Figure 8.3.3/3).

Co-stained sites of active transcription, varied in number and fluorescence intensity. As introns are spliced and degraded co-transcriptionally (Levesque and Raj, 2013; Vargas et al., 2011), co-stained dots were mainly found inside the nucleus. However, more than two TSS were enumerated using this approach for all targets except SESN1 (Figure 8.3.3/5). To validate this number (n), a DNA FISH staining of CDKN1A loci was performed in A549 cells (Figure 8.3.3/4). As expected, the maximum number of TSS did not exceed the number of genomic loci, and is thus used as (n) in further analyses.

3.3.3. P53 TARGET GENE TRANSCRIPTION IS REGULATED BY BURST FREQUENCY

The RNA levels of all selected p53 targets rise after **γ**-irradiation and the distribution and variability in the population changes (Figure 3.2.2.B). Based on promoter activity, RNA numbers per cell can increase by a higher rate of transcription in an active period (burst size) or more frequently appearing active promoter states (burst size) (Figure 3.3.2.D). The inverse correlation between noise levels and RNA expression as analyzed in Chapter 3.3.1 indicates that p53 activation induces a change in burst frequency. However, it has not been shown yet how p53 changes stochastic bursting features. Also, a quantitative characterization of the number of RNAs transcribed from an individual promoter, and the fraction of active promoters remains elusive. The high variability in gene expression of different p53 targets as displayed in Figure 3.2.2 could also have other sources than bursty transcription. For example, dynamic changes in RNA stability could lead to different expression patterns and changes in noise levels (Porter et al., 2016; Hafner et al., 2017; Hanson et al., 2019).

To measure promoter states of p53 target genes unambiguously, TSS in individual cells were identified based on co-staining of smFISH probes targeting introns and exons. The resulting data of RNA counts, as well as the number and fluorescence intensity of TSSs was then used to inform a mathematical model of promoter activity as described in Chapter 3.3.2. An overview of the quantified average parameters is listed in Table 8.3.3. Surprisingly, all p53 targets had a high number of transcriptionally active cells in the absence of DNA damage (Figure 3.3.3.A, grey). The lowest average fractions of active promoters were found for DBB2 (0.06) and PPM1D (0.09), while for BAX (0.40) and MDM2 (0.36) many

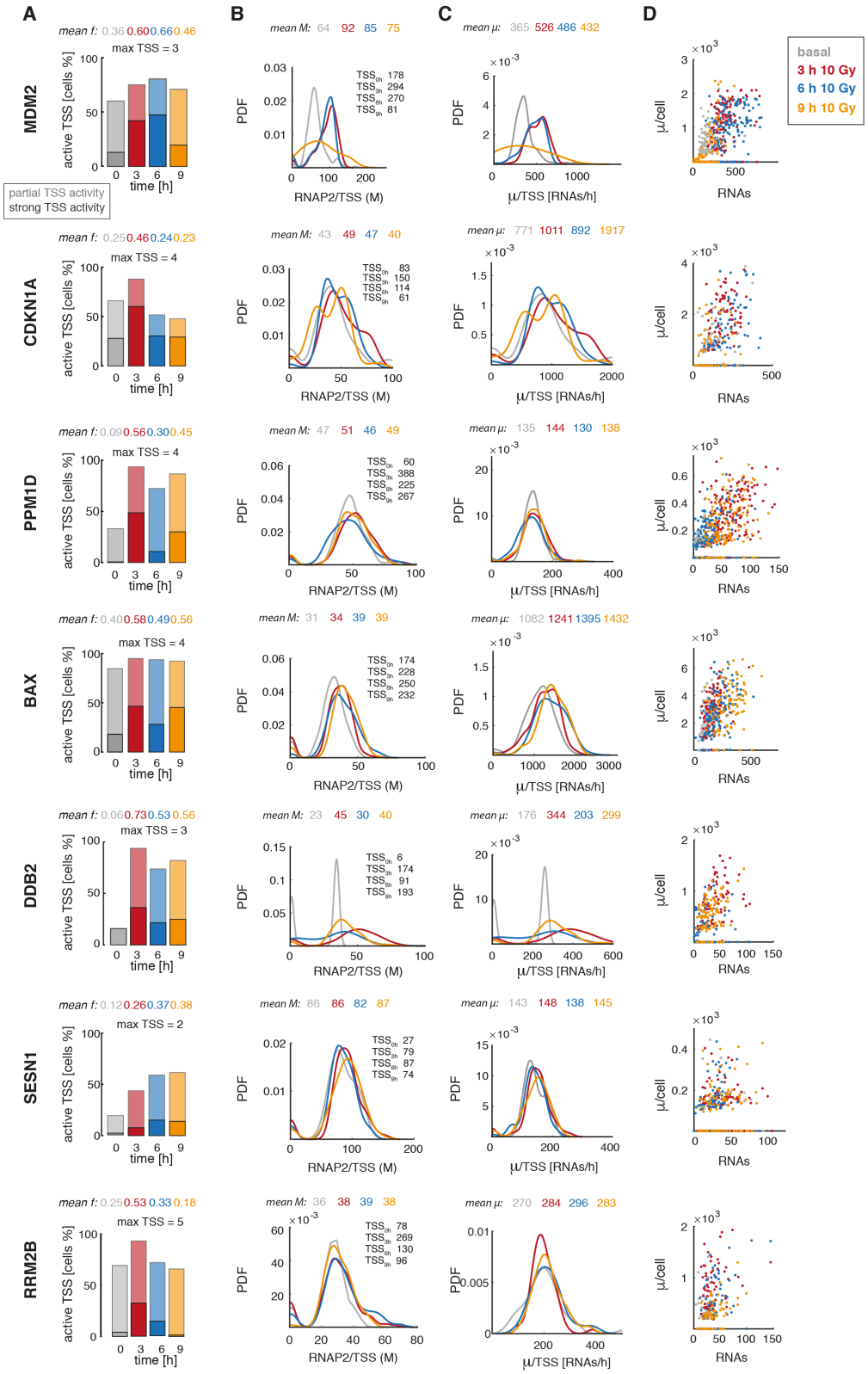

Figure 3.3.3 Bursting kinetics of target gene promoters change with p53 activation.

(A) Column A shows the fraction of active promoters for each target gene at the different time-points after DNA damage in a stacked bar plot. The average burst frequency (mean f) was calculated as the mean of the fraction of active promoters in the population of cells. Solid colors indicate strong TSS activity with 2 (SESN1) or >2 active TSS (other targets) per cell, while the fraction of cells showing partial TSS activity per time-point is indicated by shaded colors. Due to a different number of expected genomic loci in A549 cells, the applied bins vary. Details in the analysis can be found in the methods section in Chapter 5.3.

Figure description continues on the next page.

Figure 3.3.3 Bursting kinetics of target gene promoters change with p53 activation. ***(continued)***

(B) The RNAP2 occupancy (M) derived from TSS intensity measurements extracted from *FISH-Quant* relative to the fluorescence intensity of an average RNA spot, as described in equation [4] and Figure 3.3.2.D. Curves show density functions relative to the expected number of RNAP2 per promoter. The number of quantified TSS for each time-point is indicated. For most p53 target genes the RNAP2 occupancy (M) at promoters remained similar regarding the average and distribution over all analyzed time-points.
(C) Analog to (B), this column shows the calculated relative burst size/ TSS calculated as described in Chapter 3.3.2, Figure 3.3.2.D. As directly derived from RNAP2 occupancy measurements, the relative burst size per TSS displayed as RNA/h remains similar for most target genes at all time-points.
(**D**) The burst size per cell (μ [RNAs/h]), shows a correlation to the number of RNA counts, indicating that bursting features strongly impact RNA abundance.

promoters were found to be actively transcribing before γ-irradiation. When comparing the distribution of cells with inactive, partial and strong TSS activity for each target (Figure 3.3.3.A, grey) this effect was even stronger with only 15% cells that were found to be transcriptionally inactive for BAX and 40% for MDM2. With the rise of the first p53 pulse at 3 h after 10 Gy γ-IR, the fraction of active promoters increased for all targets (Figure 3.3.3.A), mainly affecting the fraction of cells that were only partially active before. At later time-points, p53 target promoters were regulated more gene-specifically. While the burst fraction for BAX remained sustained after the first peak, other targets showed transient promoter activity with a lower rate specifically at 9 h post damage as visible for MDM2 (0.46) and CDKN1A (0.23). At the same time, the RNAP2 occupancy indicating the burst sizes (Figure 3.3.3.B), did not change strongly for most target genes with DNA damage (Figure 3.3.3.B).

Despite some differences for individual time-points such as 3 h and 6 h after 10 Gy for MDM2, the distribution of RNAP2 and the relative transcription rate at a TSS, as derived from the mathematical calculation of promoter activity, remained similar for one target gene at all time-points. The summed transcription rate per cell can differ in its dynamics from the relative comparison at one TSS. Though, as the current literature does not provide evidence for allele-specific bursting kinetics of p53 targets and the distribution of cells with multiple active sites did not show strongly differing bursting modes, the relative burst size as an equal quota from the total RNA counts per cell is shown allowing a better comparison of TSS activity. Quantitatively, significant differences in the transcription rate for target genes were found, and the transcription rate per cell correlates with higher RNA abundance for all time-points (Figure 3.3.3.C). In general, the calculated transcription rates (transcribed RNAs per hour) and RNAP2 occupancies were higher than expected with a range of 32 RNAP2/TSS (BAX, basal) to 91 RNAP2/TSS (SESN1, 9 h 10 Gy) (Figure 3.3.3.C/D).

3.3.4. RNA HOMEOSTASIS OF P53 TARGET GENES

The direct measurement of transcription at active promoters showed time-dependent changes in their activity (Chapter 3.3.3), suggesting a contribution of TSS activity to the gene-specific patterns of RNA abundance as seen at the different time-points after γ-irradiation. In contrast, previous work indicated a close correlation between RNA and protein lifetimes and target gene expression levels (Porter et al., 2016; Hafner et al., 2017;

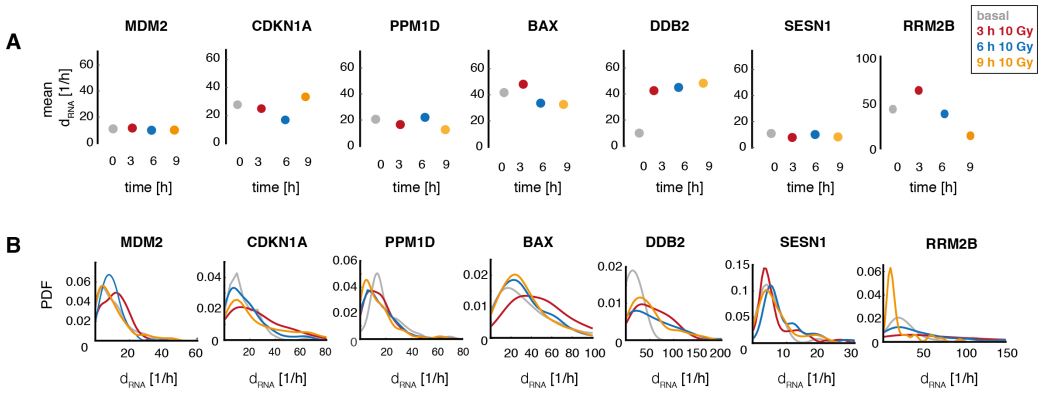

Figure 3.3.4 RNA homeostasis and nuclear export rate of p53 target genes remain similar upon damage.

(A) Panel (A) shows the quantified mean degradation rate [1/h] (d_{RNA}), calculated based on the promoter activity from smFISH images. Only actively transcribing cells were considered in this analysis. The RNA decay rate was similar at all time-points for most p53 target genes. As the only target gene, DDB2 shows a strong increase from basal state to time-points were detected. In general, the measured degradation rates that relate to a lifetime of a few minutes were short compared to literature data that suggest an average lifetime of 50 min in mammalian cells (Schwalb et al., 2016).
(B) Density functions of RNA decay rates calculated for single cells based on transcription site activity (burst size), the number of active TSS and the RNA counts per cell. Colors indicate the different time-points after DNA damage, basal (grey), and 3 h 10 Gy (red), 6 h after 10 Gy (blue) and 9 h after 10 Gy (orange).

Hanson et al., 2019). One reason could be that RNA abundance, promoter activity and degradation rate have not been measured simultaneously in single cells in these mentioned studies. Therefore, I characterized changes in RNA homeostasis after DNA damage by determining the RNA degradation (d_{RNA}) rate based on the two-state burst model of promoter activity derived from equation [6] (Bahar Halpern et al., 2015b; Bahar Halpern and Itzkovitz, 2016; Raj et al., 2008). To this end, the mean RNA decay rate was calculated and compared for all p53 targets at different time-points after DNA damage (Figure 3.3.4.A). Based on this analyses, the mean degradation rate varied for the different targets but did not strongly change after DNA damage for most p53 targets. Exceptions are DDB2 showing an increase in degradation from 3 h onwards and RRM2B with a higher RNA decay at 3 h after γ-irradiation (Figure 3.3.4.A). Only small fluctuations for individual time-points were observed. Remarkably, the measured changes of degradation rates over time did not directly correspond to changes in gene expression patterns, suggesting that besides RNA stability (Hanson et al., 2019; Porter et al., 2016), other factors as the observed changes in burst frequency may contribute to gene-specific expression patterns as well. Also, degradation rates did show a broad, overlapping range at all time-points instead of a multimodal distribution (Figure 3.3.4.B), indicating that RNA stability does not change mechanistically in cellular sub-populations. RNA lifetimes ($t_{1/2}$) can be calculated from the decay rate (Chen et al., 2009), with d_{RNA} being the RNA degradation rate.

$$t_{\frac{1}{2}} = \frac{ln(2)}{d_{RNA}} \qquad [7]$$

Notably, while only comparing the relative differences at the time-points after DNA damage was in the scope of the analyses of this work, the derived RNA lifetimes were very low for all

p53 targets, within a few minutes, while median RNA lifetimes of about 50 min have been previously measured by transient transcriptome sequencing (TT-Seq) for K562 cells (Schwalb et al., 2016). In validation experiments by transcription shutdown, as shown for BAX, decay rates were slightly lower compared to those at basal state calculated from the transcription model, but also suggest very short lifetimes (BAX $dRNA_{DRB}$ = 18.4, $dRNA_{model}$ = 42). However, as the smFISH based calculations are indirect analyses, estimating RNA stability from RNA counts and promoter bursting features, a more comprehensive view on RNA homeostasis could be provided by genome-wide tracing methods based on 4-thiouridine (4sU) incorporation (Herzog et al., 2017; Schofield et al., 2018). With these, the RNA stability can be estimated from the ratio of newly transcribed (4sU-labeled) to unlabeled RNA (transcribed before a 4sU-pulse), or from RNA profiling upon a shutdown of transcription after DRB treatment. As this was beyond the scope of this study, the decrease of RNA counts upon inhibition of transcription was only calculated and validated based on smFISH measured as described in Chapter 3.3.3, while half-lives can be derived from equation [7].

RNA export from the nucleus to the cytoplasm has been previously quantified on a time-scale of a few minutes to a maximum of half an hour (Oeffinger and Zenklusen, 2012; Shav-Tal et al., 2004; Vargas et al., 2005). The export dynamics for p53 target genes were estimated based on the resulting data of bursting kinetics and RNA stability (Bahar Halpern et al., 2015a). As indicated by the characteristics of gene expression noise in Chapter 3.2.3, RNA export rates were similar for an individual p53 target at the different conditions (Figure 8.3.3/6).

3.3.5. ARCHETYPES OF P53-MEDIATED PROMOTER ACTIVITY

When comparing how the characteristic measures of p53 dependent gene expression differ among target genes (Figure 3.3.5.A), it became clear that burst frequency is a major driver of induced gene expression after p53 activation by γ-IR. Also, the distinct patterns of RNA expression levels reflect the general dynamics of changes in the fraction of active promoters and thus burst frequency (Figure 3.2.2, Figure 3.3.3). Concentration sensitive transcription factor binding can modulate the frequency of transcriptional bursting (Senecal et al., 2014; Larson et al., 2013; Kafri et al., 2016). Therefore, Chromatin Immunoprecipitation (ChIP) experiments were performed at the defined time-points after 10 Gy (with Laura Friedel). As expected, p53 promoter binding reached a maximum with the first accumulation pulse (Figure 3.3.5.B). Interestingly, it was not possible to detect binding above IgG control levels for PPM1D. For a better comparison of p53 binding dynamics after this first peak, the relative change in p53 binding was normalized to the 3 h time-point (Figure 3.3.5.B). Surprisingly, p53 binding does not return to basal levels at 6 h (Figure 3.3.5.B). Instead, for all analyzed promoters, p53 binding decreased gradually to intermediate levels, although its global concentration varied significantly between the trough and the second peak at 9 h. This disconnect between nuclear protein levels and DNA binding after the first pulse is unexpected as total nuclear p53 levels change significantly at

the same time-points (Figure 3.3.5.B). Notably, these data suggest that p53's regulatory potency at promoter sites differs between the first and the second pulse, as the total bound p53 protein only shows a gradual descend.

The burst frequency could also be correlated with the interaction of distal *cis*-regulatory elements and the H3K27ac state of promoters (Nicolas et al., 2018). While enhancer contacts were not evaluated in more detail, the H3K27me and H3K27ac states were analyzed in promoter-proximal regions for the targets CDKN1A, MDM2, and BAX by ChIP. H3K27ac remained at high levels at the measured time-points without notable differences, while H3K27me was reduced (Figure 8.3.3/7). Though, gene-specific differences

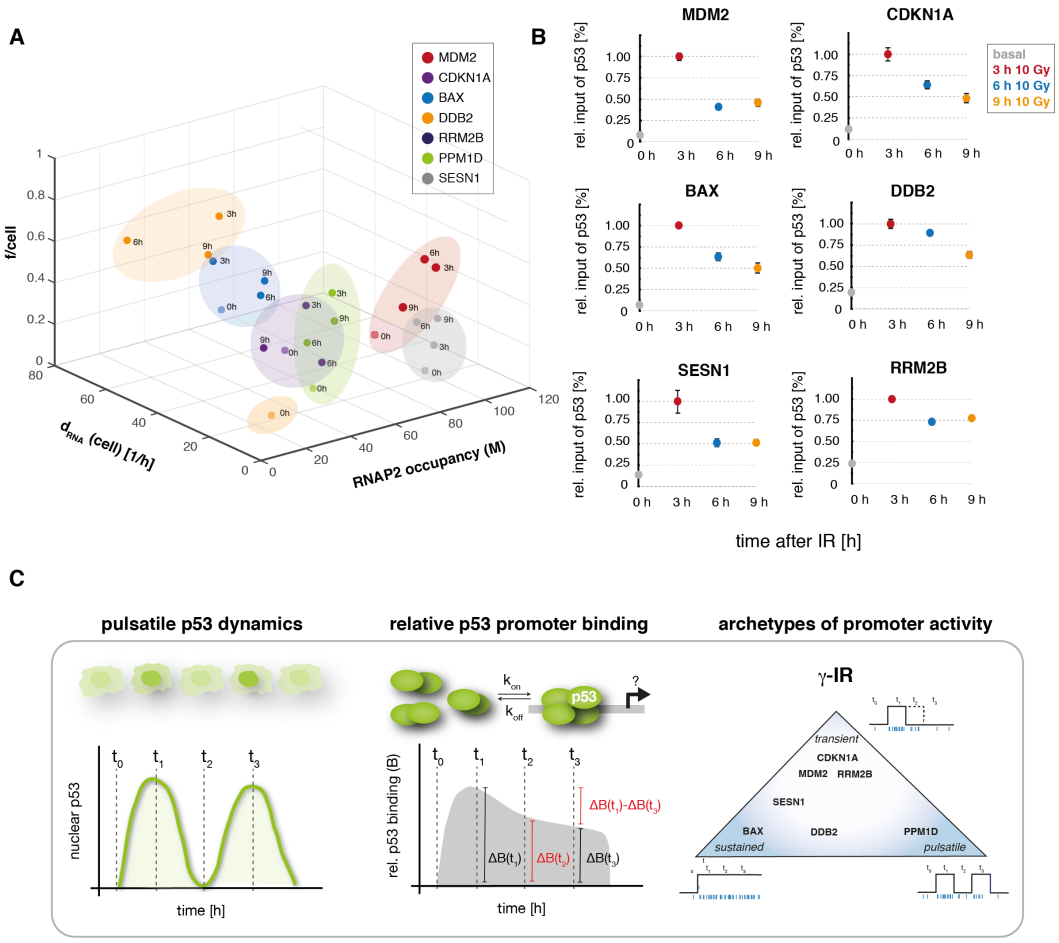

Figure 3.3.5 P53 targets can be grouped into archetypes of promoter activity.

(A) 3D-scatter plot of transcription features for all p53 target genes. Shaded areas provide a better visualization of the range of measured parameters (for visualization only, not calculated) for the different time-points. The burst frequency (f) for the fraction of actively transcribing cells, RNAP2 occupancy (M) as an indicator for burst size and RNA degradation rate (d) are plotted as mean levels.
(B) Chromatin Immunoprecipiation (ChIP) experiments of p53 binding to target gene promoters, displayed as relative % of p53 binding. All data are normalized to the first p53 peak at 3 h. Error bars represent RQ min and RQ max values from triplicate quantifications in qRT-PCR measurements. For PPM1D, no binding above the IgG control was detected at any of the time-points. ChIP experiments and initial qRT-PCR analysis of raw data for this experiment were generated by Laura Friedel (TU Darmstadt).
(C) P53 targets can be grouped based on the stochastic nature of their promoter activity. While the p53 input and p53 binding is similar, p53 target gene promoters can be classified along distinct archetypes of activity, ranging between pulsatile, sustained and transient bursting as indicated in this triangle.

that could point towards the modulation of γ-IR induced expression patterns could not be found. In particular, transiently active target gene promoters that do not respond equally to the first and second p53 pulse cannot be explained by these modifications. Notably, target genes with higher expression rates and burst sizes showed a trend towards a higher H3K27ac onset upon DNA damage in the first 3 h (Figure 8.3.3/7).

The smFISH based analysis allowed to characterize p53 target gene expression in single cells and at individual promoters after γ-IR-induced pulses of p53. From these quantifications, it became clear that p53 targets are regulated gene-specifically after a similar initial increase with the first p53 peak, while neither RNA stability nor p53 promoter binding can explain these gene-specific differences. To allow a comparison of the transcriptional activity of p53 targets, I classified target genes along three archetypes of promoter activity: *transient, pulsatile,* and *sustained* (Figure 3.3.5.C). PPM1D showed pulsatile activity. CDKN1A, MDM2 and RRM2B were transiently active and BAX, DDB2 and SESN1 showed more sustained activity.

3.3.6. THE ACTIVATION STATE OF THE P53 NETWORK

The different archetypes of promoter bursting as introduced in the previous chapter indicate that the second p53 pulse has a different potency to activate transcription than the first pulse. Particularly for genes that are transiently expressed, such as MDM2 and CDKN1A it became clear that despite high levels of p53 binding, the transcription activity is lower at the second pulse. As this indicates a change in p53 activity, I characterized changes in the p53 signaling network (Figure 3.3.6.A) based on quantitative immunofluorescence. To this end, I quantified pChk1, pChk2, p53S15 and p53S45 abundance after 10 Gy γ-IR at the four different time-points (Figure 3.3.5.B).

Surprisingly, while the total p53 levels show a pulse (Figure 3.2.1), pChk1 and pChk2 levels are reduced after the first p53 pulse (Figure 3.3.6.B). Also, ATM dependent S15 phosphorylation of p53 is decreased after the first p53 pulse, while ATR specific S46 phosphorylation remains at similar levels after γ-IR (Figure 3.3.6.B). This finding suggests that the conventional view on repeated pulses of nuclear p53 may not display the full picture of p53 network activity. So far, ATM and other kinases upstream of p53 have been described to reactivate p53 in recurring pulses of the same activity as long as DNA damage is still present (Batchelor et al., 2008). In contrast, a change in p53's PTM patterns and Chk2 activation may hint towards either another layer of regulation downstream of PI3K-like kinases or additional co-regulatory factors that reduce p53 PTMs.

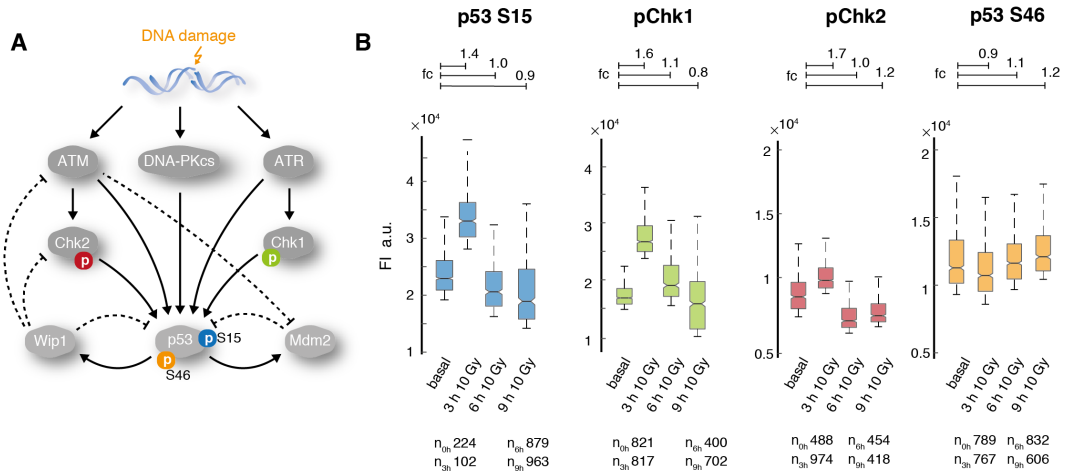

Figure 3.3.6 The p53 network changes its state between the first and the second pulse.

(A) Schematic view of selected components of the p53 signaling network that were analyzed by immunofluorescence staining to detect changes in the phosphorylation state of the p53 network.
(B) Boxplot quantification of protein levels in single cells based on immunofluorescence data at the defined time-points (basal, 3 h, 6 h and 9 h). Protein levels have been measured as integrated intensities in nuclei of cells with the highest 10% of signal. Whisker represent 25th to 75th percentile. Notches display interval endpoints. If notches do not overlap, they represent a significance at the 5% confidence level. Outliers are not displayed. The sample size was n >100 for all conditions as indicated on the x-axis.

3.4. MODULATING P53 DYNAMICS AND POST-TRANSLATIONAL MODIFICATIONS TO CHANGE BURSTING KINETICS

3.4

The results presented so far suggest gene-specific promoter archetypes. A gradual descend in p53 promoter binding was found (Figure 3.3.5.B), while the potency of p53 as a transcriptional activator changes between the first and the second pulse, after an initial similar up-regulation in the early DNA damage response at 3 h (Figure 3.3.3.B). Additionally, previous studies suggested differences in the modulation of p53 targets by pulsatile and sustained p53 levels, inducing genes that are specific for different cell fate regulation (Purvis et al., 2012). It thus remains unclear if p53 acts as a pioneering TF on promoters and to which extent nuclear p53 levels change transcriptional activity beyond the first pulse. To this end, bursting features of target genes in the context of different p53 nuclear dynamics must be compared.

IN THIS CHAPTER

3.4.1. INDUCING TRANSIENT P53 BY CHK2 INHIBITION LEADS TO REDUCED STOCHASTIC BURSTING

The previous results highlighted that p53 targets show gene-specific archetypes of stochastic bursting after a similar initial activation upon DNA damage by γ-IR. Interestingly, some target genes were transiently expressed (MDM2, CDKN1A) and did not respond with an increase in transcription to the second p53 pulse. This questions if p53 is required for transcription of these targets at later time-points. In line with this, it was recently suggested that p53 can function as a pioneer factor, with pronounced non-specific nucleosome binding that enables the interaction with closed chromatin in genomic regions close to response elements (Sahu et al., 2010; Yu and Buck, 2019). Through binding to condensed chromatin, pioneer factors prime a promoter to a transcriptionally active or repressed conformation by recruiting co-regulatory factors such as chromatin-modifying enzymes and other TFs. However, they are not necessary for downstream transcriptional activity. To analyze the dependence of promoter bursting on a second p53 pulse, I tuned nuclear p53 levels into a transient response (Figure 3.4.1.A). Therefore, cells were γ-irradiated by 10 Gy to conserve the initial activation and induced PTMs of the first pulse. Afterwards, cells were treated with 10 µM of the Chk-2 inhibitor BML-277 at 4 h, repressing the second pulse as validated by quantitative Immunofluorescence of nuclear p53 levels (Figure 3.4.1.B). Subsequently, stochastic bursting was analyzed for a set of four target genes that were allocated to different archetypes based on previous experiments (Figure 3.4.1.C-G). In the context of pulsatile p53, PPM1D showed pulsatile bursting, BAX exhibited sustained transcriptional activity, and CDKN1A and MDM2 promoters were transiently active (Figure 3.4.1.C). The fraction of active promoters and the RNA levels per cell were reduced for the p53 targets BAX and PPM1D after Chk2 inhibition (Figure 3.4.1.D, E; Table 8.3.4/1). Particularly a direct

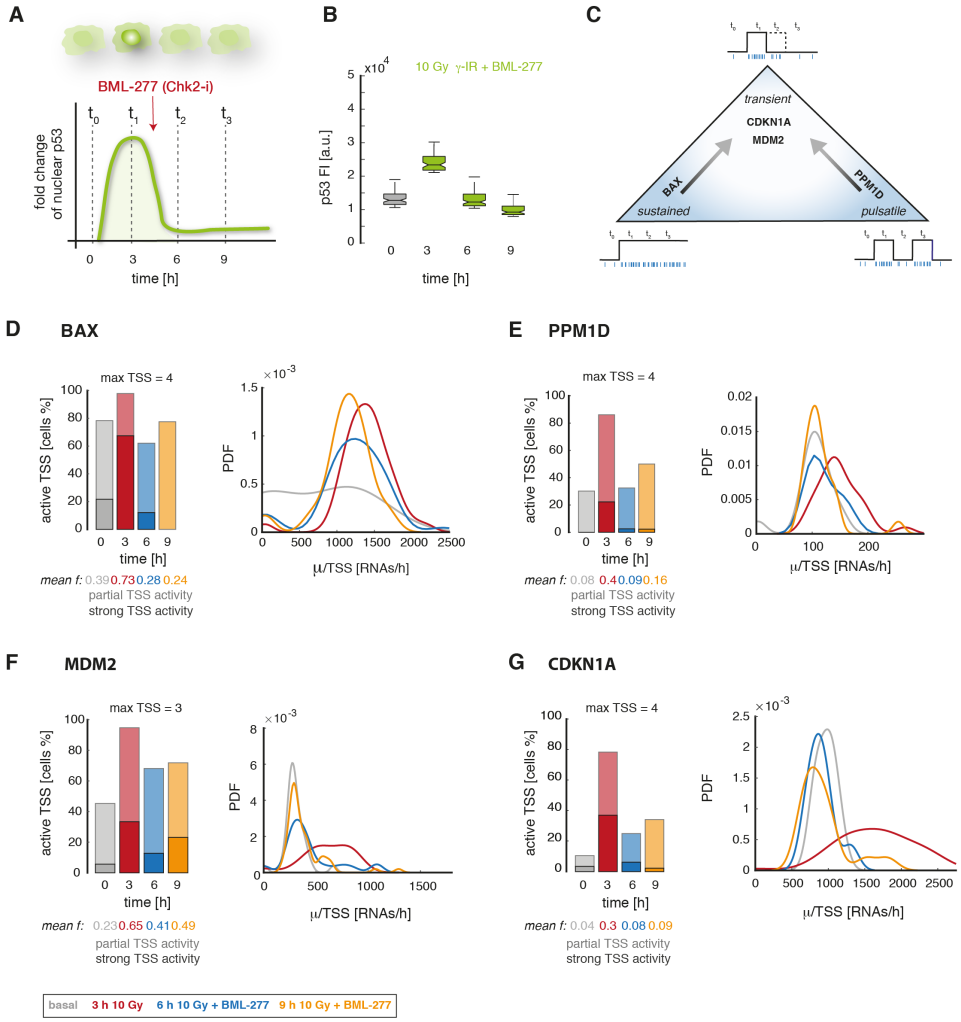

Figure 3.4.1 Chk2 inhibition induces transient p53 in the nucleus and leads to reduced promoter activity at later time-points.

(A) Schematic illustration of the experimental design**.** Chk2 inhibition was performed using the small molecule inhibitor BML-277 at 4 h, that induces transient p53 dynamics with only one pulse after 10 Gy γ-IR.

(B) Immunofluorescence based quantification of p53 levels in A549 wild-type cells after 10 Gy γ-IR and addition of 10 μM BML-277 at 4 h. Shown are boxplots of the integrated fluorescence intensity levels in nuclei of the 10% cells with strongest signal. Over >2000 cells per condition were quantified in total. Whisker represent 25th to 75th percentile and notches display interval endpoints. If notches do not overlap, they represent a significance at the 5% confidence level. Outliers are not displayed.

(C) Schematic illustration of the proposed archetypes of promoter activity and their dynamic changes, when p53 levels are transient and do not show a second pulse at 9 h.

(D-G) Promoter activity of BAX (D), PPM1D (E), MDM2 (F) and CDKN1A (G) after inhibiting the second p53 pulse by Chk2 inhibition (BML-277). The relative fraction of active promoters [% active TSS/cell] (left panel) was reduced at 6 h and 9 h after 10 Gy for all target genes. Shaded colors display the proportion of partially active cells, solid colors show cells in which a majority of TSS are actively transcribing. Average fractions of active promoters are indicated at the bottom of each panel (mean f). The relative transcription rate per TSS μ/TSS [RNAs/h] is shown as a density function for each time point (right panel).

comparison at the 9 h time-point shows a reduction of the mean fraction of active promoters for BAX and, to a lesser extent PPM1D (Figure 3.4.1.D, E). At the same time, MDM2 and CDKN1A retained their transient promoter activity, with a further reduced mean fraction of active promoters (Figure 3.4.1.F, G, Table 8.3.4/1).

Notably, the fraction of active promoters at 9 h was reduced, but similar (BAX) or above (CDKN1A, MDM2 and PPM1D) the fraction that was measured in the absence of DNA damage (basal state). This indicates that the recurrence of a second p53 pulse is fundamental to conserve transcriptional activity at later time-points, but also suggests that the initial p53-dependent activation leads to persistent conformational changes at individual promoters. At the same time, the relative transcription rate (μ/TSS) (Figure 3.4.1.D-G) was in a similar range as before. Though for CDKN1A a higher rate at 3 h was found compared to in basal state in this experiment, which was not seen before. This may be due to the smaller dataset and should be further validated in future experiments. The same holds true for detected average RNA degradation rates, that were found to be in a similar range for most targets and time-points, but with a broader distribution in the population and slightly different dynamics (Table 8.3.4/1). An overview of the average transcription parameters is provided in Table 8.3.4/1. In summary, the promoter activity of the four characterized target genes changed from distinct gene-specific regulation in the context of IR-induced p53 pulsing, to a transient expression, when repressing p53 accumulation from 4 h onwards. These results indicate that the proposed archetypes of promoter activity are not a static, gene-specific feature, but represent a dynamic stochastic bursting regime that changes dependent on nuclear p53 levels (Figure 3.4.1.C).

3.4.2. SUSTAINED P53 LEVELS INCREASE PROMOTER ACTIVITY

Previous work suggested that pulsatile dynamics and sustained accumulation lead to differential gene expression profiles and subsequent cell fate (Purvis et al., 2012). P53 levels were tuned to sustained dynamics by sequential treatment with the small molecule Nutlin-3, a MDM2 inhibitor (Vassilev et al., 2004) (Figure 3.4.2.A), to analyze if persistent levels of p53 affect stochastic bursting of target genes. Nutlin-3 has been previously shown to change pulsatile p53 into sustained dynamics (Purvis et al., 2012), which was validated by quantitative immunofluorescence in A549 wild-type cells (Figure 3.4.2.B). I analyzed promoter activity in the context of sequential Nutlin-3 treatment after **γ**-IR focusing on CDKN1A and MDM2. Both target genes have shown transient promoter activities, which were reduced during the second pulse after 10 Gy **γ**-IR (Figure 3.3.3.B). In contrast, persistent nuclear p53 led to an increase in promoter activity of both target genes with a substantial rise in the fraction of active promoters at 6 h and especially at 9 h after **γ**-irradiation (Figure 3.4.2.D, E). Interestingly, when p53 levels were sustained, not only an increase of active promoters was found for CDKN1A and MDM2, but also a higher transcription rate (Figure 3.4.2.D, E). This is particularly visible when calculating the fold change at the different time-points in cells treated with Nutlin-3 compared to cells that were only **γ**-irradiated (insets in Figure 3.4.2.D-G). Based on these data, a mechanistic shift in

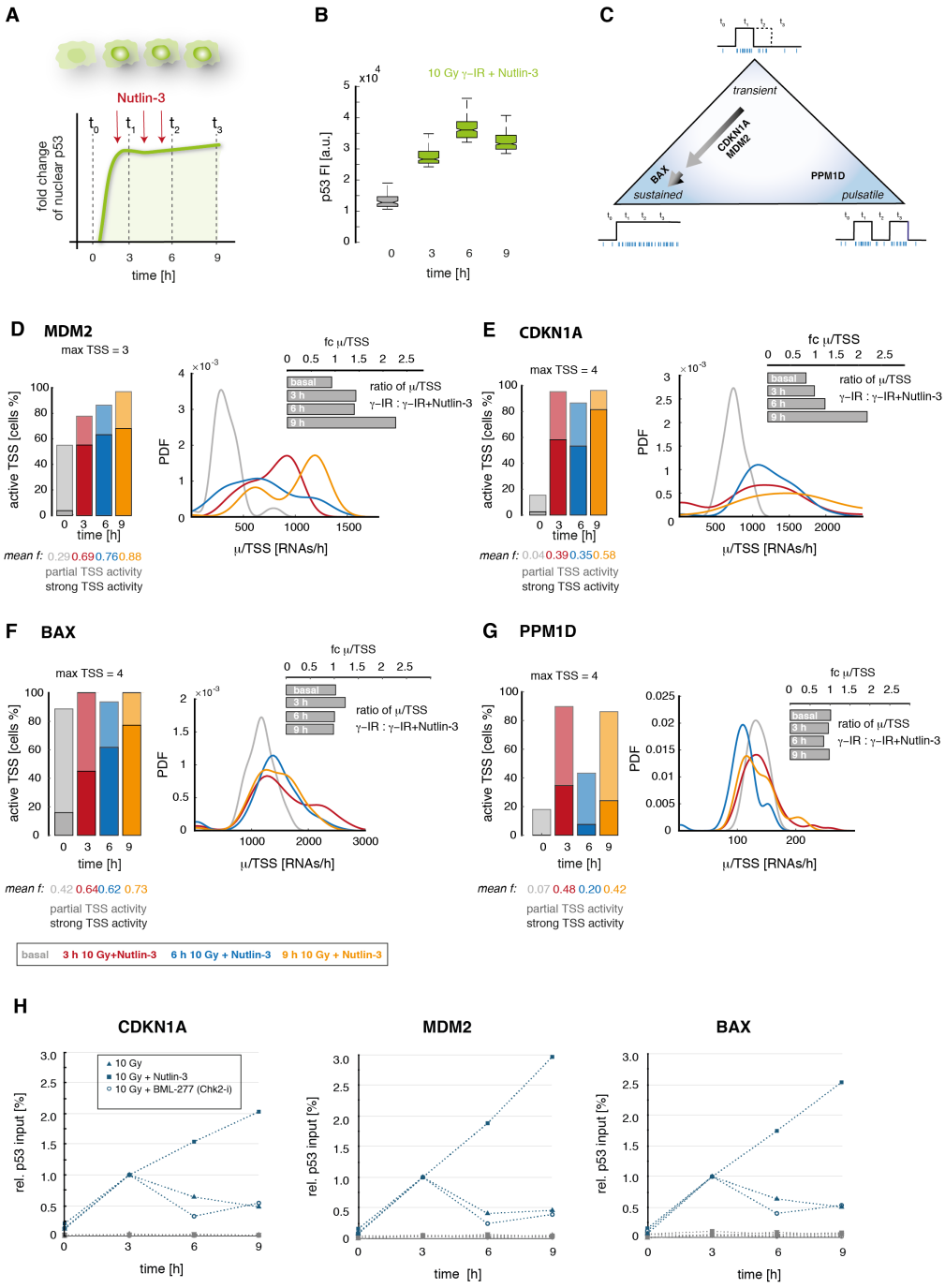

Figure 3.4.2 Transient promoter activity of target genes changes in the context of persistent p53 levels.

(A) Schematic representation of the sequential treatment with Nutlin-3 leading to a conversion of pulsatile p53 dynamics into persistent nuclear levels.

(**B**) P53 levels in A549 wild-type cells after **γ**-irradiation with 10 Gy and sequential treatment with 0.75 μM Nutlin-3 at 2.5 h, with 2.25 μM at 3.5 h and 4 μM at 5.5 h post **γ**-IR based on immunofluorescence staining are shown, represented as boxplots of the integrated fluorescence intensity levels in the 10% cells with strongest signal. Over >2500 cells per condition were quantified. Whisker represent 25th to 75th percentile and notches display interval endpoints. If notches do not overlap, they represent a significance at the 5% confidence level. Outliers are not displayed.

(C) Schematic illustration of the proposed archetypes of promoter activity and their dynamic changes, when p53 levels are persistent at 9 h.

Figure description continues on the next page.

Figure 3.4.2 Transient promoter activity of target genes changes in the context of persistent p53 levels. ***(continued)***

(D-G) The promoter activity of MDM2 (D), CDKN1A (E), BAX (F) and PPM1D (G) upon sequential Nutlin-3 treatment is shown. The relative fraction of active promoters (left panel) strongly increased, changing transient into sustained archetypes. Shaded colors display the proportion of partially active cells, solid colors show cells in which a majority of TSS are actively transcribing. Average fractions of active promoters are indicated at the bottom of each panel (mean f). The relative transcription rate per TSS is displayed as density function in RNAs/h (right panel), showing an increase compared to basal levels and to previous experiments with pulsatile p53 dynamics for CDKN1A and MDM2 (inset, fold change calculated for each time-point.
(H) ChIP measurements of relative p53 binding at different target gene promoters in perturbed and unperturbed cells, after Nutlin-3 and BML-277 treatment for the selected p53 target genes after 10 Gy γ-IR. From left to right: CDKN1A, MDM2 and BAX (p53 binding at the PPM1D promoter was not detectable above IgG controls in repeated experiments). Results were normalized to the 3 h time-point post γ-IR. Grey symbols indicate the corresponding IgG control. On the one hand, pulsatile p53 and inhibition of the second p53 pulse both lead to a gradual decrease of p53 binding after the first peak. On the other hand, Nutlin-3 treatment increases p53 binding and may thereby contribute to the observed increase in promoter activity. ChIP experiments and qRT-PCR data for these experiments were generated by Laura Friedel (TU Darmstadt).

promoter regulation towards a higher burst size can be hypothesized, for example, through RNAP2 initiation and elongation (Figure 3.4.2.D, E). At the same time, the transcriptional activity at BAX promoters remained sustained without a significant increase in the rate of transcription or the fraction of active promoters (Figure 3.4.2.F). Unexpectedly however, the stochastic bursting of the PPM1D promoter did not increase with sustained p53 levels, retaining a pulsatile phenotype (Figure 3.4.2.G). An overview of average bursting parameters is provided in Table 8.3.4/2. In general, also gene expression levels increased in the context of sustained p53 compared to the basal state. The RNA degradation rate for most p53 target showed slightly different dynamics compared to after γ-IR only (Table 8.3.4/2). In summary, these results suggest that persistent nuclear p53 does strongly change p53 dependent promoter activity towards a more productive transcriptional output. Target genes that were transiently expressed when p53 is pulsing change to sustained activity. However, gene-specific regulation can be found as well, as for the PPM1D promoter that retains its pulsatile activity (Figure 3.4.3.C).

To understand how the relative binding of p53 to target gene promoters change, when p53 levels are tuned, ChIP experiments were performed for the three conditions: pulsatile (γ-IR), transient (γ-IR + BML-277) and sustained p53 (γ-IR + Nutlin-3) (with Laura Friedel). Based on these experiments, an increase of relative p53 binding at all analyzed promoters for sustained p53 (BAX, CDKN1A and MDM2) was found (Figure 3.4.2.H). At the same time, transient p53 accumulation upon Chk2 inhibition by BML-277, led to comparable binding profiles as seen for pulsatile p53 instead of a complete loss of binding (Figure 3.3.4.H).

3.4.3. REGULATORY PTMS IN P53'S C-TERMINAL DOMAIN AFFECT STOCHASTIC BURSTING

The previous results highlighted that p53's potency as a transcriptional activator differs depending on the dynamics of nuclear accumulation, particularly for target genes that were transiently expressed in response to pulsatile p53. Multiple studies revealed the influence of p53's highly unstructured C-terminal domain (CTD) on gene expression (reviewed in Sullivan et al., 2018). More precisely, p53's regulatory potential on activating transcription highly depends on the post-translational modifications state of the CTD (Bode and Dong,

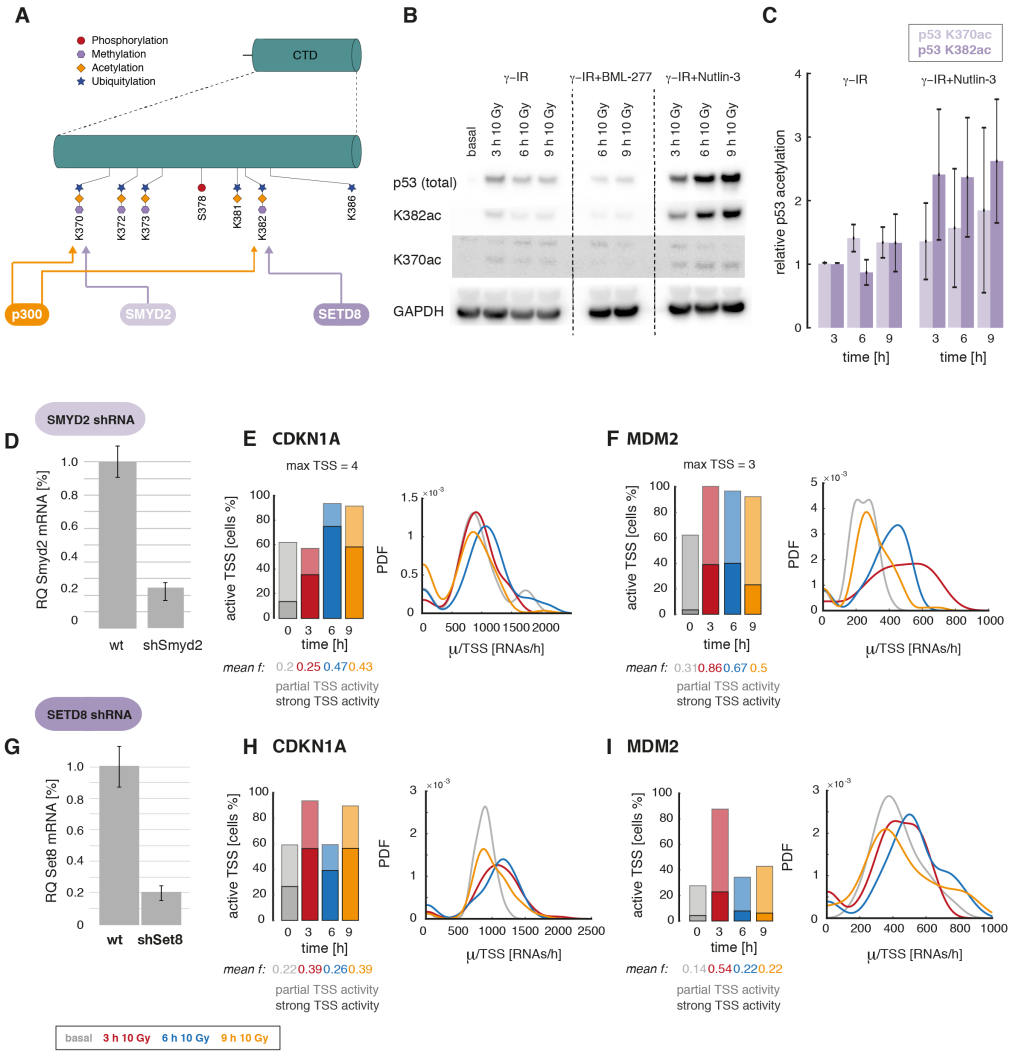

Figure 3.4.3 P53's C-terminal acetylation state changes stochastic bursting.

(A) P53's C-terminal (CTD) can be modified at multiple sites, including by the key-regulatory methylases Smyd2 and SetD8 as well as p300 as the major p53 acetylase (a more detailed view is provided in Figure 1.2.3)
(B) Western Blot measurement of total p53, p53 acetylated at K382 and K370 and GAPDH. Cells were harvested at indicated time-points in the context of different p53 dynamics: pulsing p53 (10 Gy γ-IR), transient p53 (10 Gy γ-IR + BML-277, central lanes) and sustained p53 (10 Gy γ-IR + Nutlin-3, right lanes).
(C) The relative change in p53 acetylation at K370 (light purple) and K382 (dark purple) was quantified from the Western Blot and normalized to the total abundance of p53 3 h after γ-IR. Means and standard errors from three independent experiments are indicated. Acetylation increased over time in the context of sustained p53.
(D) The knock-down efficiency of the p53-K370 methylase Smyd2 in a clonal stable A549 cell line expressing a corresponding shRNA, measured in A549 wild-type and knock-down cells by qRT-PCR. Mean levels and standard deviation from technical replicates are shown.
(E-F) The Promoter activity of CDKN1A (E) and MDM2 (F) were quantified in Smyd2 knock-down cells. A higher fraction of active promoters [%] after 10 Gy γ-IR compared to A549 wild-type cells can be seen (left panel). The relative burst size per TSS [RNAs/h] (right panel) remains similar. Shaded colors show the fraction of cells that are partially active. Solid colors highlight the fractions of cells in which a majority of TSS are actively transcribing. The average fractions of active promoters (mean f) are indicated at the bottom.
(G) The knock-down efficiency of the p53-K382 methylase SetD8 in a clonal stable A549 cell line expressing a corresponding shRNA, measured in A549 wild-type and knock-down cells by qRT-PCR. Mean levels and standard deviation from technical replicates are shown.
(H-I) Promoter activity of CDKN1A (G) and MDM2 (H) were quantified in SetD8 knock-down cells. A higher fraction of active promoters [%] after 10 Gy γ-IR compared to A549 wild-type cells is found for CDKN1A (left panel).The relative transcription rate [RNAs/h] (right panel) remains similar. Shaded colors show the fraction of cells that are partially active. Solid colors highlight the fractions of cells in which the majority of TSS are actively transcribing. The average fractions of active promoters (mean f) are indicated at the bottom.

2004; Sims et al., 2004; Loffreda et al., 2017). On the one hand, C-terminal acetylation of the lysine residues K370, K372/73 and K381/82 by p300/CBP has been associated with a transcriptionally active state (Figure 3.4.3.A) (Gu and Roeder, 1997; Gu et al., 1997). On the other hand, methylation of K370, K373 and K382 inhibit target gene expression (Figure 3.4.3.A) (Huang et al., 2006; Shi et al., 2007). When comparing lysine modification states in absence and presence of DNA damage, repressive methylation marks keep p53 transcriptionally inactive, while DNA damage leads to a fast change towards CTD acetylation to enhance target gene expression (Loewer et al., 2010; Berger et al., 2010). To test if this dynamic interplay of mutually exclusive C-terminal lysine acetylation or methylation can explain the transient MDM2 and CDKN1A expression during the second pulse, changes in K372ac and K382ac were measured by Western Blot (Figure 3.4.3.B). Therefore, pulsatile, transient and sustained p53 accumulation was induced as described in the previous paragraphs and the relative levels of K370ac and K382ac p53 were quantified relative to overall p53 levels (Figure 3.4.3.C). While K370ac levels showed only a slight increase, K382ac levels were higher under sustained p53 conditions compared to pulsatile p53 (Figure 3.4.3.B), suggesting stabilization of acetylated p53 due to reduced methyl-transferase activity or protein turnover (Li et al., 2002). These results indicate that a higher proportion of C-terminally acetylated p53 may induce the shift in bursting kinetics for the transient targets CDKN1A and MDM2.

To test to which extent this change in p53's modification state affects promoter activity, stable clonal cell lines expressing shRNAs against the two corresponding methylases, Smyd2 and SetD8 were generated. These A549 shRNA knock-down cell lines had reduced RNA levels of 22% for Smyd2 and 20% for SetD8 (Figure 3.4.3.D, G). I then characterized promoter activity of CDKN1A and MDM2 in these cell lines. While the fraction of active promoters remained similar at 3 h after 10 Gy compared to A549 wild-type cells, it strongly increased at 9 h from 23% to 43% for CDKN1A and only slightly from 46% to 50% for MDM2 in Smyd2 knock-down cells (Figure 3.4.3.E, F). Even though the observed increase in the fraction of active promoters indicating higher burst frequencies at 9 h after sequential treatment with Nutlin-3 was even more pronounced, this suggests a contribution of Smyd2 mediated methylation to reduced transcription during the second p53 pulse for transient p53 targets. While p53 levels were also sustained in knock-down cells dependent on upstream kinase signaling (Figure 8.3.4), other co-regulatory mechanisms may effect the transcriptional increase of promoter activity beyond p53 abundance leading to enhanced bursting after Nutlin-3 treatment, as well. For CDKN1A, persistent expression through burst frequency modulation, as shown by a higher fraction of active promoters was also detected in SetD8 knock-down cells (Figure 3.4.3.H), but to a lesser extent than upon Smyd2 knock-down. The quantified RNAP2 occupancies and resulting transcription rates did not show significant changes upon knock-down (Table 8.3.4/2). It has been previously shown that the different lysine residues in p53's CTD act in concert, thereby establishing partially redundant mechanisms to provide robustness (West and Gozani, 2011; Beckerman and Prives, 2010; Reed and Quelle, 2015). Therefore, combinatorial effects of different residues or additional co-factor interaction may modulate the transient transcription of MDM2 and CDKN1A.

3.5. LIVE-CELL RNA IMAGING OF P53 TARGET GENES

3.5

IN THIS CHAPTER

In the previous chapters, I analyzed p53 dependent transcription at defined time-points upon DNA damage after fixing cells and staining with smFISH probes for individual RNA molecules. While this analysis has its strength in the detection of RNA levels and localization in many cells and allows to infer promoter activity in genetically unperturbed (wild-type) cells, the approach is limited regarding the time-resolution and cell history due to its requirement of fixing cells at a certain time-point. Hence, it leads to snapshots of the RNA and TSS state, which cannot be connected with past and future RNA levels or the transcriptional activity of a cell. Therefore, it is not possible to correlate the promoter activity induced by DNA damage with preceding stochastic bursting that can change for example in different cell cycle phases and may have been active before applying γ-irradiation. Also, to gain a representative picture of single-cell kinetics, it is necessary to acquire data from many cells at multiple time-points. When analyzing multiple genes, this leads to large efforts in image acquisition and processing. Importantly, also predicting cell fate decisions that result from a certain gene expression activation is not easily possible when working with fixed cells. To tackle these questions and further expand our understanding of p53 dependent promoter activity, it is therefore inevitable to visualize transcriptional activity in living cells as well.

3.5.1. ESTABLISHING LIVE-CELL RNA IMAGING REPORTERS TO TRACK TSS ACTIVITY OF P53 TARGET GENES

To characterize p53-mediated promoter regulation with TSS activity, I examined different live-cell RNA imaging systems. I tested the Spinach2 and the Mango aptamers (Paige et al., 2011; Song et al., 2014; Dolgosheina et al., 2014), but a significant transcriptional turn-on for both was not detectable. Also, in close collaboration with the research group of Oliver Seitz (Humboldt-Universität zu Berlin), an RNA repeat-tag that is targeted by forced intercalation of thiazole orange (FIT) probes was generated. These efforts, i.e. establishing a FIT-probe based RNA reporter system (F-tag) for quantitative live-cell imaging, have been previously published and will thus not be further discussed in this thesis (Chamiolo et al., 2019; Fang et al., 2018; Hövelmann, 2015). In essence, the designed strategy was applicable for live-cell RNA imaging, but the homogenous delivery of FIT probes into cells for reproducible quantitative imaging on longer time-scales requires further optimization. Also, FIT-probe bound RNAs were not yet identifiable as single spots despite of applying up to 45x F-tag repeats.

Therefore, I employed live-cell RNA imaging using MS2 hairpins (Chapter 1.3.3) to track promoter activity of p53 target genes. First, a lentivirus expression plasmid was generated, which continuously expresses the MS2 binding (MCP) coat protein fused to an

mVenus fluorescence protein from an EF1α promoter. It was used jointly with an H2B-eCFP-Hygromycin reporter construct that enables to visualize nuclei based on histone-2-B (H2B) labeling as described before (Chapter 3.2.1). After parallel infection with generated virus particles from these plasmids, stable clonal reporter cells were selected based on antibiotic resistance using a combination of Hygromycin B (for H2B) and Puromycin dihydrochloride (for MCP) to screen for positive genomic integration of the reporters (Figure 3.5.1.A). Limited dilution cloning then led to clonal, genetically identical cell lines. A clone with moderate MCP-mVenus expression and a strong signal of H2B-eCFP nuclear fluorescence was selected based on FI measurements from time-lapse imaging. The selected clone was then used for genomic integration of 24xMS2 stem loops as RNA reporters employing CRISPR/Cas9-based genome editing for knock-in (Figure 3.5.1.A). Therefore, a

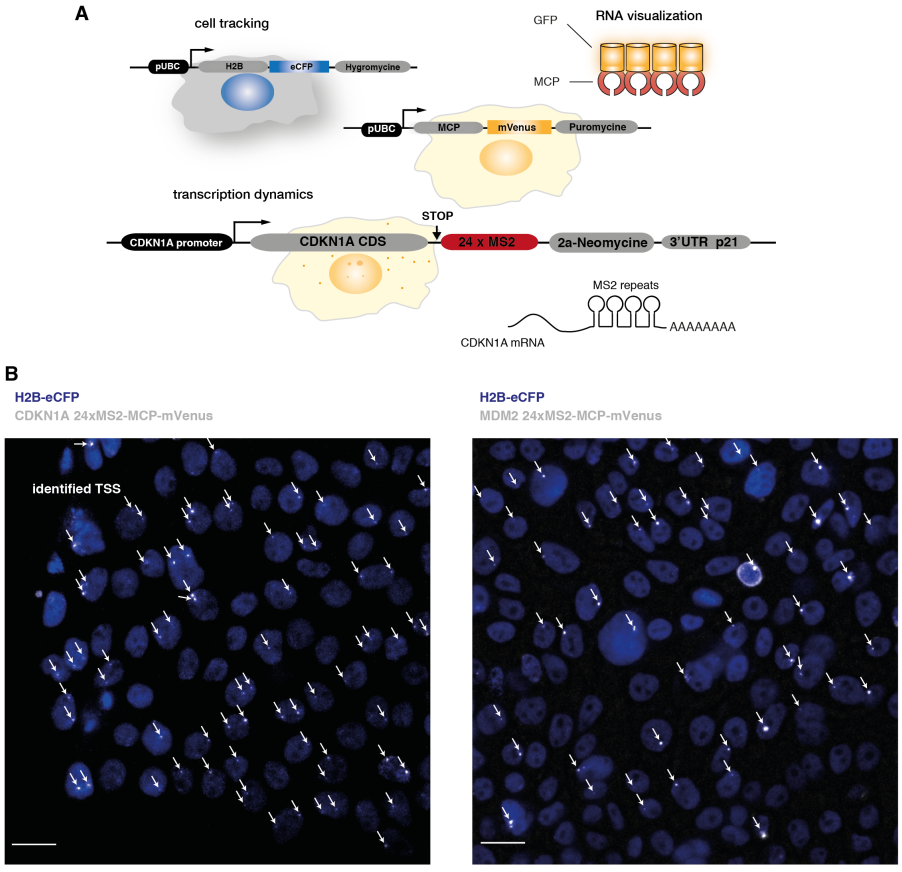

Figure 3.5.1 Reporter cells for live imaging of CDKNA1 and MDM2 promoter activity.

(A) Schematic illustration of live-cell imaging reporter cell lines. CDKN1A is presented as an example; MDM2 cell lines were generated with an analog strategy. CDKN1A reporters were homozygous and MDM2 reporters heterozygous. H2B-eCFP was used for nuclei tracking, MCP-mVenus is the MS2-loop binding protein. 24 MS2-loop repeats are integrated by CRISPR/Cas9 into the 3'UTRs of CDKN1A and MDM2.
(**B**) Representative images of MS2 reporter cells in basal state are depicted. Images show example frames of CDKN1-24xMS2 (left) and MDM2-24xMS (right) reporter cell lines from a 12 h time-lapse experiment. Composite images show maximum projected images from 9 z-stacks (300 nm) of MCP-mVenus (grey) and H2B-CFP (blue) fluorescence signal. For visualization purposes, images are brightness and contrast enhanced and a median filtered reference image (20px) was subtracted from MCP-mVenus images at each time-point, before filtering with gaussian blur (px1), to increase visualization of TSS activity in the MCP-mVenus channel. Arrows indicate identified active TSSs. Scale bar corresponds to 20 µm. Interestingly, p53 target genes are actively transcribing in absence of extrinsically applied DNA damage in MCF10A reporter cells.

new version of the randomized 24xMS2 stem-loop system was utilized to generate repair templates for targeted genomic integration (Wu et al., 2015). I focused on the p53 target genes MDM2 and CDKN1A as these featured high, tunable TSS activities in smFISH experiments upon activation with different p53 dynamics. To avoid amplification of genomic loci as observed by smFISH and DNA FISH in A549 cells, the knock-in of reporters for live-cell imaging was performed in diploid MCF10A cells (Debnath et al., 2003). Single guide RNAs (sgRNAs) and the molecular cloning strategy for reporter constructs with flanking genomic regions and MS2 stem loops for Cas9-mediated integration by homologues repair was designed based on validated protocols that were established in a previous project, employing fluorescence protein knock-in into MDM2 and CDKN1A loci in MCF10A cells (Sheng et al., 2019; Sheng, 2018). 24xMS2 stem-loops were integrated into the 3'UTR of MDM2 and CDKN1A after the stop codon. In the 3'UTR, a Neomcyine resistance gene was incorporated to allow for antibiotic selection of positive clones using G418 (Figure 3.5.1.A). To overcome limitations with IRES based expression, the Neomycin resistance gene is used with a 2A self-cleaving peptide (Ibrahimi et al., 2009). Clones were validated by direct PCR and sequencing to identify homozygous and heterozygous knock-in of the MS2 repeats. For MDM2, only heterozygous reporter expression was achieved, while CDKN1A was successfully tagged on both alleles. Accordingly, only one TSS was detectable in MDM2 reporter cells, while a maximum of two TSS was found in CDKN1A reporters (Figure 3.5.1.B). Interestingly, similar to what has been measured by smFISH in A549 cells, for both target genes a distinct promoter activity was found in basal state, with many cells actively transcribing (Figure 3.5.1.B). Also, individual MS2-tagged RNAs were visible in the nucleus and cytoplasm, but bleaching occurred in 1-2 min when acquiring stacks with high exposure times for short time-scales.

3.5.2. CHARACTERIZING MDM2 AND CDKN1A PROMOTER ACTIVITY BY LIVE-CELL IMAGING

Next, by using the generated reporters, robust live-cell RNA imaging in different signaling contexts and the quantitative analysis of TSS activity were established. First, imaging conditions were optimized to reduce fluorescence bleaching and enable long-term detection of TSS activity for time-scales in the range of one or two p53 pulses. Optimized microscopy conditions allowed 12 h continuous acquisition of nine 300 nm z-stacks, imaged every 90-150 sec. As shown in Figure 3.5.2.A, TSS activity was detectable for up to 12 h for both p53 target genes (CDKN1A and MDM2) in basal cycling conditions and after applying chemotherapeutic treatment (Neocarcinostatin, NCS). For technical reasons, this strategy was chosen for pilot experiments, to apply DNA damage directly during microscopy imaging in the early time-points of live-cell imaging. NCS is often used equivalent for γ-irradiation in experimental studies, but has been shown to induce a mixture of DNA damage breaks and leads to a rise in nuclear p53 that differs in its dynamics by cell line (Stewart-Ornstein and Lahav, 2017).

To quantitatively assess changes in promoter activity for CDKN1A and MDM2, the

first steps for quantitative image analysis of TSS traces from MS2 signals were established using custom scripts and available plug-ins. Generally, individual nuclei are first identified and tracked over time based on the H2B-eCFP fluorescence before MS2 TSS traces are quantified from MCP-mVenus signals in each nucleus. As a benchmark for setting up the image analysis pipeline for future experiments and for an initial analysis of CDKN1A and MDM2 TSS activity, the FIJI manual tracking plug-in was employed in conjunction with custom MATLAB scripts for post-processing. Active TSSs were tracked per cell in maximum projected image stacks, generated from all z-planes at each time-point. Nuclei were identified by the H2B-eCFP fluorescence signal. Measured FI pixel values were plotted over time as single-cell trajectories of fold change of TSS activity. First, a background correction per cell was applied, referencing to the median FI of the 10% time-points with lowest FI signal. This measure was introduced to allow better comparison between cells, as nuclear background of MCP-mVenus varied strongly between cells. A TSS activity threshold was then applied to identify transcriptional bursting as indicated by the dashed lines in Figure 3.5.2.B,C. A bursting threshold of >1.1 fold of the median activity was set, leading to a binary representation of time-points with active (on-state) and inactive (off-state) promoters.

This analysis revealed a distinct variability of TSS activity for both target gene promoters (Figure 3.5.2.B,C, Figure 8.3.5.A,B). Also, CDKN1A TSS measurements showed that the activity of both TSSs (red/grey) in one cell is not generally synchronized in the presence and absence of DNA damage, while certain periods of higher bursting activity exist (Figure 3.5.2.B, Figure 8.3.5.A). This can increase transcriptional activity from both loci, as shown for cell#2 in Figure 3.5.2.B. Image acquisition in the first time-points led to a substantial drop in mVenus fluorescence intensity, both in cells and at TSS, suggesting bleaching of background fluorescence of mVenus-MCP (Figure 3.5.2.B). Therefore, these time-points need to be excluded for future mechanistic analyses, and DNA damage should be applied afterwards if possible, when stable imaging conditions are achieved. When comparing the activity of both promoters, especially the on-times of promoters varied strongly (Figure 3.5.2.B,C). This was not only visible in the basal state (Figure 8.3.5.A,B), but in particular when DNA damage was applied (Figure 3.5.2.B,C). CDKN1A showed fast switching between active (on) and inactive (off) states, often changing from one to the next frame with a high frequency. This indicates on-times of 2.5-7.5 min, which need to be further systematically validated as this is close to the acquisition time between two stacks. MDM2 TSS tracking on the other hand revealed that the promoter activity was often in the *on*-state for long time-periods, followed by periods of inactivity (up to 2.5 h as measured for cell#1 in Figure 3.5.2.C). This effect was even more pronounced after NCS induced DNA damage. However, due to the strong cell-to-cell heterogeneity, a high number of TSS from multiple experiments in the presence and absence of DNA damage needs to be analyzed. Therefore, a computational analysis pipeline is currently under development, to gain mechanistic insights into MDM2 and CDKN1A promoter activity from TSS trajectories and extract *on*-times, burst size and frequency.

In summary, the presented approach along with the development of an initial computational image analysis pipeline allowed to observe promoter activity from live cell

MS2 data of p53 target genes for the first time. It is possible to track fluorescence intensity changes in reporter cells in basal state and upon DNA damage. This approach already highlights differences in promoter bursting for CDKN1A and MDM2. In future experiments, a comparison with smFISH data and a more comprehensive analysis of p53 target gene bursting based on MS2 based TSS activity tracking can be performed.

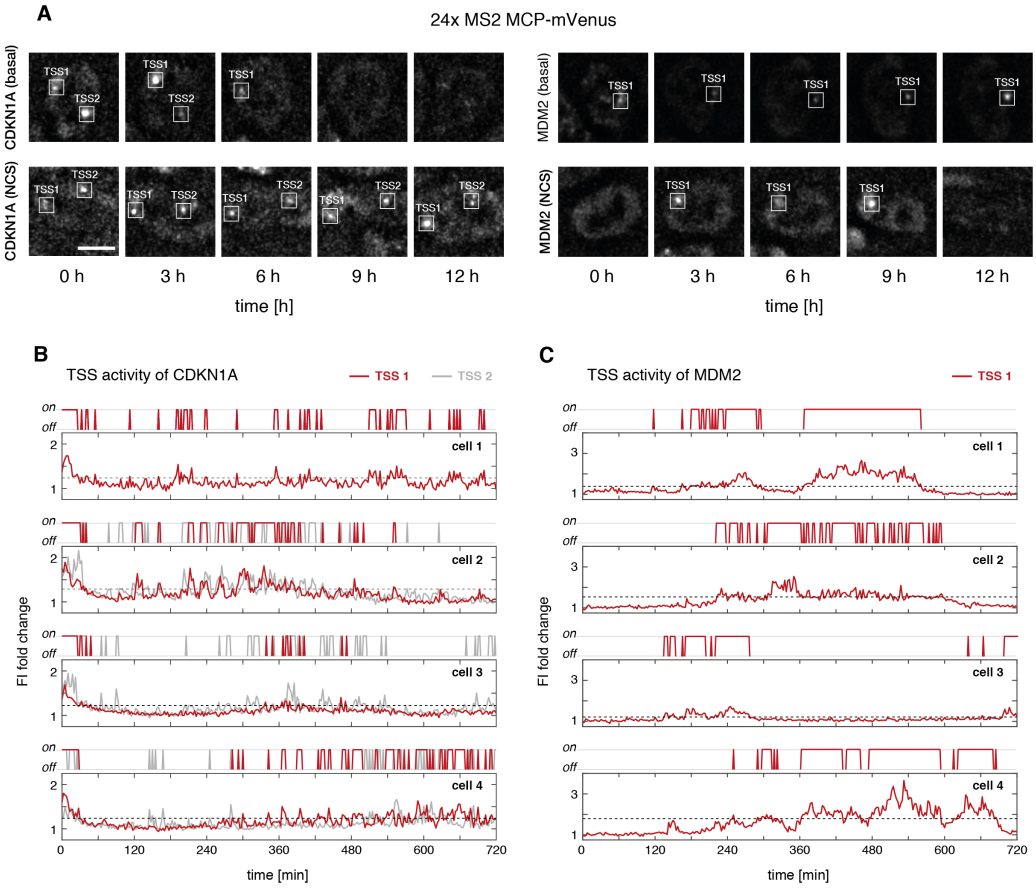

Figure 3.5.2 Tracking CDKN1A and MDM2 promoter activity after DNA damage in living cells.

(A) Example images of 24xMS2-MCP-mVenus signal at TSS. Selected cells are shown in basal state (upper row) and after 250 ng/mL NCS addition. Images represent selected time-points every 3 h from continuous time-lapse imaging for 12 h. CDKN1A-24xMS2-MCP-mVenus is shown on the left, MDM2-24xMS2-MCP-mVenus detection on the right. For visualization purposes, images were maximum projected, brightness and contrast enhanced and a gaussian filter (1 px) was applied after subtracting 20 px median filtered planes per time-point. TSS detection is indicated by white boxes. Images have the same scale, scale bar corresponds to 10 µm.

(B) Quantified traces of active CDKN1A transcription sites based on 24xMS2-MCP-mVenus signals after applying 250 ng/mL NCS. Quantifications from four cells are shown, with either one (cell1) or two detectable TSS. Traces are 12 h [720 min] and images were taken every 2.5 min as nine z-stacks of 300 nm distance. For analysis, images were maximum projected and TSSs were tracked using the FIJI manual tracking tool (Cordelieres, 2004; Schindelin et al., 2012). Pixel intensities were measured as maximum intensities in a range of 10 px. When no TSS spot was detectable, the nuclear background was measured. To correct for differences in nuclear MCP-mVenus background, TSS traces were normalized to the median FI of the 10% lowest measured intensity values per TSS and plotted as fold change. Dashed lines indicate the fold change threshold, which was set to 10% above median fold change fluctuations per cell and used to identify burst activity. The on/off TSS activity shows a binary representation of TSS activity below (off) or above (on) the threshold per cell, indicating a stochastic burst.

(C) Selected quantified traces of active MDM2 transcription sites based on 24xMS2-MCP-mVenus detection after applying 250 ng/mL NCS 2 h after starting image acquisition. Traces from four representative cells are shown. Only one TSS per cell was detectable as only heterozygous reporter expression was achieved.

CHAPTER 4 DISCUSSION & OUTLOOK

4.1. P53-MEDIATED TRANSCRIPTIONAL BURSTING MODULATES CELLULAR RNA LEVELS

4.1

IN THIS CHAPTER

P53 and other transcription factors show stimulus-specific dynamics correlated with cell fate. However, the underlying molecular networks and mechanisms beyond p53 binding to response elements are widely unexplored. Therefore, it remains elusive how TFs regulate gene expression mechanistically in single cells and at individual promoters.

In this thesis, I show that p53 mediated transcription upon DNA damage by γ-irradiation is intrinsically stochastic. Transcription bursts of p53 target genes are regulated primarily by changing the fraction of active promoters leading to distinct patterns of gene expression. Based on targeted perturbations, I demonstrate that a change in p53 dynamics affects the regulation of promoter activity. I further provide evidence that this change in the gene-specific regulation is due to specific lysine acetylation in p53's C-terminal domain. My work includes an in-depth analysis of RNA expression features on the single-cell level highlighting a differential increase in noise levels from the nucleus to the cytoplasm for the selected panel of target genes.

4.1.1. EXPRESSION PATTERNS AND PROMOTER ARCHETYPES

By enumerating RNAs from smFISH images, I demonstrate that p53 target genes are expressed in distinct patterns over time. While these patterns highlight a strong single-cell variability of expression levels, the relative changes in mean RNAs are similar to what has been previously found in population studies (Porter et al., 2016). Using mathematical modeling based on datasets from qRT-PCR and RNA sequencing, RNA and protein stability of p53 target genes have been suggested to shape expression after DNA damage (Porter et al., 2016; Hafner et al., 2017; Hanson et al., 2019). However, beyond these findings, the single-cell analyses of promoter activity performed in this thesis suggest a fundamental contribution through modulation of stochastic bursting. The concurrence of transcription, translation and RNA degradation to control RNA levels over time and their impact on each other will be interesting to explore in more detail in future studies.

In this work I provide evidence that differential regulation of the fraction of active promoters that correlates with the *on:off* rate of promoter bursting (burst frequency) contributes to gene-specific kinetics and thus RNA state. At the same time, the transcription rate corresponding to the burst size, remains unchanged. Employing mathematical calculations based on promoter activity and the cellular RNA state in line with the two-state promoter model, I did not find proof for a substantial change in RNA degradation for target

genes, except for DDB2. However, the RNA half-life has been shown to play a key-role in modulating gene expression in other systems, e.g. in the yeast stress response and NFκ-B-dependent transcription in mammalian cells (Shalem et al., 2008; Hao and Baltimore, 2009). Importantly, while the applied strategy to estimate RNA decay rates has been validated and applied in other contexts (Bahar Halpern et al., 2015b), it is an indirect approach based on a series of assumptions that may mask actual RNA stability (Chapter 3.3.4). Also, only selected target genes were analyzed. Therefore, a more direct measurement of RNA stability and transcription kinetics would allow to analyze this aspect in more detail. For example, kinetic labelling techniques in combination with transcription inhibition facilitate measuring transcriptome-wide transcription rates and mRNA turnover and could thereby provide a more comprehensive view on RNA homeostasis in the p53-mediated DNA damage response (Tani and Akimitsu, 2012; de Pretis et al., 2015; Russo et al., 2017; Wolfe et al., 2019).

Based on the characterization of single-cell transcription features, I allocated promoter-specific dynamics of stochastic bursting along three archetypes of activity: *transient, pulsatile,* and *sustained.* The main difference in these archetypes is their quantified promoter activity at 6 h and 9 h after damage induction. Remarkably, promoter features were not static but changed dependent on upstream p53 dynamics, suggesting a flexible, but defined range of rendered bursting parameters from a certain promoter. When comparing targets representing each archetype, I found that genes that resemble *pulsatile* promoter activity tend to have lower overall expression levels. On the other hand, genes that were only *transiently* expressed and showed a reduced activity at later time-points, did not show decreased initial activation (Chapter 3.3.3). However, it was not possible to identify distinct molecular mechanisms leading to the specific suggested archetypes based on the selected panel of p53 targets. Both the positioning and the number of response elements do not allow a prediction of the dynamic range of bursting activity. Furthermore, p53 target genes involved in different response pathways and thus determining different cell fate decisions, contributed to all

PROMOTER ARCHETYPES
- *pulsatile*
- *transient*
- *sustained*

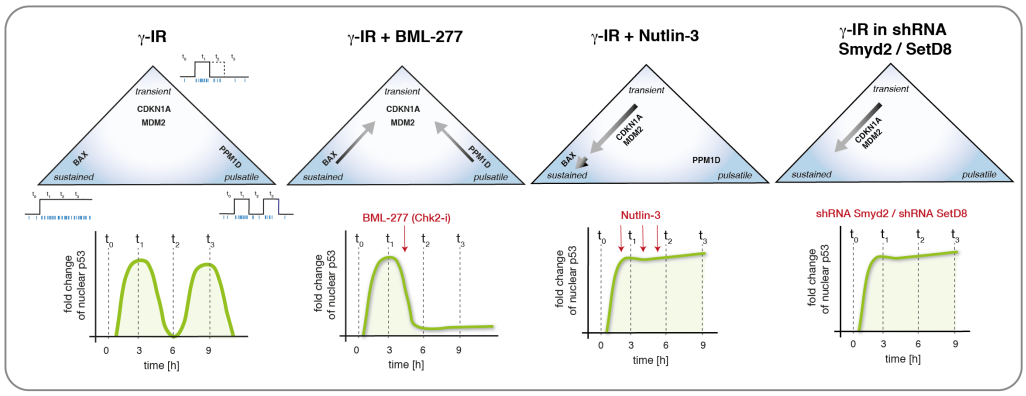

Figure 4.1.1 Dynamic changes of target gene promoter activity in the context of different p53 nuclear levels.

A schematic overview of the different analyzed conditions in this thesis and the dynamic changes of promoter activity dependent on p53 nuclear dynamics is shown. The upper row illustrates the target genes that were analyzed in the different experiments and how their promoter activity changed. The lower row schematically shows how p53 nuclear levels changed dependent on treatment with inhibitors and after knock-down of Smyd2 and SetD8 shRNA.

archetypes. This suggests that a direct correlation between the archetype and cell fate regulation is not existent. It can therefore be hypothesized that the plasticity in bursting activity of an individual promoter is not exclusively intrinsic in the *cis*-architecture, but further shaped by secondary mechanisms. In this regard, analyzing changes of co-regulatory factors as epigenetic markers, interacting proteins, enhancer contacts and combinatorial control at different time-points after DNA damage may help to decipher the gene-specific modulation of stochastic bursting in response to p53 activation.

4.1.2. STOCHASTIC BURSTING OF P53 TARGET GENE PROMOTERS

In this work, I suggest that differential regulation of the *on:off* rate of promoter bursting (burst frequency) contributes to gene-specific kinetics of p53 target gene transcription after DNA damage. At the same time, the transcription rate that corresponds to the RNAP2 initiation rate and burst size remains on similar levels before and after DNA damage. A regulation of burst frequency to modulate gene expression has previously been shown for other signaling pathways such as light-controlled transcription in *Neurospora* by the White Collar Complex (WCC) (Li et al., 2018), dose-dependent transcriptional regulation by steroid receptors after ligand binding (Larson et al., 2013) and c-Fos mediated transcription after induction by serum or zinc (Senecal et al., 2014). Also, a recent study using targeted perturbation of the transcription cycle could show that frequency modulation and RNAP2 pause release regulate transcription, while the recruitment of RNAP2 is downstream to burst initiation (Bartman et al., 2019). Furthermore, theoretical and experimental studies suggested that the regulation of stochastic promoter switching (burst frequency) is modulated through noise and bistable states in positive feedback loops (Eldar and Elowitz, 2010).

According to the classical model of gene expression regulation through sequence-specific TFs, binding of a TF to *cis*-regulatory elements can serve as a proxy for transcriptional activity (Ptashne and Gann, 2002). In this regard, frequency modulation is defined by the rate of TF binding to a response element, while downstream processes mediate the transcription rate in the active promoter state. In line with this view, I observed an increase in promoter binding with the first pulse for all target genes as measured by ChIP (Chapter 3.3.5). Also, targeted perturbation using the Chk2-inhibitor BML-277 to terminate p53 activity after 4 h indicate that the ongoing transcriptional activity of target genes allocated to the *pulsatile* or *sustained* archetype depends on a recurring p53 pulse (Chapter 3.4.1). However, two observations argue against an TF-affinity-based regulation of stochastic bursting after DNA damage. First, ChIP experiments measuring p53 promoter binding do not indicate gene-specific regulation related to the different archetypes. Second, I observed a surprising disconnect between the recurring p53 pulse and a gradual descend in p53 binding at the analyzed target gene promoters. This decrease in binding of p53 to target gene promoters after the first peak instead of coupling to its nuclear levels is remarkable as it was detected both in absence and presence of a second pulse after γ-IR and treatment with BML-277. Therefore, it remains mechanistically unclear how promoter-bound p53 is

stabilized while the nuclear p53 levels are reduced after 3 h to the basal state. This is further surprising as p53 has been shown to follow fast binding kinetics of only a few milliseconds at target gene promoters (Loffreda et al., 2017). As the relative binding curves were similar for all target genes, a global enrichment of DNA binding activity, a selective stabilization of chromatin-bound p53 or a local clustering close to active promoters are possible. It has been previously shown that tetramerization of p53 leads to a stabilization of DNA binding in response to DNA damage by UV radiation (Gaglia et al., 2013; Gaglia and Lahav, 2014). In future studies, it would therefore be interesting to investigate, for example by using fluorescence correlation spectroscopy, if an increase in the tetrameric p53 population can be observed at 6 h after γ-IR compared to the basal state.

4.1.3. P53'S POST-TRANSLATIONAL MODIFICATIONS AND THEIR IMPACT ON TRANSCRIPTION

Based on Western Blot experiments, I show that the C-terminal modifications of p53 after DNA damage by γ-IR change between the first and the second pulse. Also, when protein turnover was inhibited after treatment with Nutlin-3, different activities at p53 target gene promoters were observed. In essence, sustained p53 levels that correlate with prominent C-terminal lysine acetylation induce a change in the promoter archetype of *transient* genes to *sustained* activity, which was further confirmed by knocking-down the corresponding methylases Smyd2 and SetD8. Interestingly, the transcription rate was increased in the context of persistent nuclear p53 as well. For pulsatile p53, these data indicate that transient PTMs are stabilized and accumulated when p53 levels are sustained.

The differences in p53's activity at the time of the first and second pulse, alongside with reduced promoter binding as shown by ChIP, suggest a change in upstream processes that re-initiate the p53 response after the first trough (6 h). This observation contradicts the common view that repeated pulses of nuclear p53 are re-initiated through ATM and other upstream kinases as long as DNA damage persists (Batchelor et al., 2008). It is possible that the p53 fraction that is bound at target gene promoters as a tetramer, has a different PTM state at the CTD, preventing ubiquitination by MDM2 and degradation in the proteasome. Therefore an additional layer of regulation can be postulated for changing PTM's during the second pulse. Phosphorylation of p53 may contribute to the different gene expression archetypes. S15 and S46 phosphorylation have been shown to correlate with promoter-specific binding of p53 after treatment with etoposide or actinomycin D regulating transcription (Smeenk et al., 2011). In response to DNA damage, several PTMs of p53 are induced, leading to stabilization of nuclear p53 and a variety of secondary interactions. In the ChIP experiments performed in this thesis, only the binding of total p53 was resolved. It is therefore not possible to conclude a PTM-specific contribution in the DNA-bound p53 pool without additional experiments.

According to the presented results, stochastic bursting of p53-mediated gene expression after γ-IR is modulated by changing the number of active promoters (burst

frequency). At the same time, inducing sustained p53 by a perturbation with Nutlin-3 leads to an increase in K370 and K382 acetylation. This up-regulation of p53's C-terminal lysine acetylation is correlated with an increase in the fraction of active promoters and higher transcription rates for some target genes. Even though this was clearly detected in smFISH based measurements, the underlying molecular mechanism remains unsolved. Also, the current literature provides a controversial discussion about the function of the CTD and its differential regulation (Sullivan et al., 2018; Laptenko et al., 2015). It has been shown that the CTD binds to DNA in a non-sequence specific manner, due to the basic nature of its lysine residues. This unspecific DNA binding is hypothesized to allow sliding of p53 along the DNA, fostering the sequence-specific binding of the DNA binding domain (DBD) at p53 REs (Laptenko et al.,2015; McKinney and Prives, 2002). Additionally, the intrinsically disordered topology of the CTD allows a variety of interactions with co-regulatory factors (Fuxreiter et al., 2008; Oldfield et al., 2008). This structural plasticity is further enhanced by the variety of post-translational modifications that can affect the protein structure. These changes, induced by the PTM-state, could modulate stochastic bursting kinetics directly or indirectly at individual promoters.

Regarding the identified archetypes of promoter activity, I showed that transient expression of CDKN1A and MDM2 after **γ**-IR is differentially regulated by opposing acetylation and methylation of the K370 and K382 residues. SmFISH data suggest that these changes tune promoter activity to different modes of stochastic bursting. In line with these findings, K382 mono-methylation by the SetD8 methylase has been shown to promote binding of the chromatin compaction factor L3MBTL1 at the p53 target gene promoters CDKN1A and PUMA (West et al., 2010). Additionally, a previous study indicated reduced p53 promoter binding and resulting transcription through Smyd2 mono-methylation of K370 (Huang et al., 2006). Accordingly, Set7/9 mediated inhibition of Smyd2 is changing overtime during the first p53 pulse after DNA damage by **γ**-IR (Ivanov et al., 2007). However, I still observe over 50% p53 promoter binding at 9 h after **γ**-IR as shown by ChIP measurements. A reduction in promoter binding due to Smyd2 dependent K370 mono-methylation alone cannot explain the transient expression of MDM2 and CDKN1A. While lysine methylation in the CTD is correlated with inhibition of transcription, acetylation of C-terminal lysine residues increases transcriptional activity (Tang et al., 2008). The impact of lysine acetylation on DNA binding has been characterized in population studies, however, leading to controversial results about an increase or decrease in binding affinity (Gu and Roeder, 1997; Friedler et al., 2005; Nakamura et al., 2000). Also, single-molecule fluorescence imaging highlighted that transient interactions between p53 and surrounding chromatin are modulated upon p53 activation, while the time of interaction corresponds to the acetylation state of the CTD (Loffreda et al., 2017).

Furthermore, the direct regulation of the transcription cycle occurs via *trans* interaction of TFs with RNAP2's CTD (Kwon et al., 2013). In this respect, disordered regions of transcription factors such as p53's CTD can lead to recruitment and transactivation of RNAP2 into an elongation competent form (Kwon et al., 2013; Sullivan et

al., 2018). These mechanisms may affect stochastic bursting through PIC stability or the release of paused RNAP2, increasing initiation. However, it is so far unexplored how these processes change stochastic bursting at individual promoters in the time-scale of repeated nuclear pulses of p53. It has also been hypothesized that Smyd2 can directly affect the RNAP2 elongation rate, leading to reduced transcription (Brown et al., 2006). In this study, though, I could not detect a change in burst-size upon Smyd2 knock-down, as would be expected when RNAP2 distribution at promoters is altered. This suggests that p53-independent inhibition of the RNAP2 elongation rate at transient promoters plays only a minor role in regulating the transcription cycle in the context of DNA damage.

To gain a more comprehensive view on how CTD modifications affect stochastic bursting it would therefore be informative to analyze the binding dynamics of C-terminally acetylated p53 in the context of different upstream dynamics by ChIP. Also, site-directed mutagenesis of the lysine residues in the CTD may help to decipher the mechanistic background.

4.1.4. REGULATION OF STOCHASTIC BURSTING BY THE CHROMATIN CONTEXT

In this thesis, I focused on the role of p53's post-translational modifications in regulating stochastic, gene-specific transcription of target genes. However, other mechanisms have been shown to modulate promoter specific gene expression as well. Based on a synthetic gene-regulatory network in yeast, allowing for differential positioning of a gene along the chromosome, the chromosomal gene position has been suggested to influence noise and bursting kinetics (Becskei et al., 2005). Additionally, long-range enhancer-promoter interactions and forced chromatin looping affect the burst frequency (Fukaya et al., 2016; Bartman et al., 2016). In line with this, it has been hypothesized that enhancer-promoter contacts are fundamental for every burst of transcription (Chen et al., 2019). One example is the *Hbb1-1* promoter that depends on enhancer-promoter contacts to modulate burst frequency, while distinct perturbations of the transcription cycle suggest that the burst initiation is prior to RNAP2 initiation (Bartman et al., 2019). Beyond these direct interactions of enhancers and promoters, inhibitory histone marks, CTCF boundaries and cohesine, as markers of a repressed chromatin state, correlate with inducible expression of p53 targets and have been proposed to play a role in gene-specific dampening of the p53 mediated expression after DNA damage (Su et al., 2015).

Also, a broad body of literature has shown that histone modifications affect burst frequency modulation. Histone methylation leads to a conservation of burst frequency transferred from mother to daughter cells (Muramoto et al., 2012). On the other hand, histone acetylation affects transcriptional bursting, mainly by increasing the burst frequency (Nicolas et al., 2018; Suter et al., 2011; Harper et al., 2011). In a recent study, bursting kinetics of the *Fos* promoter in neurons were perturbed by changing promoter-proximal histone acetylation using dCas9-p300 and dCas9-HDAC8 (Chen et al., 2019). While an increase in acetylation led to an enhancement of the burst size, reduced acetylation decreased

the burst frequency. These examples highlight the diverse regulatory potential on the level of chromatin modifications to define bursting kinetics at specific promoters. However, for the selected set of p53 target genes, I did not observe a clear contribution of H3K27me or H3K27ac to the different promoter archetypes.

Additionally, distinct nucleosome positioning and remodeling at actively transcribing promoters can introduce transcriptional noise and thus affect bursting kinetics, e.g. by limiting the rate of transcriptional activation (Boeger et al., 2008; Kim and O'Shea, 2008; Mao et al., 2010; Brown and Boeger, 2014). However, also the opposite may be true, as stochastic bursting could induce differences in nucleosome positioning (Brown and Boeger, 2014; Boeger, 2014). Both of these mechanisms have only been explored in a limited number of promoter contexts. In a recent study focusing on the GAL4 promoter, it has been shown that the dwell time of the TF defines bursting, with multiple initiation events of RNA polymerases being induced, evolving into a burst of transcription (Donovan et al., 2019). At the same time, dissociation of GAL4 from promoters leads to a termination of bursting. In this study, it has also been shown that GAL4 binding to the DNA is defined by the affinity to response elements, but is strongly reduced by nucleosome positioning, thus indirectly affecting bursting kinetics (Donovan et al., 2019). To my knowledge, none of these mechanisms have yet been described for p53 target gene regulation. It will therefore be interesting to analyze if nucleosome positioning, other histone marks or chromatin architecture contribute to specific promoter regulation after DNA damage in future studies.

4.1.5. NOISE IN P53 TARGET GENE EXPRESSION

Previous work suggested a correlation between cell cycle state and cellular volume with RNA expression and gene expression noise (Padovan-Merhar et al., 2015; Battich et al., 2013). To analyze the effect of these parameters on p53 targets, I characterized RNA levels and gene expression noise. The impact of these factors was estimated by normalization for cell volume and cell cycle state. In general, computational normalization of nuclear and cell area led to a trend of reduction in the variability for all target genes, with slightly reduced CVs in both cases and individual gene-specific and time-point specific effects. However, the applied measures only allow an indication of the general trends, as the segmented area in 2D was used to approximate the 3-dimensional shape of the nucleus and cell volume. A more comprehensive analysis can be achieved by co-staining with an additional smFISH probe targeting a housekeeping gene (tagged with a different fluorescent dye). Recently published software allows to implement such analysis into the current workflow using the *FISH-Quant* based RNA localization package *locFISH* (Samacoits et al., 2018). Therein, a 3D model of each cell is generated as a computational net from high expressed RNAs, which allows more precise measurements of the volume from 3D spot data as well as sub-cellular localization of p53 target genes.

When characterizing noise levels in nuclear and cytoplasmic fractions, I found a noise amplification for all p53 target genes from the nucleus to the cytoplasm. Also, nuclear export rates did not change strongly, as calculated from transcription rate and RNA levels in the

nucleus and the cytoplasm. These findings, while in line with a recent transcriptome-wide study (Hansen et al., 2018), oppose a previously suggested concept of noise-attenuation from nucleus to cytoplasm due to passive filtering by nuclear RNA export (Stoeger et al., 2016; Bahar Halpern et al., 2015a). One explanation for this discrepancy may be that noise buffering was observed in previous measurements upon starving Hek293 and mouse liver cells (Battich et al., 2015; Bahar Halpern et al., 2015a). Starvation influences the cellular metabolism and thus RNA homeostasis. For example, in a recent study RNA localization in the intestinal epithelium of mice was characterized, suggesting that cell starvation affects RNA transport and localization (Moor et al., 2017). Upon re-feeding fasted mice, it was shown that mRNAs that encode ribosomal proteins shift to ribosome-rich sub-cellular regions to foster translation.

Similar to previously published studies, I used the Fano factor (variance over mean) instead of CV^2 (standard deviation over mean) to characterize a change in noise between nucleus and cytoplasm (Munsky et al., 2012; Sanchez and Golding, 2013; Thattai and van Oudenaarden, 2001; Hansen et al., 2018). Both parameters are commonly used for measuring cell-to-cell heterogeneity. However, as highlighted in these previous studies, the difference in mean RNA counts has to be scaled to correct for the noise introduced by the changes in mean levels, to allow a comparison of nuclear and cytoplasmic noise based on the CV^2 (Hansen et al., 2018). The Fano factor, on the other hand, is independent of this Poisson scaling and allows a more direct comparison, as it measures noise as the deviation from a Poisson process which has a Fano factor of 1 (Hansen et al., 2018).

CV^2
$CV^2 = \sigma^2/m^2$
σ: *standard deviation*
m: *mean*

FANO FACTOR
$f = v/m$
v: *variance*
m: *mean*

In this thesis, the molecular background of noise amplification from the nucleus to the cytoplasm remains unexplored. Previously suggested mechanisms that lead to heterogeneity in cytoplasmic RNA levels could play a role in amplifying the noise in p53 target RNA counts. While the RNA decay rates, approximated by smFISH, did not indicate differential degradation rates for most p53 targets before and after DNA damage, an amplification in expression noise in the cytoplasm has been shown to be in line with bimodal degradation (Meyer et al., 2010; Parker, 2012; Pelechano et al., 2015; Hansen et al., 2018). Such correlations of noise amplification and bimodality in degradation, suggest that translation initiation and RNA degradation are two mutually exclusive processes, leading to a shielding of actively translated RNAs. Along these lines, one hypothesis could be that mechanisms regulating translation and thereby affecting RNA decay rates of p53 targets, increase the cytoplasmic RNA heterogeneity. For example it has been shown, that expression noise propagates from stochastic transcription in the nucleus to the cytoplasm due to a high translation efficiency, as an individual mRNA can be translated into protein over a hundred times (Ozbudak et al., 2002). Additionally, cytoplasmic mRNA processing and translation as multi-state processes add noise by their inherent stochasticity due the limited number of molecules involved (Pichon et al., 2016; Arbel-Goren et al., 2013). In this regard, various factors can introduce heterogeneity, for example the variability in the number of ribosomes and tRNAs. Furthermore, translation requires binding of eukaryotic initiation factors (eIFs) in the 5'UTR of an mRNA to initiate translation (Jackson et al., 2010). This process is regulated by cellular signaling cascades including MAPK, PI3K, and mTOR that may

introduce other sources of heterogeneity (Roux and Topisirovic, 2012). Additionally, p-bodies and stress granules have been suggested to regulate degradation and translation initiation (Decker and Parker, 2012). However, smFISH images did not indicate fluorescence spots that would suggest RNA aggregation of p53 target genes. Besides these mechanisms, cellular stress and p53 activation lead to a global shift of translation through different mechanisms, potentially affecting RNA noise levels (Marcel et al., 2018). Cap-dependent translation is sensitive to stress, e.g. heat-shock, nutrient deprivation or irradiation; these factors thus lead to a shift to non-canonical translation initiation, while inhibiting canonical translation (Lacerda et al., 2017; Ryoo and Vasudevan, 2017). This may explain an increase in cytoplasmic noise after **γ**-irradiation as compared to the basal state for the target genes BAX, PPM1D, and RRM2B (Figure 3.2.4). Indirect regulation of translation by p53 includes the transcriptional regulation of miRNAs, long noncoding RNAs and RBPs. Furthermore, p53 inhibits RNAP1 and RNAP3 reducing the biogenesis of tRNAs and ribosomal RNA (Cairns and White, 1998; Zhai and Comai, 2000). Also, it affects translation initiation through eIF4E transcription, fosters 4E-BP1 dephosphorylation and upregulates TRIM22, forming a complex with eIF4E/eIF4G, thereby changing the efficiency of cap-dependent translation (Jackson et al., 2010; Zhu et al., 2005; Horten et al., 2002; Petersson et al., 2012). Additionally, p53 can also directly change translation efficiency through binding to RNAs. One example is the sequence specific binding within the 5'UTR, leading to an inhibition of both cap-dependent and internal ribosome entry site (IRES)-mediated translation (Riley and Maher III, 2007; Marcel et al., 2018). While the underlying molecular mechanisms remain to be explored, examples include the p53-mRNA itself (Mosner et al., 1995), MDMX (Tournillon et al., 2017), FGF-2 (Galy et al., 2001) and CDK4 (Ewen et al., 1995).

On the protein level, heterogeneity can also be introduced through positive feedbacks that increase expression noise by up-regulating transcription (Raj and van Oudenaarden, 2008; Balázsi et al., 2011; Eldar and Elowitz, 2010). In this regard, both self- and cross-regulation of p53 targets could play a role. Though, this would affect both nuclear and cytoplasmic noise levels, but Fano factors in the nucleus remain on similar levels after **γ**-IR as shown in Chapter 3.2.4 and mainly negative feedback regulation has been described for the p53 network (Harris and Levine, 2005). Although the current literature suggests fundamental functions of p53 beyond transcriptional control, a comprehensive analysis of its impact on the translatome in the context of DNA damage remains to be performed. The translation efficiency after Nutlin-3 treatment has been measured by RiboSeq and polysome profiling (Loayza-Puch et al., 2013, Zaccara et al., 2014; Liang et al., 2018). These studies showed that Nutlin-3 treatment induces a shift in translation due to p53-mediated transcription, additionally altering protein synthesis of >25% genes that are not validated as p53 targets. However, for a better understanding of the connection of cytoplasmic RNA noise levels with transcription rates and translation, future mechanistic studies correlating p53-mediated transcription kinetics transcriptome-wide with an analysis of the translatome are required. Such experiments could help to disentangle the regulatory potential of p53 on the RNA state of a cell, ranging from transcription to translation.

4.2. QUANTITATIVE ANALYSIS OF RNA COUNTS AND TRANSCRIPTIONAL ACTIVITY FROM SINGLE-CELL MEASUREMENTS

4.2

IN THIS CHAPTER

I employed smFISH to characterize p53 target gene expression in the DNA damage response to γ-irradiation. I optimized and further developed existing experimental protocols and software for quantitative image analyses to enable the characterization in a high number of single cells for seven p53 target genes. This allowed to confirm distinct gene expression patterns that have been previously described for the selected set of targets in population studies. Furthermore, I provide a novel, single-cell view of RNA distribution in individual cells as well as on stochastic promoter activity. While my work builds on a previously described approach to characterize transcription properties in mouse liver cells (Bahar-Halpern and Itzkovitz, 2016), I apply these techniques to multiple time-points in the p53 signaling response. Furthermore, the presented quantitative dataset consists of several thousand individual cells, thus being two orders of magnitude larger than previously reported imaging-based datasets. The achieved results can therefore serve as a resource for studies that focus on mathematical modeling of gene expression noise and promoter regulation in the p53 pathway. This may help to establish a basis for understanding quantitative transcription of p53 target gene expression on the single-cell level.

4.2.1. SOFTWARE TOOLS TO ANALYZE THE RNA STATE OF A CELL FROM SMFISH STAINING

In this work I show that *FISH-Quant* (Mueller et al., 2013) is a powerful software tool to characterize smFISH counts in a high number of cells and large datasets when complemented with custom scripts. I analyzed both RNA counts and promoter activities based on microscopy images in thousands of cells. However, while *FISH-Quant* (Mueller et al., 2013) is useful for these purposes, I had to further develop and add-on custom scripts to automatize single-cell outline detection and extract the resulting quantitative data for downstream analyses of promoter activity. Interestingly, despite the broad applications employing RNA imaging, only a few software tools for the standardized quantitative analysis of smFISH microscopy images are currently available. Besides *FISH-Quant* (Mueller et al., 2013), these include *Localize/AirLocalize* (Zenklusen et al., 2008; Lionnet et al., 2011; Trcek et al., 2012), *TransQuant* (Bahar Halpern and Itzkovitz, 2016) and *StarSearch* (Raj lab, rajlab.seas.upenn.edu). However, as smFISH is also broadly applied in research areas traditionally not specialized on image analysis, a high demand for maintenance and development of standardized tools exist.

In comparison to the other mentioned tools, the advantage of *FISH-Quant* is it's broad applicability and maintenance. It allows a series of pre-processing steps to filter images from smFISH staining and provides analyses of spot-counts in 3D (Chapter 1.3.3). Also, the implemented batch-processing tool enables to characterize a bundle of images based on the same settings. Beyond the advantages exploited in this thesis, *FISH-Quant* features a multicolor analysis, and RNA counts can be localized, facilitating a comprehensive view on RNA expression from single-cell imaging data (Mueller et al., 2013; Samacoits et al., 2018). *TransQuant*, employing a combination of *FIJI* and *MATLAB*, has the significant advantage of a direct implementation of a two-state mathematical model of promoter activity (Bahar Halpern and Itzkovitz, 2016). Therefore, it directly results in data of promoter activity without further need for processing. While this is a benefit when only a few samples are analyzed, options for intermediate processing steps and additional features to characterize RNAs or applying different models remain to be integrated. I employed *TransQuant* to validate my data and extract the correction factor η for probe position. However, its usability for batch processing images is limited, reducing the applicability to quantify a high number of cells. Also, it is questionable if the implemented two-state promoter model of transcriptional bursting activity is sufficient in most contexts, as it implies steady-state conditions. While similar in the general approach to quantify smFISH counts, *localize/ AirLocalize* (Zenklusen et al., 2008; Lionnet et al., 2011; Trcek et al., 2012) is currently not accessible as a maintained software tool for the scientific community, limiting its potential for broad applications. *StarSearch* (Raj lab, rajlab.seas.upenn.edu), is from a user's perspective the most simple and easiest accessible tool to analyze RNA counts from smFISH images. It allows a browser-based quantification of RNA counts in individual images. However, the analysis is performed on maximum projected images, limiting its application for quantitative studies beyond enumerating RNA counts. These two software tools, were not tested in more detail in this study. One potential disadvantage of all presented tools is that they are based on the commercial programming language *MATLAB*. While *MATLAB* is predominantly used in many areas of engineering and scientific research, a change to a non-commercial programming language (e.g. R or python) would considerably expand their accessibility for the scientific community. Notably, all approaches have advantages, depending on the aims of the analysis. However, additional software extensions are usually required to adopt these tools for the specific needs of individual research projects.

4.2.2. INFERRING TRANSCRIPTION RATES FROM SMFISH DATA

Using the *FISH-Quant* build-in approach based on integrated intensities (Mueller et al., 2013), I quantified the fluorescent intensity of the TSSs after the detection of mature RNAs. While particularly the resulting RNAP2 counts and quantified burst size per hour were high, the obtained data fit to previously published measurements of promoter activities: For example, using the same approach to study promoter activities of mouse liver genes, the RNAP2 occupancy has been show to be up to 39.3 RNAP2/TSS (Ass1) on average (Bahar Halpern et al., 2015b). Also, the MDM2 transcription rate has been proposed to be >500

mRNAs/h, measured by 4-thiouridine (4sU) labeling in NIH3T3 mouse fibroblasts in the basal state (Schwanhäusser et al., 2011), which suggests a high promoter activity of p53 targets compared to average RNAs.

As an alternative approach, using fluorescence intensities of the TSSs to calculate transcription rates directly, *FISH-Quant* provides a tool to measure nascent RNAs. Therefore, an average cytoplasmic spot is quantified after batch detection of RNAs by aligning the center of the PSF with sub-pixel accuracy (Mueller et al., 2013). This spot is then fitted with a 3D Gauss function to calculate the integrated intensity from the area under the curve. Along the lines of previous approaches for 2D projections (Zenklusen et al., 2008), nascent RNAs are estimated as the quotient of the integrated intensity of the TSS and the integrated intensity of the average mRNA molecule (Mueller et al., 2013). This leads to the direct output of nascent RNAs per TSS, which can also be used to inform the two-state promoter model (Bahar Halpern and Itzkovitz, 2016). In this case, the quantified nascent RNAs allow approximating RNAP2 occupancies, neglecting correction factors for probe position and RNAP2 occupancy. In this thesis, this second approach was employed in parallel, leading to similar results when comparing dynamics at different time-points. However, particularly the resulting transcription rate was lower, as were RNAP2 occupancies. Both approaches quantify the equivalent amount of full-length transcripts, giving rise to the fluorescence signal at the TSS (Mueller et al., 2013). However, different reasons can lead to over- or underestimation of the number of transcribed nascent RNAs. First, TSSs are neglected that exhibit lower intensities than one full-length RNA. Second, the number of nascent RNAs that are transcribed could be higher, as these are not full length, especially for expanded TSSs.

Considering the molecular mechanisms of the involved processes, the binding of proteins that mediate co-transcriptional RNA processing could inhibit smFISH probe binding. This could be avoided by placing smFISH probes towards the 3' end of transcripts, as the fluorescence signal then only appears when an RNA is almost completely transcribed. However, in that case, abortive or stalled transcription would not be visible, resulting in an interpretation of the productive RNA output as the transcription rate. This approach would therefore require validation, as the accessibility of a cytoplasmic RNA for smFISH probes could be more restricted when targeting sites that are closer to each other. In this regard, targeting sites that are widely disseminated over the mRNA is advantageous due to averaging of the fluorescence signal. However, due to the length of RNAs, it is not always possible to follow this approach. A dual-color experiment would allow for comparison by visualizing nascent RNAs through targeting the 5' end with a probe set of a second color. Differentiation based on these two stainings for one gene would also facilitate estimation of RNAP2 clustering and relative elongation versus 3' processing and release time. The transcription sites of p53 targets stained by smFISH probes mostly showed elongated structures in 3D, larger than the diffraction limit and the PSF of an individual RNA molecule. RNA accumulation during or after transcription could further lead to these elongated structures with high fluorescence intensity. One reason could be the before-mentioned abortive transcription, RNAP2 pausing, but also co-transcriptional processing (Bentley, 2014).

Furthermore, as mature cytoplasmic RNAs are used as a reference to approximate the

intensity of an individual RNA, lower intensities of cytoplasmic RNAs due to the limited access of probes would cause an overestimation of transcribed RNAs. For example, RNA 3D structures or RNA-protein interactions, e.g. to promote translation or RNA transport, would reduce the accessibility for smFISH probes. However, RNA aggregates as p-bodies or stress granules would be quantifiable from *FISH-Quant* images as well. I approached this by including co-stained spots exclusively inside the nucleus, since p-bodies and stress granules have been shown to be localized in the cytoplasm (Decker and Parker, 2012; Buchan and Parker, 2009). Also, the staining with an intron probe set was used to avoid false positive TSS identifications from other RNA aggregates. Though, nuclear retention of incompletely processed RNAs (including intronic sequences) that aggregate in the nucleus would not be distinguishable with this approach. Recently, it has been shown in genome-wide studies that a considerable proportion of RNAs have one or two unspliced introns leading to nuclear retention of these RNAs (Jacob and Smith, 2017). These incomplete RNAs can be exported into the cytoplasm in response to cellular stress such as DNA damage, hypoxia or viral infection (Boutz et al., 2015; Ninomiya et al., 2011; Brady et al., 2017). For the selected panel of p53 targets, co-stained cytoplasmic spots were not found. Hence, there is yet no indication of retained introns in p53 target genes after DNA damage by γ-irradiation.

To quantify p53 dependent transcription, I used A549 cells. Early in this study, it became evident that more than two transcription sites were enumerated by co-staining of intronic and exonic sequences for most p53 target genes. While it cannot be entirely excluded that not all detected co-stained nuclear dots are transcription sites, this is likely due to a similar number of maximum TSS at different time-points in the DNA damage response to γ-IR. The elongated structures as well as selective validation by DNA FISH are further indicative that this is the case. However, DNA FISH has not been applied for all p53 targets that were analyzed. While A549 cells have been used in p53 related research for a long time due to their intact p53 pathway, a recent genome-wide study showed that genetic and transcriptional evolution induces substantial differences in response to chemotherapeutic drug treatment (Ben-David et al., 2018). This could also affect the p53 pathway. Similar findings have been recently confirmed, determining the degree of heterogeneity in HeLa cell samples from different laboratories by a multi-omics approach (Liu et al., 2019). This is one reason why focusing on the relative changes between cells in basal state and after DNA damage, as used in this work, is advantageous in mechanistic studies, compared to absolute RNA levels.

4.2.3. THE TWO STATE PROMOTER MODEL

No matter which approach is applied to quantify burst size and frequency, several approximations are implied that change the resulting burst size. Most importantly, the speed of RNAP2 elongation is estimated as a constant. However, the processing speed of RNAP2 during the different phases of the transcription cycle is changing due to RNAP2 pausing, co-transcriptional proof-reading and splicing (Mayer et al., 2017; Saldi et al., 2016). Additionally, it is conceivable that the RNAP2 speed changes upon activation of the p53

pathway since p53 and RNAP2 interact directly with each other (Singh et al., 2016; Kim et al., 2011; Liu et al., 2018). Due to the different identities of target gene transcripts regarding lengths and number of introns, the processing speed may not be the same for all target genes (Saldi et al., 2016). In particular, this affects the quantification of transcription rates per hour (burst size), which scales strongly with a different RNAP2 speed, as highlighted by the example of MDM2 basal transcription (Figure 8.3.3/2). In this thesis, the elongation speed for p53 target genes has not been measured, which could be achieved by positioning of smFISH probes to the 3' and 5' ends of the RNAs. It thus remains unclear if 3 kb/min, that is used as a constant in the performed analyses, are realistic for the studied targets.

Furthermore, transcription is a multi-layer process regulated on numerous levels. In the classical description, TF occupancy at *cis*-regulatory elements can serve as an estimate for transcriptional output (Ptashne and Gann, 2002; Setty et al., 2002; Rosenfeld et al., 2005). However, beyond binding of TFs to their response elements and recruitment of the general transcription machinery, it has been shown that TFs can modulate transcription through the recruitment of co-factors, e.g. chromatin-modifying enzymes in *trans* (Coulon et al., 2013; Voss and Hager, 2014). The random telegraph model assumes steady-state conditions and does not include these aspects. As transcription is a multi-state process that changes in different cellular contexts, recent studies challenge the view of only two states. Due to the high complexity of the molecular processes and numerous interactions involved in transcription, these point towards multi-state descriptions (Zoller et al., 2015; Fritzsch and Baumgaertner et al., 2018; Corrigan et al., 2016). The most obvious extension is including a third refractory state before transcription (re-)initiation, as done in the refractory-cycling model (Li et al., 2018). Therefore, more sophisticated models aim to encounter for these co-regulatory functions of TFs by integrating cooperative TF binding, direct interactions with nucleosomes and chromatin remodelers, as well as multiple TF binding sites (Segal et al., 2008; Teif et al., 2013; Sanchez et al., 2013). Also, while previous models of gene-regulation operated on equilibrium distributions, more recent non-equilibrium models describe dynamic transitions between different states in the transcription cycle, taking the chromatin state and the influence of TF binding into account (Ahsendorf et al., 2014; Estrada et al., 2016; Scholes et al., 2017; Li et al., 2018; Corrigan et al., 2016). It would be interesting to see whether any of these complex models allow for a more comprehensive view on p53 target gene expression using the presented data.

4.2.4. ALTERNATIVE APPROACHES TO CHARACTERIZE TRANSCRIPTION

Fluorescence imaging-based techniques allow to detect individual RNA molecules with sub-cellular localization of nanometer precision in single cells (Vera et al., 2016). Besides, it is possible to measure noise in a population of cells and transcription kinetics for low abundant RNAs. SmFISH techniques that hybridize fluorescent-labeled oligonucleotide probes in fixed, permeabilized cells (Femino et al., 1998; Raj et al., 2008) have been applied and further developed in this study (Figure 4.2.4.A). From these initial methods, the zoo of smFISH based techniques continues to grow beyond the characterization of RNA abundance

(Vera et al., 2016). Different applications of smFISH have been used to characterize nuclear to cytoplasmic distributions (Bahar Halpern et al., 2015a; Battich et al., 2015; Hansen et al., 2018), RNA half-life dynamics (Trcek et al., 2011), single nucleotide variants (Levesque and Raj, 2013) and non-coding RNAs (Cabili et al., 2015). Recently, allele-specific expression (Urbanek and Krzyzosiak, 2017), RNA editing (Mellis et al., 2017) and RNA detection in cleared and expanded (tissue) samples (Sylwestrak et al., 2016; Asano et al., 2018) have been shown. Similar approaches focus on amplifying the signal from shorter hybridization reactions to detect short RNA target sites, specifically for studying miRNAs or circular RNAs. Examples for such techniques are RNAScope and clampFISH (Figure 4.2.4.B/C). In the RNAScope approach, a branched DNA strand with a Christmas-tree-like structure can bind many fluorescent probes, but the individual target hybridization sequence is short (Figure 4.2.4.B) (Battich et al., 2013; Wang et al., 2012). ClampFISH, on the other hand, uses a primary landing probe that targets the RNA of interest. In subsequent protocol steps, fluorescent-labeled DNA-loop-probes are then bound by using a click-chemistry strategy that covalently links 5' end 3' azide links of a probe forming a loop around the present one (Rouhanifard et al., 2019) (Figure 4.2.4.C).

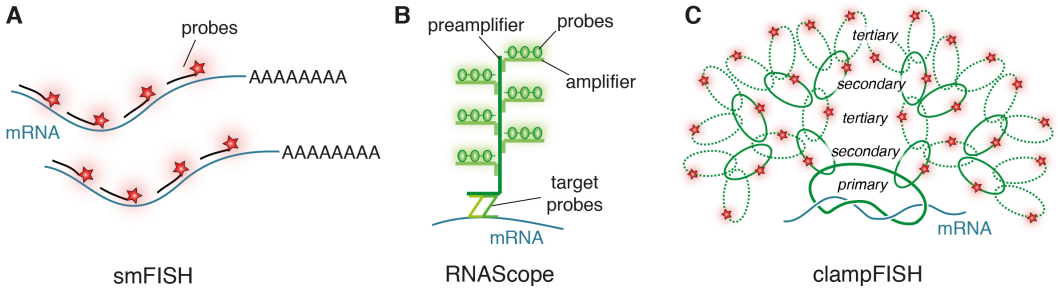

Figure 4.2.4 Experimental approaches for fixed cell RNA imaging.

(A) Illustration of the traditional smFISH strategy, hybridizing fluorescently labeled, sequence-specific oligonucleotides to a target RNA of interest after fixing and permeabilizing samples.
(B) RNA Scope as an examples for an amplification strategy based on smFISH. RNAscope uses target probes that are sequence-specific and hybridize with pre-amplifier and amplifier branches that can then be targeted by fluorescent probes (Battich et al., 2013; Wang et al., 2012).
(C) ClampFISH, on the other hand, is based on primary landing probes that target the RNA of interest, to which then fluorescent labeled secondary probes (followed by tertiary probes) can be bound using a click-chemistry strategy to form loops (Rouhanifard et al., 2019).

However, while the advantage of these approaches is the amplification of the fluorescence signal, it is challenging to quantify fluorescence intensities due to non-linear amplification. Beyond single oligo-labeling approaches, applications for multiplexing exist as well, ranging from sequential hybridization, followed by stripping protocols (Lubeck et al., 2014) to an error-robust encoding of probes employing Hamming code (MERFISH) (Chen et al., 2015). Another strategy is based on fluorescence in situ RNA sequencing (FISSEQ), which makes use of rolling cycling amplification of complementary DNA targets, followed by in situ cross-linking that locks amplicons as localized templates for three-dimensional sequencing (Lee et al., 2014). However, as these techniques also require complex detection

algorithms, e.g. to gain error-robust identification of different RNA species from barcode labeling (MERFISH) and complex microscope-associated pump-systems for sequential labeling, most are applied exclusively by the inventors. Imaging-based techniques in fixed cells provide the advantage to quantify RNA numbers and transcription site activity jointly with single-cell distributions and RNA localization to gain mechanistic insights. However, the multiplexing capacity is limited even with newer approaches such as MERFISH. Therefore, only a small number of RNAs can be analyzed simultaneously. While smFISH imaging allows for precise information on the regulation of specific subsets of target genes, sequencing-based technologies enable a transcriptome-wide view on gene expression.

Significant technological advances by recently developed RNA-Seq methods and the corresponding computational analyses can be broadly applied to study RNA expression kinetics (Tanay and Regev, 2017). Pseudotime strategies require a comparison of different cell states, as shown for studies on precursor and differentiated cells (Cannoodt et al., 2016). To establish single-cell RNA trajectories, the gene expression profiles of both states are connected employing geometric models (Trapnell et al., 2014; Svensson and Patcher, 2018). RNA velocity, the mRNA abundance over time, is the first derivative of the gene expression state. It yields information on the kinetics of the RNA life-cycle directly and can be extracted from standard RNA-sequencing experiments (La Manno et al., 2018; Svensson et al., 2018). In this approach, mathematical models of transcription kinetics are used to connect the time-dependent relation between spliced (mature) and unspliced (nascent) RNA. For example, in a recent analysis of neuronal progenitors and differentiated neurons, the future RNA abundance was predicted (La Manno et al., 2018, Svensson et al., 2018). Interestingly, this approach also allows re-analyzing existing, conventional RNA-Seq data, and it can be combined with techniques that measure RNAs and proteins simultaneously in single cells, such as CITE-Seq (Stoeckius et al., 2017). Also, time-series experiments that use metabolic labeling by 4-thiouridine (4sU) allow characterizing RNA kinetics based on differential detection of newly synthesized and mature RNAs. Protocols of 4sU-Seq employ a short exposure to 4-thiouridine for incorporation into nascent RNAs, while subsequent biotinylation enables purifying nascent RNAs using streptavidin beads (Dölken et al., 2008). The purified fraction can then be sequenced. Transient transcriptome sequencing (TT-Seq) detects newly synthesized RNA in a time-scale of 5 min, allowing to estimate transcription and degradation rates (Schwalb et al., 2016). Thiol(SH)–linked alkylation for the metabolic sequencing of RNA (SLAM-Seq) (Herzog et al., 2017) and TimeLapse-Seq (Schofield et al., 2018) are based on the quantification of RNAs labeled with 4sU relative to total RNA. Both approaches differ in how they foster T-to-C conversions detected by sequencing and have been applied in various biological contexts. These techniques have been used to study RNA kinetics, for example to analyze the transcriptional response of BRD4 and MYC target genes upon treatment with BET bromodomain inhibitors (Muhar et al., 2018), to characterize cell-type-specific transcription (Matsushima, et al., 2018) or to assess the relation between RNA stability and translation (Wu et al., 2019). Furthermore, they have been employed to analyze RNA kinetics based on single-cell RNA-Seq (Erhard et al., 2019; Hendriks et al., 2019; Ziegenhain et al., 2018).

Technologies that detect nascent RNA to derive kinetics of RNA metabolism can be combined with measuring RNAP2 state to gain mechanistic insights into transcriptional regulation. For example, in a recent study, Chromatin Immunoprecipitation Sequencing (ChIP-Seq) in combination with nascent RNA-Seq has been applied to analyze the connection between stochastic bursting and RNAP2 recruitment using targeted perturbations (Bartman et al., 2019). Besides, several RNA sequencing techniques have been developed to characterize nascent RNA from active RNAP2 at TSSs. Widely applied technologies are global run-on sequencing (GRO-Seq), native elongation transcript sequencing (NET-Seq) and precision nuclear run-on sequencing (PRO-Seq) (Core et al., 2008; Churchman et al., 2011; Kwak et al., 2013; Mahat et al., 2016). GRO-Seq results in snapshots of RNAP2 position and quantity of genes through the incorporation of bromo-tagged nucleotides into the RNA during a run-on. These modified nucleotides are subsequently identified by RNA sequencing with a resolution of approximately 50 bp. A change to biotinylated nucleotides for incorporation increases the resolution to single nucleotides in PRO-Seq (Jonkers and Lis, 2015).

4.2.5. LIVE-CELL RNA IMAGING

In Chapter 3.5, I present the first steps to image p53 target gene expression in living cells by tagging CDKN1A and MDM2 RNAs with MS2 stem-loops. Using these cell lines, an initial set of experiments showing the feasibility of long-term imaging of transcriptional activity for up to 12 h is demonstrated. Initially, I tagged CDKN1A with identical MS2 and PP7 stem-loop repeats (Larson et al., 2011). However, while genomic integration by CRISPR/Cas9 was successful as clones showed antibiotic resistance, it was not possible to validate the proper integration of 24 stem-loops by PCR and Sanger sequencing, probably due to the identical repeat structure of the hairpin loops. While initial experiments with these cell-lines have been performed, a new attempt was undertaken using a novel, randomized version of MS2 repeats (Wu et al., 2015), allowing for validation of the correct insertion with direct PCR and sequencing as described in Chapter 3.5. The presented pilot experiments highlight the potential of MS2 based TSS imaging and reveal differences in promoter activity between CDKN1A and MDM2 as well as upon DNA damage. However, the quantification of TSS activity from many cells and a more in-depth analysis of MS2 trajectories, comparing for example different kinds of DNA damage, is inevitable. To achieve this, an automatic tracking of TSSs from image stacks, local background correction and the quantification of TSS fluorescence intensities in 3D have to be further established. This robust analysis will allow to learn more about specific features of promoter activity from MS2-TSS trajectories over time to extract on-times, burst size and frequency in a high number of cells and understand gene-specific and DNA damage specific differences mechanistically. Additionally, this analysis provides a quantitative view on the velocity of genomic loci movement in the nucleus over time (when actively transcribing), which can be combined with other reporters as Mint-bodies (Sato et al., 2013) to visualize surrounding chromatin marks in parallel or detecting inactive loci by additional dCas9-based imaging (Ma et al., 2016).

MS2 and PP7 based RNA imaging is the most widely used technique for live-cell RNA imaging. Besides the application in RNA imaging, MS2 has also been used for RNA pull-down experiments using a biotinylated version to probe RNA-protein interactions (Marchese et al., 2016). The main disadvantage of using MS2 loops is the insertion of the repeat sequences into the target RNA. Multiple stem-loop repeats (at least 12) are necessary for live imaging to bind enough coat protein fused to a fluorescent protein. Split-GFP approaches have been employed to reduce the background fluorescence and overcome these limitations (Weil et al., 2010). However, once the two halves of the split version of GFP consolidate, they remain stable even when the MCP-coat proteins are not bound to RNA anymore. Also, MS2 tagging does only allow for reduced multiplexing, as merely PP7 and boxB have been shown to work jointly with MS2 to tag different RNAs simultaneously (Lange et al., 2008). Besides, introducing RNA hairpins and the binding of the GFP-MCP-coat protein fusion may alter the 3D RNA structure, its intracellular transport due to a change in the diffusion coefficient, as well as the accessibility for RNA binding proteins. These alterations may interfere with different layers of regulation of RNA metabolism. Additionally, the MCP-coat protein often has a nuclear localization signal (NLS), to allow RNA detection at the transcription site. However, the NLS may affect the RNA localization when the MCP protein binds to mature RNA in the cytoplasm, and MS2 tagging has been suggested to perturb RNA transport and localization (Haimovich et al., 2017). Concerning

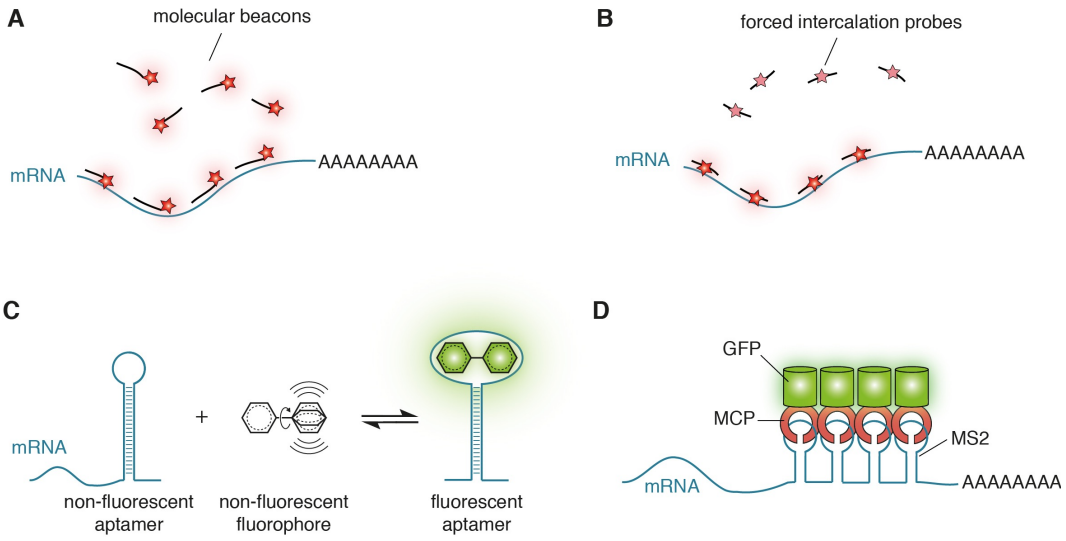

Figure 4.2.5 Experimental approaches for live-cell RNA imaging.

(A) Molecular beacons are dye-labelled oligonucleotides, following a similar principle as smFISH in live-cells. The probes have to be delivered to the cells via transfection or injection and can then bind their RNA targets.
(B) Forced intercalation of thiazoleorange (FIT) probes show a high fluroescence turn-on when hybridizing with the target RNA.
(C) The general principal of RNA aptamers for life cell RNA imaging, is based on the integration of the non-fluorescent aptamer into a target RNA (can also be applied in repeats). In a second step, a fluorogenic dye that is non-fluorescent in the unbound state is delivered. Upon binding of the dye by the aptamer, a characteristic fluorescence turn-on can be measured that is specific for the RNA-aptamer fusion (Ouellet, 2016).
(D) Repeats of RNA hairpins (e.g. MS2), can be integrated into the mRNA, e.g. into the 5' or 3' UTR, which are then specifically bound by a coat protein (MCP) that is co-expressed as a fluorescent protein fusion (Buxbaum et al., 2015).

imaging of the TSS activity of MDM2 and CDKN1A promoters as presented in this thesis, these aspects certainly have to be considered. However, since only the fluorescence intensity at the TSS was measured, neglecting transport of RNAs out of the nucleus, these are not as important for the presented results.

Besides MS2/PP7 based imaging, other live-cell RNA imaging methods exist. Fluorogenic oligonucleotide-based probes, so-called molecular beacons that are transfected or injected into cells, are similar to the smFISH approach (Chen et al., 2017). Likewise, forced intercalation (FIT) probes, nuclease resistant oligonucleotide probes, contain a fluorescent dye such as thiazole orange as a base surrogate, which is forced into a nucleic acid double-strand upon hybridization of a probe to a target RNA, leading to a fluorescence turn-on. For example, FIT probes have been used to visualize mRNP trafficking in Drosophila oocytes (Hövelmann et al., 2014; Hoevelmann et al., 2016). Beyond these, different RNA aptamers that fluoresce when bound to cell-permeable small-molecule dyes exist (Figure 4.2.5.B). To date, there are several different aptamers for live-cell RNA imaging: Spinach/Spinach2 (Paige et al., 2011; Song et al., 2014), Broccoli (Filonov et al., 2014), Corn (Song et al., 2017) and Mango (Dolgosheina et al., 2014). Furthermore, a split approach for the Spinach aptamer is available for live-cell RNA imaging, reducing the background fluorescence (Kikuchi et al., 2016). However, only limited applications for these aptamers have been shown so far in live-cell imaging, despite their advantageous features, e.g. regarding the size of the tag. Reasons may be the dependence on delivery and equal cellular distribution of the fluorogenic dye as well as limited brightness. The surrounding sequence can further influence proper folding of aptamers and thus the fluorescence properties. Similar to the MS2/PP7 system is the lambdaN22-GFP reporter system (Daigle and Ellenberg, 2007) that binds a unique RNA motif (boxB). It can be integrated into the target RNA while the readout is a fluorescent protein such as GFP. A related approach is the PUM-HD system, using fluorescent labeling of the RNA binding protein domain of human PUMILIO1 (Yoshimura and Ozawa, 2016). PUM-HD recognizes a specific eight nucleotide long sequence that can be integrated into the RNA of interest by mutagenesis, while the fluorescence background can be kept low through a split fluorescent protein approach (Yoshimura and Ozawa, 2016). Additionally, mRNA targeting by dCas13 has been used in an initial application for RNA imaging (Abudayyeh et al., 2017).

While many of these techniques need to be further optimized and supported by sophisticated computational image analysis to extract kinetics of transcription, RNA localization and homeostasis, they are powerful approaches to address a plethora of questions. In future studies, this may help to understand more details of how p53 target gene expression is regulated in living cells.

4.3. CONCLUSION & OUTLOOK

P53 is a major tumor suppressor and a well-studied transcription factor exhibiting differential stimulus-specific dynamics. As p53 dynamics have been shown to drive cell fate through the distinct modulation of target gene expression, studying the underlying mechanism of this modulation at individual promoters may help to further decipher the regulatory code of p53-mediated transcription. This will allow to gain a mechanistic understanding of how a fundamental transcription factor affects the transcription cycle, but could also provide crucial information to develop therapeutic strategies for p53-related diseases such as cancer. I show that pulsatile p53 dynamics feature different archetypes of promoter activity, while persistent nuclear p53 promotes sustained transcription with high rates. It needs to be further evaluated if the selected panel of p53 target genes is representative for p53-mediated gene expression in general. However, it can be hypothesized that pulses in contrast to sustained nuclear p53 allow for a broader plasticity of promoter specific transcriptional bursting. In this regard, my data indicate that the pulsatile nature of the p53 response to DNA damage enables fine-tuning of transcriptional activity through other co-regulatory mechanisms. This aspect may play a key-role for expanding the regulatory potential beyond DNA binding kinetics of TFs at target gene promoters over time. A more detailed mechanistic analysis of promoters that represent the individual archetypes and are connected with stimulus specific cell fate regulation is crucial to understand the molecular background that defines the archetype and plasticity of stochastic bursting.

In this work, I provide the first steps to characterize p53 dependent transcription in single cells and at individual promoters. Therefore, I selected a set of target genes and focused on p53 activation in response to DNA damage by γ-irradiation. As a correlation with subsequent cell fate regulation was not further investigated, it can be only speculated that terminal cell fates such as apoptosis require a higher promoter activity with persistent promoter *on*-times. The reasonable first consecutive experiment to better understand stochastic bursting is to analyze transcription properties of the same target genes in response to other kinds of DNA damage such as UV radiation or treatment with chemotherapeutic drugs that have been shown to induce different dynamic patterns of p53. As such different manipulations also induce differential PTMs on p53, this could help to further disentangle their contribution to stochastic transcription on the molecular level. Interestingly, I found a change in p53's PTM-state between the first two pulses. This observation suggests that recurring pulses of p53 are not exclusively regulated by the upstream kinases ATM, ATR and DNA-PKcs, suggesting an additional layer of regulation, e.g. on the level of the Checkpoint kinases (Chk1/Chk2). This finding challenges the current view on how p53 dynamics are regulated by upstream kinase signaling. It is therefore interesting to understand this aspect in more detail and test p53's PTMs in multiple cell lines at the time-points of the first three pulses. To approach this, a mass-spectrometry based analysis may help to gain a better overview of a change in dominant modifications. However, particularly with regard to the

gene-specific effects on promoter activity, it may be informative to understand how the PTM state of p53 changes with respect to promoter regulation. Therefore, a combinatorial MS2-based approach for live-cell imaging and subsequent staining for p53's post-translational modifications in the same cells could be applied. Also, an analysis of stochastic bursting after inducing targeted mutation of key lysine-residues in the C-terminal domain by CRISPR/Cas9 could allow to further decipher the contributions of CTD acetylation to stochastic bursting. In this regard, also the combination with the discussed technologies to measure kinetic rates and RNP2 distribution transcriptome-wide may be informative. Additionally, the molecular background of p53 promoter binding in single cells at specific promoters is quantitatively widely unexplored. It would be exciting to further study p53's DNA binding to the analyzed promoters, beyond the acquired ChIP data. Such exploration is particularly interesting in the context of the current predominant hypothesis that p53 pulsing reveals robustness of cellular signaling. Experiments focusing on how the binding of p53 is stabilized at promoters, despite the change in total nuclear p53 levels, could be performed.

The first steps to perform live-cell RNA imaging of the transcriptional activity at p53 target gene promoters are presented in this study. While smFISH already allowed to infer quantitative promoter activity from snapshots of fixed cells, this development will enable to gain deeper insights with a high temporal resolution. As a next step, it would be exciting to put transcriptional activity in the context of promoter activities before and after different DNA damage treatments and during the cell cycle. This will help to understand the transcriptional activity and heterogeneity at individual promoters in more detail. Also, directly correlating p53 promoter residence times with transcriptional activity and RNAP2 state may help to decipher p53 dependent transcriptional regulation mechanistically. Therefore, a combination with a fluorescent live-cell p53 reporter could be helpful as well as correlating RNAP2 occupancy. In this regard, a focus on promoters from different archetypes would be informative. Finally, to link transcription and translation with cell fate, live reporters could be further extended by visualizing the transcribed proteins through a fluorescent protein knock-in. Novel probes to visualize chromatin marks by live-cell imaging could be used as well. Besides these mechanistic insights into the molecular basis of promoter activity, a focus on cell fate regulation would be allowed by live-cell RNA imaging. Systematic analyses of treatment with inhibitors and chemotherapeutic drugs would facilitate to follow both transcriptional activity and the resulting cell fate from long-term imaging data. One could thereby learn how promoter activity needs to be tuned to drive cells specifically into apoptosis, and how perturbations of the p53 network could help in the context of cancer therapy. This would be of particular interest, as manipulation of potential co-regulatory mechanisms could establish a basis to modulate transcription to the desired level. In summary, we learned a great deal about promoter regulation of p53 targets in this study, but many new, exciting questions and research directions remain to be explored.

CHAPTER 5

MATERIALS & METHODS

5.1. FLUORESCENCE IN-SITU HYBRIDIZATION (FISH) AND IMMUNOFLUORESCENCE

5.1.1. SINGLE MOLECULE FLUORESCENCE IN-SITU HYBRIDIZATION AND COMPUTATIONAL IMAGE ANALYSIS

Tissue culture

For each experiment $0.5*10^5$ A549 cells per well were seeded in 12-well tissue culture plates on 18 mm uncoated high precision coverglasses (thickness #1) (Marienfeld GmbH, Lauda-Königshofen, GER) and cultured for 24 h in McCoy's 5A growth medium (GE Healthcare, Solingen, GER) supplemented with 100 U/mL Penicillin, 100 µg/mL Streptomycin, 2 mM GlutaMAX and 10% (v/v) Fetal Bovine Serum. The procedure was identical for smFISH of MCF7 and MCF10A cells, while culturing media differed. MCF7 cells were cultured in Dulbecco's Modified Eagle Medium (DMEM) supplemented with 100 U/mL Penicillin and 100 µg/mL Streptomycin, 2 mM GlutaMAX and 10% (v/v) Fetal Bovine Serum (FBS). MCF10A cells were cultured in Dulbecco's Modified Eagle Medium/ Nutrient Mixture F-12 (DMEM-F12) supplemented with 100 U/mL Penicillin, 100 µg/mL Streptomycin, 2 mM GlutaMAX and 5% (v/v) Horse Serum (PAN-Biotech GmbH, Aidenbach, GER). Additionally, 100 ng/mL Choleratoxin (Sigma Aldrich, St. Louis, USA), 10 µg/mL Insulin (Sigma Aldrich, St. Louis, USA), 0.5 µg/mL Hydrocortisone (Sigma Aldrich, St. Louis, USA) and 20 ng/mL EGF (PeproTech, Hamburg, GER) were added. If not stated differently, all standard culturing media and tissue culture additives were purchased from the suppliers Thermo Fisher Scientific (Waltham, MA, USA) or PAN-Biotech GmbH (Aidenbach, GER).

Irradiation and treatment with chemical inhibitors

γ-irradiation was applied using a cesium-137 source. The irradiation time changed over time from ranging between 87-90 sec for 10 Gy. Inhibitor treatments were always performed in McCoy's 5A medium (GE Healthcare, Solingen, GER) as described above. DRB (5,6-dichlorobenzimidazole-1-b-D-ribofuranoside) was used at 10 µM concentration (#1001030250; Cayman Chemical, Ann Arbor, USA). Checkpoint kinase-2 inhibitor II BML-277 (Sigma Aldrich, St. Louis, USA) was applied at 10 µM final concentration at 4 h after γ-irradiation. Nutlin-3 was used at final concentrations of 0.75 µM, 2.25 µM and 4 µM and applied with increasing concentration at 2.5 h, 3.5 h and 5.5 h after γ-irradiation (#N6287, Sigma Aldrich, St. Louis, USA).

Single molecule fluorescence in-situ hybridization

After treatment of cells by γ-irradiation, cells were washed on ice at the indicated time-points with sterile, ice-cold 1x phosphate-buffered saline (PBS), fixed with 2% para-formaldehyde (PFA) (EM-grade) (Electron Microscopy Sciences, Hatfield, USA) for 10 min at room temperature and permeabilized over night with 70% Ethanol at 4°C. All buffers used after

permeabilization were produced with RNAse/DNAse free H_2O (QIAGEN, Venlo, NL). Custom probe sets for smFISH were designed using the online tool for Stellaris probe design (Biosearch Technologies Inc, Petaluma, USA) with two different conjugated dyes - CAL Fluor Red 610 for exon probe sets and Quasar 670 for intron probe sets. Starting from manufacturers instructions for Stellaris probe hybridization (Biosearch Technologies Inc, Petaluma, USA), a novel composition of hybridization buffer with additional 0,5% (v/v) sodium dodecyl sulfate (SDS) (Sigma Aldrich, St. Louis, USA) and 5% (w/v) ethylene carbonate (EC) (Sigma Aldrich, St. Louis, USA) was used for probe hybridization to improve the SNR as described in Chapter 3.1.3. Sequences of designed probes can be found below. SmFISH probes were pre-diluted in Tris-EDTA (Sigma Aldrich, St. Louis, USA) and hybridized at a final concentration of 0.1 µM based on manufacturers instructions over night at 37°C. Following hybridization, cells were washed with 2x SSC (Applichem GmBH, Darmstadt, GER) and incubated with Alexa Fluor 488 N-Hydroxysuccinimid (NHS-AF88) (Molecular Probes/Life technologies, Carlsbad, USA) for 10 min at RT for unspecific cytoplasmic protein staining, followed by Hoechst 33342 (Molecular Probes/Life technologies, Carlsbad, USA) nuclear counterstain. Coverglasses were mounted on 15 µL Prolong Gold Antifade (Molecular probes/Life technologies, Carlsbad, USA) and surrounded by transparent nail polish to avoid moving. Slides were stored at 4°C until imaging, which was performed approximately 4 h after mounting.

Fluorescence Microscopy Imaging of smFISH stained cells

Cells were imaged on a Nikon Ti-E inverted fluorescence microscope (Nikon instruments, Tokyo, JPN) with an EMCCD camera (ANDOR, DU iXON Ultra 888), Lumen 200 Fluorescence Illumination System (Prior Scientific, Cambridge, UK) and a 60× plan apo objective (NA 1.4) using appropriate filter sets (Hoechst: 387/11 nm excitation (EX), 409 nm dichroic beam splitter (BS), 447/60 nm emission (EM); Alexa Fluor 488: 470/40 nm (EX), 495 nm (BS), 525/50 nm (EM); CAL Fluor Red 610: 580/25 nm (EM), 600 nm (BS), 625 nm (EX); Quasar 670: 640/30 nm (EX), 660 nm (BS), 690/50 nm (EM)). Microscopy filter sets were purchased from AHF (AHF Analysentechnik AG, Tübingen, GER). Images were acquired as multipoints of 21 z-stacks of each group of cells in a field of view with 300 nm step-width using Nikon Elements software (Nikon instruments, Tokyo, JPN).

Analysis of RNA counts and promoter activity from smFISH data

The quantification of RNA counts per cell was performed in *MATLAB* (MathWorks, Natick, USA) using the *FISH-Quant* analysis tool (Mueller et al., 2013) and custom written *MATLAB* software. Therefore, multicolor z-stacks from Nikon Element software (.nd2 format) were extracted into individual .tif stacks and imported into FISH-Quant (Mueller et al., 2013). For nuclei and cytoplasmic segmentation, two approaches were applied, dependent on the quality of cytoplasmic staining by NHS-AF488, were used. For high-quality cytoplasmic staining and low cell density, the *FISH-Quant* build-in *CellProfiler* (Carpenter et al., 2006) interface for automatic cell outline detection was used. Parameters for filtering, local focus projection and segmentation were optimized for each dataset when

necessary. For dense cells and lower intensity cytoplasmic staining, nuclei were automatically detected in *FISH-Quant's* outline-detection GUI, and cytoplasmic outlines were drawn manually. In both cases each cell outline and nucleus was manually checked for correct segmentation before analysis. TSS were identified based on co-localization of exon and intron signal in nuclei. After identification based on co-localization, the area of a TSS was defined using the exon signal in all z-planes. All analysis parameters were kept constant for spot and TSS detection in one dataset. In brief, according to the *FISH-Quant* work-flow for spot detection, images were filtered, pre-detection was performed, then spots were fitted and fits were further thresholded to exclude outliers. For TSS detection, an average cytoplasmic spot was computed. Each analysis was performed using the *FISH-Quant* batch processing tool-box. RNA spots counts and respective localizations were directly taken from the *FISH-Quan*t based analysis.

Calculating transcription properties from smFISH data

The bursting activity was characterized based on previously published models (Raj et al., 2008; Bahar Halpern et al. 2015b, Bahar Halpern and Itzkovitz, 2016), as described in detail in Chapter 1.3.3 and Chapter 3.3.2. To calculate the TSS intensity, the *FISH-Quant* parameter TS_Pix_sum (sum of all pixels around brightest pixel of TSS) was used, as well as the mean intensity of all quantified spots. Furthermore, I calculated the correction factor η for probe position using the *TransQuant* software (Bahar Halper and Itzkovitz, 2016). Obtained correction factors for each gene and the positioning of the corresponding probe set is plotted in Appendix Figure 8.3.3/1. As correction factor $\varkappa$ = 1.5 was used for inferred RNAP2 occupancies, as previously suggested (Bahar Halpern et al., 2015b). To estimated the RNAP2 speed, 50 nt/sec was used, as a range of 6.3 - 71.6 nt/sec has been previously measured in mammalian cell lines (Darzaq et al., 2007). How RNAP2 speed affects the calculated transcription rates is displayed in Figure 8.3.3/2. In general, all quantified cells were used for the calculation of transcription properties. The only exception is the RRM2B dataset. For some conditions, cells had a minority of cells with >5 co-stained spots in the nucleus with low intensity and questionable co-localization of intron and exon staining. DNA FISH has not been performed for RRM2B in A549 cells and thereby it remains unclear how many genomics loci exist (cells with >5 TSS were excluded from the analysis of TSS activity to avoid a bias of the calculated bursting parameters). This rule led to exclusion of nine cells at 3 h, and two cells in both the 6 h and 9 h conditions (only for RRM2B).

SmFISH probe oligo sequences

SmFISH probe libraries are listed as 5'-3' complementary oligo sequences. Oligos were designed using the Stellaris Probe designer (Biosearch Technologies Inc, Petaluma, USA) with 22 nt length, masking level 5 and a minimum spacing length of 2 nt. To design intron probe sets, the respective intron sequences were pasted separately and found probes were manually spread over the unspliced RNA sequence based on hits from the Stellaris probe designer. This approach was based on recommendation by K. Bahar-Halpern, who established the protocol for exon-intron identification of TSS in mouse liver cells (Bahar-Halpern et al., 2015b).

Table 5.1.1 Labeled oligonucleotides for smFISH.

SmFISH probes targeting exon and intron regions of each p53 target gene as designed by the Stellaris Probe designer (Biosearch Technologies Inc, Petaluma, USA) with 22 nt length, masking level 5 and a minimum spacing length of 2 nt are listed below (Sequences are given in 5'->3'direction). Exon probe sets were labeled with CAL Fluor Red 610 and intron probe sets were labeled with Quasar 610 dye.

BAX Exon	BAX Intron	DDB2 Exon	DDB2 Intron
sequence (5'->3')	sequence (5'->3')	sequence (5'->3')	sequence (5'->3')
atctgctcagagctggtg	tcctgtgtcctgaaggag	ttgttcaaaccagcttggag	aactgtgcaagaaccctgat
gaagcaaaagggcccctg	gagaatgcggggctgaga	tagccgagctaagccaactt	ccaggaaaggtaggattctc
ctgctcgatcctggatga	ctcctagttcttagggga	cggggactacaaaactgcgg	gaggacgtgcagctaacaag
cttcttggtggacgcatc	ttgcgctgagttgtgggg	aggcctctggggagaaacaa	gagtgtctcgaaactcctta
cgcttgagacactcgctc	ggctgggagtccggaatg	agatcatggagggaggattg	ctgtatttgaggacccaatc
gttactgtccagttcgtc	agatcctggcagagagga	aaggggtactgtgctctatg	aactaggttacttctgggga
caatcatcctctgcagct	tccctgaaggagggtttt	ctggggcgtaatacaatctc	aggaataggaaggcctggaa
aaaagacctctcgggggg	cccaagccaggctgaaat	cttcgcacagagcttcttgg	gggactgggtcacaatttta
aacatgtcagctgccact	ggaaaattcccgcatcca	tgagtcacatcttctgctag	cagtttgggctgcaaaactc
ccagttgaagttgccgtc	caggcatcaggctgatgg	agaatccagagtgtgcaaaa	aaatacagtcgtgcagggtt
aaaagggcgacaacccgg	gagaggagaaccagtgcc	cagccttttgtaatatccgg	cggttaatctctgtctcatc
ccagtttgctggcaaagt	gatctgagggggagcatc	atgtagccctcctgtcaaag	catattttcctctccaatct
ttggtgcacagggccttg	gggggttgataccacgat	ccttgatgccaaaattccag	cttgaggcaaaaaatgcctt
ggttctgatcagttccgg	catgccctctgtggtcac	ggttggtattgagagggtta	tgcacgtgtaaaccctgag
ggaagtccaatgtccagc	cagacacccagtgcacag	ctccattgaggaggcgtaaa	tgggagcatgcaatagtaaa
gtcgcttcagtgactcgg	cccatcagctcaatcttg	aaagtcttgcagcctagttg	tgaaccaagccatcatctaa
tcctggagacagggacat	tcatctcggacgttcagg	aaactcgtagaatgttgcct	tcggaccactctgacaagct
gtcccaaagtaggagagg	tcacctgcactgctattc	tgttgatggtgtctgagctg	atttttacctggctgagtg
tcacggtctgccacgtgg	ctctgtaggtggtgccac	acatccaggctacaaaacca	gctgggacctttacaacata
cactcccgccacaaagat	ttctattctatcatcccc	caccattcggctactagcag	aaggaaagctaactgcctgc
atggtgagtgaggcggtg	tcctgcagcctttatctg	atgttcagcaggatcacgtt	atgagccctagatccaagtc
ctcagcccatcttcttcc	tcccaactcccaagactt	ggactgaaacaagctgcgtt	ttaaaacccaagttctgggt
aacacagtccaaggcagc	ggacttttctggaccaga	taaactcggatctcgctctt	cctttcatgccttcaacaaa
aagaccactcttccccac	cacttcctgttttgtgcc	tgtgaggtgctggaagtgac	ctcaattacacttcaagccc
aggaggtttattaccccc	tgacctcactccacctttt	aattaggatctgggtatcgg	tcgtatgtatacatcccatc
	ctgtgtgcaggctttggc	tcgtcctcaattcataaggg	aagaactctgtgccaaacct
	cacagtgcagcccacaag	ctgagtttccatcgaacacg	ccctcagcaatggatgataa
	accctcaggatgaagacc	ggtcatagagctgacacatc	taaaggtcctagaggggacg
	ctgagccttctgtggctc	gcgaactgatgccagaagat	acagtcatctctagtttacc
	tgttactctcaactgccc	cccatgggattgaattcatt	tttagtttcattcagtgcca
	gccacccacaattgaagt	tctttagtgtctctcacttc	ctgaagcagaattcggctga
	cctcccctcaaagatttc	aggacttgatcccatgtgtg	aatccctccacttaagagac
	acctcctttgtcaattct	tttaacaaatcgccacctct	cccatctcacactttgaatt
	actgcctggagatagtgg	aaccctaaccttggatactt	tctttagctgggcaggaaac
	agggactgaaccttgtcc	taaaagtgtcccagtcccac	caacttcaagctgccttatt
	tgtggggagtggagtggg	aggcaagtccagagcattaa	ccaggcataagctaaattcc
		ctgtgtcaccaactctggag	tagaataccctacactgctt
		caggctagatacagaggggc	tgttagtcaggaagctcttc
		agttccaagataaccttggt	tcagtctggcacaagttcaa
		cccactgagaggagaaaagt	agaaggttacacgcatgtca
		aataactgcttgatccctct	aatgcctagaccaatcttca
		tggttttattggccatatca	tgtcagcatctgggagtaaa
			tgtaaaggtcacagccaagg
			tgtaatacatgttcccttgc
			tgcacagagggatgctgaaa
			cttctctggagtaggactac
			aaagaagcttagtgatcccc
			caggaccatatgtaatcgca

Table 5.1.1 Labeled oligonucleotides for smFISH. ***(continued)***

RRM2B Exon	RRM2B Intron	PPM1D Exon	PPM1D Intron
sequence (5'->3')	sequence (5'->3')	sequence (5'->3')	sequence (5'->3')
cgcaacagcaacatttacct	gaggtcatgaggatttcgtg	cggccaactattgtttatct	gaactgcctgaaaaaggggc
gcaacttgcaatctaacggg	ctctctgaagtatcacttcc	gctccacaacgatttgagta	cacttccatcagtgtatact
ataacatttcctacagcggt	tttcgtggcactttgcataa	cgtcgcacacggcgaaaaag	caagaataggctgcagggag
ctttcgttggtgtctgaaga	caacaggttccagtagtaca	acaagcgagaaagcctttgc	ttcaaacacgtttcctctgg
taggagtggctcttcatttg	tggggtggaaacgtttgttt	agtttcttccacatggcaag	atcgatttatcttttggcca
tgacaaaccggcgagaactc	gtgccattagcataaacagc	aagacccgtcatagtctttg	gcccttctaaattagcttac
gatcctttgataagtcgacc	tgttaagcctgaatcactgc	cctacgtgagctacatacat	ccgcgtttttagttttcata
ctttaagcttgttccagtga	cgggtctgtatcattgagat	tcctgaattccaagaaccac	caacgttattatgctgccat
tccatcactggctgcaaaaa	tgcactctggcatctagaaa	ctgacaaagtcatccttcgg	ccggctaatctacaactcta
atagaaacagcgagcctctg	gcctaaactttaccttgaca	tccaaactacacgattcacc	aatgtggagccatccaagaa
gattttctatctgctatcca	ggcatgccatttaatgtttt	attgtgagtgagtcgaggtc	agaggtcaagcttaacacca
aaaactccttctacagcagc	tctgacggaaccaatgggat	ctcttgctactgccagaaaa	acttcttcacgatttccttg
ctctcttctttagccagaat	tttcacttctattcccacaa	tcatagctccacaaatcacc	ttaaaccttccccatataca
ggaaaaagtgagtcctggca	gctgtatgttgtcatagtca	aagagtgtggacacttgtgt	catgtctctgcattgctaac
attggaacatcaggcaagca	cctttatgtctcttctactt	tatacttgtgcttctgaggg	aaggacacacagccatactg
ctcctgctcaattttgacag	aatctaggctggcatcatac	acaagattgtccatgctcac	ggaaatagagtatgccacca
ctggcaaggcttctgttaaa	tgactcaatttctggtcacc	gctcgattcacaagcatttt	tagcctgaaaggaggttcat
tccacaagtaatctgtcagc	tatagccgcacaggtgtaaa	ggtaaagtttccctgattgt	ttctcaccttcacaatcaca
agacgttatctgtggtttct	ggcactggtctaatgaagga	ggttcaggtataactcatct	acaaccagcagagatgtcag
gtggtgctaacagtagtagt	tcttttgggagtttttggg	ttataggaagggctgtcagt	tgcaaaaagttacctgctcc
aactaccatgataacctcct	gcagcttcaacaagacttca	agtcatcacacaggtttctt	cagctctctcgacacttaat
tccagagctaaatctggcaa	gatgtggcagttagcatgaa	tgacttgactggtggtgtag	ttgctaaaccttctccttac
cccttcctctatgtataaat	gaggtggcattaggaagact	tatggtccttagaattcacc	cattctgccttaataccatc
aataatccctaccatgttct	aaatctgtaccccacagatt	tctgagaaggcattgctacg	ttgccattcacaagaatcca
acactattcaggctggtata	ttcatagcagggtacagttt	ctatctcagctgaaacctct	taaaccttcccctcaattag
acagcctaagtcaattgctg	aaggctcatactccaattct	gtatgactacaccttggaca	gtaattctctagccttcttt
gctatcatgttgcatagtca	tcttcaaacatcggaggtct	agtggttctggatcttttga	gcatagccaaggtaagacac
actcttctagagaaacctcc	aggaatcaattttgtggcca	tatccttaaagtcagggctt	ttgttacttctgcctacatt
gggcagacttctcaaaaacc	ctgcagaacacgagtgatgg	aaggccaattggaaggctat	ccaaccctcaaatgaaacca
cttcatccaaagacaggtct	gccaggcgacaacaacaaag	ttggactcttctaatgtcct	cgattttctcttataagccc
actgcttgaaggggtataca	gtttaatttaactcctccca	tttcgtctatgcttcttcat	gtatttccatgcaacaagct
acagtttgttgggaatggga	gttaaagatgcccttgatgt	accactacttcgacttaagc	ccgtaaaccataagggtgtg
tctctaagttttagcatcca	gcagcctactagacatagaa	gtcgcatggtgagtttaaca	aaggagacatctattcccac
ctcccagttttgattagatt	gcatcttgaaactctaggct	cagttttcctgtgttgatga	tcatcagtgtctatagggtg
tccttttgcattcacttgag	gtatacacattctcctgttc	ccctcttatatcctaagttt	gctacatttgtacttgggta
gcttcacattaaggcatctg	ctgctgaagactagtacctt	aggccaggataaaactgctg	cagagtgcttcatacacact
gacttcttcatccaaatcca	tgccctgacgatgaatgaag	tttacagcaacttataccct	ttacccactagcagatcaag
ctggccatatttctatgtga	atcacaagcagtcactcttc	ccctattgtcacaattactg	aagtcagtggttgtgtgttt
aaactgtcttctcaagtcct	tgggttaggttccagatata	tacatcacttttccagtctg	cgtttcacaggccaatttat
ccagtcctgtctaaaagcaa	tacatcagtgagacaaccca	aactgtagcatggctcaaca	attccagatacttccatgtg
ggccagcttagttgtaagaa	agctaagtaaatgggctgct	cacttccttctatgctgaag	aggataacccatctttggat
aatcagctcctgacattagc	agcttagtatcgtgtcaagc	aataatgccattggtctggg	tgcttccttcaatactcatc
aagtccactaccaattcact	cttgtttaaaggtatgggcc	aattagcagcaccatctgtt	tcttccaggtctcataagac
gattctgctggggaagattt	tttatacctactgccatcac	cagaatgtgtggacatggtt	gcagtcttgtgaagttttct
tttcaattctgtgccattca	ctcgccaaagcaactgttat	tggcataagacacaccgatc	cagagtctctctaagtgcat
ggagcagagcacttaaaggg	gagtcgcacatgtgtgagaa	aatgcttttaacttccaggt	agaataccatgagccttgtg
taagccccaaattgaaggga	tgcatatgatctcactgtgg	cataactattgcacacccta	gtgtagttatgtccactcaa
cattcctttattagggtagc	atcttagccttctgatactc	actccactagagcaatcttc	cctctgtgagatctactttg

Table 5.1.1 Labeled oligonucleotides for smFISH. ***(continued)***

SESN1 Exon	SESN1 Intron	MDM2 Exon	MDM2 Intron
sequence (5'->3')	sequence (5'->3')	sequence (5'->3')	sequence (5'->3')
gtcgaggaattctaatgcca	ttaacagggtgggtttttct	ctatcagatttgtggcgttt	ccagaggtagcacactttaa
tccttttctgggatgaatct	tggctcctgatcctaaaatt	atctcccttattacacacag	cagtttttaactccacgcag
taaagcatgcatctgtgcgt	caccttctatattggtgcaa	tagattcactgctactgctt	cgtaacttcaaccacgctta
gtaatgttatccaaacggcc	actgaacttgctctgtttca	tcaagatccggattcgatgg	ggtcctctgtctaactttaa
tgcagtagatagtgctgagt	aaacccttgctttttcacta	cctgaatgttcacttacacc	tgcacctctctttaatatgc
ataatgtaggggtaacggcc	gaatactctcttggatcctc	aactgaatcctgatccaacc	aagtatctttacagcttgcc
gccattattccaatgtagtg	agaagaatccatctcctagc	ccttcttcactaaggctata	ccctttatctagaggttttac
gtaggagcactgatgtcttg	aagtatccaacttacctggg	ctgcctgatacacagtaact	tgatccaacgagcttattgc
catttacatgcaggttcact	catcagggtaggccataaac	attgcatgaagtgcatttcc	tttatctgagttcctagctg
tctaaaccattgagccactt	agagctgagtcagatactgg	gtgttgagttttccagtttg	aaatggtcaagcacccttac
tctgtagtttttgaggagca	tttgttccttcactgatctg	ttcctcaacacatgactctc	atgaatcagctcacctctat
aaggtctatgggctaacact	ggtttcatgacaggatgact	ggctgagaatagtcttcact	aaattctgcctaaggttgct
cctcaatgtgttctttggta	ccagttattcctgacataga	actctttcacatcttcttgg	tgtggattggacagattgct
ctgtgctcttcagcttttaa	ctgaagattcttgtggtgca	tcacacaaggttcaatggca	ctaagtctttatgatggcct
tactgcatgtaccaattccg	agtattaagccctttctcta	cacatgtaaagcaggccata	ctgcccagatacttagatac
atttctggactgattccaca	ggttatacttctataccctg	ttggttgtctacatactggg	gggtaaacaaccaggaacca
aaggaggtctgaatgtgtgg	gacaaaggactggccaagtg	tagacaggtcaactagggga	gtctcaggtgaacgtattca
cacagatgcagtagttgcta	aagatgtctacatggctgga	ggttgtctaaattcctaggg	tctgtcatctcctaatgttc
cactgtgattgccatttgta	aactgtgtacactgggcata	gaggcattttctcactttga	ctcctatttcttatctctca
tgtaactgcctcatcttttc	gtcattaccatttatgctgt	gtattcactattccactacc	catcaagcttcaacttcctt
ctcttcttcatctcgacatt	tttggcccagaggaaaacat	catcccttactatggtttat	tttttagctctgtgcttagt
tgctggtgtaacttcttcat	cagaggggcaatataagggt	acgggtaaatggtggctatt	tgcaagcaggaagaggttga
gccataactagtatcctcaa	agctgtacttcaaatgccag	gcctgatgtaatctaggtta	atcattggcaagcttgtagg
tcccatgtctagagaaatct	ccattgaggaggctaaagtc	taggctgggaaccatgtaac	ctggatctaaccagacttct
cctggacacgaaatgttgga	tcttgcaaagctggttctac	ctggccttaagcaaaagtct	gaacctcagtatgtggtttt
gaataaccatgatcttccca	ttccaatcacataggcactg	ttctgaattcacgggtttct	aactctgatatcccaagtct
atcaatcaactgtcccacat	atcatgaacacgtagccaca	atttttaggaaacctctgcc	cactcctaaacaggagcttt
atatagttccaaattgcccg	gggtaccaagcaatagtgta	ggttctaagtctccaaagga	tatttcccaaagcctttcaa
ctacgatccaatagctggtt	tcctcaacacaatcccataa	aatcacctttcatcggagtg	tccacttccacaaattggta
cttctcagagtgcttgaact	atcttctcacatgttgggat	ggccattttgttctaagaca	gagatacttttctgggcttt
gcatcctagcttctataaga	aagcattgttggcttacagt	ttcaggcaaaccttattcgg	ccgcagatacttcagaatct
tggctctcagagcataaagg	gttccagtcagatgtttcaa	agcttgttctaccaggaatg	cccttatgcaatttaaccttt
ccttgtagactatatctgct	gttgacagtagtaccacaga	agatcattgctaggctcgaa	tgctgtagtcagccagaaaa
ttgaagctgccaaacagtca	tcccctcaacaacctaataa	ggcactgagataacatctgc	agagtttatatgcctgtctc
aatactgtgaatggcagcct	tgaaggtgtggctggaagat	ggccaaagggattagtactt	ttctcgtctactacgtctac
acagttacacagcatcttgt	accaacaaatggccttgttg	ttacctcagtcctattctaa	atacggtcttagttactgcg
gcaacaggatttggagagtt	tcatagcttcctatttaggt	cctccacaggtaaactacta	catgtacgagattctggtct
tgctccaattcttgttatct	accaaattgcctttcagttt	cttggttctagcttcagtat	gaccaacagtttatcagtgc
taagtcattatccaagtccc	attaataacactgtctcccc	agacttgtgccttttgttac	cttataatgctggggtggag
ggaatagcagcaccaagatc	ccctattgccaaatttagtg	ctctcaagttgctctcattg	gtccaactgttacagcagaa
aacagccatctattcattcc	ttccaagaaggtggctatga	tgccatgtgacctaagagaa	tgctgtagtcagccagaaaa
ggctcagatagtagcaatgt	aggcacttaattcactggtc	accattcacgatcacttagg	agagtttatatgcctgtctc
gctgtgtgagtaggaattct	tagtccatccttacactgaa	tttcacgctgacaagtggta	ttctcgtctactacgtctac
caaaagatcgccagcttctt	tggtcccagcaaatgaaagt	cctacagacctacacactaa	atacggtcttagttactgcg
agtgtcaggatcctgtgaaa	catgtgtcagcaatccaaga	acaacttgtggttaccatca	catgtacgagattctggtct
gtaatgcacaagacagctgc	tctctccttactgcttttaa	ttgaaagctggctacatggt	gaccaacagtttatcagtgc
cagcagtctacagcaacatg	cagtgactctagaatcctgt	tgctttcagatatctacctc	cttataatgctggggtggag
tatttaaggagctgcacagc	cgaacagagacaggcttgtt	ttctgaacaccttccaagtg	gtccaactgttacagcagaa

Table 5.1.1 Labeled oligonucleotides for smFISH. ***(continued)***

HMBS Exon	HMBS Intron	CDKN1A Exon	CDKN1A Intron
sequence (5'->3')	sequence (5'->3')	sequence (5'->3')	sequence (5'->3')
tacagtctgactcctggtct	atagacgactgaggatggca	catgggttctgacggacatc	cagagaggcccatcacaa
ttggaaagtaggctgtgtgt	tactggccctttaaaagcta	cattagcgcatcacagtcgc	ataacctctatccaccct
cattgccgttaccagacatg	ggtcactaaatctagagccg	tcgaagttccatcgctcacg	aaaggggtcacccagtac
gcgaatcactctcatctttg	gtagacgaacgttcttggtc	cagtggtgtctcggtgacaa	aaggccaaaggccactgc
gtctgtatgcgagcaagctg	cgcacttctaagacgtttgt	cgtgggaaggtagagcttgg	ccctgagtcatacagcta
ctgtggtggacatagcaatg	attcagtaggtgtgtcacag	gacagtgacaggtccacatg	ggtaacttcacaccaagt
gcagtatcaagaatcttgtc	caagcaggctcgtaatggaa	tgagcgaggcacaagggtac	ggttgggagaggaggctc
tttctctccaatcttagaga	tgcaagagcaaagatcccag	ttttcgaccctgagagtctc	cacagtttcacgtcccag
caagctccttggtaaacagg	tgaatgtgcacagcatatcc	gaaatctgtcatgctggtct	tgcttgtgatcagtggag
ccttcaaggagtgaacaacc	agaaaggactctaaggtccc	cttcctcttggagaagatca	ggggtgaaagctctgctg
cttcccaacaaattttgggt	tgatattaaacgtggccacc	agggtatgtacatgaggagg	agtcccaacttgcagttt
ttctctggcagggtttctag	cctttgcaaattaggctagg	actcttaggaacctctcatt	actggattttcctaggga
tgaactccagatgcgggaac	tccatgtgatcactccaata	cgggatgaggaggctttaaa	gagtgactgcacgacctt
ttgaggtttccccgaatact	gacagtagccactgtagata	gacaagtggggaggaggaag	gagagtgagtttgcccat
agcatacatgcattcctcag	ttcagtctaagacggaggtc	gtgacagcgatgggaaggag	cccttcaggagagggaaa
agatccaagatgtcctggtc	ttcactgctaagcacgtaga	ccaggaaaggggtgaattt	ttgcctgtgtccaaggaa
ctttcagcgatgcagcgaag	aatattaacaggccagagcc	cttcaaagtgccatctgttt	agtctagacacctggcag
cttcatagctgtatgcacgg	ctaaagttcgtgcacctaga	aaagtttttgatgatgcccc	tggcctaggggtaaggag
catggtctcttgtatgctat	gtggggaaagctgacagtat	caaccttagaggaggtgagg	tcccaaggatgtcgtcag
caactgtgggtcatcctcag	gtcaagaggatgaagatccc	ctaggctgtgctcacttcag	caggtgctgtaggctgag
cgtggaatgttacgagcagt	agtctaagagcagcaagctg	tatcaagagccaggagggta	cagttttactgagcctcc
aagttctgggcagccaactg	ctgagtcactggaggataga	ctgccttcacaagacagagg	tcacagagtccatgcagc
ggatgtttttggctcctttg	tgggtaaagagataaggccc	aaggctcaacactgagacgg	agcatggctacagacaca
ttaagctgccgtgcaacatc	tcagagtggggaaatactcc	aaggtacaggggagccaaag	taaccctgctctgccaag
ccacaaaccagttaatgggc	tgtttctagtgttcctcaac	gggtactgaagggaaaggac	acccagatccccaagtag
gtgagaatggggcactgagg	ccgtcactcttctaaaagga	ctgcctgaggtagaactagg	agtccagcagtttcctaa
ggtaatcactccccagatag	ctccgtcactcttccaaaag	ctaacacagagataacccca	ccctcatgggtgtgaatg
ttgaaccctgcagttcagtc	ctctagaccttgtctttttc	tctactcccccatcatatac	gtttgccaccaggtatta
gtgaggcaaatccctggaag	actgtaaatgagtggacgga	cagtgtctcccctcctagaaa	agagcaaggaccagggtc
cacatactgaggaggcaagg	tgtctggggctaagaaaaca	gaaggtcgctggacgatttg	agcaggcaactgaagggc
tgttgcttggacttctctaa	aatgccttgcactctgaaca	ttgttccgctgctaatcaaa	cacaccaaggtcactggg
	gtttatcttgctcaccatta	gccaccatcttaaaatgtct	acgtcttcctaccagagg
	aactctacatatgcagggaa	acgttagtgccaggaaagac	ttgctgtgtcacctcagg
	agtataactgcattatccct	ctccaagtacactaagcact	ctatgttacctggccggg
	cctccagaagtagtcactat	ccgagagaaaacagtccagg	gtcacggcggagattaga
	cacttattggagcacttagc		gagatacaaggaaggccc
	gtttccagaaaattcccaac		agtccttccgtgcacatg
	cttctgtgtttagatgttcc		agaatcctggtcccttac
	tgagaaaccttccctgacac		cccttggaccatggattc
	agagttgctaaggaccacag		ccatgggtctgctctaag
	atgagctggggagaggatag		ttatccatcaccgcaccc
	gggatgactgtaaggcagaa		catgcttcacagatgtga
	tggggtggtcaagaagtgaa		ggtattatggagtgtccc
	ctgattcacaatcttcccag		gtccactctgtctcttga
	catctagaaagcctgggtag		acaggaagaactcgggga
	tggcagtgagatgggagttc		aatggggccgactgctga
	gacacgggggtgtctaaaag		gaggaagacagtgggggg
	ggcggaacagggagtcaaaa		aagaagaggacgcggcgg

5.1.2. IMMUNOFLUORESCENCE STAINING AND COMPUTATIONAL IMAGE ANALYSIS

Irradiation and treatment with chemical inhibitors

$0.5x10^5$ cells/well were seeded in 12-well plates on high precision coverglasses (thickness #1) (Marienfeld GmbH, Lauda-Königshofen, GER) and cultured for 24 h in McCoy's 5A growth medium before experiments (GE Healthcare, Solingen, GER). At the indicated time-points after DNA damage, cells were fixed with 2% PFA (EM-grade) (Electron Microscopy Sciences, Hatfield, USA) in 1xPBS for 10 min at room temperature. Simultaneous to smFISH experiments, **γ**-irradiation was applied by a cesium-137 source. Inhibitor treatments were always performed in McCoy's 5A wild-type growth medium (GE Healthcare, Solingen, GER). Checkpoint kinase-2 inhibitor II BML-277 (Sigma Aldrich, St. Louis, USA) was applied at 10 µM final concentration at 4 h after **γ**-irradiation. Nutlin-3 was used at final concentrations of 0.75 µM, 2.25 µM and 4 µM and applied with increasing concentration at 2.5 h, 3.5 h and 5.5 h after **γ**-irradiation (#N6287, Sigma Aldrich, St. Louis, USA). ATM inhibitor KU-55933 (Axon Medchem) was used at 10 µM final concentration and added jointly with 10 µM BML-277 at 4 h after **γ**-irradiation in immunofluorescence experiments to detect p53 levels in SetD8 and Smyd2 knock-down cells lines.

Immunofluorescence staining

Cells were permeabilized with 0.1% (v/v) Triton X-100 (Carl Roth GmBH, Karlsruhe, GER) in 1xPBS and blocked with 10% (v/v) goat serum (PAN-Biotech GmbH, Aidenbach, GER). Cells were then incubated with respective antibodies over night at 37°C. All used antibodies and commercial suppliers can be found below. Concentrations used were based on manufacturers instructions. Cells were washed with 1x PBS and incubated with the secondary antibody coupled to Alexa Fluor 647/488 (Molecular Probes/Life technologies, Carlsbad, USA), and washed again. Finally, they were stained with 2 µg/mL Hoechst 33342 (Molecular Probes/Life technologies, Carlsbad, USA) in 0.1% (v/v) Triton X-100 in 1xPBS for 10 min in the dark. Coverglasses were mounted on 15 µL Prolong Gold Antifade (Molecular probes/Life technologies, Carlsbad, USA) and surrounded by transparent nail polish to avoid moving. Slides were stored at 4°C until imaging and imaged usually 4 h after mounting.

Antibodies used for immunofluorescence stainings

anti p53 DO-1 (mouse), Santa Cruz Biotechnology #sc-126
anti p53 Fl393 (rabbit), Santa Cruz Biotechnology #sc-6243
p53 phospho-Ser15 (rabbit), Cell Signaling Technologies #9284
p53 phospho-Ser46 (rabbit), Cell Signaling Technologies #2521
Chk1 phospho-Ser317 (rabbit), Cell Signaling Technologies #2344
Chk2 phospho-Thr68 C13C1 (rabbit), Cell Signaling #2197
anti rabbit Alexa Fluor 488 (goat), Life Technologies #A-11034

anti rabbit Alexa Fluor 647 (goat), Life Technologies #A-21245
anti mouse Alexa Fluor 488 (goat), Life Technologies #A-11029
anti mouse Alexa Fluor 647 (goat), Life Technologies #A-21236

Fluorescence microscopy imaging and quantification of antibody stained cells
The used microscopy set-up was identical to the above mentioned for smFISH. Images were acquired with a 20× Plan Apo objective (NA 0.75) using appropriate filter sets (Hoechst: 387/11 nm excitation (EX), 409 nm dichroic beam splitter (BS), 447/60 nm emission (EM); Alexa Fluor 647: 640/30 nm (EX), 660 nm (BS), 690/50 nm (EM)). Images were acquired as multi-point datasets. Automated segmentation of nuclei and quantitive analysis of p53 levels based on integrated intensity of the fluorescence signal in each nucleus was performed in *MATLAB* (MathWorks, Natick, USA) using custom written software based on previously published algorithms from *CellProfiler* (Carpenter et al., 2006). The quantification is based on integrated intensities of antibody staining in the nuclear area of A549 cells before (basal) and 3 h, 6 h, 9 h after 10 Gy of γ-IR.

5.1.3. DNA FISH

Probe synthesis
Probes were amplified from genomic DNA using custom designed primers (see below). Probes were labelled using the PCR DIG probe Synthesis (Hoffmann-La Roche, Basel, Switzerland). For detection, five reactions were pooled after labelling. Before use, probes were denaturated for 10 min at 70°C and then kept on ice until incubation.

DNA FISH staining protocol
Cells were grown on high precision coverslips #1 and fixed with 2% para-formaldehyde, then washed with PBS and 2x SSC following RNAse A incubation for 2 h. Afterwards a 70% formamide shock/2xSSC was applied for 5 min to reduce secondary structures. The DNA was denaturated for 10 min at 80°C. Afterwards, cells were rinsed in 50% formamide/ 2xSSC, washed with 1xPBS and incubated with denaturated probe for 72 h in a humidified chamber sealed with rubber cement on a hybridization slide (Thermo Fisher Scientific, Waltham, MA, USA). Cells were then washed with 50% formamide/2xSSC at 42°C, 0.1%SCC at 60°C and 4x SSC/0.1% Tween at 42°C and PBS. To detect DIG labelled DNA probes, anti-DIG antibody (sheep) (Hoffmann-La Roche, Basel, Switzerland; #11333089001) was used and visualized via secondary staining with anti-sheep IgG (donkey)- Alexa Fluor 647 (Thermo Fisher Scientific, Waltham, USA, #A-21448). Finally, cells were stained with 2 µg/mL Hoechst 33342 (Molecular Probes) in 1x PBS for 10 min in the dark and mounted in 15 µL Prolong Gold Antifade (Thermo Fisher Scientific, Waltham, MA, USA).

Primer sequences (5'-3')
1. GTGTGCTGGGAGTCAGATTC (fwd), GTCACCTCTCCCAGAAGCAC (rev)

2. CAGCTGCATTGGGTAAATCC (fwd), GCTCTCATAGGCCTCTCCTC (rev
3. GCTAGTTGCCCAGGCTAGTC (fwd), TGGTCTACCTGGCTCCTCTC(rev)
4. TGGCTGACTTCTGCTGTCTC (fwd), GCTTGGCACTGTCAGTC (rev)
5. AAGTGCTGCTGGCACGTTAC (fwd), ACAGCCGTATGTGGCTCGTG (rev)

Antibodies for DNA FISH probe detection

anti-sheep IgG (donkey)- Alexa Fluor 647 #A-21448 (Thermo Fisher Scientific)
anti-DIG (sheep) #11333089001 (Hoffmann-La Roche)

5.1.4. DISTRIBUTION STATISTICS AND DATA REPRESENTATION

The statistical comparison of single-cell distributions from different datasets was performed by employing the DABEST package (Ho et al., 2019). Therefore, either the online tool (http://www.estimationstats.com/) or the *MATLAB* package was used to calculate confidence intervals. A detailed description for each analysis is found in the respective figures displaying the respective plots. Accordingly, statistical comparisons are based on effect size measurements of the paired sets of distributions. The median difference between datasets is represented in a Gardner-Altman plot, with the median difference plotted on a floating axis as a bootstrap sampling distribution. The median difference is depicted as a dot, while the 95% confidence interval (CI) is indicated by the ends of the error bar. 5000 bootstrap samples were taken; the CI is bias-corrected and accelerated. The p-values are the likelihoods of observing the effect sizes, if the null hypothesis of zero difference is true (Ho et al., 2019). The fractions of active promoters are represented as stacked bargraphs with low and high transcriptional activity. Therefore, the transcriptional activity was binned dependent on the number of active TSS. Bins were kept constant for all analyzed datasets of one target gene. Bins by target gene were as follows. SESN1: 1 TSS (shaded), 2 TSS (solid); MDM2: 1-2 TSS (shaded), 3 TSS (solid); CDKN1A: 1 TSS (shaded), >1 (solid), BAX/PPM1D/DDB2: 1-2 TSS (shaded), 3-4 TSS (solid); RRM2B: 1-3 TSS (shaded), 4-5 TSS (solid). In boxplots, whisker represent 25th to 75th percentile. Notches display interval endpoints. If notches do not overlap, they represent a significance at the 5% confidence level. Outliers are not displayed. For plotting single-cell distributions of RNA spots as well as transcription rates and comparing time-points, the *MATLAB* function *ksdensity* was employed. *Ksdensity* is a Kernel smoothing function to estimate univariate and bivariate data. It returns a probability density estimate based on a normal kernel function, and is evaluated at equally-spaced points covering the range of the data. The kernel probability density estimate is a nonparametric representation of the probability density function (pdf). This is used to avoid making assumptions about the distribution of the data *(MATLAB* online documentation, MathWorks, Natick, USA). For better comparison with density functions in other Figure panels, also a distribution smoothing function is fitted to histograms, e.g. representing RNA counts per cell (Figure 3.2.2.A). For visualization in Figure panels, selected images of individual cells were extracted from raw data, maximum projected, median filtered and contrast enhanced, as described in the respective figure captions.

5.2. LIVE-CELL IMAGING AND KNOCK-DOWN CELL LINES

5.2.1. GENERATION OF P53-MVENUS REPORTER CELLS AND IMAGE ANALYSIS

Lentiviral constructs and infection

Lentiviral reporter constructs were generated for p53 and H2B using the MultiSite Gateway recombination system (Thermo Fisher Scientific, Waltham, MA, USA) as described previously for MCF10A cells (Strasen et al., 2018). The p53 coding sequence was fused to the yellow fluorescent protein mVenus (YFP) under the control of a constitutive human EF1a promoter. A549 cells were infected with corresponding lentiviral particles. Additionally, viral particles of histone 2B fused to cyan fluorescent protein (H2B-CFP) under the control of UbCp as a nuclear marker was used from a previous study (Strasen et al., 2018).

Stable clonal cells and validation

DNA clones were analyzed by restriction digestion before generating lentiviral particles in 293T cells. A549 cells were cultured in McCoy's medium (GE Healthcare, Solingen, GER) supplemented with 10% (v/v) fetal bovine serum, 2 mM Glutamax (Thermo Fisher Scientific, Waltham, MA, USA), 100 U/mL Penicillin and 100 µg/mL Streptomycin (Thermo Fisher Scientific, Waltham, MA, USA). 24 hours after infection, the growth medium was supplemented with 50 µg/mL Hygromycin B (Thermo Fisher Scientific, Waltham, MA, USA) and 400 µg/mL G418 (Carl Roth GmBH, Karlsruhe, GER) to selectively screen for cells that contain both reporters and thus exhibit antibiotic resistance from expression of each transgene. After one week, limited dilution cloning was performed in 96-well plates to gain single clone populations. Cells were under antibiotic control whenever cultured to maintain resistance, while experiments were performed in imaging medium (DMEM/Fluorobrite) (Thermo Fisher Scientific, Waltham, MA, USA) without antibiotics. Single clones were passaged and duplicated for screening by fluorescence microscopy. Based on this, ten clones were selected and expanded. These were then screened for fluorescence intensity values in absence and presence of DNA damage and their nuclear p53 dynamics were compared to previously obtained reporters.

Live-cell time lapse microscopy of p53

A549 reporter cells with both p53-mVenus and H2B-CFP nuclear marker for automated cell tracking were used for live-cell time-lapse microscopy in a custom chamber for up to 24 h at 5% CO_2 and 37°C as stable imaging conditions. Therefore, 1.5×10^5 cells were plated in 35 mm poly-D-lysine-coated glass bottom plates two days prior to experiments (MatTek, Ashland, MA, USA or Ibidi GmbH, Gräfelfing, GER). Before imaging, cells were washed with 1×PBS to remove phenol-red and the growth medium was exchanged to DMEM/Fluorobrite imaging medium (Thermo Fisher Scientific, Waltham, MA, USA) supplemented with 10% (v/v) FBS and 100 U/mL Penicillin and 100 µg/mL Streptomycin (Thermo Fisher Scientific, Waltham, MA, USA). The imaging medium was buffered by 10 mM HEPES

(Thermo Fisher Scientific, Waltham, MA, USA). Cells were imaged on a Nikon Ti-E inverted fluorescence microscope (Nikon instruments, Tokyo, JPN) with a Hamamatsu Orca R2 camera or an EMCCD camera (ANDOR, DU iXON Ultra 888), a Lumen 200 Fluorescence Illumination System (Prior Scientific, Cambridge, UK). A 20× Plan Apo objective (NA 0.75) and appropriate filter sets (mVenus: 500/20 nm excitation (EX), 515 nm dichroic beam splitter (BS), 535/30 nm emission (EM); eCFP: 436/20 nm EX, 455 nm BS, 480/40 nm EM) were used for live-cell imaging experiments. Images were acquired as single planes every 10 min for 24 h in a multipoint experiment with automating time-point specific stage positioning using the Nikon (NIS) Elements software.

Automated tracking of cells and analysis of p53 dynamics

Automated segmentation of nuclei and quantitive analysis of p53 levels was performed in *MATLAB* (MathWorks, Natick, USA) using custom written software as previously described (Strasen et al., 2018) based on code developed by the Alon laboratory (Cohen et al., 2008) and the *CellProfiler* project (Carpenter et al., 2006). Flat field correction and background subtraction was applied to raw images before segmenting individual nuclei from image planes of the H2B-CFP nuclear marker. For segmentation, thresholding and seeded watershed algorithms were used. Segmented cells were then assigned to corresponding cells in following images using a greedy match algorithm (Strasen et al. 2018). Only cells tracked from the first to last time-point were considered for quantitative analysis. For the presented experiments, cells were only tracked in forward direction from the first to the last time-point. The integrated nuclear fluorescence intensity was used to extract p53 abundance and generate single-cell trajectories between individual cells at the different measurement time-points. Single-cell trajectories were normalized to the first time-point to gain fold change differences.

5.2.2. STABLE SETD8/SMYD2 KNOCK-DOWN CELL LINES

Lentiviral constructs and infection

Stable SetD8/Smyd2 knock-down cell lines were generated by lentivirus transduction. Therefore, previously published shRNA vectors were used to generate Smyd2 and SetD8 knock down cells. I used shRNAs targeting Smyd2 and SetD8 employing expression of specific oligonucleotides from pRetroSuper.puro as previously described (Brummelkamp et al., 2002a; Loewer et al., 2010). VSV-G pseudotyped retroviral particles expressing SETD8 shRNA or p53 shRNA (Brummelkamp et al., 2002b) were produced in 293T cells and subsequently used to infect A549 wild-type cells.

Stable cell lines and knock-down validation

A549 cells were cultured in McCoy's medium (GE Healthcare, Solingen, GER) supplemented with 10% fetal bovine serum, 100 U/mL Penicillin and 100 µg/mL Streptomycin (Thermo Fisher Scientific, Waltham, MA, USA). 0.5 µg/mL Puromycin dihydrochloride (Carl Roth GmBH, Karlsruhe, GER) was added to the growth medium to screen for infected cells. Cells were used as polyclonal populations in further experiments.

The level of Smyd2 and SetD8 knock-down was validated by qRT-PCR using specific primers (Chapter 5.3.1). For experiments, cells were seeded identical to A549 wild-type cells, as described in the respective paragraphs and were therefore seeded in growth medium without antibiotics during experiments.

5.2.3. CAS9-BASED GENERATION OF MS2 REPORTER CELLS AND IMAGE ANALYSIS

Lentiviral constructs and infection

Both H2B-CFP and the MS2 binding protein MCP were integrated as transgenic reporters to cells as described before (Chapter 5.2.1/2). Lentiviral reporter constructs were generated for MCP and H2B using the MultiSite Gateway recombination system (Thermo Fisher Scientific, Waltham, MA, USA). The MCP coding sequence was amplified from Addgene plasmid #40649 using optimized primers for Gateway cloning and fused to the yellow fluorescent protein mVenus (YFP) under the control of a constitutive human EF1a promoter. Additionally, the Puromycin resistance was used to allow screening for positive clones based on antibiotic selection. UbCP-H2B-eCFP lentiviral particles, where used from previous experiments as described in Chapter 5.2.1 to gain a nuclear marker based on selection for 50 µg/mL Hygromycin (Thermo Fisher Scientific, Waltham, MA, USA) resistance.

Crispr/Cas9 repair templates

Crispr/Cas9 based cell line generation of MS2 knock-in cell lines was performed based on protocols from a previous study (Sheng et al., 2019; Sheng, 2018). Cas9, Cas9n and sgRNA cloning vectors (Addgene plasmid #41815, #41816, #41824) were gifts from the Church lab (Mali et al., 2013). The sgRNA cloning vector was modified as previously described by inserting about 80 base pairs and an AgeI site (Sheng, 2018) and guide sequences were selected using the CRISPR online tool for sgRNA design (http://crispr.mit.edu). Targeting efficiency of sgRNAs for CDKN1A and MDM2 3' was tested previously (Sheng, 2018) using the T7 endonuclease assay (New England Biolabs Inc., Ipswitch, USA) in HEK293T cells (Ran et al., 2013). Repair templates were generated using Gibson Assembly Mix (New England Biolabs Inc., Ipswitch, USA). For cloning of MS2 repair templates, two different MS2 sequences were used. In an initial trial, the 24x MS2 repeat sequenced, from Addgene plasmid #40651 was used. In a following approach, a newer version (24x MS2v5) was used (Wu et al., 2015). The plasmid was a gift from the Singer lab. A repair template was cloned into pAAV vector backbone, including a Neomycin (Neo) resistance gene to allow for selection of positive clones based on treatment with G418. Homology arms of the flanking 5' and 3' regions differed in length. The general reporter structure was $HA_{\textit{left}}$-24xMS2v5-p2A-Neo-$HA_{\textit{right}}$. To remove the antibiotic resistance later on p2A-Neo was flanked by Cre/locP sites.

Cas9 based genomic integration

For knock-in, MCF10A cells were cultured in MCF10A cells were cultured in Dulbecco's

Modified Eagle Medium/Nutrient Mixture F-12 (DMEM-F12) (Gibco/ Thermo Fisher Scientific, Waltham, MA, USA) supplemented with 5% (v/v) horse serum (PAN-Biotech GmbH, Aidenbach, GER), 20 ng/mL EGF (PeproTech, Hamburg, GER), 0.5 µg/mL Hydrocortisone (Sigma Aldrich, St. Louis, USA), 100 ng/mL Cholera-toxin (Sigma Aldrich, St. Louis, USA) and 10 µg/mL Insulin (Sigma Aldrich, St. Louis, USA) according to previously published protocols with 2 mM Glutamax (Thermo Fisher Scientific, Waltham, MA, USA), 100 U/mL Penicillin and 100 µg/mL Streptomycin (Thermo Fisher Scientific, Waltham, MA, USA) (Debnath et al., 2003). MCF10A cells were seeded in 12-well plates at $2.5x10^5$ cells/well density, 24 h before transfection with 495 ng Cas9, 495 ng sgRNA and 10 ng linearized repair template DNA. Cells were transfected for 24 h using Lipofectamine 3000 (Thermo Fisher Scientific, Waltham, MA, USA) according to manufacturers protocols. Cells were then seeded into 10 cm culturing plates using growth medium supplemented with 400 µg/mL G418 (Carl Roth GmBH, Karlsruhe, GER). Approximately two weeks after seeding, individual clones were picked directly from the 10 cm plate, passaged and screened for the genomic insertion of MS2 by direct PCR using the Phire Animal Tissue Direct PCR Kit (Thermo Fisher Scientific, Waltham, MA, USA) according to manufacturer's instructions.

Live-cell time lapse microscopy and image processing of MS2 reporter cells

MCF10A MS2 reporter cells with MCP-mVenus and H2B-CFP nuclear marker were used for live-cell time-lapse microscopy in a custom chamber for up to 24 h at 5% CO_2 and 37°C as stable imaging conditions. 1.5×10^5 cells were plated in 35 mm glass bottom plates two days prior to experiments (MatTek, Ashland, MA, USA). Before imaging, cells were washed with 1×PBS to remove phenol-red and the medium was changed to DMEM/Fluorobrite (Thermo Fisher Scientific, Waltham, MA, USA) supplemented with 5% (v/v) Horse Serum and 100 U/mL Penicillin, 100 µg/mL Streptomycin (Thermo Fisher Scientific, Waltham, MA, USA), buffered by 10 mM HEPES (Thermo Fisher Scientific, Waltham, MA, USA). The microscopy set-up was identical to the before-mentioned experiments. The EMCCD camera (ANDOR, DU iXON Ultra 888) and 60× or 100x plan apo oil objectives (NA 1.4) with appropriate filter sets (mVenus: 500/20 nm excitation (EX), 515 nm dichroic beam splitter (BS), 535/30 nm emission (EM); eCFP: 436/20 nm EX, 455 nm BS, 480/40 nm EM) were used for detection. Images were acquired every 90-150 sec for up to 12 h. Nine 300 nm z-planes per time-point were imaged. For analyzing transcription site activity from MS2 based live-cell imaging data, z-planes were maximum projected. Projected stacks were not further processed for analysis. Tracking of TSS based on MS2 signals was performed using the manual tracking plug-in in FIJI (Cordelieres, 2004; Schindelin et al., 2012). Post-processing of fluorescence intensity data was performed as described in Chapter 3.5.1/2 based on custom scripts in *MATLAB*. When image aberrations appeared due to technical reasons at an individual time-point, values were interpolated from the preceding measurement time-point. For visualizations in Figure panels, images of individual cells were extracted, median filtered and contrast enhanced. Gaussian filtering was applied to optimize visibility.

5.3. FURTHER TECHNIQUES

5.3.1. QUANTITATIVE REAL-TIME PCR

RNA extraction, reverse transcription and quantification

$1x10^5$ cells were seeded two days prior to the experiment in 5 cm culture dishes. RNA was extracted at the indicated time-points using the High Pure RNA Isolation kit (Hoffmann-La Roche, Basel, Switzerland). CDNA was generated from 1 µg or 500 ng extracted RNA using M-MuLV or Protoscript II reverse transcriptase and Oligo-dT primers (both New England Biolabs Inc., Ipswitch, USA) and SYBR Green reagent (Applied Biosystems/Thermo Fisher Scientific, USA; Merck, Darmstadt, GER) on a CFX96 PCR machine (Bio-Rad, Feldkirchen, GER) or a StepOnePlus PCR machine (Applied Biosystems/Thermo Fisher Scientific, USA). The final concentration of used primers was 243.2 nM.

Primer sequences (5'-3')

β-ACTIN forward	GGCACCCAGCACAATGAAGATCAA
β-ACTIN reverse	TAGAAGCATTTGCGGTGGACGATG
SETD8 forward	CCCTTCCACGGGCTGCTAC
SETD8 reverse	GTGCAGTTTGGTTTGGCAGTTCC
SMYD2 forward	CCTCAACGTGGCCTCCATGTG
SMYD2 reverse	TGGATGATCTTTGCCGTGAGCTAC
HMBS forward	CTGTTTACCAAGGAGCTGGAAC
HMBS reverse	TGAAGCCAGGAGGAAGCA
HPRT1 forward	GACCAGTCAACAGGGGACAT
HPRT1 reverse	CCTGACCAAGGAAAGCAAAG
PUM1 forward	CAGGCTGCCTACCAACTCAT
PUM1 reverse	GTTCCCGAACCATCTCATTC
SDHA forward	TGGTTGTCTTTGGTCGGG
SDHA reverse	GCGTTTGGTTTAATTGGAGGG
HER2 forward	TGACACCTAGCGGAGCGA
HER2 reverse	GGGGATGTGTTTTCCCTCAA

5.3.2. WESTERN BLOT

Protein purification, electrophoretic separation and blotting

Cells were plated 2 days before experiments in 6 cm dishes at $5x10^5$ cell density. After γ-IR, cells were harvested at indicated time-points and proteins were isolated by lysis in the presence of protease and phosphatase inhibitors (Carl Roth GmBH, Karlsruhe, GER and Sigma Aldrich, St. Louis, USA), Trichostatin A (APExBio) and Deacetylase Inhibitor Cocktail (MedChemExpress). Total protein concentrations were measured by Bradford assay (Carl Roth GmBH, Karlsruhe, GER). Equal amounts of protein were separated by electrophoresis on NuPAGE 4-12% Bis-Tris Gels (Invitrogen/ Thermo Fisher Scientific, Carlsbad USA) and transferred to PVDF membranes (GE Healthcare, Solingen, GER) by electroblotting (Bio-Rad, Feldkirchen, GER).

Immunodetection and quantification

Membranes were blocked with 5% (w/v) bovine serum albumin (BSA) in TBS-T and incubated overnight with primary antibody. Used concentrations were dependent on manufacturer's instructions. The next day, membranes were washed with TBS-T, incubated with secondary antibody coupled to peroxidase, washed again, and protein levels were determined using chemoluminescence (Western Bright Quantum, Advansta). Precision Plus Protein Dual Color Standard (Bio-Rad, Feldkirchen, GER) was used for molecular mass comparison. GAPDH and acetylated p53 were detected on the same membrane. To detect total p53 levels, antibodies were stripped and detection was performed as described above after blocking again with 5% (w/v) BSA . Blots were quantified using FIJI (Schindelin et al., 2012).

Used antibodies:

anti-GAPDH (Sigma Aldrich, St. Louis, USA, G9545
anti-p53 (Santa Cruz Biotechnology, Dallas, USA, #DO1 Cell Signaling, #9282
anti-p53K70ac (abcam, ab183544)
anti-p53K382ac (abcam, ab75754)
goat-anti-rabbit-HRP (Thermo Fisher Scientific, Waltham, MA, USA)
goat-anti-mouse-HRP (Thermo Fisher Scientific, Waltham, MA, USA).

5.3.3. CHROMATIN IMMUNO-PRECIPITATION (CHIP) ASSAYS

ChIP experiments were performed by Laura Friedel. A549 cells were seeded to $1.6x10^7$ density. First, plates were washed once with 1xPBS and fixed for 10 min with 1% formaldehyde. After washing once with cold 1xPBS, cells were incubated for 5 min in 1x PBS with 125 mM Glycine and washed again with cold 1x PBS. For harvesting, 1xPBS with 1 mM PMSF was used. To lyse samples, they were incubated for 20 min with 5 mM Tris-HCl, 85 mM KCl, 0.5% (v/v) Igepal with protease inhibitor cocktail (Carl Roth GmBH, Karlsruhe, GER) and 1 mM PMSF. Nuclei pellets were then separated by centrifugation and resuspended in 50 mM Tris-HCl, 0.3% SDS (w/v), 10 mM EDTA with 1 mM PMSF and Protease Inhibitor Cocktail for 30 min on ice. Chromatin was then crosslinked using the Covaris S220 Sonicator (PIP 105, Duty Factor 2%, CPB 200, 2 min) and afterwards separated by centrifugation. 80 µg for each sample were diluted in 16.7 mM Tris-HCl, 167 mM NaCl, 0.01% SDS (w/v), 1.2 mM EDTA, 1.1% Triton X-100 (v/v) buffer with 1 mM PMSF and protease inhibitor cocktail. Samples were then incubated overnight at 4°C with 5 µg specific antibody (p53 Fl-393, H3K27ac, H3K27me), or a control IgG (rabbit IgG, EMD Millipore). To collect Immunocomplexes, samples were incubated for 2 h at 4 °C with 25 µL Dynabeads Protein G (Thermo Fisher Scientific, Waltham, MA, USA) on the next day and then beads were washed with four buffers. First, with 0.1% SDS (w/v), 2 mM EDTA, 20 mM Tris–HCl, 1% Triton X-100 (v/v). Second, with 150 mM NaCl, then with 0.1% SDS (w/v), 2 mM EDTA, 20 mM Tris–HCl, 1% Triton X-100 (v/v), 500 mM NaCl. Third, with 10 mM Tris-HCl, 1 mM EDTA, 1% IGEPAL (v/v), 1% Deoxycholic acid (w/v), 250 mM

LiCl and last with 10 mM Tris-HCL, 1 mM EDTA buffer. The DNA was then eluted twice for 30 min at 37°C in 1% SDS (w/v), 1 mM $NaHCO_3$ buffer and crosslinks were reversed by adding 200 mM NaCl and incubation at 65°C overnight. Samples were incubated with 50 µg/mL RNase A for 10 min at 37°C and incubated with 100 µg/mL Proteinase K, 10 mM EDTA and 40 mM Tris-HCl buffer for 3 h at 45°C. Finally, the DNA was purified using the Monarch PCR & DNA Cleanup Kit (New England Biolabs Inc., Ipswitch, USA) and 3 µL of each sample was used for qRT-PCR.

Primer sequences (5'-3')

BAX forward	AACCAGGGGATCTCGGAAG
BAX reverse	AGTGCCAGAGGCAGGAAGT
MDM2 forward	GTTCAGTGGGCAGGTTGACT
MDM2 reverse	CGGAACGTGTCTGAACTTGA
CDKN1A forward	AGCCTTCCTCACATCCTCCT
CDKN1A reverse	GGAATGGTGAAAGGTGGAAA
DDB2 forward	CTCCAAGCTGGTTTGAAC
DDB2 reverse	CACAGGTAGCCGAGCTAAG
SESN1 forward	GCCGCGGTCATGTAAATGAAAG
SESN1 reverse	GACTTGTCCAGACGACAATG
RRM2B forward	GCTTGCTGGGAAATCTTGAC
RRM2B reverse	CTGGTCACCCAGTTGGAAG
PPM1D forward	CGGACAAGTCCAGACATC
PPM1D reverse	TTCGACGACGCCGAGAAG

5.3.5. RNA-SEQ META-ANALYSIS

As previously described by Finzel, 2016 RNA sequencing and processing of raw data was performed as follows in a previous study (Finzel, 2016a): RNA quality was analyzed with the Agilent RNA 6000 Nano Kit, and concentration was measured using the Qubit RNA Assay Kit (Invitrogen/ Thermo Fisher Scientific, Carlsbad, USA). Library preparation was carried out with the TruSeq RNA Preparation Kit (Illumina Inc., Sand Diego, USA) using barcoded primers. Libraries were sequenced on a Illumina Hi-Seq (Illumina Inc., Sand Diego, USA) with a single read protocol (1×100 nt). For data analysis p53 target genes from previously published ChIP- and RNA-Seq data were used (Nikulenkov et al., 2012; Menendez et al., 2013).

For meta-analysis, first all genes with less than 1.0 RPKM under basal conditions in A549 wild-type cells or 0.0 RPKM under other conditions were removed, as well as all genes that showed a mean RPKM fold-change of 0.75-1.25, indicating no up- or down-regulation upon DNA damage by IR. This led to a subset of 2161 genes. Of those, 636 genes were down-regulated by >0.25 fold and 1523 were up-regulated by >1.5 fold. All genes that showed a difference between knock-down and wild type conditions between 0.75 and 1.25 fold at 4 h and 0 h, indicating that the p53 knock-down did not affect gene expression regulation were removed. Based on this, 71 genes were found to be down-regulated. Similarly, genes that showed an opposing effect, being down-regulated in knock-down by more than 25%, while being up-regulated in wild-type condition by less then 25%, were excluded. This filtering led

to a set of 184 up-regulated target genes, leading to 255 targets that are regulated by p53. To identify genes that are overlapping in all three datasets (Finzel, 2016a; Fischer, 2017 and Hafner et al. 2017), the list of up-regulated genes as depicted in Table 8.3.1 was compared with 183 up-regulated target genes that showed >2.0 fold change 4 h after 10 Gy in MCF7 cells (Hafner et al., 2017) and 127 up-regulated genes with a score of or above 6 in the curated target gene list by Fischer, 2017.

CHAPTER 6 BIBLIOGRAPHY

6.1. REFERENCES A-Z

References are listed in alphabetical order, based on the last name of the first author. Inside the main text, citations are labelled by the last name of the first author and the year of publication.

Abudayyeh, O.O., Gootenberg, J.S., Essletzbichler, P., Han, S., Joung, J., Belanto, J.J., Verdine, V., Cox, D.B.T., Kellner, M.J., Regev, A., et al. (2017). RNA targeting with CRISPR-Cas13. Nature *550*, 280–284.

Ahsendorf, T., Wong, F., Eils, R., and Gunawardena, J. (2014). A framework for modelling gene regulation which accommodates non-equilibrium mechanisms. BMC Biol. *12*, 102.

Allen, B.L., and Taatjes, D.J. (2015). The Mediator complex: a central integrator of transcription. Nat. Rev. Mol. Cell. Biol. *16*, 155–166.

An, W., Kim, J., and Roeder, R.G. (2004). Ordered Cooperative Functions of PRMT1, p300, and CARM1 in Transcriptional Activation by p53. Cell *117*, 735–748.

Appella, E., and Anderson, C.W. (2001). Post-translational modifications and activation of p53 by genotoxic stresses. Eur. J. Biochem. *268*, 2764–2772.

Arbel-Goren, R., Tal, A., and Stavans, J. (2013). Phenotypic noise: effects of post-transcriptional regulatory processes affecting mRNA. WIREs RNA *5*, 197–207.

Ardehali, M.B., and Lis, J.T. (2009). Tracking rates of transcription and splicing *in vivo*. Nat. Struc. Mol. Biol. *16*, 1123–1124.

Asano, S.M., Gao, R., Wassie, A.T., Tillberg, P.W., Chen, F., and Boyden, E.S. (2018). Expansion Microscopy: Protocols for Imaging Proteins and RNA in Cells and Tissues. Curr. Protoc. Cell Biol. *80*, e56.

Avalos, J.L., Celic, I., Muhammad, S., Cosgrove, M.S., Boeke, J.D., and Wolberger, C. (2002). Structure of a Sir2 enzyme bound to an acetylated p53 peptide. Mol. Cell *10*, 523–535.

Aylon, Y., Ofir-Rosenfeld, Y., Yabuta, N., Lapi, E., Nojima, H., Lu, X., and Oren, M. (2010). The Lats2 tumor suppressor augments p53-mediated apoptosis by promoting the nuclear proapoptotic function of ASPP1. Genes Dev. *24*, 2420–2429.

Bahar Halpern, K., Caspi, I., Lemze, D., Levy, M., Landen, S., Elinav, E., Ulitsky., I., and Itzkovitz, S. (2015a). Nuclear Retention of mRNA in Mammalian Tissues. Cell Rep. *13*, 2653–2662.

Bahar Halpern, K., Tanami, S., Landen, S., Chapal, M., Szlak, L., Hutzler, A., Nizhberg, A., and Itzkovitz, S. (2015b). Bursty Gene Expression in the Intact Mammalian Liver. Mol. Cell *58*, 147–156.

Bahar Halpern, K., and Itzkovitz, S. (2016). Single molecule approaches for quantifying transcription and degradation rates in intact mammalian tissues. Methods *98*, 134–142.

Balázsi, G., van Oudenaarden, A., and Collins, J.J. (2011). Cellular Decision Making and Biological Noise: From Microbes to Mammals. Cell *144*, 910–925.

Bar-Even, A., Pualsson, J., Meheshri, N., Carmi, M., O'Shea, E., Pilpel, Y., Barkai, N. (2006). Noise in protein expression scales with natural protein abundance. Nat. Gen. *38*, 636-643.

Barlev, N.A., Liu, L., Chehab, N.H., Mansfield, K., Harris, K.G., Halazonetis, T.D., and Berger, S.L. (2001). Acetylation of p53 activates transcription through recruitment of coactivators/histone acetyltransferases. Mol. Cell *8*, 1243–1254.

Bartman, C.R., Hamagami, N., Keller, C.A., Giardine, B., Hardison, R.C., Blobel, G.A., and Raj, A. (2019). Transcriptional Burst Initiation and Polymerase Pause Release Are Key Control Points of Transcriptional Regulation. Mol. Cell *73*, 519–532.

Bartman, C.R., Hsu, S.C., Hsiung, C.C.-S., Raj, A., and Blobel, G.A. (2016). Enhancer Regulation of Transcriptional Bursting Parameters Revealed by Forced Chromatin Looping. Mol. Cell *62*, 237–247.

Batchelor, E., Loewer, A., Mock, C., and Lahav, G. (2011). Stimulus-dependent dynamics of p53 in single cells. Mol. Syst. Biol. *7*, 1–8.

Batchelor, E., Mock, C.S., Bhan, I., Loewer, A., and Lahav, G. (2008). Recurrent initiation: A mechanism for triggering p53 pulses in response to DNA damage. Mol. *30*, 277–289.

Battich, N., Stoeger, T., and Pelkmans, L. (2013). Image-based transcriptomics in thousands of single human cells at single-molecule resolution. Nat. Methods *10*, 1127–1133.

Battich, N., Stoeger, T., and Pelkmans, L. (2015). Control of Transcript Variability in Single Mammalian Cells. Cell *163*, 1596–1610.

Beckerman, R., and Prives, C. (2010). Transcriptional regulation by p53. Cold Spring Harb. Perspect. Biol. *2*, a000935.

Becskei, A., Kaufmann, B.B., and van Oudenaarden, A. (2005). Contributions of low molecule number and chromosomal positioning to stochastic gene expression. Nat. Genetics *37*, 937–944.

Ben-David, U., Siranosian, B., Ha, G., Tang, H., Oren, Y., Hinohara, K., Strathdee, C.A., Dempster, J., Lyons, N.J., Burns, R., et al. (2018). Genetic and transcriptional evolution alters cancer cell line drug response. Nature *560*, 325–330.

Bensaude, O. (2011). Inhibiting eukaryotic transcription. Which compound to choose? How to evaluate its activity? Transcription *2*, 103–108.

Bentley, D.L. (2014). Coupling mRNA processing with transcription in time and space. Nat. Rev. Genet. *15*, 163–175.

Berger, S.L. (2010). Keeping p53 in Check: A High-Stakes Balancing Act. Cell *142*, 17–19.

Bertrand, E., Chartrand, P., Schaefer, M., Shenoy, S.M., Singer, R.H., and Long, R.M. (1998). Localization of ASH1 mRNA particles in living yeast. Mol. Cell *2*, 437–445.

Blake, W.J., Balázsi, G., Kohanski, M.A., Isaacs, F.J., Murphy, K.F., Kuang, Y., Cantor, C.R., Walt, D.R., and Colline, J.J. (2006). Phenotypic consequences of promoter-mediated transcriptional noise. Mol. Cell *24*, 853–865.

Blake, W.J., Kaern, M., Cantor, C.R., and Collins, J.J. (2003). Noise in eukaryotic gene expression. Nature *422*, 633–637.

Blower, M.D. (2013). Molecular insights into intracellular RNA localization. Int. Rev.Cell Mol. Biol. *302*, 1–39.

Blower, M.D., Feric, E., Weis, K., and Heald, R. (2007). Genome-wide analysis demonstrates conserved localization of messenger RNAs to mitotic microtubules. J. Cell Biol. *179*, 1365–1373.

Boutz, P.L., Bhutkar, A., and Sharp, P.A. (2015). Detained introns are a novel, widespread class of post-translationally spliced introns. Genes Dev. *29,* 63-80.

Brady, C.A., Jiang, D., Mello, S.S., Johnson, T.M., Jarvis, L.A., Kozak, M.M., Kenzelmann Broz, D., Basak, S., Park., E.J., McLaughlin, M.E., et al. (2011). Distinct p53 transcriptional programs dictate acute DNA-damage responses and tumor suppression. Cell *145*, 571–583.

Brady, L.K., Wang, H., Radens, C.M., Radovich, M., Maity, A., Ivan, M., Barash, Y., and Koumenis, C. (2017). Transcriptome analysis of hypoxic cancer cells uncovers intron retention in *EIF2B5* as a mechanism to inhibit translation. Plos Biol. *15,* (9):e2002623.

Brown, C.R., and Boeger, H. (2014). Nucleosomal promoter variation generates gene expression noise. Proc. Natl. Acad. Sci. U.S.A. *111*, 17893–17898.

Brown, M.A., Sims III, R.J., Gottlieb, P.D., and Tucker, P.W. (2006). Identification and characterization of Smyd2: a split SET/MYND domain-containing histone H3 lysine 36-specific methyltransferase that interacts with the Sin3 histone deacetylase complex. Mol. Cancer *5*, 26.

Bode, A.M., and Dong, Z. (2004). Post-translational modification of p53 in tumorigenesis. Nat. Rev. Cancer *4*, 793–805.

Boeger, H. (2014). Nucleosomes, transcription, and probability. Mol Biol Cell *25,* 3451-3455.

Boeger, H., Griesenbeck, J., and Kornberg, R.D. (2008). Nucleosome Retention and the Stochastic Nature of Promoter Chromatin Remodeling for Transcription. Cell *133*, 716–726.

Brooks, C.L., and Gu., W. (2003). Ubiquitination, phosphorylation and acetylation: the molecular basis for p53 regulation. Curr. Opin. Cell Biol. *15*, 164–171.

Brummelkamp, T.R., Bernards, R., and Agami, R. (2002a). Stable suppression of tumorigenicity by virus-mediated RNA interference. Cancer Cell *2*, 243-247.

Brummelkamp, T.R., Bernards, R., and Agami, R. (2002b). A system for stable expression of short interfering RNAs in mammalian cells. Science *296*, 550-553.

Buchan, J.R., and Parker, R. (2009). Eukaryotic Stress Granules: The Ins and Outs of Translation. Mol. Cell *36,* 932-941.

Buettner, F., Natarajan, K.N., Casale, F.P., Proserpio, V., Scialdone, A., Theis, F.J., Teichmann, S.A., Marioni, J.C., and Stegle, O. (2015). Computational analysis of cell-to-cell heterogeneity in single-cell RNA-sequencing data reveals hidden subpopulations of cells. Nat. Biotechnol. *33*, 155–160.

Buxbaum, A.R., Haimovich, G., and Singer, R.H. (2015). In the right place at the right time: visualizing and understanding mRNA localization. Nat. Rev. Mol. Cell Biol. *16*, 95–109.

Bykov, V.J., and Wiman, K.G. (2003). Novel cancer therapy by reactivation of the p53 apoptosis pathway. Ann. Med. *35*, 458–465.

Cabili, M.N., Dunagin, M.C., McClanahan, P.D., Biaesch, A., Padovan-Merhar, O., Regev, A., Rinn, J.L., and Raj, A. (2015). Localization and abundance analysis of human lncRNAs at single-cell and single-molecule resolution. Genome Biol. *16*, 20.

Cai, L., Dalal, C.K., and Elowitz, M.B. (2008). Frequency-modulated nuclear localization bursts coordinate gene regulation. Nature *455*, 485–490.

Cairns, C.A., and White, R.J. (1998). p53 is a general repressor of RNA polymerase III transcription. EMBO J. *17*, 3112–3123.

Candau, R., Scolnick, D.M., Darwin, P., Ying, C.Y., Halazonetis, T.D., and Berger, S.L. (1997). Two tandem and independent sub-activation domains in the amino terminus of p53 require the adaptor complex for activity. Oncogene *15*, 807–816.

Cannoodt, R., Saelens, W., and Saeys, Y. (2016). Computational methods for trajectory inference from single-cell transcriptomics.

Chao, J.A., Patskovsky, Y., Almo, S.C., and Singer, R.H. (2008). Structural basis for the coevolution of a viral RNA-protein complex. Nat. Struct. Mol. Biol. *15*, 103–105.

Carpenter, A.E., Jones, T.R., Lamprecht, M.R., Clarke, C., Kang, I.H., Friman, O., Guertin, D.A., Chang, J.H., Lindquist, R.A., Moffat, J., et al. (2006). CellProfiler: image analysis software for identifying and quantifying cell phenotypes. Genome Biology *7*, R100.

Cavalier-Smith, T. (1980). *r*- and *K*-tactics in the evolution of protist developmental systems: Cell and genome size, phenotype diversifying selection, and cell cycle patterns. Biosystems *12*, 43–59.

Chamiolo, J., Fang, G., Hövelmann, F., Friedrich, D., Knoll, A., Loewer, A., and Seitz, O. (2019). Comparing Agent-Based Delivery of DNA and PNA Forced Intercalation (FIT) Probes for Multicolor mRNA Imaging. Chem. Bio. Chem. *20*, 595–604.

Chartrand, P., and Singer, R.H., (2001). RNP Localization and Transport in Yeast. Annu. Rev. Cell. Biol. *17,* 297-310.

Chen, A.K., Rhee, W.J., Bao, G., and Tsourkas, A. (2011). Delivery of Molecular Beacons for Live-Cell Imaging and Anaylsis of RNA. Methods in Molecular Biology *714*, 159-174.

Chen, K.H., Boettiger, A.N., Moffitt, J.R., Wang, S., and Zhuang, X. (2015). Spatially resolved, highly multiplexed RNA profiling in single cells. Science *348*, 412–427.

Chen, X., Chen, J., Gan, S., Guan, H., Zhou, Y., Ouyang, Q., and Shi, J. (2013). DNA damage strength modulates a bimodal switch of p53 dynamics for cell-fate control. BMC Biology *11*, 73.

Chen, C.-Y.A., Ezzeddine, N., and Shyu, A.-B. (2009). Messenger RNA Half-Life Measurements in Mammalian Cells. Methods Enzymol. *448*, 335–357.

Chen, C.-S., Ho, D.-R., Chen, F.-Y., Chen, C.-R., Ke, Y.-D., and Su, J.-G.J. (2014). AKT mediates actinomycin D-induced p53 expression. Oncotarget *5*, 693–703.

Chen, L.F., Lin, Y.T., Gallegos, D.A., Hazlett, M.F., Gómez-Schiavon, M., Yang, M.G., Kalmeta, B., Zhou, A.S., Holtzman, L., Gersbach, C.A., Grandl, J., Buchler, N.E., and West, A.E. (2019). Enhancer Histone Acetylation Modulates Transcriptional Bursting Dynamics of Neuronal Activity-Inducible Genes. Cell Rep. *26*, 1174–1188.

Chen, M., Ma, Z., Wu, X., Mao, S., Yang, Y., Tan, J., Krueger, C.J., and Chen, A.K. (2017). A molecular beacon-based approach for live-cell imaging of RNA transcripts with minimal target engineering at the single-molecule level. Sci. Rep. *7*, 1550.

Chiruvella, K.K., Liang, Z., and Wilson, T.E. (2013). Repair of double-strand breaks by end joining. Cold Spring Harb. Perspect. Biol. *5*, a012757.

Cho, A., Gorina, S., Jeffrey, P.D., and Pavletich, N.P. (1994). Crystal structure of a p53 tumor suppressor-DNA complex: understanding tumorigenic mutations. Science *265*, 346–355.

Chong, S., Chen, C., Ge, H., and Xie, X.S. (2014). Mechanism of transcriptional bursting in bacteria. Cell *158*, 314–326.

Churchman, L.S., and Weissman, J.S. (2011). Nascent transcript sequencing visualizes transcription at nucleotide resolution. Nature *469,* 368-373.

Ciccia, A., and Elledge, S.J. (2010). The DNA damage response: Making it safe to play with knives. Mol. Cell *40*, 179–204.

Cimprich, K.A., and Cortez, D. (2008). ATR: An essential regulator of genome integrity. Nat. Rev. Mol. Cell Biol. *9*, 616–627.

Clore, G.M., Ernst, J., Clubb, R., Omichinski, J.G., Kennedy, W.M., Sakaguchi, K., Appella, E., and Gronenborn, A.M. (1995). Refined solution structure of the oligomerization domain of the tumour suppressor p53. Nat. Struct. Biol. *2,* 321–333.

Cohen, A.A., Kalisky, T., Mayo, A., Geva-Zatorsky, N., Danon, T., Issaeva, I., Kopito, R.B., Perzov, N., Milo, R., Sigal, A., and Alon, U. (2009). Protein Dynamics in Individual Human Cells: Experiment and Theory. PLoS One *4*, e4901.

Condeelis, J., and Singer, R.H. (2012). How and why does β-actin mRNA target? Biol. Cell *97*, 97–110.

Cordelieres, F., (2004). Manual Tracking. Retrieved from https://imagej.nih.gov/ij/plugins/track/track.html

Core L.J., Waterfall, J.J.,and Lis, J.T. (2008). Nascent RNA Sequencing Reveals Widespread Pausing and Divergent Initiation at Human Promoters. Science *322,* 1845-1848.

Corrigan, A.M., Tunnacliffe, E., Cannon, D., and Chubb, J.R. (2016). A continuum model of transcriptional bursting. Elife *5*, e13051.

Coulon, A., Chow, C.C., Singer, R.H., and Larson, D.R. (2013). Eukaryotic transcriptional dynamics: from single molecules to cell populations. Nat. Rev. Genet. *14*, 572–584.

Covert, M.W., Leung, T.H., Gaston, J.E., and Baltimore, D. (2005). Achieving stability of lipopolysaccharide-induced NF-kB activation. Science *309*, 1854–1857.

Daigle, N., and Ellenberg, J. (2007). LambdaN-GFP: an RNA reporter system for live-cell imaging. Nat. Methods *4*, 633–636.

Dar, R.D., Razooky, B.S., Singh, A., Trimeloni, T.V., McCollum, J.M., Cox, C.D., Simpson, M.L., and Weinberger, L.S. (2012). Transcriptional burst frequency and burst size are equally modulated across the human genome. Proc. Natl. Acad. Sci. U.S.A. *109*, 17454–17459.

Dar, R.D., Shaffer, S.M., Singh, A., Razooky, B.S., Simpson, M.L., Raj, A., and Weinberger, L.S. (2016). Transcriptional Bursting Explains the Noise–Versus–Mean Relationship in mRNA and Protein Levels. PloS One *11*, e0158298.

das Neves, R.P., Jones, N.S., Andreu, L., Gupta, R., Enver, T., and Iborra, F.J. (2010). Connecting variability in global transcription rate to mitochondrial variability. PLoS Biol. *8*, e1000560.

Davis, A.J., Chen, B.P.C., and Chen, D.J. (2014). DNA-PK: A dynamic enzyme in a versatile DSB repair pathway. DNA Repair *17*, 21–29.

Davison, T.S., Yin, P., Nie, E., Kay, C., and Arrowsmith, C.H. (1998). Characterization of the oligomerization defects of two p53 mutants found in families with Li-Fraumeni and Li-Fraumeni-like syndrome. Oncogene *17*, 651–656.

Donovan, B.T., Huyn, A., Ball, D.A., Patel, H.P., Poirier, M.G., Larson, D.R., Ferguson, M.L., Lenstra, T.L. (2019). Live-cell imaging reveals the interplay between transcription factors, nucleosomes, and bursting. EMBO J *38*

Debnath, J., Muthuswamy, S.K., and Brugge, J.S. (2003). Morphogenesis and oncogenesis of MCF-10A mammary epithelial acini grown in three-dimensional basement membrane cultures. Methods 30, 256–268.

Decker, C.J., and Parker, R. (2012). P-Bodies and Stress Granules: Possible Roles in the Control of Translation and mRNA Degradation. Cold Spring Harb. Perspect. Biol. *4*, a012286.

Deplancke, B., Alpern, D., and Gardeux, V. (2016) The Genetics of Transcription Factor DNA Binding Variation. Cell *166*, 538-554

de Pretis, S., Kress, T., Morelli, M.J., Melloni, G.E.M., Riva, L., Amati, B., and Pelizzola, M. (2015). INSPEcT: a computational tool to infer mRNA synthesis, processing and degradation dynamics from RNA- and 4sU-seq time course experiments. Bioinformatics *31*, 2829–2835.

Dolgosheina, E.V., Jeng, S.C., Panchapakesan, S.S., Cojocaru, R., Chen, P.S., Wilson, P.D., Hawkins, N., Wiggins, P.A., and Unrau, P.J. (2014). RNA mango aptamer-fluorophore: a bright, high-affinity complex for RNA labeling and tracking. ACS Chem. Biol. *9*, 2412–2420.

Donner, A.J., Hoover, J.M., Szostek, S.A., and Espinosa, J.M. (2007). Stimulus-specific transcriptional regulation within the p53 network. Cell Cycle *6*, 2594–2598.

Dölken, L., Ruzsics, Z., Rädle, B., Friedel, C.C., Zimmer, R., Magnes, J., Hoffmann, R., Dickinson, P., Forster, T., Ghazal, P., and Koszinowski, U.H. (2008). High-resolution gene expression profiling for simultaneous kinetic parameter analysis of RNA synthesis and decay. RNA *14,* 1959-1972.

Eldar, A., and Elowitz, M.B. (2010). Functional roles for noise in genetic circuits. Nature *467*, 167–173.

El-Deiry, W.S., Kern, S.E., Pietenpol, J.A., Kinzler, K.W., and Vogelstein, B. (1992). Definition of a consensus binding site for p53. Nat. Genet. *1*, 45–49.

Elowitz, M.B., Levine, A.J., Siggia, E.D., and Swain, P.S. (2002). Stochastic gene expression in a single cell. Science *297*, 1183–1186.

Erhard, F., Baptista, M.A.P., Krammer, T., Hennig, T., Lange, M., Arampatzi, P., Jürges, C., Theis, F.J., Saliba, A.-E., and Dölken, L. (2019). scSLAM-seq reveals core features of transcription dynamics in single cells. Nature *571,* 419-423.

Espinosa, J.M. (2008). Mechanisms of regulatory diversity within the p53 transcriptional network. Oncogene *27*, 4013–4023.

Espinosa, J.M., Verdun, R.E., and Emerson, B.M. (2003). p53 functions through stress- and promoter-specific recruitment of transcription initiation components before and after DNA damage. Mol. Cell *12*, 1015–1027.

Estrada, J., Wong, F., DePace, A., and Gunawardena, J. (2016). Information Integration and Energy Expenditure in Gene Regulation. Cell *166*, 234–244.

Ewen, M.E., Oliver, C.J., Sluss, H.K., Miller, S.J., and Peeper, D.S. (1995). p53-Dependent repression of CDK4 translation in TGF-b-induced G1 cell-cycle arrest. Genes & Dev. *9*, 204–217.

Fang, G., Chamiolo, J., Kankowski, S., Hövelmann, F., Friedrich, D., Löwer, A., Meier, J.C., and Seitz, O. (2018). A bright FIT-PNA hybridization probe for the hybridization state specific analysis of a C → U RNA edit via FRET in a binary system. Chem. Science *9*, 4794–4800.

Fazal, F.M., Han, S., Parker, K.R., Kaewsapsak, P., Xu, J., Boettiger, A.N., Chang, H.Y., and Ting, A.Y. (2019). Atlas of Subcellular RNA Localization Revealed by APEX-Seq. Cell *178*, 473–490.

Femino, A.M., Fay, F.S., Fogarty, K., and Singer, R.H. (1998). Visualization of Single RNA Transcripts in Situ. Science *280*, 585–590.

Fields, S., and Jang, S.K. (1990). Presence of a potent transcription activating sequence in the p53 protein. Science *249*, 1046–1049.

Filonov, G.S., Moon, J.D., Svensen, N., and Jaffrey, S.R. (2014). Broccoli: rapid selection of an RNA mimic of green fluorescent protein by fluorescence-based selection and directed evolution. J. Am. Chem. Soc. *136*, 16299–16308.

Finzel Pérez, A. (2016a). Upstream control and downstream responses of p53 are involved in its tumor suppression functions upon genotoxic stress. PhD Thesis, Freie Universität Berlin.

Finzel, A., Grybowski, A., Strasen, J., Christiano, E., and Loewer, A. (2016b). Hyperactivation of ATM upon DNA-PKcs inhibition modulates p53 dynamics and cell fate in response to DNA damage. Mol. Biol. Cell *27*, 2341–2517.

Fischer, M. (2017). Census and evaluation of p53 target genes. Oncogene *36*, 3943–3956.

Flores, E.R., Tsai, K.Y., Crowley, D:, Sengupta, S., Yang, A., McKeon, F., and Jacks, T. (2002). p63 and p73 are required for p53-dependent apoptosis in response to DNA damage. Nature *416*, 560–564.

Follis, A.V., Llambi, F., Merritt, P., Chipuk, J.E., Green, D.R., and Kriwacki, R.W. (2015). Pin1-Induced Proline Isomerization in Cytosolic p53 Mediates BAX Activation and Apoptosis. Mol. Cell *59*, 677–684.

Friedler, A., Veprintsev, D.B., Freund, S.M.V., von Glos, K.I., and Fersht, A.R. (2005). Modulation of Binding of DNA to the C-Terminal Domain of p53 by Acetylation. Structure *13*, 629–636.

Friedman, N., Cai, L., and Sunney Xie, X. (2006). Linking Stochastic Dynamics to Population Distribution: An Analytical Framework of Gene Expression. Phys. Rev. Lett. *97*, 168302.

Friedrich, D., Friedel, L., Finzel, A., Herrmann, A., Preibisch, S., and Loewer, A. (2019). Stochastic transcription in the p53-mediated response to DNA damage is modulated by burst frequency. Mol. Syst. Biol. *15*, e9068.

Fritzsch, C., Baumgärtner, S., Kuban, M., Steinshorn, D., Reid, G., and Legewie, S. (2018). Estrogen-dependent control and cell-to-cell variability of transcriptional bursting. Mol. Syst. Biol. *14*, e7678.

Fuchs, G., Voichek, Y., Benjamin, S., Gilad, S., Amit, I., and Oren, M. (2014). 4sUDRB-seq: measuring genomewide transcriptional elongation rates and initiation frequencies within cells. Genome Biol. *15*, R69.

Fuda, N.J., Ardehali, M.B., and Lis, J.T. (2009). Defining mechanisms that regulate RNA polymerase II transcription in vivo. Nature *462*, 186–192.

Fukaya, T., Lim, B., and Levine, M. (2016). Enhancer Control of Transcriptional Bursting. Cell *166*, 358–368.

Fulton, D.L., Sundararajan, S., Badis, G., Hughes, T.R., Wasserman, W.W., Roach, J.C., and Sladek, R. (2009). TFCat: the curated catalog of mouse and human transcription factors. Genome Biol. *10*, R29.

Funk, W.D., Pak, D.T., Karas, R.H., Wright, W.E., and Shay, J.W. (1992). A transcriptionally active DNA-binding site for human p53 protein complexes. Mol. Cell. Biol. *12*, 2866–2871.

Fuxreiter, M., Tompa, P., Simon, I., Uversky, V.N., Hansen J.C., and Asturias, F.J. (2008). Malleable machines take shape in eukaryotic transcriptional regulation. Nat. Chem. Biol. *4*, 728–737.

Gaglia, G., Guan, Y., Shah, J.V. and Lahav, G. (2013). Activation and control of p53 tetramerization in individual living cells. Proc. Natl. Acad. Sci. U.S.A. *110*, 15497–15501.

Gaglia, G., and Lahav, G. (2014). Constant rate of p53 tetramerization in response to DNA damage controls the p53 response. Mol. Syst. Biol. *10*, 753.

Gagniuc, P., and Ionescu-Tirgoviste, C. (2012). Eukaryotic genomes may exhibit up to 10 generic classes of gene promoters. BMC Genomics *13*, 512.

Galy, B., Créancier, L., Zanibellato, C., Prats, A. C., and Prast H. (2001).Tumor suppressor p53 inhibits human fibroblast growth factor 2 expression by a pots-transcriptional mechanism. Oncogene *20,* 1669-1677.

Geva-Zatorsky, N., Rosenfeld, N., Itzkovitz, S., Milo, R., Sigal, A., Dekel, E., Yarnitzky, T., Liron, Y., Polak, P., Lahav, G., and Alon, U. (2006). Oscillations and variability in the p53 system. Mol. Syst. Biol. *2*, 1–13.

Giorgetti, L., Siggers, T., Tiana, G., Caprara, G., Notarbartolo, S., Corona, T., Parparakis, M., Milani, P., Bulyk, M.L., and Natoli, G. (2010). Noncooperative Interactions between Transcription Factors and Clustered DNA Binding Sites Enable Graded Transcriptional Responses to Environmental Inputs. Mol. Cell *37*, 418–428.

Göhler, T., Reimann, M., Cherny, D., Walter, K., Warnecke, G., Kim, E., and Deppert, W. (2002). Specific interaction of p53 with target binding sites is determined by DNA conformation and is regulated by the C-terminal domain. J. Biol. Chem. *277*, 41192–41203.

Golding, I., Paulsson, J., Zawilski, S.M., and Cox, E.C. (2005). Real-time kinetics of gene activity in individual bacteria. Cell *123*, 1025–1036.

Gregory, T.R. (2001). Coincidence, coevolution, or causation? DNA content, cellsize, and the C-value enigma. Biol. Rev. *76*, 65–101.

Grossman, S.R. (2001). p300/CBP/p53 interaction and regulation of the p53 response. FEBS J. *268*, 2773–2778.

Grossman, S.R., Perez, M., Kung, A.L., Joseph, M., Mansur, C., Xiao, Z.X., Kumar, S., Howley, P.M., and Livingstone, D.M. (1998). p300/MDM2 complexes participate in MDM2-mediated p53 degradation. Mol. Cell *2*, 405–415.

Gu, B., and Zhu, W.G. (2012). Surf the post-translational modification network of p53 regulation. Int. J. Sci. *8*, 672–684.

Gu, W., and Roeder , R.G. (1997). Synergistic activation of transcription by CBP and p53. Nature *387*, 819–823.

Gu, W., Shi, X.-L., and Roeder , R.G. (1997). Activation of p53 sequence-specific DNA binding by acetylation of the p53 C-terminal domain. Cell *90*, 595–606.

Hafner, A., Bulyk, M.L., Jambhekar, A., and Lahav, G. (2019). The multiple mechanisms that regulate p53 activity and cell fate. Nat. Rev. Mol. Cell Biol. *20*, 199–210.

Hafner, A., Stewart-Ornstein, J., Purvis, J.E., Forrester, W.C., Bulyk, M.L., and Lahav, G. (2017). p53 pulses lead to distinct patterns of gene expression albeit similar DNA-binding dynamics. Nat. Struct. Mol. Biol. *24*, 840–847.

Hager, C.L., McNally, J.G., and Mistelli, T. (2009). Transcription dynamics. Mol. Cell *35*, 741–753.

Hahn, S. (1998). The role of TAFs in RNA polymerase II Transcription. Cell *95*, 579–582.

Haimovich, G., Ecker, C.M., Dunagin, M.C., Eggan, E., Raj, A., Gerst, J.E., and Singer, R.H. (2017). Intercellular mRNA trafficking via membrane nanotube-like extensions in mammalian cells. PNAS *114,* E9873-E9882.

Hainaut, O., and Milner, J. (1993). A structural role for metal ions in the "wild-type" conformation of the tumor suppressor protein p53. Cancer Res. *53,* 1739–1742.

Hainaut, P., and Hollstein, M. (1999). p53 and Human Cancer: The First Ten Thousand Mutations. Adv. Cancer Res. *77,* 87–137.

Hansen, M.M.K., Desai, R.V., Simpson, M.L., and Weinberger, L.S. (2018). Cytoplasmic Amplification of Transcriptional Noise Generates Substantial Cell-to-Cell Variability. Cell Syst. *7*, 384–397.

Hanson, R.L., Porter, J.R., and Batchelor, E. (2019). Protein stability of p53 targets determines their temporal expression dynamics in response to p53 pulsing. J. Cell Biol. *218*, 1282.

Hao, N., and O'Shea, E.K. (2011). Signal-dependent dynamics of transcription factor translocation controls gene expression. Nat. Struct. Mol. Biol. *19*, 31–39.

Hao, S., and Baltimore, D. (2009). The stability of mRNA influences the temporal order of the induction of genes encoding inflammatory molecules. Nat. Immunol. *10*, 281–288.

Harper, J.W., and Elledge, S.J. (2007). The DNA damage response: Ten years after. Mol. Cell *15*, 739–745.

Harper, C.V., Finkenstädt, B., Woodcock, D.J., Friedrichsen, S., Semprini, S., Ashall, L., Spiller, D.G., Mullins, J.J., Rand, D.A., Davis, J.R.E., and White, M.R.H. (2011). Dynamic Analysis of Stochastic Transcription Cycles. PLoS Biol. *9*, e1000607.

Harris, S.L., and Levine, A.J. (2005). The p53 pathway: positive and negative feedback loops. Oncogene *24*, 2899–2908.

Haupt, Y., Maya, R., Kazaz, A., and Oren, M. (1997). Mdm2 promotes the rapid degradation of p53. Nature *387*, 296–299.

Heim, R., and Tsien, R.Y. (1996). Engineering green fluorescent protein for improved brightness, longer wavelengths and fluorescence resonance energy transfer. Current Biology *6*, 178–182.

Hendriks, G.J., Jung, L.A., Larsson, A.J.M., Lidschreiber, M., Andersson, O.F., Lidschreiber, K., Cramer, P., and Sandberg, R. (2019). NASC-seq monitors RNA synthesis in single cells. Nat. Com. *10, 3138*

Herzog, V.A., Reichholf, B., Neumann, T., Rescheneder, P., Bhat, P., Burkard, T.R., Wlotzka, W., von Haeseler, A., Zuber, J., and Ameres, S.L. (2017). Thiol-linked alkylation of RNA to assess expression dynamics. Nat. Methods *14*, 1198–1204.

Hill, R., Bodzak, E., Blough, M.D., and Lee, P.W. (2008). p53 Binding to the p21 promoter is dependent on the nature of DNA damage. Cell Cycle *7*, 2535–2543.

Hinow, P., Rogers, C.E., Barbieri, C.E., Pietenpol, J.A., Kenworthy, A.K., and DiBenedetto, E. (2006). The DNA binding activity of p53 displays reaction-diffusion kinetics. Biophys. J. *91*, 330–342.

Ho, J., Tumkaya, T., Aryal, S., Choi, H., and Claridge-Chang, A. (2019). Moving beyond P values: data analysis with estimation graphics. Nat. Methods *16*, 565–566.

Hocine, S., Raymond, P., Zenklusen, D., Chao, J.A., and Singer, R.H. (2013). Single-molecule analysis of gene expression using two-color RNA labeling in live yeast. Nat. Methods *10*, 119–121.

Hocine, S., Vera, M., Zenklusen, D., and Singer, R.H. (2015). Promoter-Autonomous Functioning in a Controlled Environment using Single Molecule FISH. Sci. Rep. *5*, 9934.

Holt, C.E., and Bullock, S.L. (2009). Subcellular mRNA Localization in Animal Cells and Why It Matters. Science *326*, 1212–1216.

Horten, L.E., Bushell, M., Barth-Baus, D., Tilleray, V.J., Clemens, M.J., and Hensold, J.O. (2002). p53 activation results in rapid dephosphorylation of the eIF4E-binding protein 4E-BP1, inhibition of ribosomal protein S6 kinase and inhibition of translation initiation. Oncogene *21,* 5325-5334.

Hövelmann, F. (2015). Synthese und Charakterisierung einfach und mehrfach intern-markierter DNA-Sonden zur erzwungenen Interkalation. PhD Thesis, Humboldt-Universität zu Berlin.

Hoevelmann, F., Gaspar, I., Chamiolo, J., Kasper, M., Steffen, J., Ephrussi, A., and Seitz, O. (2016). LNA-enhanced DNA FIT-probes for multicolour RNA imaging. Chem. Sci. *7*, 128–135.

Hövelmann, F., Gaspar, I., Loibl, S., Ermilov, E.A., Röder, B., Wengel, J., Ephrussi, A., and Seitz, O. (2014). Brightness through Local Constraint-LNA-Enhanced FIT Hybridization Probes for In Vivo Ribonucleotide Particle Tracking. Chem.Bio.Chem. *20,* 595-604.

Hoffmann, A., Levchenko, A., Baltimore, D., and Scott, M.L. (2002). The IkB and NF-kB signaling module: Temporal control and selective gene activation. Science *298*, 1241–1244.

Horn, H.F., and Vousden, K.H. (2007). Coping with stress: Multiple ways to activate p53. Oncogene *26*, 1306–1316.

Huang, J., Perez-Burgos, L., Placek, B.J., Sengupta, R., Richter, M., Dorsey, J.A., Kubicek, S., Opravil, S., Jenuwein, T., and Berger, S.L. (2006). Repression of p53 activity by Smyd2-mediated methylation. Nature *444*, 629–632.

Hubbard, T., Barker, D., Birney, E., Cameron, G., Chen, Y., Clark, L., Cox, T., Cuff, J., Curwen, V. Down, T., et al. (2002). The Ensembl genome dataset project. Nucleic Acids Res. *30,* 38-41

Hupp, T.R., and Lane, D.P. (1994). Allosteric activation of latent p53 tetramers. Curr. Biol. *4*, 865–875.

Ibrahimi, A., Vande Velde, G., Reumers, V., Thiry, I., Vandeputte, C., Vets, S., Deerose, C., Bormans, G, Baekelandt, V., and Gijbers, R. (2009). Highly efficient multicistronic lentiviral vectors with peptide 2A sequences. Hum Gene Ther *8,* 845-860.

Imagawa, T., Terai, T., Yamada, Y., Kamada, R., and Sakaguchi, K. (2009). Evaluation of transcriptional activity of p53 in individual living mammalian cells. Anal. Biochem. *387*, 249–256.

Inga, A., Storici, F., Darden, T. A. & Resnick, M. A. (2002). Differential transactivation by the p53 transcription factor is highly dependent on p53 level and promoter target sequence. Mol. Cell. Biol. *22,* 8612–8625.

Ivanov, G.S., Ivanova, T., Kurash, J., Ivanov, A., Chuikov, S., Gizatullin, F., Herrera-Medina, E.M., Rauscher, F., Reinberg, D.,and Barlev, N.A. (2007). Methylation-Acetylation Interplay Activates p53 in Response to DNA Damage. Mol. Cell. Biol. *27*, 6756–6769.

Iyer, G., Wang, A.R., Brennan, S.R., Bourgeois, S., Armstrong, E., Shah, P., and Harari, P.M. (2017). Identification of stable housekeeping genes in response to ionizing radiation in cancer research. Sci. Rep. *7*, 43763.

Jacob, A.G., and Smith, C.W.J. (2017). Intron retention as a component of regulated gene expression programs. Hum. Genet. *136,* 1043-1057.

Jackson, R.J., Hellen, C.U.T. and Pestova, T.V. (2010). The mechanism of eukaryotic translation initiation and principles of its regulation. Nat. Rev. Mol. Cell. Biol. *11*, 113–127.

Johnstone, O., and Lasko, P. (2001). Translational Regulation and RNA Localization in Drosophila Oocytes and Embryos. Annu. Rev. Genet. *35*, 365–406.

Jonkers, I., and Lis, J.T. (2015). Getting up to speed with transcription elongation by RNA polymerase II. Nat. Rev. Mol. Cell. Biol. *16*, 167–177.

Joo, W.S., Jeffrey, P.D, Cantor, S.B., Finnin, M.S., Livingston, D.M. and Pavletich, N.P. (2002) Structure of the 53BP1 BCRT region bound to p53 and its comparison to Bcra1 BCRT structure. Genes Dev. *16,* 583-593

Jürges, C., Dölken, L., and Erhard, F. (2018). Dissecting newly transcribed and old RNA using GRAND-SLAM. Bioinformatics *34*, i218–i226.

Kaern, M., Elston, T.C., Blake, W.J., and Collins, J.J. (2005). Stochasticity in gene expression: from theories to phenotypes. Nat. Rev. Genet. *6*, 451–464.

Kafri, P., Hasenson, S.E., Kanter, I., Sheinberger, J., Kinor, N., Yunger, S., and Shav-Tal, Y. (2016). Quantifying β-catenin subcellular dynamics and cyclin D1 mRNA transcription during Wnt signaling in single living cells. eLife *5*, e16748.

Kapoor, M., and Lozano, G. (1998). Functional activation of p53 via phosphorylation following DNA damage by UV but not y radiation. Proc. Natl. Acad. Sci. U.S.A. *95*, 2834–2837.

Kaufmann, B.B., and van Oudenaarden, A. (2007). Stochastic gene expression: from single molecules to the proteome. Curr. Opin. Genet. Dev. *17*, 107–112.

Kawaguchi, T., Kato, S., Otsuka, K., Watanabe, G., Kumabe, T., Tominaga, T., Yoshimoto, T., and Ishioka, C. (2005). The relationship among p53 oligomer formation, structure and transcriptional activity using a comprehensive missense mutation library. Oncogene *24*, 6976–6981.

Kempe, H., Schwabe, A., Crémazy, F., Verschure, P.J., and Bruggeman, F.J. (2015). The volumes and transcript counts of single cells reveal concentration homeostasis and capture biological noise. Mol. Biol. Cell *26*, 797–804.

Kepler, T.B., and Elston, T.C. (2001). Stochasticity in Transcriptional Regulation: Origins, Consequences, and Mathematical Representations. Biophys. J. *81*, 3116–3136.

Kikuchi, N., and Kolpashchikov, D.M. (2016). Split Spinach Aptamer for Highly Selective Recognition of DNA and RNA at Ambient Temperatures. Chem. Bio. Chem. *17*, 1589–1592.

Kim, H.D., and O'Shea, E.K. (2008). A quantitative model of transcription factor–activated gene expression. Nat. Struct. Mol. Biol. *15*, 1192–1198.

Kim, S., Balakrishnan, S.K., and Gross, D.S. (2011). p53 interacts with RNA Polymerase II through Its Core Domain and Impairs Pol II Processivity *In Vivo.* PLoS ONE *6,* (8):e22183.

Kitayner, M., Rozenberg, H., Kessler, N., Rabinovich, D., Shaulov, L., Haran, T.E., and Shakked, Z. (2006). Structural basis of DNA recognition by p53 tetramers. Mol. Cell *22*, 741–753.

Kitayner, M., Rozenberg, H., Rohs, R., Suad, O., Rabinovich, D., Honig, B., and Shakked, Z. (2010). Diversity in DNA recognition by p53 revealed by crystal structures with Hoogsteen base pairs. Nat. Struct. Mol. Biol. *4*, 423–429.

Ko, M.S., Nakauchi, H., and Takahashi, N. (1990). The dose dependence of glucocorticoid-inducible gene expression results from changes in the number of transcriptionally active templates. EMBO J. *9*, 2835–2842.

Kornberg, R.D. (1999). Eukaryotic transcriptional control. Trends Cell Biol. *9*, M46–M49.

Kracikova, M., Akiri, G., George, A., Sachidanandam, R., and Aaronson, S.A. (2013). A threshold mechanism mediates p53 cell fate decision between growth arrest and apoptosis. Cell Death Differ. *20*, 576–588.

Kremers, G.J., Goedhart, J., van Munster, E.B., and Gadella, T.W.J. (2006). Cyan and Yellow Super Fluorescent Proteins with Improved Brightness, Protein Folding, and FRET Förster Radius. Biochemistry *45*, 6570–6580.

Kubbutat, M.H., Jones, S.N., and Vousden, K.H. (1997). Regulation of p53 stability by Mdm2. Nature *387*, 299–304.

Kwak, H., Fuda, N.J., Core, L.J., and Lis, T.J. (2013). Precise Maps of RNA Polymerase Reveal How Promoters Direct Initiation and Pausing. Science *339,* 950-953.

Kwon, I., Kato, M., Xiang, S., Wu, L., Theodoropoulos, P., Mirzaei, H., Han, T., Xie, S., Corden, J.L., and McKnight, S.L. (2013). Phosphorylation-Regulated Binding of RNA Polymerase II to Fibrous Polymers of Low-Complexity Domains. Cell *155*, 1049–1060.

Lacerda, R., Meneszes, J., and Romao, L. (2017). More than just scanning: the importance of cap-independent mRNA translation initiation for cellular stress response and cancer. Cell. Mol. Life Sci. *74*, 1659-1680.

Lahav, G., Rosenfeld, N., Sigal, A., Geva-Zatorsky, N., Levine, A.J., Elowitz, M.B., and Alon, U. (2004). Dynamics of the p53-Mdm2 feedback loop in individual cells. Nat. Genet. *36*, 147–150.

Lai, W.S., Arvola, R.M., Goldstrohm, A.C., and Blackshear, P.J. (2019). Inhibiting transcription in cultured metazoan cells with actinomycin D to monitor mRNA turnover. Methods *155*, 77–87.

Lakin, N.D., and Jackson, S.P. (1999). Regulation of p53 in response to DNA damage. Oncogene *18*, 7644–7655.

La Manno, G., Soldatov, R., Zeisel, A., Braun, E., Hochgerner, H., Petukhov, V., Lidschreiber, K., Kastriti, M.E., Lönnerberg, P., Furian, A., et al. (2018). RNA velocity of single cells. Nature *560,* 494-498.

Lange, S., Katayama, Y., Schmid, M., Burkacky, O., Bräuchle, C., Lamb, D.C., and Jansen, R.P. (2008). Simultaneous Transport of Different Localized mRNA Species Revealed by Live Cell Imaging. Traffic *9,* 1256-1267.

Laptenko, O., Shiff, I., Freed-Pastor, W., Zupnick, A., Mattia, M., Freulich, E., Shamir, I., Kadouri, N., Kahan, T., Manfredi, J., et al. (2015). The p53 C terminus controls site-specific DNA binding and promotes structural changes within the central DNA binding domain. Mol. Cell *57*, 1034–1046.

Larson, D.R., Fritzsch, C., Sun, L., Meng, X., Lawrence, D.S., and Singer, R.H. (2013). Direct observation of frequency modulated transcription in single cells using light activation. eLife *2*, e00750.

Larson, D.R., Singer, R.H., and Zenklusen, D. (2009). A single molecule view of gene expression. Trends Cell Biol. *19*, 630–637.

Larson, D.R., Zenklusen, D., Wu, B., Chao, J.A., and Singer, R.H. (2011). Real-time observation of transcription initiation and elongation on an endogenous yeast gene. Science *332*, 475–478.

Lavin, M.F., Delia, D., and Chessa, L. (2006). ATM and the DNA damage response. EMBO Rep. *7*, 154–160.

Lécuyer, E., Yoshida, H., Parthasarathy, N., Alm, C., Babak, T., Cerovina, T., Hughes, T.R., Tomancak, P., and Krause, H.M. (2007). Global Analysis of mRNA Localization Reveals a Prominent Role in Organizing Cellular Architecture and Function. Cell *131*, 174–187.

Lee, J.H., Daugharthy, E.R., Scheiman, J., Kalhor, R., Yang, J.L., Ferrante, T.C., Terry, R., Jeanty, S.S., Li, C., Amamoto, R., et al. (2014). Highly multiplexed subcellular RNA sequencing in situ. Science *343*, 1360–1363.

Lee, R.E.C., Walker, S.R., Savery, K., Frank, D.A., and Gaudet, S. (2014). Fold Change of Nuclear NF-kB Determines TNF-Induced Transcription in Single Cells. Mol.Cell. *53,* 867-879

Lenstra, T.L., Rodriguez, J., Chen, H., and Larson, D.R. (2016). Transcription Dynamics in Living Cells. Annu. Rev. Biophys. *45*, 25–47.

Lev Bar-Or, R., Maya, R., Segel, L.A., Alon, U., Levine, A.J., and Oren, M. (2000). Generation of oscillations by the p53-Mdm2 feedback loop: A theoretical and experimental Study. Proc. Natl. Acad. Sci. U.S.A. *97*, 1–6.

Levesque, M.J., and Raj, A. (2013). Single-chromosome transcriptional profiling reveals chromosomal gene expression regulation. Nat. Methods *10*, 246–248.

Li, B., Carey, M., and Workman, J.L. (2007). The Role of Chromatin during Transcription. Cell *128,* 707-719.

Li, C., Cesbron, F., Oehler, M., Brunner, M., and Höfer, T. (2018). Frequency Modulation of Transcriptional Bursting Enables Sensitive and Rapid Gene Regulation. Cell Syst. *6*, 409–423.

Li, M., Luo, J., Brooks, C.L., and Gu, W. (2002). Acetylation of p53 Inhibits Its Ubiquitination by Mdm2. J. Biol. Chem. *277*, 50607–50611.

Liang, S., Bellato, H.M., Lorent, J., Lupinacci, F.C.S., Oertlin, C., van Hoef, V., Andrade, V.P., Roffé, M., Masvidal, L., Hajj, G.N.M., and Larsson, O. (2018). Polysome-profiling in small tissue samples. Nucleic Acids Res. *46*, e3.

Lickwar, C.R., Mueller, F., Hanlon, S.E., McNally, J.G., and Lieb, J.D. (2012). Genome-wide protein-DNA binding dynamics suggest a molecular clutch for transcription factor function. Nature *484*, 251–255.

Lionnet, T., Czaplinski, K., Darzacq, X., Shav-Tal, Y., Wells, A.L., Chao, J.A., Park, H.Y., de Turris, V., Lopez-Jones,M., and Singer, R.H. (2011). A transgenic mouse for in vivo detection of endogenous labeled mRNA. Nat. Methods *8*, 165–170.

Lionnet, T., and Singer, R.H. (2012). Transcription goes digital. EMBO Rep. *13*, 313–321.

Liu, L., Scolnick, D.M., Trievel, R.C., Zhang, H.B., Marmorstein, R., Halazonetis, T.D., and Berger, S.L. (1999). p53 sites acetylated in vitro by PCAF and p300 are acetylated in vivo in response to DNA damage. Mol. Cell. Biol. *19*, 1202–1209.

Liu, Y., Mi, Y., Mueller, T., Kreibich, S., Williams, E.G., van Drogen, A., Borel, C., Frank, M., Germain, P.-L., Bludau, I., et al. (2019). Multi-omic measurements of heterogeneity in HeLa cells across laboratories. Nat. Biotechnol. *37,* 314-322.

Liu, W.-L., Coleman, R.A., and Singh, K.S. (2018). A new era of studying p53-mediated transcription activation. Transcription *9,* 102-107.

Loayza-Puch, F., Drost, J., Rooijers, K., Lopes, R., Elkon, R. and Agami, R. (2013). p53 induces transcriptional and translational programs to suppress cell prolifertaion and growth. Genome Biology *14,*

Loewer, A., Batchelor, E., Gaglia, G., and Lahav, G. (2010). Basal dynamics of p53 reveal transcriptionally attenuated pulses in cycling cells. Cell *142*, 89–100.

Loewer, A., and Lahav, G. (2011). We are all individuals: causes and consequences of non-genetic heterogeneity in mammalian cells. Curr. Opin. Genet. Dev. *21*, 753–758.

Loffreda, A., Jacchetti, E:, Antunes, S., Rainone, P., Daniele, T., Morisaki., T., Bianchi, M.E., Tacchetti, C., and Mazza, D. (2017). Live-cell p53 single-molecule binding is modulated by C-terminal acetylation and correlates with transcriptional activity. Nat. Commun. *8*, 313.

Long, H.K., Prescott, S.L., and Wysocka, J. (2016) Ever-Changing Landscapes: Transcriptional Enhancers in Development and Evolution. Cell *167,* 1170-1187

Lu, H., Fisher, R.P., Bailey, P., and Levine, A.J. (1997). The CDK7-cycH-p36 complex of transcription factor IIH phosphorylates p53, enhancing its sequence-specific DNA binding activity in vitro. Mol. Cell. Biol. *17*, 5923–5934.

Lu, X., Nannenga, B., and Donehower, L.A. (2005). TPPM1D dephosphorylates Chk1 and p53 and abrogates cell cycle checkpoints. Genes Dev. *19*, 1162–1174.

Lubeck, E., Coskun, A.F., Zhiyentayev, T., Ahmad, M., and Cai, L. (2014). Single cell in situ RNA profiling by sequential hybridization. Nat. Methods *11*, 360–361.

Lue, N.F., and Kornberg, R.D. (1987). Accurate initiation at RNA polymerase II promoters in extracts from Saccharomyces cerevisiae. Proc. Natl. Acad. Sci. U.S.A. *84*, 8839–8843.

Luo, J., Li, M., Tang, Y., Laszkowska, M., Roeder, R.G., and Gu, W. (2004). Acetylation of p53 augments its site-specific DNA binding both in vitro and in vivo. Proc. Natl. Acad. Sci. U.S.A. *101*, 2259–2264.

Ma, B., Pan, Y., Zheng, J., Levine, A.J., and Nussinov, R. (2007). Sequence analysis of p53 response-elements suggests multiple binding modes of the p53 tetramer to DNA targets. Nucleic Acids Res. *35*, 2986–3001.

Ma, H., Tu, L.C., Naseri, A., Huisman, M., Zhang, S., Grunwald, D., and Pederson, T. (2016). Multiplexed labeling of genomic loci with dCas9 and engineered sgRNAs using CRISPRainbow. Nat Biotechnol. *34*, 528-30

Mahat, D.B., Kwak, H., Booth, G.T., Jonkers, I.H., Danko, C.G., Patel, R.K., Waters, C.T., Munson, K.,Core, L.J., and Lis, T.L. (2016). Base-pair-resolution genome-wide mapping of active RNA polymerases using precision nuclear run-on (PRO-Seq). Nat. Prot. *11,* 1455-1476.

Mali, P., Yang, L., Esvelt, K.M., Aach, J., Guell, M., DiCarlo, J.E., Norville, J.E., and Church, G.M. (2013). RNA-guided human genome engineering via Cas9. Science 339, 823–826.

Mao, C., Brown, C.R., Falkovskaia, E., Dong, S., Hrabeta-Robinson, E., Wenger, L., and Boeger, H. (2010). Quantitative analysis of the transcription control mechanism. Mol. Syst. Biol. *6*, 431.

Marcel, V., Van Long, F.N., and Diaz, J.-J. (2018). 40 Years of Research Put p53 in Translation. Cancers *10*, 152.

Marchenko, N.D., Hanel, W., Li, D., Becker, K., Reich, N., and Moll, U.M. (2010). Stress-mediated nuclear stabilization of p53 is regulated by ubiquitination and importin-α3 binding. Cell Death Differ. *17*, 255–267.

Marchese, D., de Groot, N.S., Gotor, N.L., Livi, C.M., and Tartaglia, G.G. (2016). Advances in the characterization of RNA-binding proteins.

Margaritis, T., and Holstege, F.C. (2008). Poised RNA polymerase II gives pause for thought. Cell *133*, 581–584.

Marshall, C.J. (1995). Specificity of receptor tyrosine kinase signaling: Transient versus sustained extracellular signal-regulated kinase activation. Cell *80*, 179–185.

Martin, K.C., and Ephrussi, A. (2009). mRNA Localization: Gene Expression in the Spatial Dimension. Cell *136*, 719–730.

Matsushima, W., Herzog, V.A., Neumann, T., Gapp, K., Zuber, J., Ameres, S.L., and Miska, E.A. (2018). SLAM-ITseq: sequencing cell type-specific transcriptomes without cell sorting.

Matsui, T., Segall, J., Weil, P.A., and Roeder, R.G. (1980). Multiple factors required for accurate initiation of transcription by purified RNA polymerase II. J. Biol. Chem. *225*, 11992–11996.

Matthiesen, S.H., and Hansen C.M. (2012). Fast and Non-Toxic In Situ Hybridization without Blocking of Repetitive Sequences. PLoS One *7*, e40675.

Mattia, M., Gottifredi, V., McKinney, K., and Prives, C. (2007). p53-Dependent p21 mRNA elongation is impaired when DNA replication is stalled. Mol. Cell Biol. *27*, 1309–1320.

Mayer, A., Landry, H.M., and Churchman, L.S. (2017). Pause & Go: from the discovery of RNA polymerase pausing to its functional implications. Curr Opin Cell Biol. *46*, 72-80.

Mazza, D., Abernathy, A., Golob, N., Morisaki, T., and McNally J.G. (2012). A benchmark for chromatin binding measurements in live cells. Nucleic Acids Res. *40*, e119.

McKinney, K., and Prives, C. (2002). Efficient Specific DNA Binding by p53 Requires both Its Central and C-Terminal Domains as Revealed by Studies with High-Mobility Group 1 Protein. Mol. Cell. Biol. *22*, 6797–6808.

McKnight, S.L., and Miller Jr., O.L. (1979). Post-replicative nonribosomal transcription units in D. melanogaster embryos. Cell *17*, 551–563.

McLure, K.G., and Lee, P.W. (1998). How p53 binds DNA as a tetramer. EMBO J. *17*, 3342–3350.

Melanson, B.D., Bose, R., Hamill, J.D., Marcellus, K.A., Pan, E.F., and McKay, B.C. (2011). The role of mRNA decay in p53-induced gene expression. RNA *17*, 2222–2234.

Mellis, I.A., Gupte, R., Raj, A., and Rouhanifard, S.H. (2017). Visualizing adenosine to inosine RNA editing in single mammalian cells. Nat. Methods *14*, 801–804.

Menendez, D., Inga, A., and Resnick, M.A. (2009). The expanding universe of p53 targets. Nat. Rev. Cancer *9*, 724–737.

Meyer, S., Temme, C., and Wahle, E. (2010). Messenger RNA Turnover in Eukaryotes: Pathways and Enzymes. Crit. Rev. Biochem. Mol. Biol. *39*, 197–216.

Moffit, J.R., Hao, J., Wang, G., Chen, K.H., Babcock, H.P., and Zhuang, X. (2016). High-throughput single-cell gene-expression profiling with multiplexed error-robust fluorescence in situ hybridization. Proc. Natl. Acad. Sci. U.S.A. *113*, 11046–11051.

Molina, N., Suter, D.M., Cannavo, R., Zoller, B., Gotic, I., and Naef, F. (2013). Stimulus-induced modulation of transcriptional bursting in a single mammalian gene. Proc. Natl. Acad. Sci. U.S.A. *110*, 20563–20568.

Moor, A.E., Golan, M., Massasa, E.E., Lemze, D., Weizman, T., Shenhav, R., Baydatch, S., Mizrahi, O., Winkler, R., Golani, O., et al. (2017). Global mRNA polarization regulates translation efficiency in the intestinal epithelium. Science *357*, 1299–1303.

Morisaki, T., Müller, W.G., Golob, N., Mazza, D., and McNally, J.G. (2014). Single-molecule analysis of transcription factor binding at transcription sites in live cells. Nat. Commun. *5*, 4456.

Mosner, J., Mummenbrauer, T., Bauer, C., Sczakiel, G., Grosse, F., and Deppert, W. (1995). Negative feedback regulation of wild-type p53 biosynthesis. EMBO J. *14*, 4442–4449.

Mueller, F., Senecal, A., Tantale, K., Marie-Nelly, H., Ly, N., Collin, O., Basyuk, E., Bertrand, E., Darzacq, X., and Zimmer, C. (2013). FISH-quant: automatic counting of transcripts in 3D FISH images. Nat. Methods *10*, 277–278.

Mueller, F., Wach, P, and McNally, J.G. (2008). Evidence for a common mode of transcription factor interaction with chromatin as revealed by improved quantitative fluorescence recovery after photobleaching. Biophys. J. *94*, 3323–3339.

Muhar, M., Ebert, A., Neumann, T., Umkehrer, C., Jude, J., Wieshofer, C., Rescheneder, P., Lipp, J.J., Herzog, V.A., Reichhoff, B. et al. (2018). SLAM-Seq defines direct gene-regulatory functions of the BRD4-MYC axis. Science *360,* 800-805.

Munsky, B., Neuert, G., and van Oudenaarden, A. (2012). Using Gene Expression Noise to Understand Gene Regulation. Science *336*, 183–187.

Muramoto, T., Cannon, D., Gierlínski, M., Corrigan, A., Barton, G.J., and Chubb, J.R. (2012). Live imaging of nascent RNA dynamics reveals distinct types of transcriptional pulse regulation. PNAS *109,* 7350-7355

Murphy, K.F., Balázsi, G., and Colline, J.J. (2007). Combinatorial promoter design for engineering noisy gene expression. Proc. Natl. Acad. Sci. U.S.A. *104*, 12726–12731.

Murphy, L.O., Smith, S., Chen, R.-H., Fingar, D.C., and Blenis, J. (2002). Molecular interpretation of ERK signal duration by immediate early gene products. Nat. Cell Biol. *4*, 556–564.

Murray-Zmijewski, F., Slee, E.A., and Lu, X. (2008). A complex barcode underlies the heterogeneous response of p53 to stress. Nat. Rev. Mol. Cell Biol. *9*, 702–712.

Nagaich, A.K., Appella, E., and Harrington, R.E. (1997a). DNA bending is essential for the site-specific recognition of DNA response elements by the DNA binding domain of the tumor suppressor protein p53. J. Biol. Chem. *272*, 14842–14849.

Nagaich, A.K., Zhurkin, V.B., Sakamoto, H., Gorin, A.A., Clore, G.M., Gronenborn, A.M., Appella, E., and Harrington, R.E. (1997b). Architectural accommodation in the complex of four p53 DNA binding domain peptides with the p21/waf1/cip1 DNA response element. J. Biol. Chem. *272*, 14830–14841.

Nagaich, A.K., Zhurkin, V.B., Durell, S.R., Jernigan, R.L., Appella, E., and Harrington, R.E. (1999). p53-induced DNA bending and twisting: p53 tetramer binds on the outer side of a DNA loop and increases DNA twisting. Proc. Natl. Acad. Sci. U.S.A. *96*, 1875–1880.

Nakamura, S., Roth, J.A., and Mukhopadhyay, T. (2000). Multiple Lysine Mutations in the C-Terminal Domain of p53 Interfere with MDM2-Dependent Protein Degradation and Ubiquitination. Mol. Cell. Biol. *20*, 9391–9398.

Nelson, D.E., Ihekwaba, A.E.C, Elliott, M., Johnson, J.R., Gibney, C.A., Foreman, B.E., Nelson, G. et al. (2004). Oscillations in NF-kB signaling control the dynamics of gene expression. Science *306*, 704–708.

Nguyen, T.T., Scimeca, J.C., Filloux, C., Peraldi, P., Carpentier, J.L., and Van Obberghen, E. (1993). Co-regulation of the mitogen-activated protein kinase, extracellular signal-regulated kinase 1, and the 90-kDa ribosomal S6 kinase in PC12 cells. J. Biol. Chem. *268*, 9803–9810.

Nicolas, D., Zoller, B., Suter, D.M., and Naef, F. (2018). Modulation of transcriptional burst frequency by histone acetylation. Proc. Natl. Acad. Sci. U.S.A. *115*, 7153–7158.

Nielson, S., Bassler, N., Grzanka, L., Swakon, J., Olko, P., Andreassen, C.N., Alsner, J., and Sorensen, B.S. (2018). Optimal reference genes for normalization of qPCR gene expression data from proton and photon irradiated dermal fibroblasts. Sci. Rep. *8*, 121688.

Nikulenkov, F., Spinnler, C., Li, H., Tonelli, C., Shi, Y., Turunen, M., Kivioja, T., Ignatiev, I., Kel, A., Taipale, J., and Selivanova, G. (2012). Insights into p53 transcriptional function via genome-wide chromatin occupancy and gene expression analysis. Cell Death Differ. *19*, 1992–2002.

Ninomiya, K., Kataoka, N., and Hagiwara, M. (2011). Stress-response maturation of Clk1/4 pre-mRNAs promotes phosphorylation of SR splicing factors. JCB *195(1):27.*

Oda, K., Arakawa, H., Tanaka, T., Matsuda, K., Tanikawa, C., Mori, T., Nishimori, H., Tamai, K., Tokino, T., Nakamura, Y., et al. (2000). p53AIP1, a potential mediator of p53-dependent apoptosis, and its regulation by Ser-46-phosphorylated p53. Cell *102*, 849–862.

Oeffinger, M., and Zenklusen, D. (2012). To the pore and through the pore: A story of mRNA export kinetics. BBA Gene Regulatory Mechanisms *1819*, 494–506.

Oldfield, C.J., Jingwei, M., Yang, J.Y., Yang, M.Q., Uversky, V.N., and Dunker, A.K. (2008). Flexible nets: disorder and induced fit in the associations of p53 and 14-3-3 with their parents. BMC Genom. *9,* 1471-2164

Olivier, M., Eeles, R., Hollstein, M., Khan, M.A., Harris, C.C., and Hainaut, P. (2002). The IARC TP53 database: New online mutation analysis and recommendations to users. Human Mutation *19*, 607–614.

Orphanides, G., and Reinberg, D. (2002). A Unified Theory of Gene Expression. Cell *108*, 439–451.

Ouellet, J. (2016). RNA Fluorescence with Light-Up Aptamers. Front. Chem. *4*, 1–12.

Ozbudak, E.M., Thattai, M., Kurtser, I., Grossman, A.D., and van Oudenaarden, A. (2002). Regulation of noise in the expression of a single gene. Nature Genetics *31*, 69–73.

Padovan-Merhar, O., Nair, G.P., Biasch, A.G., Mayer, A., Scarfone, S., Foley, S.W., Wu, A.R., Churchman, L.S., Singh, A., and Raj, A. (2015). Single mammalian cells compensate for differences in cellular volume and DNA copy number through independent global transcriptional mechanisms. Mol. Cell *58*, 339–352.

Parker, R. (2012). RNA Degradation in Saccharomyces cerevisae. Genetics *191*, 671–702.

Paige, J.S., Wu, K.Y., and Jaffrey, S.R. (2011). RNA mimics of green fluorescent protein. Science *333,* 642–646.

Pant, V., Xiong, S., Jackson, J.G., Post, S.M., Abbas, H.A., Quintás-Cardama, A., Hamir, A.N., and Lozano, G. (2013). The p53–Mdm2 feedback loop protects against DNA damage by inhibiting p53 activity but is dispensable for p53 stability, development, and longevity. Genes Dev. *27*, 1857–1867.

Paré, A., Lemons, D., Kosman, D., Beaver, W., Freund, Y., and McGinnis, W. (2009). Visualization of Individual Scr mRNAs during Drosophila Embryogenesis Yields Evidence for Transcriptional Bursting. Curr Biol. *19,* 2037-2042.

Paulsson, J. (2004). Summing up the noise in gene networks. Nature *427*, 415–418.

Pavletich, N.P., Chambers, K.A., and Pabo, C.O. (1993). The DNA-binding domain of p53 contains the four conserved regions and the major mutation hot spots. Genes Dev. *7,* 2556–2564.

Peccoud, J., and Ycart, B. (1995). Markovian Modeling of Gene-Product Synthesis. Theor. Popul. Biol. *48*, 222–234.

Pei, D., Zhang, Y., and Zheng, J. (2012). Regulation of p53: A collaboration between Mdm2 and MdmX. Oncotarget *3*, 228–235.

Pelechano, V., Wei, W., and Steinmetz, L.M. (2015). Widespread Co-translational RNA Decay Reveals Ribosome Dynamics. Cell *161*, 1400–1412.

Petersson, J., Ageberg, M., Sandén, C., Olofsson, T., Gullberg, U., and Drott, K. (2012). The p53 target gene TRIM22 directly or indirectly interacts with the translation initiation factor eIF4E and inhibits the binding of eIF4E to eIF4G. Biol. of the Cell *104*, 462-475.

Pichon, X., Bastide, A., Safieddine, A., Chouaib, R., Samacoits, A., Basyuk, E., Peter, M., Mueller, F. and Bertrand, E. (2016). Visualization of single endogenous polysomes reveals the dynamics of translation in live human cells. JCB *6*, 769-781.

Porrua, O., and Libri, D. (2015). Transcription termination and the control of the transcriptome: why, where and how to stop. Nat. Rev. Mol. Cell. Biol. *16*, 190–202.

Porter, J.R., Fisher, B.E., and Batchelor, E. (2016). p53 pulses diversify target gene expression dynamics in an mRNA half-life-dependent manner and delineate co-regulated target gene subnetworks. Cell Syst. *2*, 272–282.

Proteinatlas.org; The Human Protein Atlas, version 19 (see also Uhlén et al., 2010; Thul et al., 2017)

Ptashne, M., and Gann, A. (2002). Genes and Signals. Cold Spring Harb. Lab. Press 978-087969633-7.

Purvis, J.E., and Lahav, G. (2013). Encoding and decoding cellular information through signaling dynamics. Cell *152*, 945–956.

Purvis, J.E., Karhohs, K.W., Mock, C., Batchelor, E., Loewer, A., and Lahav, G. (2012). p53 dynamics control cell fate. Science *336*, 1440–1444.

Qian, H., Wang, T., Naumovski, L., Lopez C.D., and Brachmann, R.K. (2002). Groups of p53 target genes involved in specific p53 downstream effects cluster into different classes of DNA binding sites. Oncogene *21*, 7901–7911.

Raj, A., Peskin, C.S., Tranchina, D., Vargas, D.Y., and Tyagi, S. (2006). Stochastic mRNA Synthesis in Mammalian Cells. PLoS Biol. *4,* (10):e309.

Raj, A., van den Bogaard, P., Rifkin, S.A., van Oudenaarden, A., and Tyagi, S. (2008). Imaging individual mRNA molecules using multiple singly labeled probes. Nat. Methods *5*, 877–879.

Raj, A., and van Oudenaarden, A. (2008). Nature, nurture, or chance: stochastic gene expression and its consequences. Cell *135*, 216–226.

Raj, A., and van Oudenaarden, A. (2009). Single-molecule approaches to stochastic gene expression. Annu. Rev. Biophys. *38*, 255–270.

Raj lab (Raj, A. et al.), n.d. StarSearch, retrieved from https://rajlab.seas.upenn.edu/resources

Ran, F.A., Hsu, P.D., Lin, C.Y., Gootenberg, J.S., Konermann, S., Trevino, A.E., Scott, D.A., Inoue, A., Matoba, S., Zhang, Y., and Zhang, F. (2013). Double nicking by RNA-guided CRISPR Cas9 for enhanced genome editing speci- ficity. Cell 154, 1380–1389.

Raser, J.M., and O'Shea, E.K. (2004). Control of stochasticity in eukaryotic gene expression. Science *304,* 1811–1814.

Rashi-Elkeles, S., Warnatz, H.-J., Elkon, R., Kupershtein, A., Chobod, Y., Paz, A., Amstislavskyi, V., Sultan, M., Safer, H., Nietfeld, W., et al. (2014). Parallel Profiling of the Transcriptome, Cistrome, and Epigenome in the Cellular Response to Ionizing Radiation. Science Signaling *7,* 1–11.

Raycroft, L., Wu, H.Y., and Lozano, G. (1990). Transcriptional activation by wild-type but not transforming mutants of the p53 anti-oncogene. Science *249*, 1049–1051.

Reed, S.M., and Quelle, D.E. (2015). p53 Acetylation: Regulation and Consequences. Cancers *7*, 30–69.

Reiter, F., Wienerroither, S., and Stark, A. (2017). Combinatorial function of transcription factors and cofactors. Curr. Opin. Genet. Dev. *43*, 73–81.

Reisser, M., Palmer, A., Popp, A.P., Jahn, C., Weidinger, G., and Gebhardt, C.M. (2018). Single-molecule imaging correlates decreasing nuclear volume with increasing TF-chromatin associations during zebrafish development. Nat. Commun. *9*, 5218.

Richard, P., and Manley, J.L. (2009). Transcription termination by nuclear RNA polymerases. Genes Dev. *23*, 1247–1269.

Riley, K.J.-L., and Maher III, L.J., A. (2007). p53–RNA interactions: New clues in an old mystery. RNA *13*, 1825–1833.

Riley, T., Sontag, E., Chen, P., and Levine, A. (2008). Transcriptional control of human p53-regulated genes. Nat. Rev. Mol. Cell Biol. *9*, 402–412.

Roeder, R.G., and Rutter, W.J. (1969). Multiple forms of DNA-dependent RNA polymerase in eukaryotic organisms. Nature *224*, 234–237.

Rosenfeld, N., Young, J.W., Alon, U., Swain, P.S., and Elowitz, M.B. (2005). Gene Regulation at the Single-Cell Level. Science *307*, 1962–1865.

Rouhanifard, S.H., Mellis, I.A., Dunagin, M., Bayatpour, S., Jiang, C.L. Dardani, I., Symmons, O., Emert, B., Torre, E., Cote, A., Sullivan, A., Stamatoyannopoulos, J.A., and Raj, A. (2019). ClampFISH detects individual nucleic acid molecules using click chemistry–based amplification. Nat. Biotechnol. *37*, 84–89.

Roux, P.P., and Topisirovic, I. (2012). Regulation of mRNA Translation by Signaling Pathways. Cold Spring Harb. Perspect. Biol. *4*, a012252.

Russo, J., Heck, A.M., Wilusz, J., and Wilusz, C.J. (2017). Metabolic labeling and recovery of nascent RNA to accurately quantify mRNA stability. Methods *120*, 39–48.

Rust, R.R., Baldisseri, D.M., and Weber, D.J. (2000). Structure of the negative regulatory domain of p53 bound to S100(ββ). Nat. Struct. Biol. *7,* 570-574

Ryoo, H.D. and Vasudevan, D. (2017). Two distinct nodes of translational inhibition in the Integrated Stress Response. BMB Reports *50,* 539-545.

Sage, D., and Unser, M. (2003). Teaching image-processing programming in Java. IEEE Xplore *20*, 43–52.

Sahu, G., Wang, D., Chen, C.B., Zhurkin, V.B., Harrington, R.E., Appella, E., Hager, G.L., and Nagaich, A.K. (2010). p53 Binding to Nucleosomal DNA Depends on the Rotational Positioning of DNA Response Element. J. Biol. Chem. *285*, 1321–1332.

Saji, S., Nakashima, S., Hayashi, S., Toi, M., Saji, S., and Yoshinori, N. (1999). Overexpression of MDM2 in MCF-7 Promotes Both Growth Advantage and p53 Accumulation in Response to Estradiol. Jpn. J. Cancer Res. *90*, 210–218.

Sakaguchi, K., Herrera, J.E., Saito, S., Miki, T., Bustin, M., Vassilev, A., Anderson, C.W., and Appella, E. (1998). DNA damage activates p53 through a phosphorylation-acetylation cascade. Genes Dev. *12*, 2831–2841.

Saldi, T., Cortazar, M.A., Sheridan, R.M., and Bentley, D.L. (2016). Coupling of RNA Polymerase II Transcription Elongation with Pre-mRNA Splicing. J Mol Biol *428,* 2623-2635.

Samacoits, A., Chouaib, R., Safieddine, A., Traboulsi, A.-M., Ouyang, W., Zimmer, C., Peter, M., Bertrand, E., Walter, T., and Mueller, F. (2018). A computational framework to study sub-cellular RNA localization. Nat. Commun. *9*, 4584.

Samuels-Lev, Y., O'Connor, D.J., Bergamaschi, D., Trigiante, G., Hsieh, J.-K., Zhong, S., Campargue, L., Naumovski, L., Crook, T., and Lu, X. (2001). ASPP Proteins Specifically Stimulate the Apoptotic Function of p53. Mol. Cell *8*, 781–794.

Sanchez, A., Chouby, S., and Kondev, J. (2013). Stochastic models of transcription: From single molecules to single cells. Methods *62*, 13–25.

Sanchez, A., and Golding, I. (2013). Genetic determinants and cellular constraints in noisy gene expression. Science *342*, 1188–1193.

Santos, S.D.M., Verveer, P.J., and Bastiaens, P.I.H. (2007). Growth factor-induced MAPK network topology shapes Erk response determining PC-12 cell fate. Nat. Cell Biol. *9*, 324–330.

Sato, Y., Mukai, M., Ueda, J., Muraki, M., Stasevich, T.J., Horikoshi, N., Kujirai, T., Kita, H., Kimura T., Hira, S., et al. (2013). Genetically encoded system to track histone modification in vivo. Sci Rep *3*, 2436.

Saunders, A., Core, L.J., and Lis, J.T. (2006). Breaking barriers to transcription elongation. Nat. Rev. Mol. Cell Biol. *7*, 557–567.

Schindelin, J., Arganda-Carreras, I., Frise, E., Kaynig, V., Longair, M., Pietzsch, T., Preibisch, S., Rueden, C., Saalfeld, S., Schmid, B., et al. (2012). Fiji: an open-source platform for biological-image analysis. Nat. Methods. *9*, 676–682.

Schofield, J.A., Duffy, E.E., Kiefer, L., Sullivan, M.C., and Simon, M.D. (2018). TimeLapse-seq: adding a temporal dimension to RNA sequencing through nucleoside recoding. Nat. Methods. *15*, 221–225.

Scholes, C., DePace, A.H., and Sánchez, A. (2017). Combinatorial gene regulation through kinetic control of the transcription cycle. Cell Syst. *25*, 97–108.

Schwalb, B., Michel, M., Zacher, B., Frühauf, K., Demel, C., Tresch, A., Gagneur, J., and Cramer, P. (2016). TT-seq maps the human transient transcriptome. Science *352*, 1225–1228.

Schwanhäusser, B., Busse, D., Li, N., Dittmar, G., Schuchhardt, J., Wolf, J., Chen, W., and Selbach, M. (2011). Global quantification of mammalian gene expression control. Nature *473*, 337–342.

Segal, E., Raveh-Sadka, T., Schroeder, M., Unnerstall, U., and Gaul, U. (2008). Predicting expression patterns from regulatory sequence in *Drosophila* segmentation. Nature *451*, 535–540.

Senecal, A., Munsky, B., Proux, F., Ly, N., Braye, F.E., Zimmer, C., Mueller, F., and Darzacq, X. (2014). Transcription factors modulate c-Fos transcriptional bursts. Cell Rep. *8*, 75–83.

Setty, Y., Mayo, A.E., Surette, M.G., and Alon, U. (2003). Detailed map of a cis-regulatory input function. Proc. Natl. Acad. Sci. U.S.A. *100*, 7702–7707.

Shaked, H., Shiff, I., Kott-Gutkowski, M., Siegfried, Z., Haupt, Y., and Simon, I. (2008). Chromatin immunoprecipitation-on-chip reveals stress-dependent p53 occupancy in primary normal cells but not in established cell lines. Cancer Res. *68*, 9671–9677.

Sharp, J.A., Plant, J.J., Ohsumi, T.K., Borowsky, M., and Blower, M.D. (2011). Functional analysis of the microtubule-interacting transcriptome. Mol. Biol. Cell *22*, 4312–4323.

Sharungbam, G.D., Schwager, C., Chiblak, S., Brons, S., Hlatky, L., Haberer, T., Debus, J., and Abdollahi, A. (2012). Identification of stable endogenous control genes for transcriptional profiling of photon, proton and carbon-ion irradiated cells. Radiat. Oncol. *7*, 1–12.

Shalem, O., Dahan, O., Levo, M., Rodriguez Martinez, M., Furman, I., Segal, E., and Pilpel, Y. (2008). Transient transcriptional responses to stress are generated by opposing effects of mRNA production and degradation. Mol. Syst. Biol. *4*, 4.

Shav-Tal, Y., Darzacq, X., Shenoy, S.M., Fusco, D., Janicki, S.M., Spector, D.L., and Singer, R.H. (2004). Dynamics of Single mRNPs in Nuclei of Living Cells. Science *304*, 1797–1800.

Sheng, C. (2018). Cellular heterogeneity in the DNA damage response is determined by cell cycle specific p21 degradation. PhD Thesis, Humboldt-Universität zu Berlin

Sheng, C., Mendler, I.-H., Rieke, S., Snyder, P., Jentsch, M., Friedrich, D., Drossel, B., and Loewer, A. (2019). PCNA-Mediated Degradation of p21 Coordinates the DNA Damage Response and Cell Cycle Regulation in Individual Cells. Cell Rep. *27*, 48–58.

Sherman, M.S., Lorenz, K., Hunter Lanier, M., and Cohen, B.A. (2015). Cell-to-cell variability in the propensity to transcribe explains correlated fluctuations in gene expression. Cell Syst. *1*, 315–325.

Shi, X., Kachirskaia, I., Yamaguchi, H., West, L.E., Wen, H., Wang, E.W., Dutta, S., Appella, E., and Gozani, O. (2007). Modulation of p53 Function by SET8-Mediated Methylation at Lysine 382. Mol. Cell *27*, 636–646.

Sims III, R.J., Subhrangsu, S.M., and Reinberg, D. (2004). Recent highlights of RNA-polymerase-II-mediated transcription. Curr. Opin. Cell Biol. *16*, 263–271.

Singh, A., and Bokes, P. (2012). Consequences of mRNA Transport on Stochastic Variability in Protein levels. Biophys. J. *103*, 1087-1096

Singh, J., and Padgett, R.A. (2009). Rates of *in situ* transcription and splicing in large human genes. Nat. Struc. Mol. Biol. *16*, 1128–1133.

Singh, A., Razooky, B., Cox, C.D., Simpson, M.L., and Weinberger, L.S. (2010). Transcriptional Bursting from the HIV-1 Promoter Is a Significant Source of Stochastic Noise in HIV-1 Gene Expression. Biophysical J. *98*, 32–34.

Singh, K.S., Qiao, Z., Song, L., Jani, V., Rice, W., Eng, E., Coleman, R.A., and Liu, W.-L. (2016). Structural visualization of the p53/RNA polymerase II assembly. Genes Dev. *30,* 2527-2537.

Skinner, S.O., Xu, H., Nagarkar-Jaiswal, S., Freire, P.R., Zwaka, T.P., and Golding, I. (2016). Single-cell analysis of transcription kinetics across the cell cycle. Elife *5*, e12175.

Smeenk, L., van Heeringen, S.J., Koeppel, M., Gilbert, B., Janssen-Megens, E., Stunnenberg, H.G., and Lohrum, M. (2011). Role of p53 serine 46 in p53 target gene regulation. PLoS One *6,* e17574.

Smith, J., Tho, L.M., Xu, N., and Gillespie, D.A. (2010). Chapter 3 - The ATM–Chk2 and ATR–Chk1 Pathways in DNA Damage Signaling and Cancer. Adv. Cancer Res. *108,* 73–112.

Snijder, B., and Pelkmans, L. (2011). Origins of regulated cell-to-cell variability. Nat. Rev. Mol. Cell. Biol. *12*, 119–125.

Sobell, H.M. (1985). Actinomycin and DNA transcription. Proc. Natl. Acad. Sci. U.S.A. *82*, 5328–5331.

Song, W., Filonov, G.S., Kim, H., Hirsch, M., Li, X., Moon, J.D., and Jaffrey, S.R. (2017). Imaging RNA polymerase III transcription using a photostable RNA-fluorophore complex. Nat. Chem. Biol. *13*, 1187–1194.

Song, W., Strack, R.L., Svensen, N., and Jaffrey, S.R. (2014). Plug-and-Play Fluorophores Extend the Spectral Properties of Spinach. J. Am. Chem. Soc. *136*, 1198–1201.

Spitz, F., and Furlong E.E.M., (2012). Transcription factors: from enhancer binding to developmental control. Nat.Rev.Genet. *13,* 613-626

Stewart-Ornstein, J., Cheng, H.W., and Lahav, G. (2017). Conservation and Divergence of p53 Oscillation Dynamics across Species. Cell Systems *5*, 410–417.

Stewart-Ornstein, J., and Lahav, G. (2017). p53 dynamics in response to DNA damage vary across cell lines and are shaped by efficiency of DNA repair and activity of the kinase ATM. Science Signaling *10*, eaah6671.

Stoeckius, M., Hafemeister, C., Stephenson, W., Houck-Loomis, B., Chattopadhyay, P.K., Swerdlow, H., Satija, R., and Smibert, P. (2017). Simultaneous epitope and transcriptome measurement in single cells. Nat. Methods *14,* 865-868.

Stoeger, T., Battich, N., and Pelkmans, L. (2016). Passive Noise Filtering by Cellular Compartmentalization. Cell *164*, 1151–1161.

Stommel, J.M., Marchenko, N.D., Jimenez, G.S., Moll, U.M., Hope, T.J., and Wahl, G.M. (1999). A leucine-rich nuclear export signal in the p53 tetramerization domain: regulation of subcellular localization and p53 activity by NES masking. EMBO J. *18*, 1660–1672.

Strasen, J., Sarma, U., Jentsch, M., Bohn, S., Sheng, C., Horbelt, D., Knaus, P., Legewie, S., and Loewer, A. (2018). Cell-specific responses to the cytokine TGFβ are determined by variability in protein levels. Mol. Syst. Biol. *14*, e7733.

Süel, G.M., Kulkarni, R.P., Dworkin, J., Garcia-Ojalvo, J., and Elowitz, M.B. (2007). Tunability and noise dependence in differentiation dynamics. Science *315*, 1716–1719.

Su, D., Wang, X., Campbell, M.R., Song, L., Safi, A., Crawford, G.E., and Bell, D.A. (2015). Interactions of Chromatin Context, Binding Site Sequence Content, and Sequence Evolution in Stress-Induced p53 Occupancy and Transactivation. PloS Genetics *11*, e1004885.

Sullivan, K.D., Galbraith, M.D., Andrysik, Z., and Espinosa, J.M. (2018). Mechanisms of transcriptional regulation by p53. Cell Death Differ. *25*, 133–143.

Suter, D.M., Molina, N., Gatfield, D., Schneider, K., Schibler, U., and Naef, F. (2011a). Mammalian genes are transcribed with widely different bursting kinetics. Science *332*, 472–474.

Suter, D.M., Molina, N., Naef, F., and Schibler, U. (2011b). Origins and consequences of transcriptional discontinuity. Curr. Opin. Cell Biol. *23*, 657–662.

Svensson, V., and Pachter, L. (2018). RNA Velocity: Molecular Kinetics from Single-Cell RNA-Seq. Mol. Cell *72,* 7-9.

Svensson, V., Vento-Tormo, R. and Teichmann, S. (2018). Exponential scaling of single-cell RNA-seq in the past decade. Nat. Prot. *13,* 599-604.

Swain, P.S., Elowitz, M.B., and Siggia, E.D. (2002). Intrinsic and extrinsic contributions to stochasticity in gene expression. Proc. Natl. Acad. Sci. U.S.A. *99*, 12795–12800.

Swetzig, W.M., Wang, J., and Das, G.M. (2016). Estrogen receptor alpha (ERα/ESR1) mediates the p53-independent overexpression of MDM4/MDMX and MDM2 in human breast cancer. Oncotarget *7*, 16049–16069.

Sykes, S.M., Mellert, H.S., Holbert, M.A., Li, K., Marmorstein, R., Lane, W.S., and McMahon, S.B. (2006). Acetylation of the p53 DNA-binding domain regulates apoptosis induction. Mol. Cell *24*, 841–851.

Sylwestrak, E.L., Rajasethupathy, P., Wright, M.A., Jaffe, A., and Deisseroth, K. (2016). Multiplexed Intact-Tissue Transcriptional Analysis at Cellular Resolution. Cell *164*, 792–804.

Tafvizi, A., Huang, F., Leith, J.S., Fersht, A.R., Mirny, L.A., and van Oijen, A.M. (2008). Tumor suppressor p53 slides on DNA with low friction and high stability. Biophys. J. *95*, L01–3.

Tanaka, H., Arakawa, H., Yamaguchi, T., Shiraishi, T., Fukuda, S., Matsui, K., Takei, Y., and Nakamura, Y. (2000). A ribonucleotide reductase gene involved in a p53-dependent cell-cycle checkpoint for DNA damage. Nature *404*, 42–49.

Tanay, A., and Regev, A. (2017). Scaling single-cell genomics from phenomenology to mechanism. Nature *541*, 331–338.

Tang, Y., Zhao, W., Chen, Y., Zhao, Y., and Gu, W. (2008). Acetylation Is Indispensable for p53 Activation. Cell *133*, 612–626.

Tani, H., and Akimitsu, N. (2012). Genome-wide technology for determining RNA stability in mammalian cells. RNA Biol. *9*, 1233–1238.

Tay, S., Hughey, J.J., Lee, T.K., Lipniacki, T., Quake, S.R., and Covert, M.W. (2010). Single-cell NF-kB dynamics reveal digital activation and analogue information processing. Nature *466*, 267–271.

Teif, V.B., Erdel, F., Beshnova, D.A., Vainshtein, Y., Mallm, J.-P., and Rippe, K. (2013). Taking into account nucleosomes for predicting gene expression. Methods *62*, 26–38.

Thattai, M., and van Oudenaarden, A. (2001). Intrinsic noise in gene regulatory networks. Proc. Natl. Acad. Sci. U.S.A. *98*, 8614–8619.

Thul, P.J., Akesson, L., Wiking, M., Mahdessian, D., Geladaki, A., Blal, H.A, Alm, T., Asplund, A., Björk, L., Breckels, L.M. et al. (2017). A subcellular map of the human proteome. Science *356,* 820-834.

Toledo, F., and Wahl, G.M. (2006). Regulating the p53 pathway: in vitro hypotheses, in vivo veritas. Nat. Rev. Cancer *6*, 909–923.

Tong, Q., Cui, G., Botuyan, M.V., Rothbart, S.B., Hayashi, R., Musselman, C.A., Singh, N., Appella, E., Strahl, B.D., Mer, G., et al. (2015). Structural plasticity of methyllysine recognition by the tandem tudor domain of 53BP1. Structure *23*, 312–321.

Tournillon, A.-S., López, I., Malbert-Colas, L., Finakly, S., Naski, N., Olivares-Illana, V., Karakostis, K., Vojtesek, B., Nylander, K., and Fåhraeus, R. (2017). p53 binds the *mdmx* mRNA and controls its translation. Oncogene *36*, 723–730.

Trapnell, C., Cacchiarelli, D., Grimsby, J., Pokharel, P., Li, S., Morse, M., Lennon, N.J., Livak, K.J., Mikkelsen, T.S., and Rinn, J.L. (2014). The dynamics and regulators of cell fate decisions are revealed by pseudotemporal ordering of single cells. Nat. Biotechnol. *32,* 381-386.

Trcek, T., Chao, J.A., Larson, D.R., Park, H.Y., Zenklusen, D., Shenoy, S.M., and Singer, R.H. (2012). Single-mRNA counting using fluorescent in situ hybridization in budding yeast. Nat. Protoc. *7*, 408–419.

Trcek, T., Larson, D.R., Moldón, A., Query, C.C., and Singer, R.H. (2011). Single-molecule mRNA decay measurements reveal promoter- regulated mRNA stability in yeast. Cell *147*, 1484–1497.

Tyner, C., Barber, G.P., Casper, J., Clawson, H., Diekhans, M., Eisenhart, C., Fischer, C.M., Gibson, D., Navarro Gonzales, J., Guruvadoo, L. et al. (2017). The UCSC Genome Browser database: 2017 update. Nucleic Acid Res. *45,* 626-634.

Uhlén, M., Oksvold, P., Fagerberg, L., Lundberg, E., Jonasson, K., Forsberg, M., Zwahlen, M., Kampf, C., Wester, K., Wester, K., et al. (2010). Towards a knowledge-based Human Protein Atlas. Nature Biotechnology *28,* 1248-1250.

Urbanek, M.O., and Krzyzosiak, W.J. (2017). Discriminating RNA variants with single-molecule allele-specific FISH. Mutat. Res. *773*, 230–241.

Vaquerizas, J.M., Kummerfeld, S.K., Teichmann, S.A., and Luscombe, N.M. (2009). A census of human transcription factors: function, expression and evolution. Nat. Rev. Genet. *10*, 252–263.

Veprintsev, D.B., Freund, S.M., Andreeva, A., Rutledge, S.E., Tidow, H., Cañadillas, J.M., Blair, C.M., and Fersht, A.R. (2006). Core domain interactions in full-length p53 in solution. Proc. Natl. Acad. Sci. U.S.A. *103*, 2115–2119.

Vargas, D.Y., Raj, A., Marras, S.A.E., Kramer, F.R., and Tyagi, S. (2005). Mechanism of mRNA transport in the nucleus. Proc. Natl. Acad. Sci. U.S.A. *102*, 17008–17013.

Vargas, D.Y., Shah, K., Batish, M., Levandoski, M., Sinha, S., Marras, S.A.E., Schedl, P., and Tyagi, S. (2011). Single-Molecule Imaging of Transcriptionally Coupled and Uncoupled Splicing. Cell *147*, 1054–1065.

Vassilev, L.T., Vu, B.T., Graves, B., Carvajal, D., Podlaski, F., Filipovic, Z., Kong, N., Kammlott, U., Lukacs, C., Klein, C., Fotouhi, N., and Liu, E.A. (2004). In Vivo Activation of the p53 Pathway by Small-Molecule Antagonists of MDM2. Science *303*, 844–848.

Veloso, A., Kirkconnell, K.S., Magnuson, B., Biewen, B., Paulsen, M.T., Wilson, T.E., and Ljungman, M. (2014). Rate of elongation by RNA polymerase II is associated with specific gene features and epigenetic modifications. Genome Res. *24*, 896–905.

Vera, M., Biswas, J., Senecal, A., Singer, R.H., and Yoon Park, H. (2016). Single-Cell and Single-Molecule Analysis of Gene Expression Regulation. Annu. Rev. Genet. *50*, 267–291.

Verfaillie, A., Svetlichnyy, D., Imrichova, H., Davie, K., Fiers, M., Kalender Atak, Z., Hulselmans, G., Christiaens, V., and Aerts, S. (2016). Multiplex enhancer-reporter assays uncover unsophisticated TP53 enhancer logic. Genome Res. *26*, 882–895.

Vogelstein, B., Lane, D., and Levine, A. (2000). Surfing the p53 network. Nature *408*, 1–4.

Voss, T.C., and Hager, G.L. (2013). Dynamic regulation of transcriptional states by chromatin and transcription factors. Nat. Rev. Genet. *15*, 69–81.

Vousden, K.H., and Lu, X. (2002). Live or let die: The cell's response to p53. Nat. Rev. Cancer *2*, 594–604.

Vousden, K.H., and Prives, C. (2009). Blinded by the light: The growing complexity of p53. Cell *137*, 413–431.

Wade, M., Li, Y.C., and Wahl, G.M. (2013). MDM2, MDMX and p53 in oncogenesis and cancer therapy. Nat. Rev. Cancer *13*, 83–96.

Wadgaonkar, R., and Collins, T. (1999). Murine double minute (MDM2) blocks p53-coactivator interaction, a new mechanism for inhibition of p53-dependent gene expression. J. Biol. Chem. *274*, 13760–13767.

Walker, K.K., and Levine, A.J. (1996). Identification of a novel p53 functional domain that is necessary for efficient growth suppression. Proc. Natl. Acad. Sci. U.S.A. *93*, 15335–15340.

Wang, F., Flanagan, J., Su, N., Wang, L.C., Bui, S., Nielson, A., Wu, X., Vo, H.T., Ma, X.J., and Luo, Y. (2012). RNAscope: a novel in situ RNA analysis platform for formalin-fixed, paraffin-embedded tissues. J. Mol. Diagn. *13*, 22–29s.

Wang, Y., Schwedes, J.F., Parks, D., Mann, K., and Tegtmeyer, P. (1995). Interaction of p53 with its consensus DNA-binding site. Mol. Cell. Biol. *15*, 2157–2165.

Weake, V.M., and Workman, J.L. (2010). Inducible gene expression: diverse regulatory mechanisms. Nat. Rev. Genet. *11*, 426–437.

Weil, T.T., Parton, R.M., and Davis, I. (2010). Making the message clear: visualizing mRNA localization. Trends Cell Biol. *20,* 380-390.

Weinberg, R.A. (1995). The retinoblastoma protein and cell cycle control. Cell *81*, 323–330.

Weinberg, R.L., Veprintsev, D.B., Bycroft, M., and Fersht, A.R. (2005). Comparative binding of p53 to its promoter and DNA recognition elements. J. Mol. Biol. *248*, 589–596.

Werner, S.L., Barken, D., and Hoffmann, A. (2005). Stimulus specificity of gene expression programs determined by temporal control of IKK activity. Science *309*, 1857–1861.

West, L.E., and Gozani, O. (2011). Regulation of p53 function by lysine methylation. Epigenomics *3*, 361–369.

West, L.E., Roy, S., Lachmi-Weiner, K., Hayashi, R., Shi, X., Appella, E., Kutateladze, T.G., and Gozani, O. (2010). The MBT repeats of L3MBTL1 link SET8-mediated p53 methylation at lysine 382 to target gene repression. J. Biol. Chem. *285*, 37725–37732.

Wienert, B., Feng, S.J., Locke, M., Nguyen, D.N., Wyman, S.K., Kazane, K.R., Marson, A., Richardson, C.D., and Corn, J.E. (2018). Timed inhibition of CDC7 increases CRISPR-Cas9 mediated templated repair. bioRxiv, 500462.

Wingender, E., Schoeps, T., Haubrock, M., and Dönitz, J. (2015). TFClass: a classification of human transcription factors and their rodent orthologs. Nucleic Acid Res. *43*, D97–D102.

Wolfe, M.B., Goldstrohm, A.C., and Freddolino, P.L. (2019). Global analysis of RNA metabolism using bio-orthogonal labeling coupled with next-generation RNA sequencing. Methods *155*, 88–103.

Wong, V.C., Mathew, S., Ramli, R., Gaudet, S., and Miller-Jensen, K. (2019). Fold-Change Detection of NF-kB at Target Genes with Different Transcript Outputs. Biophys. J. *116,* 709-724

Wu, B., Miskolci, V., Sato, H., Tutucci, E., Kenworthy, C.A., Donnelly, S.K., Yoon, Y.J., Cox, D., Singer, R.H. and Hodgson, L. (2015). Synonymous modification results in high-fidelity gene expression of repetitive protein and nucleotide sequences. Genes Dev.. *29*, 876–886.

Wu, Q., Medina, S.G., Kushawah, G., DeVore, M.L., Castellano, L.A., Hand, J.M., Wright, M., and Bazzini, A.A. (2019). Translation affects mRNA stability in a codon-dependent manner in human cells. Elife *8,* e45396.

Yazinski, S.A., and Zou, L. (2016). Functions, Regulation, and Therapeutic Implications of the ATR Checkpoint Pathway. Annu. Rev. Genet. *50*, 155–173.

Yoshimura, H., and Ozawa, T. (2016). Monitoring of RNA Dynamics in Living Cells Using PUM-HD and Fluorescent Protein Reconstitution Technique. Methods Enzymol. *572*, 65–85.

Yu, X., and Buck, M.J. (2019). Defining TP53 pioneering capabilities with competitive nucleosome binding assays. Genome Res. *29*, 107–115.

Yudkovsky, N., Ranish, J.A., and Hahn, S. (2000). A transcription reinitiation intermediate that is stabilized by activator. Nature *408*, 225–229.

Yunger, S., Rosenfeld, L., Garini, Y., and Shav-Tal, Y. (2010). Single-allele analysis of transcription kinetics in living mammalian cells. Nat. Methods *7*, 631–633.

Zaccara, S., Tebaldi, T., Pederiva, C, Ciribilli, Y., Bisio, A., and Inga, A. (2014). p53-directed translational control can shape and expand the universe of *p53* target genes. Cell Death Differ. *21*, 1522–1534.

Zambrano, S., De Toma, I., Piffer, A, Bianchi, M.E., and Agresti, A. (2016). NF-κB oscillations translate into functionally related patterns of gene expression. Elife *5*, e09100.

Zaret, K.S., and Carroll, J.S. (2011). Pioneer transcription fators: establishing competence for gene expression. Genes & Dev., *25*, 2227-2241

Zechner, C., Unger, M., Pelet, S., Peter, M., and Koeppl, H. (2014). Scalable inference of heterogeneous reaction kinetics from pooled single-cell recordings. Nat. Methods *11*, 197–202.

Zenklusen, D., Larson, D.R., and Singer, R.H. (2008). Single-RNA counting reveals alternative modes of gene expression in yeast. Nat. Struct. Mol. Biol. *15*, 1263–1271.

Zhai, W., and Comai, L. (2000). Repression of RNA Polymerase I Transcription by the Tumor Suppressor p53. Mol. Cell. Biol. *20*, 5930–5938.

Zhu, N., Gu, L., Findley, H.W., and Zhou, M. (2005). Transcriptional repression of the eukaryotic initiation factor 4E gene by wild type p53. Biochem. Biophys. Res. Commun *335,* 1272-1279.

Ziegenhain, C., Vieth, B., Parekh, S., Hellmann, I., and Enard, W. (2018). Quantitative single-cell transcriptomics. Brief. Funct. Genomics *17*, 220–232.

Zoller, B., Nicolas, D., Molina, N., and Naef, F. (2015). Structure of silent transcription intervals and noise characteristics of mammalian genes. Mol. Syst. Biol. *11*, 823.

CHAPTER 7

SCIENTIFIC CONTRIBUTIONS

7.1. PUBLICATIONS

The research represented in this thesis has been partially published in peer-reviewed journals as listed below. Besides the presented data, I have been working on collaborative research projects focusing on the p53 signaling network and development of novel live-cell RNA imaging techniques. Resulting publications have been peer reviewed and contributions to these collaborative efforts are stated in each publication.

Stochastic transcription in the p53-mediated response to DNA damage is modulated by burst frequency. Friedrich D, Friedel L, Finzel A, Herrmann A, Preibisch S, and Loewer A; Molecular Systems Biology, December 2, 2019

PCNA-mediated degradation of p21 coordinates the DNA damage response and cell cycle regulation in individual cells. Sheng C, Mendler IH, Jentsch M, Friedrich D, Drossel B, Loewer A; Cell reports, April 2, 2019

Comparing Agent Based Delivery of DNA and PNA FIT-Probes for Multicolor mRNA Imaging. Chamiolo J, Fang G, Hoevelmann F, Friedrich D, Knoll A, Loewer A and Seitz O; ChemBioChem, February 15, 2019

A bright FIT-PNA hybridization probe for the state specific analysis of a C—>U RNA edit via FRET in a binary system. Fang G, Chamiolo J, Hoevelmann F, Kanowski S, Friedrich D, Loewer A , Meier JC, Seitz O; Chemical Science, May 2, 2018

Excitability in the p53 network mediates robust signaling with tunable activation thresholds in single cells. Moenke G, Cristiano E, Finzel A, Friedrich D, Herzel H, Falcke M and Loewer A.; Scientific Reports, April 18, 2017

7.2. AWARDS

Prizes and fellowships awarded for the presented research in this thesis are listed below.

2017 EMBO Poster prize, IMB Conference Gene Regulation by the numbers, Mainz
2017 Prize for the best talk, BIMSB/CRG Student Symposium, Barcelona
2016 Young Investigator Award, Advanced Lecture Course Systems Biology, Innsbruck
2016 Travel Award, Advanced Lecture Course on Systems Biology, Innsbruck
2016 Prize for the best talk, FMP/MDC Student Retreat, Joachmistal
2015 Joachim Herz Foundation Add-On Fellowship for interdisciplinary Research
2015 Poster Prize, FMP/MDC Student Retreat, Bad Saarow

7.3. SEMINARS, TALKS & POSTER PRESENTATIONS

Furthermore, the content of this thesis has been presented to an international scientific audience in seminars and conferences in the format of posters and talks select from abstracts.

2018, Oct	Poster, Berlin Institute for Medical Systems Biology (GER): Berlin Summer Meeting, Grand BIMSB Opening
2018, Aug	Seminar, Harvard Medical School, Boston (USA): Institute for Systems Biology
2018, Aug	Seminar, Harvard Medical School, Boston (USA): Institute for Cell Biology
2018, Aug	Seminar, University of Massachusetts, Worcester (USA): RNA Therapeutics Institute
2018, Mar	Talk, Ginosar, (ISR): Winter School Chromatin & Gene Expression
2018, Mar	Seminar, Technion Israel Institute of Technology, Haifa (ISR): Faculty for Biomedical Engineering
2018, Feb	Poster, BIOTEC Forum, Dresden (GER): Biophysics of the nucleus
2017, Oct	Poster, EMBL, Heidelberg (GER): Seeing is believing
2017, Jun	Selected Talk, DKFZ, Heidelberg (GER): Systems Biology of Human Disease
2017, Jun	Selected Talk, CRG, Barcelona (ESP): Joint CRG/BIMSB Retreat
2017, Jun	Selected Talk, Berlin Institute for Medical Systems Biology, Berlin (GER): Berlin Summer Meeting, Smaller, faster, clearer: Imaging gene regulation from DNA to RNA to Protein
2017, Jun	Poster, IMB, Mainz (GER): Gene regulation by the numbers
2017, Mar	Seminar, Technion, Haifa (ISR): Faculty of Biomedical Engineering
2017, Feb	Poster, Cold Spring Harbor, (USA): Global Regulation of Gene Expression
2016, Aug	Talk, Max Delbrück Center & Leibniz Institute for Molecular Pharmacology, Berlin/Joachimstal (GER): PhD Student Retreat
2016, Jun	Poster, The Broad Institute, Cambridge (USA): Systems Biology of Human Disease
2016, Feb	Selected Talk, Technion, Haifa (ISR): SignGene Winter School
2016, Feb	Poster, Innsbruck (AT): Advanced Lecture Course in Systems Biology
2015, Sep	Poster, MDC/FMP Berlin/Bad Saarow (GER): Student Retreat
2015, Sept	Poster, Neuruppin (GER): SignGene Symposium
2015, Aug	Talk, IRI Life Science Berlin (GER): Student Retreat
2015, May	Poster, EMBL, Heidelberg (GER): Symposium Cellular Heterogeneity
2015, Mar	Poster, IRI Life Sciences, Berlin, (GER): Symposium From RNA pools to single molecules
2015, Feb	Short talk & poster, Hebrew University, Jerusalem (ISR): SignGene Retreat
2014, Sep	Short talk, Max Delbrück Center, Berlin, (GER): Symposium Quantitative approaches in cell biology

CHAPTER 8 APPENDIX

8.1. ABBREVIATIONS

listed in alphabetical order

A

A	adenine/adenosine purine base
AKT1	protein kinase B/AKT1
AMPK	AMP-activated protein kinase
ASH1	achaete-scute homologue 1
ASSP1/2	argininosuccinate synthetase pseudogene 1/2
ATM	ataxia telangiectasia mutated
ATR	ataxia telangiectasia and Rad3-related protein
ATRIP	ATR interacting protein
A549	adenocarcinomic human alveolar basal epithelial cells

B

BAX	Bcl-2-associated X protein
Bmal-1	brain and muscle aryl hydrocarbon receptor nuclear translocator-like 1
bp	basepairs
Bcl-2	B-cell lymphoma 2
BSA	bovine serum albumin
BTG2	BTG family member 2

C

C	cytosine/cytidine pyrimidine base
C	cysteine
CARM1	coactivator-associated arginine methyltransferase 1
Cas9	Caspase-9
CBP	CREB binding protein
CDC25	cell division cycle phosphatase 25
CDKN1A	cyclin dependent kinase inhibitor 1A (p21)
CDK	cyclin-dependent kinase
CDK1	cyclin-dependent kinase 1
CDK2	cyclin-dependent kinase 2
CDS	coding sequence
c-Fos	cellular oncogene Fos
CFP	cyan fluorescent protein
ChIP	chromatin immunoprecipitation
ChIP-Seq	chromatin immunoprecipitation DNA-sequencing
Chk1	checkpoint kinase 1
Chk2	checkpoint kinase 2
Chr	chromosome
CI	confidence interval
ClampFISH	click-amplifying fluorescence in-situ hybridization
CO_2	carbon dioxide
CREB	cAMP response element binding protein
Ct	cycle threshold value (Cq cycle quantification value)
CtSD	standard deviation of Ct values
CTD	C-terminal domain, used for the C-term of p53 and RNAP2
C-term	C-terminus/carboxyl-terminus, end of an amino acid chain
CV	coefficient of variation

D

dB	decibel
DBD	DNA binding domain

DDB1	damage specific DNA binding protein 1
DDB2	damage specific DNA binding protein 2
DMSO	dimethyl sulfoxide
DNA	deoxyribonucleic acid
DNA-PKcs	DNA-dependent protein kinase
ΔNp63α	an isoform of tumor protein p63
DRAM	damage-regulated autophagy modulator
DSB	double strand break

E

E	Exon
EC	ethylene carbonate
ECFP	enhanced cyan fluorescent protein
ECM	extracellular matrix
EF	elongation factor
EF1α	elongation factor 1 subunit α
EGF	epidermal growth factor
ER	endoplasmatic reticulum
Erk	extracellular-regulated kinase
EtOH	Ethanol

F

f	rate of transcription
FBS	fetal bovine serum albumin
fc	fold change
FdUMP	5-fluoro-2‘-deoxyuridine-5‘-monophosphate
FdUTP	5-fluoro-2‘-deoxyuridine-5‘-triphosphate
FI	fluorescence intensity
Fig.	figure
FIJI	Fiji Is Just ImageJ
FISSEQ	fluorescent in-situ sequencing
FIT (probe)	forced intercalation probe
FPKM	fragments per kilobase of exon model per million reads mapped
FUTP	5-fluoro-uridine-5‘-triphosphate

G

G	guanine/ guanosine pyrimidine base
GADD45	growth arrest and DNA damage protein family
GAPDH	glyceraldehyde 3-phosphate dehydrogenase
GFP	green fluorescent protein
γ-IR	γ-irradiation
Golgi	Golgi apparatus
GPCR	G-protein coupled receptor
GTF	general transcription factor
Gy	gray
G1-phase	growth 1 (cell cycle) phase
G2-phase	growth 2 (cell cycle) phase
G418	geniticindisulfate

H

HAT	histone-acetyltransferase
HAL/R	genomic homology arm left/right
HDR	homology-directed repair
HER2/ERBB2	erb-B2 receptor tyrosine kinase 2
HMBS	hydroxmethylbilanesynthase
HMT	Histone Methyl Trasnferase

	HPRT	hypoxanthine Phosphoribosyltransferase 1
	HR	homologous recombination
	H2AX	histone 2AX
	H2B	histone 2B
	H3K27	lysine 27 of histone 3
I		
	IF	immunofluorescence
	IPI	inter-peak interval
	IQR	interquartile range
	IR	ionizing radiation
	IRES	internal ribosomal entry site
J		
	JAK	Janus kinase
K		
	K	Lysine
	kb	kilobases
L		
	l	gene length *(in the model to calculate transcription rate)*
	L3MBTL1	lethal(3)malignant brain tumor-like protein
	LPS	lipopolysaccharide
	LUT	lookup table
M		
	M	RNAP2 occupancy *(in the model to calculate transcription rate)*
	MAD	mean absolute deviation
	MAPK	mitogen-activated protein kinase
	MCF7	breast cancer cell line (Michigan Cancer Foundation-7)
	MCF10A	immortalized breast epithelial cell line (Michigan Cancer Foundation-10A)
	MCP	MS2 coat protein
	MDMX	mouse double minute 2, also known as MDM4
	MDM2	mouse double minute 2
	MERFISH	multiplexed error-robust fluorescence in-situ hybridization
	MES	2-(N-morpholino) ethanesulfonic acid
	min	minutes
	miR-34a	microRNA 34a
	miRNA	micro ribonucleic acid
	mInt	average fluorescence intensity
	M-phase	mitotic phase
	Mre11	double strand break repair protein MRE11A, part of the MRN complex
	MRN	protein complex consisting of Mre11, Rad50 and Nbs1
	mRNA	messenger ribonucleic acid
	Msum	RNAP2 coccupancy of all TSS per cell
	MS2	stem-loop RNA structure from the MS2 bacteriophage genome
	mTOR	mammalian target of rapamycin
	MYC	myelocytomatosis oncogene
N		
	n	sample size, or the number of genomic loci *(in the model to calculate transcription rate)* in this thesis
	NA	numerical aperture
	Nbs1	nibrin, part of the MRN complex
	NCS	neocarcinostatin

NES	nuclear export sequence
NF-κB	nuclear factor kappa-light-chain-enhancer of activated B cells
NGF	nerve growth factor
NH_2	primary amine (amino group)
NHEJ	non-homologous end joining
NHS	*N*-Hydroxysuccinimide (1-Hydroxy-2,5-pyrrolidindione)
nm	nanometer
NOXA	also known as PMAIP1, phorbol-12-myristate-13-acetate-induced protein 1
N-term	N-terminus/amino-terminus, start of an amino acid chain

O

OD	oligomerization domain

P

PAGE	polyacrylamide gel electrophoresis
PAI-1	plasminogen activator inhibitor-1
PAM	protospacer adjacent motif
PBS	phosphate buffered saline
PCNA	proliferating cell nuclear antigen
PCR	polymerase chain reaction
PC12	pheochromocytoma cell line (rat adrenal medulla)
PCP	PP7 coat protein
PFA	Paraformaldehyde
PI	propidium iodide
PIC	pre-initiation complex
PIG	p53-inducible gene
PIG3	p53-inducible gene 3
PIKK	phosphatidylinositide 3-kinase-related kinase
PIN1	peptidyl-prolyl cis-trans isomerase NIMA-interacting 1
PI3K	phosphatidylinositol 3-kinase
PKA	protein kinase A
PRMT1	protein arginine N-methyltransferase 1
PRD	proline-rich domain
PTM	post-translational modification
PPM1D	protein phosphatase Mg^{2+}/Mn^{2+} dependent 1D (Wip1)
poly-A	polyadenylation
PP7	stem-loop RNA structure from the PP7 bacteriophage genome
PUMA	p53 upregulated modulator of apoptosis
PUM-HD	pumilio homology domain
PUM1	pumilio RNA binding family member 1
p14ARF	an alternate reading frame product of p16
p16	cyclin-dependent kinase inhibitor 2A
p300/CBP	E1A binding protein p300/CREB-binding protein
p53	tumor suppressor p53

Q

QCD	quartile coefficient of dispersion
qRT-PCR	quantitative real-time PCR

R

R	stands for a purine base in the p53 response element
Rad50	DNA repair protein RAD50, part of the MRN complex
RBP	RNA binding protein
RE	response element
RNA	ribonucleic acid

RNAP1	DNA-directed RNA polymerase 1
RNAP2	DNA-directed RNA polymerase 2
RNAP3	DNA-directed RNA polymerase 3
RNAScope	Specific RNA in-situ hybridation technique
RNA-Seq	RNA sequencing
RPA	replication protein A
RPKM	reads per kilobase million
rpm	revolutions per minute
RRM2B	ribonucleotide reductase regulatory TP53 inducible subunit M2B
RQ	relative quantification
RSD	root square difference
RT	room temperature
RTK	receptor tyrosine kinase

S

S	Serine
SDHA	succinate dehydrogenase complex flavoprotein subunit1
SDS	sodium dodecyl sulfate
SE	standard error of the mean
SESN1	sestrin1
SetD8	Set8/KMT5a, SET-Domain containing Lysine Methyltransferase 5A
shRNA	small hairpin ribonucleic acid
SI	supplementary information
SMAD	SMA ('small', *phenotype in C. elegans*) and MAD ('mothers against decapentaplegic', *phenotype in D. melanogaster*)
SMC1	structural maintenance of chromosomes protein 1
smFISH	single-molecule fluorescence in-situ hybridization
Smyd2	KMT3C, SET and MYND Domain Containing Protein 2
SNR	S/N, signal to noise ratio
SP1	specificity protein 1
S-phase	synthesis phase (cell cycle)
SSB	single strand breaks
STAT	signal transducer and activator of transcription protein
STD	standard deviation
S100B	S100 calcium-binding protein B

T

T	thymine/ thymidine pyrimidine nucleobase
T	amino acid threonine
t	time
TAD	trans-activation domain (of the p53 protein)
TBP	TATA-box binding protein
TBS	tris-buffered saline
TBS-T	tris-buffered saline with Tween
TF	transcription factor
TFIIB,D,E,F,H	general transcription factors B, D, E, F, H that build the pre-initiation complex
TGFß	transforming growth factor beta
TIP60	histone acetyltransferase KAT5
TNF	tumor necrosis factor
Top II	topoisomerase II
TP53	tumor protein p53
Tris	tris (hydroxymethyl) aminomethane
TSS	transcriptional start site

U		
	UbCP	Ubiquitine C promoter
	UTR	untranslated region
	UV	ultraviolet (radiation)
	U-2 OS	human osteosarcoma cell line
V		
	v	RNAP2 elongation speed *(in the model to calculate transcription rates)*
	VDAC	voltage-dependent anion channel
W		
	W	adenine or thymine base in the p53 response element
X		
	XL413	CDC7 kinase inhibitor
	X_{RNA}	RNA counts per cell *(in the model to calculate transcription rates)*
Y		
	Y	stands for a pyrimidine base in the p53 response element
	Y	amino acid tyrosine
	YFP	yellow fluorescent protein
Z		
	Zn^{2+}	zinc ion
0-9		
	5-FU	5-fluorouracil
	53BP1	p53 binding protein 1
α-ω		
	β	RNA export rate *(in the model to calculate transcription rates)*
	δ	degradation rate *(in the model to calculate transcription rates)*
	η	correction factor for probe position *(in the model to calculate transcription rates)*
	$\varkappa$	correction factor for inferred RNAP2 occupancies *(in the model to calculate transcription rates)*
	µ	transcription rate *(in the model to calculate transcription rates)*
	µm	micrometre
	µTSS	transcription rate per TSS *(in the model to calculate transcription rates)*

8.2. LIST OF FIGURES AND TABLES

The list of figures contains all numbers and titles of figures from Chapter 1 (Introduction) to Chapter 8 (Supplementary Information).

8.2.1. INTRODUCTION - FIGURES & TABLES

8.2.2. RESULTS - FIGURES & TABLES

8.2.3. DISCUSSION, CONCLUSION, OUTLOOK - FIGURES & TABLES

8.2.4. MATERIALS & METHODS - FIGURES & TABLES

8.2.5. SUPPLEMENTARY INFORMATION - FIGURES & TABLES

8.3. SUPPLEMENTARY INFORMATION

8.3.1. SUPPLEMENTARY INFORMATION *CHAPTER 3.1.*

Table 8.3.1 Up-regulated p53 target genes after 10 Gy IR in MCF10A cells.

List of 181 identified up-regulated p53 target genes in MCF10A cells after 10 Gy γ-IR with a minimal fold change of 1.25 (Finzel, 2016a) at the time-point 4 h after 10 Gy γ-IR. These were identified as described in Chapter 5.3.4 (Material & Methods) and used for comparison with available literature datasets from Fischer, 2017 and Hafner et al., 2017. Selected p53 target genes from this study are highlighted in light blue. Genes that were only found in the meta-analysis of both γ-irradiated datasets (Finzel, 2016a and Hafner et al. 2017), but not in all three are highlighted in grey. As only up-regulated target genes were considered for this thesis, the set of 71 down-regulated genes is not listed.

Gene symbol	MCF10A wild-type RPKM basal	MCF10A wild-type RPKM 4 h 10 Gy	MCF10A p53kd RPKM basal	MCF10A p53kd RPKM 4 h 10 Gy	Fold change wild-type	Fold change knockdown
GDF15	4.27	39.81	0.13	0.63	9.3	5.0
PGF	1.56	8.85	0.87	1.38	5.7	1.6
TP53INP1	2.05	8.23	0.32	0.64	4.0	2.0
CDKN1A	62.51	246.21	15.50	24.22	3.9	1.6
FAM212B	1.24	4.74	0.51	0.80	3.8	1.6
TRIM22	5.28	19.88	0.30	0.77	3.8	2.5
PHLDB3	1.13	4.16	0.39	0.81	3.7	2.1
BBC3	1.29	4.43	0.64	1.14	3.4	1.8
MDM2	15.69	51.55	7.57	8.01	3.3	1.1
FAM198B	1.44	4.68	0.34	0.31	3.3	0.9
KITLG	1.88	6.03	1.67	3.03	3.2	1.8
RGS12	4.92	15.50	2.61	4.02	3.1	1.5
SESN1	5.23	15.61	2.72	3.61	3.0	1.3
EDA2R	2.45	7.28	0.82	1.01	3.0	1.2
PTAFR	2.19	6.36	1.78	2.49	2.9	1.4
NINJ1	18.46	53.57	9.37	15.67	2.9	1.7
CSNK1G1	1.53	4.43	1.42	1.97	2.9	1.4
CEL	1.06	3.04	0.27	0.34	2.9	1.3
IVL	2.17	6.20	0.28	0.50	2.9	1.7
RRM2B	8.10	21.93	3.43	4.41	2.7	1.3
FGFR2	1.09	2.94	0.60	0.65	2.7	1.1
MIR612	1.37	3.55	1.51	1.37	2.6	0.9
ATG16L2	3.33	8.52	2.98	4.92	2.6	1.7
NUPR1	7.93	20.14	3.12	3.97	2.5	1.3
FDXR	13.95	35.27	8.16	11.87	2.5	1.5
ICOSLG	2.04	5.10	1.68	3.07	2.5	1.8
SESN2	4.28	10.48	2.56	3.35	2.4	1.3
NOTCH1	10.55	25.76	5.34	9.70	2.4	1.8
MIR1204	1.64	3.98	1.81	1.53	2.4	0.8
PLCH2	6.55	15.36	1.19	1.41	2.3	1.2
TNFSF9	12.80	29.81	7.19	8.94	2.3	1.2
MIR4658	8.43	19.59	7.45	12.61	2.3	1.7
ZNF79	1.67	3.86	1.07	1.24	2.3	1.2
BTG2	16.51	38.01	5.24	7.32	2.3	1.4
IGFL1	10.65	24.23	3.19	5.02	2.3	1.6
INPP5D	9.90	22.47	1.62	2.20	2.3	1.4
NLRP1	1.43	3.22	0.85	1.02	2.3	1.2
POLH	4.16	9.34	2.69	3.41	2.2	1.3
PIDD	11.82	26.47	7.58	12.29	2.2	1.6

Table 8.3.1 Up-regulated p53 target genes after 10 Gy IR in MCF10A cells. ***(continued)***

Gene symbol	MCF10A wild-type RPKM basal	MCF10A wild-type RPKM 4 h 10 Gy	MCF10A p53kd RPKM basal	MCF10A p53kd RPKM 4 h 10 Gy	Fold change wild-type	Fold change knockdown
SFXN5	2.11	3.69	2.01	2.74	1.7	1.4
WFS1	3.38	5.91	2.65	4.32	1.7	1.6
CROT	2.43	4.24	1.93	2.40	1.7	1.2
GM2A	26.03	45.35	15.12	15.37	1.7	1.0
TRIAP1	26.73	46.51	20.06	19.01	1.7	0.9
IFT43	1.89	3.29	2.30	2.26	1.7	1.0
TMEM144	1.57	2.72	1.49	1.89	1.7	1.3
ARHGEF3	5.95	10.30	3.27	4.09	1.7	1.3
MAPRE3	1.83	3.17	1.50	2.32	1.7	1.5
MICALL2	5.83	10.03	4.52	6.13	1.7	1.4
FBXO6	1.24	2.12	1.33	1.57	1.7	1.2
FAS	18.81	31.99	15.87	16.94	1.7	1.1
RAP1GAP2	5.00	8.50	3.60	4.54	1.7	1.3
MIR4687	2.40	4.07	2.27	2.56	1.7	1.1
TMC7	1.10	1.86	0.81	0.92	1.7	1.1
TMEM63B	10.46	17.67	6.85	8.19	1.7	1.2
TTC23	1.96	3.31	2.06	2.30	1.7	1.1
BBS4	2.48	4.17	2.36	2.77	1.7	1.2
CCDC142	1.61	2.70	1.66	3.44	1.7	2.1
TMEM40	3.41	5.72	3.10	3.29	1.7	1.1
PLCD3	14.61	24.44	10.84	12.66	1.7	1.2
LOC100859930	1.09	1.81	0.93	1.13	1.7	1.2
ZNF654	1.41	2.35	1.07	1.51	1.7	1.4
SLC44A5	4.85	8.07	3.39	3.03	1.7	0.9
PARD6G	2.12	3.53	2.00	2.31	1.7	1.2
SLFN12	1.93	3.20	1.96	2.10	1.7	1.1
ZNF75D	1.73	2.86	1.56	2.08	1.7	1.3
TAF3	2.84	4.70	2.65	3.23	1.7	1.2
CDK18	4.97	8.23	4.63	4.11	1.7	0.9
KLHL7	4.93	8.15	5.15	5.65	1.7	1.1
FBXL18	5.81	9.57	4.97	6.29	1.6	1.3
CASZ1	1.10	1.81	0.87	1.25	1.6	1.4
APAF1	1.34	2.20	1.37	1.52	1.6	1.1
PTPN6	3.77	6.17	2.93	4.24	1.6	1.4
PI4K2A	8.17	13.32	6.64	7.63	1.6	1.1
FBXO22-AS1	21.47	34.97	19.04	20.35	1.6	1.1
ZNF385A	1.66	2.71	1.24	1.31	1.6	1.1
PRKAB2	5.59	9.05	4.81	5.51	1.6	1.1
ORAI3	2.62	4.24	1.29	1.37	1.6	1.1
FBXO22	6.67	10.79	5.46	5.83	1.6	1.1
TMEM68	7.75	12.51	8.12	7.94	1.6	1.0
C18orf56	4.54	7.33	4.12	4.45	1.6	1.1
DNAJB4	2.89	4.65	2.07	2.11	1.6	1.0
STAT2	4.01	6.41	3.27	4.74	1.6	1.4
C7orf10	4.77	7.59	0.96	0.93	1.6	1.0
FGF2	2.20	3.49	1.80	2.51	1.6	1.4
EZH1	5.37	8.52	5.16	6.11	1.6	1.2
SUV420H2	3.18	5.04	2.53	3.16	1.6	1.3
SLFN5	2.18	3.44	1.45	1.35	1.6	0.9
STARD4	3.67	5.80	3.55	3.79	1.6	1.1
MON2	2.11	3.33	1.82	2.26	1.6	1.2
PRRG2	2.73	4.32	2.28	2.55	1.6	1.1
LOC100129550	1.13	1.77	0.90	0.96	1.6	1.1
NRP2	7.28	11.39	5.39	5.37	1.6	1.0
VAMP4	1.25	1.94	1.47	1.39	1.6	0.9
ISYNA1	3.32	5.17	2.52	2.80	1.6	1.1
TCTA	3.82	5.92	3.42	3.93	1.6	1.1
RELL2	6.21	9.61	7.38	12.68	1.5	1.7
ISCU	32.00	49.54	30.25	28.38	1.5	0.9
RAD52	2.97	4.60	3.21	3.27	1.5	1.0

Table 8.3.1 Up-regulated p53 target genes after 10 Gy IR in MCF10A cells. ***(continued)***

Gene symbol	MCF10A wild-type RPKM basal	MCF10A wild-type RPKM 4 h 10 Gy	MCF10A p53kd RPKM basal	MCF10A p53kd RPKM 4 h 10 Gy	Fold change wild-type	Fold change knock down
APOC1	1.25	1.93	2.95	2.81	1.5	1.0
C10orf32	2.94	4.52	3.07	3.07	1.5	1.0
BBS1	1.98	3.04	1.62	2.11	1.5	1.3
KDM4B	3.68	5.67	3.08	3.16	1.5	1.0
MAPKBP1	6.64	10.20	5.23	6.48	1.5	1.2
FAM98C	3.87	5.92	3.20	4.37	1.5	1.4
RPS27L	31.87	48.80	18.03	16.51	1.5	0.9
CCNO	4.25	6.49	4.84	10.21	1.5	2.1
COL7A1	12.33	18.80	9.25	12.81	1.5	1.4
SERPINB7	3.35	5.11	0.72	0.83	1.5	1.1
ZNF337	19.82	30.11	15.22	20.10	1.5	1.3
C5orf62	4.18	6.33	3.71	4.55	1.5	1.2
PRODH	3.09	4.69	0.87	0.81	1.5	0.9
BTG3	20.93	31.70	18.77	19.21	1.5	1.0
C10orf118	1.05	1.59	0.83	1.00	1.5	1.2
LOC100287177	1.33	2.02	0.95	1.15	1.5	1.2
SNORD50A	3.65	5.53	4.44	3.19	1.5	0.7
ZNF446	2.33	3.53	2.13	2.21	1.5	1.0
TCP11L1	2.11	3.19	1.77	1.78	1.5	1.0
LIMK2	20.54	31.01	16.57	17.58	1.5	1.1
TPMT	2.17	3.27	2.15	2.13	1.5	1.0
HSPBAP1	3.84	5.78	3.61	4.07	1.5	1.1
LOC100527964	4.52	6.78	3.92	4.64	1.5	1.2
ZNF252	2.91	4.36	2.79	3.24	1.5	1.2
KLK7	1.46	2.19	0.33	0.27	1.5	0.8
GPR87	32.00	47.89	27.50	22.61	1.5	0.8

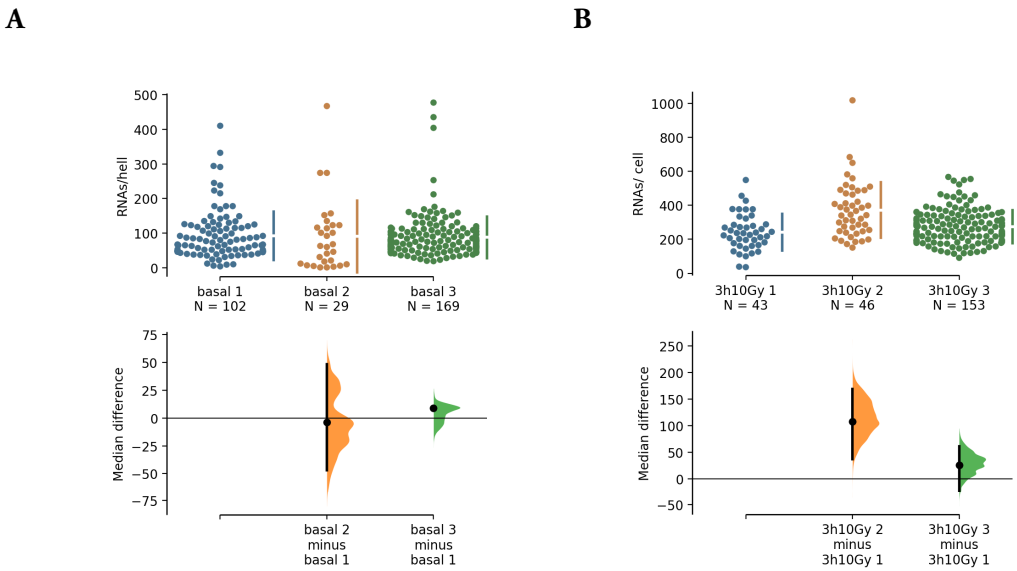

Figure 8.3.1 Comparison of basal and 3 h 10 Gy datasets among each other.

A) The median difference for both other basal datasets set2/3 comparisons against the shared control basal set1 are shown in the Cumming estimation plot. The raw data is plotted on the upper axes. On the lower axes, mean differences are plotted as bootstrap sampling distributions. Each mean difference is depicted as a dot. Each 95% confidence interval is indicated by the ends of the vertical error bars. The unpaired median difference between basal set1 and basal set2 is -4.0 [95.0%CI -47.0, 48.5].The two-sided p-value is 0.262 (Kruskal test). The unpaired median difference between basal set1 and basal set3 is 9.0 [95.0%CI 9.0, 9.0]. The two-sided p-value is 0.717. Calculations based on the DABEST package.(Ho et al., 2019).

B) As in (A) median difference for 2 comparisons against the shared control 3 h 10 Gy 1 are shown. The unpaired median difference between 3 h10 Gy 1 and 3 h10 Gy 2 is 1.08e+02 [95.0%CI 37.5, 1.69e+02]. The two-sided p-value is 3.69e-05. The unpaired median difference between 3 h10 Gy 1 and 3 h10 Gy 3 is 26.0 [95.0%CI -23.0, 61.0].The two-sided p-value is 0.0582.

8.3.2. SUPPLEMENTARY INFORMATION *CHAPTER 3.2.*

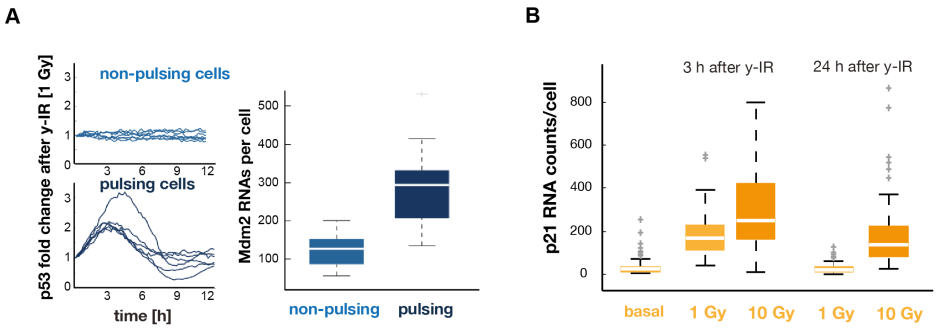

Figure 8.3.2/1 P53 live cell imaging in combination with smFISH.

Two examples for initial experiments, that indicated that p53 nuclear pulses after IR are closely connected with the transcription of target genes, suggesting that the dynamics behavior of p53 is reflected in transcription activity.
(**A**) P53 live-cell imaging was performed after 1 Gy IR and cells were fixed at 6 h, after the first p53 pulse. Then cells were fixed and smFISH staining was performed. Quantitative image analysis was performed to identify pulsing and non-pulsing cells based on single-cell trajectories, as depicted in example cells in the left panel. Then quantified RNA counts were of cells in the pulsing and the non-pulsing fraction were characterized and displayed as boxplots. In general the p53 pulsing fraction showed higher MDM2 RNA levels, than what was detected in non-pulsing cells. Interestingly, though also in non-pulsing cells, RNA levels were compared to cells that were not irradiated as shown in other datasets. This suggests that MDM2 expression levels depend on p53 nuclear pulsing.
(**B**) SmFISH of CDKN1A RNAs was performed in cells that were fixed at different time-points after 10 Gy IR. and in the context of different doses of **γ**-irradiation. In this experiment both non-pulsing and pulsing cells were analyzed jointly, also for the 1 Gy samples. 24 h after DNA damage cell irradiated with lower doses showed CDKN1A RNA levels that were similar to the basal state, while cells that were irradiated with 10 Gy remained at higher RNA levels. At the same time, with the peak of the first p53 pulse at 3 h, CDKN1A transcript levels were similar in both conditions. This indicates that p53 dependent CDKN1A transcription and thus RNA levels, are dose-dependent.

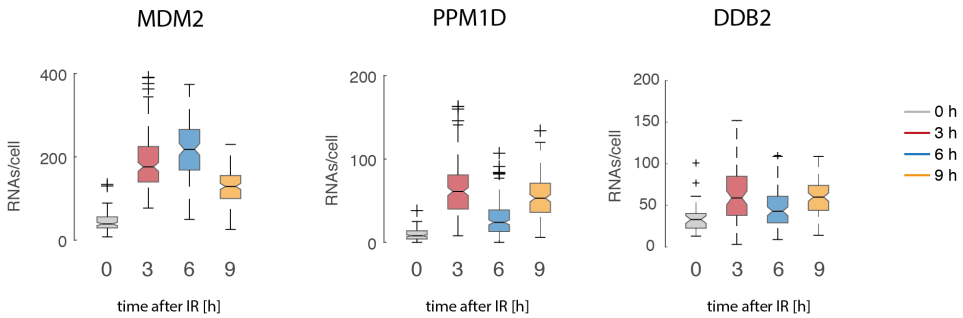

Figure 8.3.2/2 Selected smFISH repeat experiments after 10 Gy.

Quantified RNA counts per cell of selected repeat experiments for MDM2, PPM1D and DDB2 are depicted as boxplots. Time series after 10 Gy **γ**-irradiation from 0-9 h after DNA damage. Quantified as described in Chapter 5.1. A comparison experiment is shown in Chapter 3.2.2. While the absolute number of RNAs that are quantified can differ due to technical reasons of FISH-Quant based analysis, the overall dynamics are similar to the other dataset.

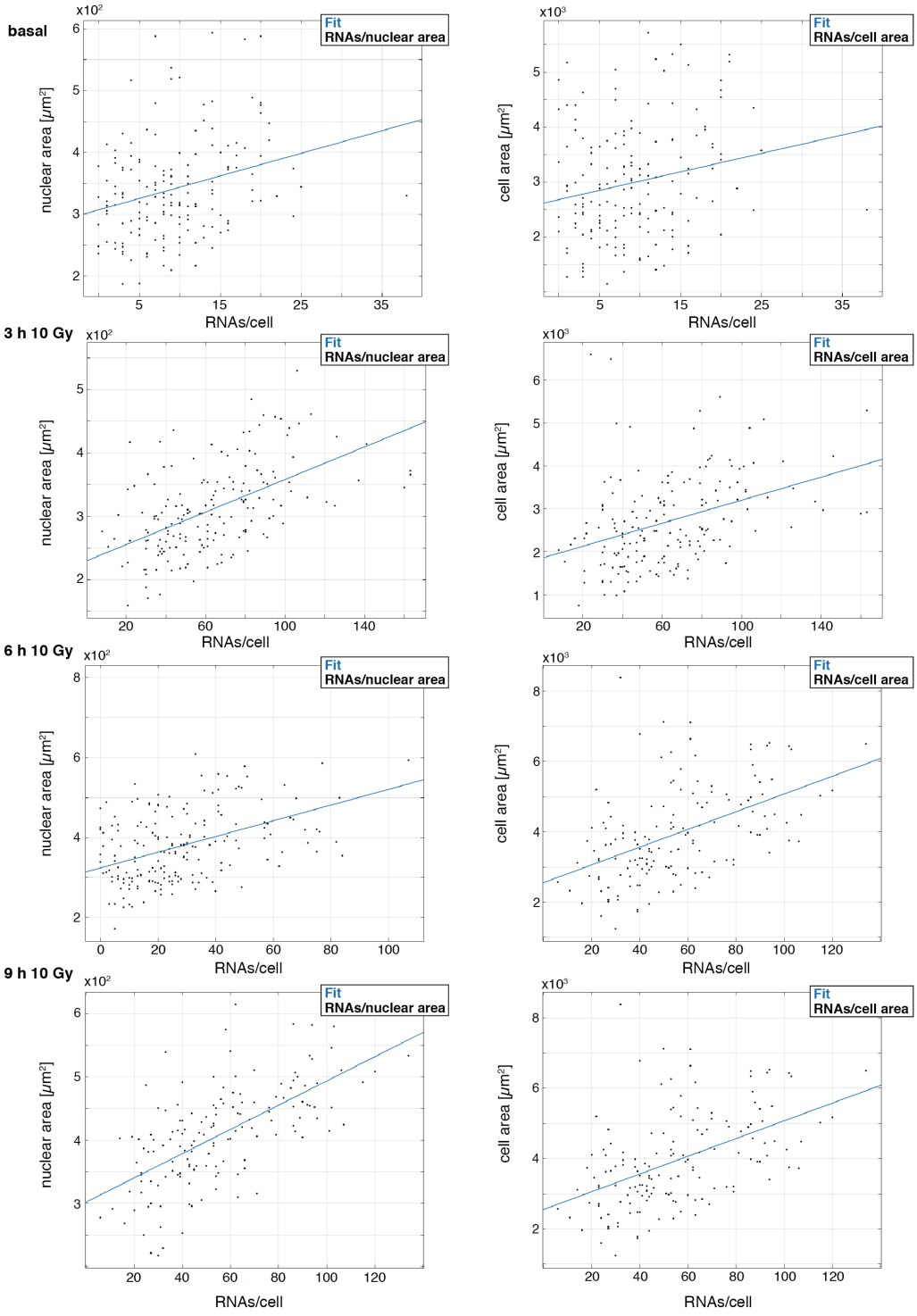

Figure 8.3.2/3 Fit of PPM1D RNA counts relative to nuclear and cytoplasmic areas.

Linear fits of total RNA counts with nuclear area (left panel) or cell area (right panel). Spots represent the same quantified dataset of PPM1D that is shown in Chapter 3.3.5. Linear fits were generated using MATLAB fitting toolbox. R^2 values are not shown here, as they are already depicted in Chapter 3.2.5. The correlation to nuclear area is shown on the left side, the correlation to cell area is shown in the right side.

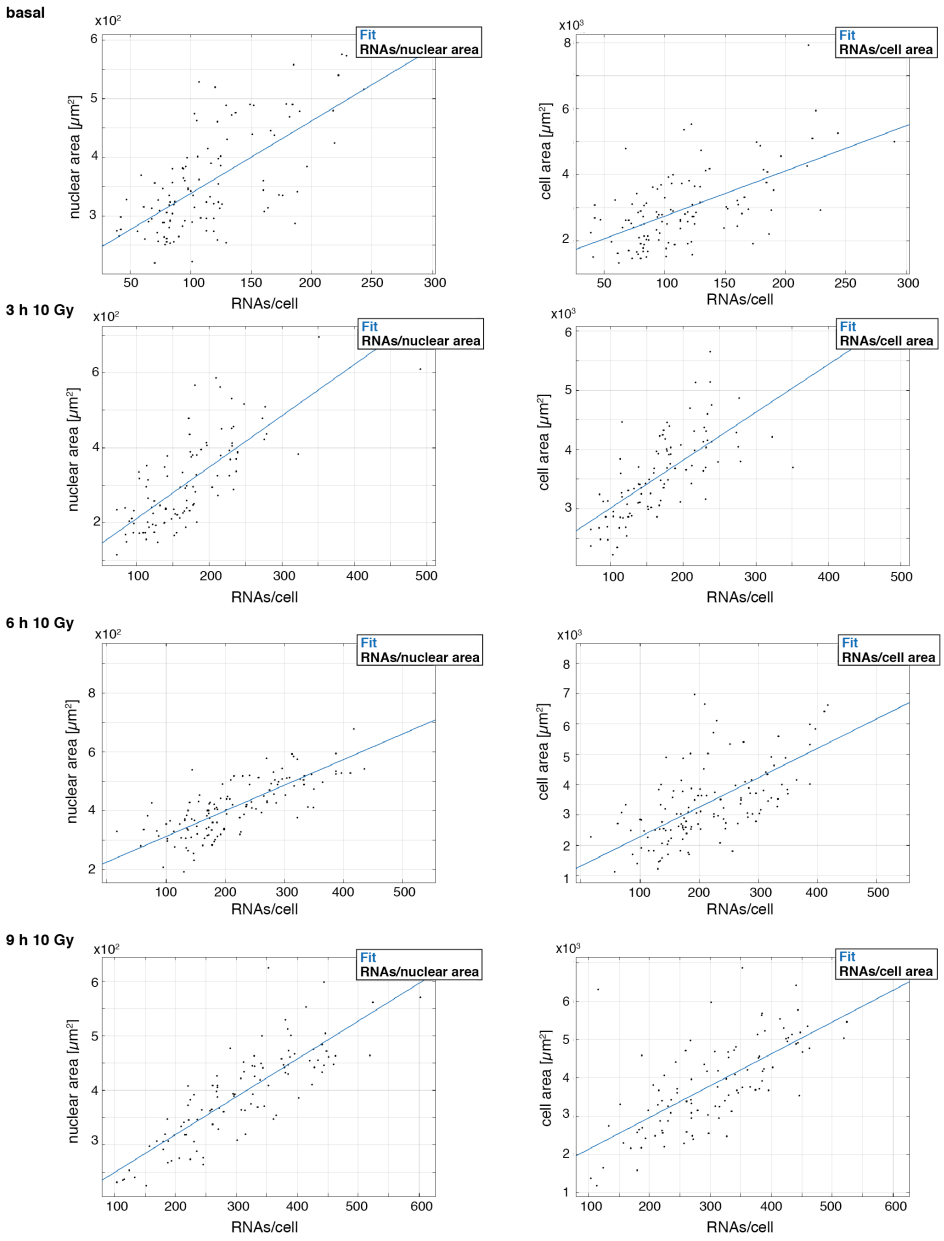

Figure 8.3.2/4 Fit of BAX RNA counts relative to nuclear and cytoplasmic areas.

Linear fits of total RNA counts with nuclear area (left panel) or cell area (right panel). Spots represent the same quantified dataset of BAX that is shown in Chapter 3.3.5. Linear fits were generated using MATLAB fitting toolbox. R^2 values are not shown here, as they are already depicted in Chapter 3.2.5. The correlation to nuclear area is shown on the left side, the correlation to cell area is shown in the right side.

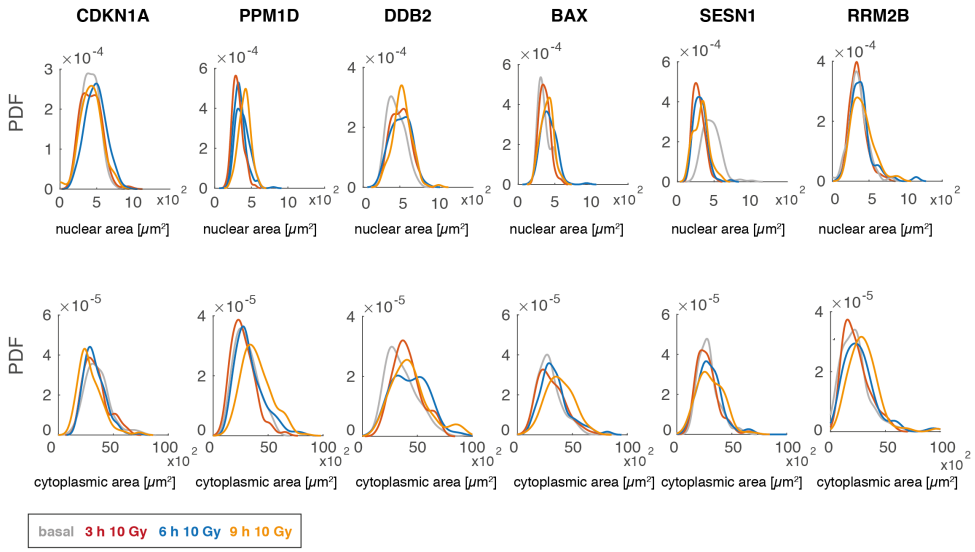

Figure 8.3.2/5 Detected nuclear and cytoplasmic area from *FISH-Quant*.

Analog to Figure 3.2.5.A, all quantified nuclear and cytoplasmic regions as quantified from *FISH-Quant* are plotted as probability density functions in the population for each stained target gene. The whole dataset is >3500 cells. Experiments were performed on different days. Plots highlight that DNA damage does not significantly change the nuclear or cell area, when comparing a high number of cells. The upper row shows quantified nuclear area and the lower row shows the corresponding quantified cytoplasmic area.

8.3.3. SUPPLEMENTARY INFORMATION *CHAPTER 3.3.*

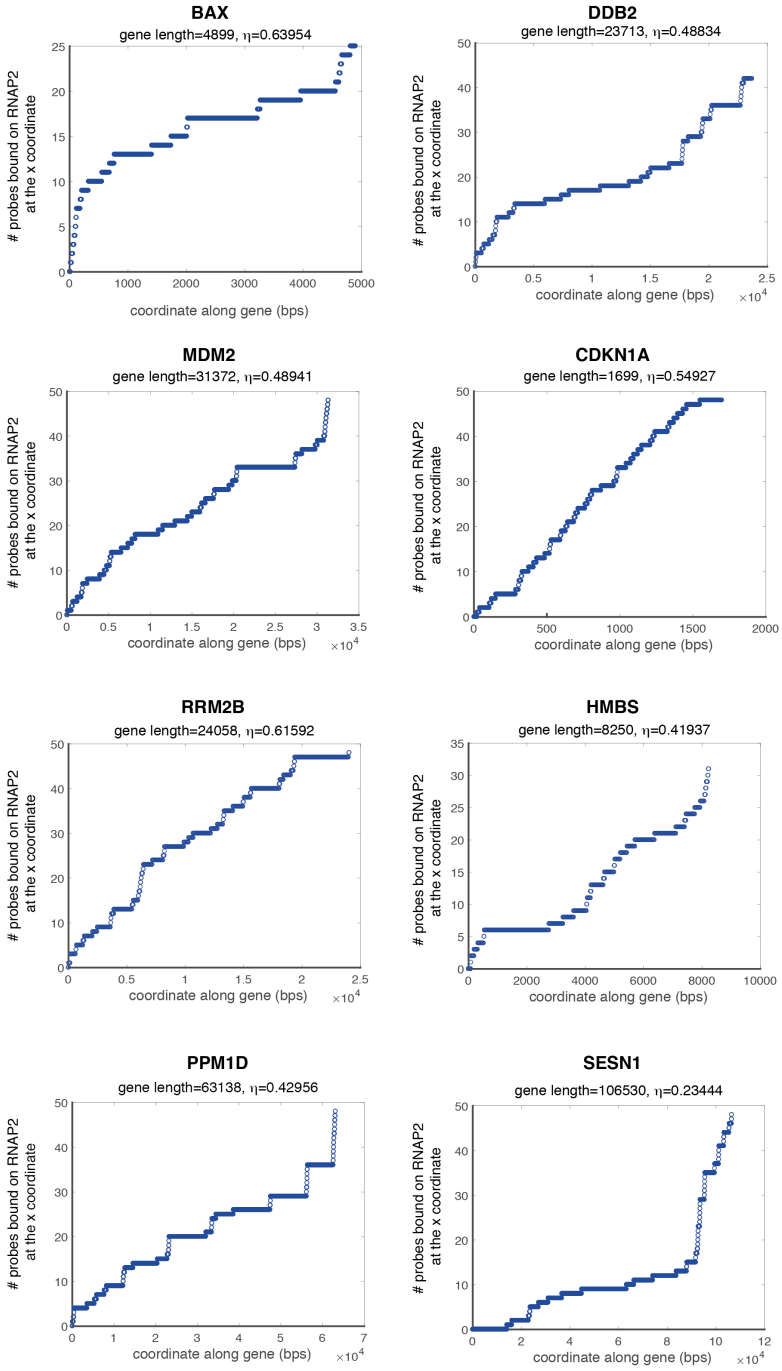

Figure 8.3.3/1 Calculation of correction factor η for probe position by *TransQuant*.

Correction factor η was calculated using *TransQuant* as described by Halpern et al., 2015 and Halpern and Itzkovitz, 2016. Plots show the number of probes bound to transcribing RNAP2 (y-axis) at each position of the RNA sequence (x-axis). Reference sequences (hg38) were used without 3' and 5' UTRs: chr19:48956199-48961097 (BAX), chr11:47215137-47238849 (DDB2), chr11:119085034-119093283 (HMBS), chr12:68808478-68839849 (MDM2), chr6:36684102-36685800 (CDKN1A), chr8:102208133-102232190 (RRM2B), chr6:108987544-109094073 (SESN1), chr17:60600415-60663552 (PPM1D).

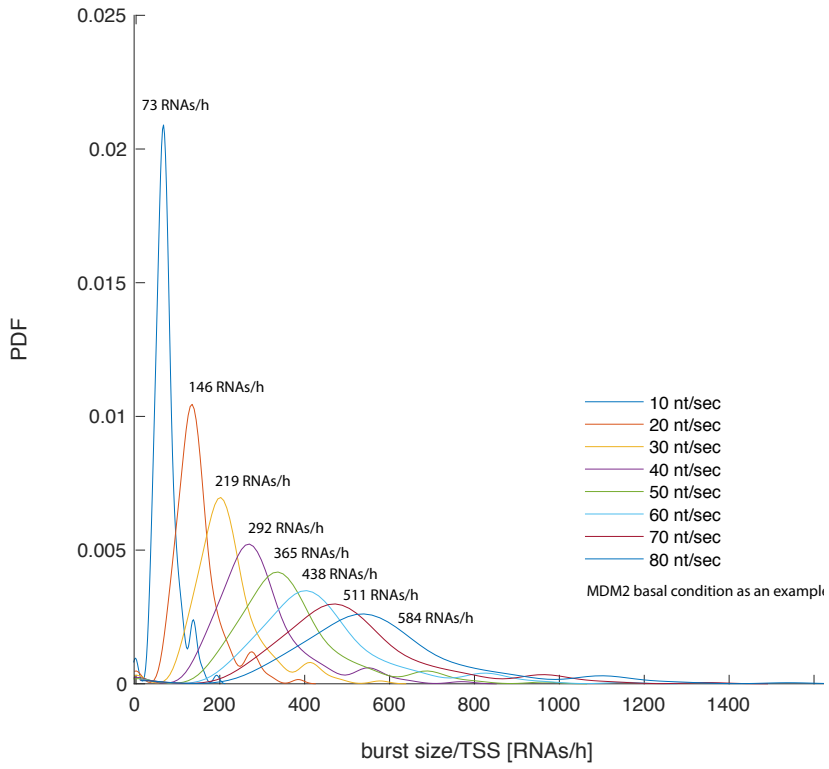

Figure 8.3.3/2 The dependence of RNAP2 and bursting rates on the selected elongation speed.

The PDF of calculated transcription rates, that indicate the burst sizes is shown on the y-axis for different values of RNAP2 elongation speed. The calculated transcription rates per hour and thus burst sizes strongly increase dependent on the chosen speed of RNAP2 elongation. For this example values between 10 nt/sec and 80 nt/sec were used. For the presented plot, the dataset of MDM2 in basal state was chosen as an example. The calculated median transcription rate per hour is depicted next to each curve.

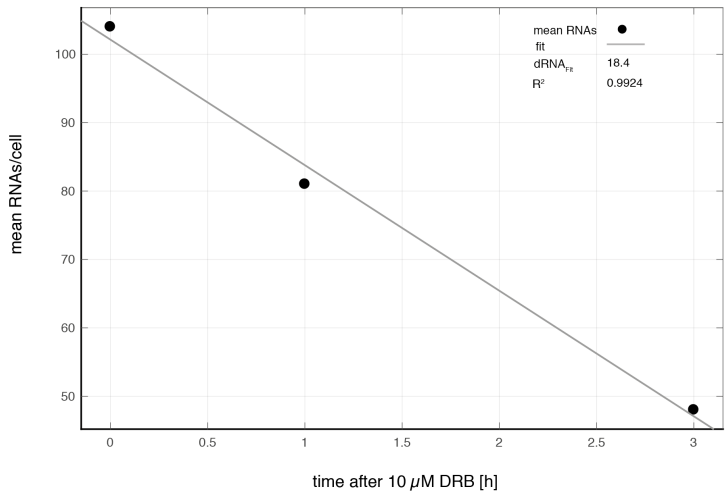

Figure 8.3.3/3 Validation of BAX RNA degradation by transcriptional shutdown using DRB treatment.

A549 wild-type cells were treated with 10 µM DRB and fixed at basal state as well as at 1 h and 3 h post DRB addition. BAX RNA counts per cell were quantified using *FISH-Quant* and plotted as mean levels. From the slope of the linear fit through measurement time-points, the RNA decay rate was obtained as described in Chapter 3.3.3 and Chapter 3.3.4. Fits and derived values for R^2 and d_{RNA} were generated using the MATLAB curve fitting toolbox.

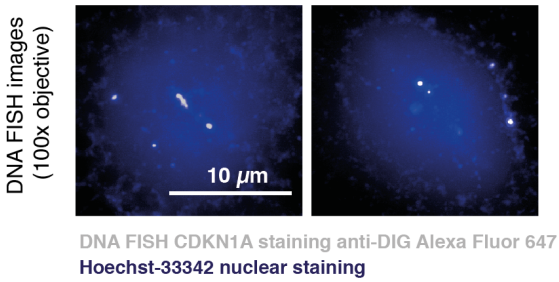

Figure 8.3.3/4 Detection of genomic loci of CDKN1A by DNA FISH.

A549 cells hybridized with CDKN1A locus specific hybridization probes, labelled with Digoxigenin-dUTP and anti-dUTP-DIG-AlexaFluor647 (see Methods section). Maximum number of detected loci was 4. Based on these data in comparison with the maximum number of detected co-stained nuclear TSS spots we concluded four genomic loci per cell for CDKN1A in our A549 cell line. Images were taken as 21 z-stacks with 100x oil immersion objective. The scale bar corresponds to 10 µM.

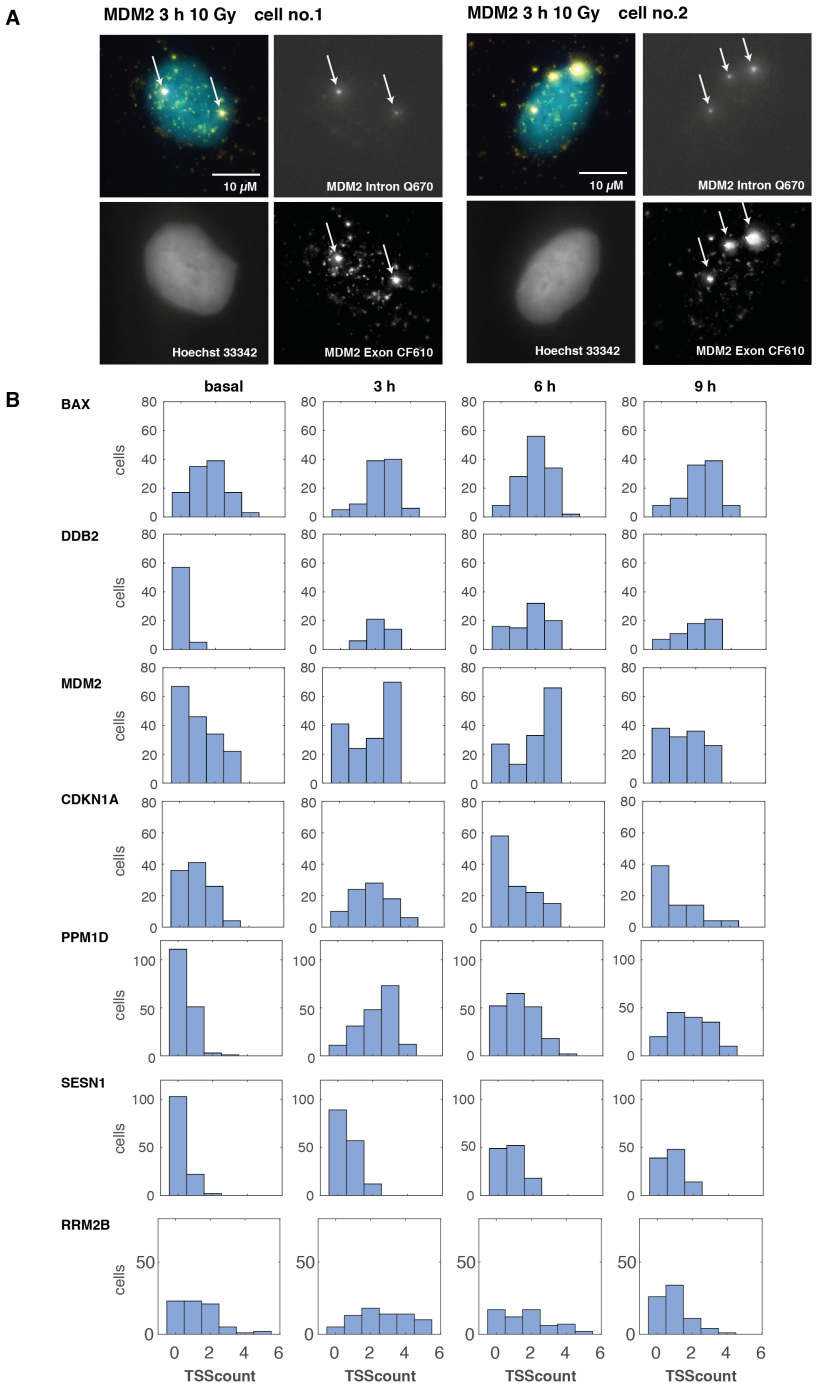

Figure 8.3.3/5 The number of detected transcription sites per condition and target gene.

(A) Representative images of Exon (CAL Fluor Red 610) and Intron (Quasar 670) co-staining in the nucleus as a basis for TSS identification for two cells, stained MDM2 Exon and Intron 3 h after 10 Gy γIR.
(B) Histograms of the number of cells (y-axis) with a certain identified TSS number (x-axis) displayed for all target genes and conditions. Enumerated TSS ranged between 2 (SESN1) and 5 (RRM2B). Surprisingly, most p53 target genes had more than two TSS that were detected based on co-stained nuclear dots for introns and exons.

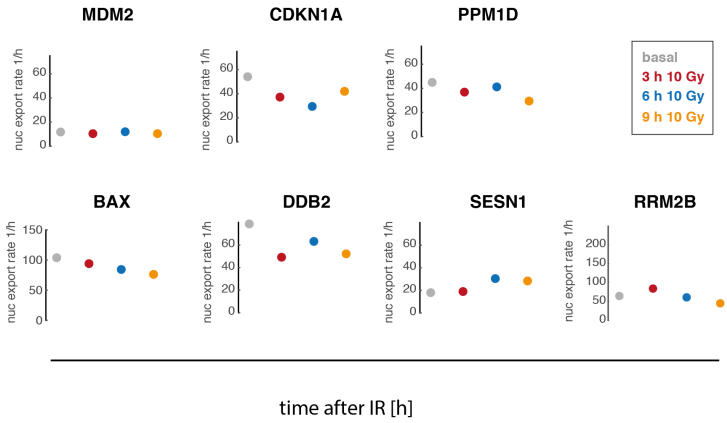

Figure 8.3.3/6 Nuclear export rates.

Nuclear export rates were quantified as previously described (Bahar Halpern et al., 2015a; Bahar Halpern and Itzkovitz, 2016), from calculated transcription rates per cell and cytoplasmic and nuclear RNA spots. Here, the mean nuclear export rate for each target gene at the different time-points is displayed. The x-axis show the different time-points from left to right: basal, 3 h 10Gy, 6 h 10Gy, 9 h 10 Gy.

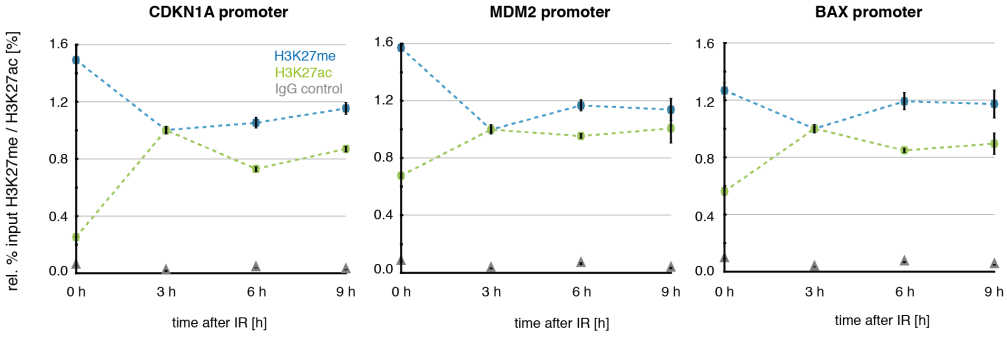

Figure 8.3.3/7 ChIP experiment to detect changes in H3K27me and H3K27ac state in promoter proximal regions of p53 target genes.

ChIP experiments (by Laura Friedel) to measure the relative fraction of H3K27ac (green) and H3K27me (blue) at representative time points after DNA damage at CDKN1A, MDM2 and BAX promoters. Error bars represent RQ min and RQ max values from triplicate quantifications in QRT-PCR measurements. Grey triangles show IgG controls. All values have been normalized to the time-point of the first p53 peak at 3 h after 10 Gy.

Table 8.3.3 Overview of mean quantified parameters of promoter activity.

The quantified parameters for transcription site activity as displayed in Figure 3.3.3 ff. are listed as mean or median values. Quantification of smFISH images and calculations were performed as described in Chapter 1.3.3 and Chapter 3.2.2. TSS: transcription start site, f: fraction of active promoters, μ: transcription rate, dRNA: mean RNA degradation rate in transcriptionally active cells, M: median RNAP2 occupancy per TSS in transcriptionally active cells.

Gene symbol	condition	max #TSS	mean f	median M/TSS [RNAP2]	median μ/TSS [RNAs/h]	mean d_{RNa} [1/h]
	smFISH staining after IR			*average TSS quantification*		
BAX	basal	4	0.40	32	1180	42
	3 h 10 Gy	4	0.58	36	1247	48
	6 h 10 Gy	4	0.49	38	1386	34
	9 h 10 Gy	4	0.56	40	1423	33
CDKN1A	basal	3	0.25	42	755	28
	3 h 10 Gy	4	0.46	46	924	25
	6 h 10 Gy	3	0.24	46	892	17
	9 h 10 Gy	4	0.23	45	1002	33
DDB2	basal	1	0.06	34	255	16
	3 h 10 Gy	3	0.73	50	369	56
	6 h 10 Gy	3	0.53	35	203	81
	9 h 10 Gy	3	0.56	40	289	54
MDM2	basal	3	0.36	60	352	11
	3 h 10 Gy	3	0.59	92	538	12
	6 h 10 Gy	3	0.66	93	484	10
	9 h 10 Gy	3	0.46	72	331	11
PPM1D	basal	1	0.09	47	134	21
	3 h 10 Gy	4	0.56	52	142	17
	6 h 10 Gy	4	0.3	46	131	22
	9 h 10 Gy	4	0.45	50	140	14
SESN1	basal	2	0.12	81	133	11
	3 h 10 Gy	2	0.26	88	149	8
	6 h 10 Gy	2	0.37	83	138	10
	9 h 10 Gy	2	0.38	91	152	8
RRM2B	basal	5	0.25	28	209	43
	3 h 10 Gy	5	0.53	29	228	64
	6 h 10 Gy	5	0.33	32	232	38
	9 h 10 Gy	3	0.18	29	212	14

8.3.4. SUPPLEMENTARY INFORMATION *CHAPTER 3.4.*

Table 8.3.4/1 Overview of mean quantified parameters of promoter activity after BML-277 and Nutlin-3 treatment.

The quantified parameters for transcription site activity as displayed in Figure 3.4.1 and 3.4.2 are listed as mean or median values. Quantification of smFISH images and calculations were performed as described before.

Gene symbol	condition	median RNAs/ cell	max #TSS	mean f	median M/TSS [RNAP2]	median μ/TSS [RNAs/h]	mean d_{RNa} [1/h]
	smFISH staining after IR				*average TSS quantification*		
BAX	basal	122	4	0.42	32	1174	41
	3 h 10 Gy Nutlin-3	151	4	0.64	39	1425	70
	6 h 10 Gy Nutlin-3	205	4	0.62	38	1421	46
	9 h 10 Gy Nutlin 3	240	4	0.73	39	1420	52
CDKN1A	basal	31	2	0.04	36	741	61
	3 h 10 Gy Nutlin-3	238	3	0.39	51	1064	12
	6 h 10 Gy Nutlin-3	191	2	0.35	57	1184	18
	9 h 10 Gy Nutlin 3	309	4	0.58	77	1596	42
PPM1D	basal	13	2	0.07	46	132	14
	3 h 10 Gy Nutlin-3	46	4	0.48	48	136	17
	6 h 10 Gy Nutlin-3	17	3	0.20	39	111	21
	9 h 10 Gy Nutlin 3	24	3	0.42	44	126	20
MDM2	basal	108	3	0.29	55	315	9
	3 h 10 Gy Nutlin-3	186	3	0.69	143	818	31
	6 h 10 Gy Nutlin-3	182	3	0.76	114	654	27
	9 h 10 Gy Nutlin 3	376	3	0.88	189	1081	22
BAX	basal	39	3	0.39	24	907	79
	3 h 10 Gy	135	4	0.73	38	1409	102
	6 h 10 Gy BML-277	136	3	0.28	34	1242	36
	9 h 10 Gy BML-277	22	2	0.24	32	1164	87
CDKN1A	basal	65	2	0.04	48	993	18
	3 h 10 Gy	188	3	0.29	81	1675	25
	6 h 10 Gy BML-277	108	2	0.08	42	871	14
	9 h 10 Gy BML-277	120	2	0.09	41	850	11
PPM1D	basal	8	2	0.08	37	105	13
	3 h 10 Gy	44	4	0.40	50	142	14
	6 h 10 Gy BML-277	24	3	0.09	41	116	9
	9 h 10 Gy BML-277	6	3	0.16	38	108	43
MDM2	basal	49	3	0.23	50	289	11
	3 h 10 Gy	90	3	0.65	109	627	35
	6 h 10 Gy BML-277	129	3	0.41	62	356	11
	9 h 10 Gy BML-277	111	3	0.49	55	317	15

Table 8.3.4/2 Overview of mean quantified parameters of MDM2 and CDKN1A promoter activity in SetD8 and Smyd2 knockdown cells.

The quantified parameters for transcription site activity as displayed in Figure 3.4.3 are listed as mean or median values. Quantification of smFISH images and calculations were performed as described before.

Gene symbol	condition	median RNAs/ cell	max #TSS	mean f	median M/TSS [RNAP2]	median μ/TSS [RNAs/h]	mean d_{RNa} [1/h]
	smFISH staining after IR				*average TSS quantification*		
MDM2	basal	66	3	0.31	42	243	10
knock-down Smyd2	3 h 10 Gy	188	3	0.86	82	472	17
	6 h 10 Gy	203	3	0.67	70	400	10
	9 h 10 Gy	95	3	0.50	49	283	11
MDM2	basal	165	3	0.14	67	386	5
knock-down SetD8	3 h 10 Gy	171	3	0.54	74	426	8
	6 h 10 Gy	131	3	0.22	90	516	14
	9 h 10 Gy	65	3	0.22	68	389	19
CDKN1A	basal	61	3	0.20	41	848	20
knock-down Smyd2	3 h 10 Gy	141	3	0.25	47	980	24
	6 h 10 Gy	154	4	0.47	51	1059	32
	9 h 10 Gy	98	4	0.43	38	800	25
CDKN1A	basal	70	3	0.22	43	889	36
knock-down SetD8	3 h 10 Gy	193	3	0.39	53	1091	18
	6 h 10 Gy	214	3	0.26	54	1120	13
	9 h 10 Gy	95	3	0.39	44	919	30

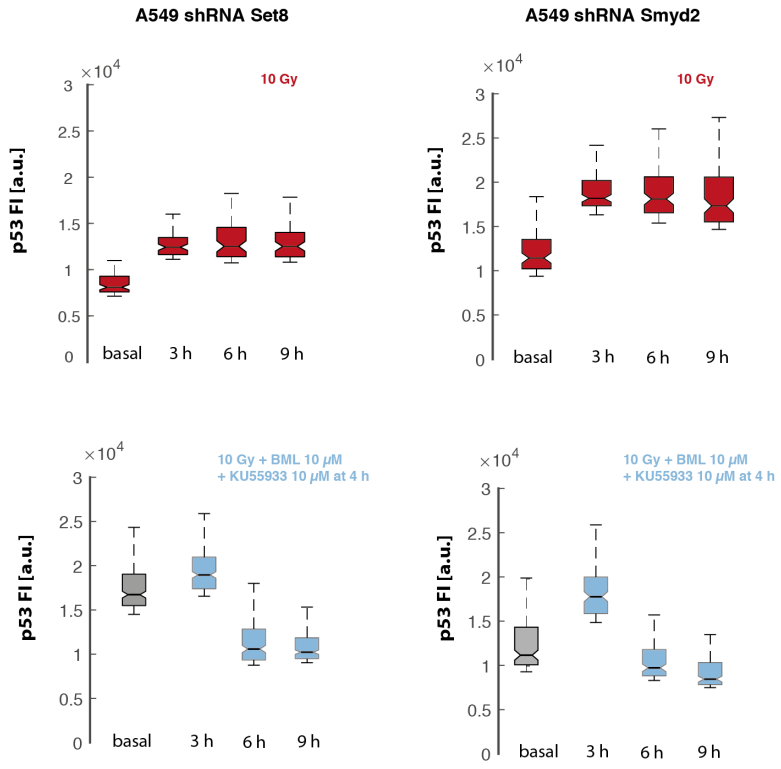

Figure 8.3.4 P53 dynamics in SetD8 and Smyd2 knockdown cells are sustained after IR, dependent on upstream kinase signaling by Chk2/ATM.

Quantitative immunofluorescence of p53 levels in stable A549 knock-down cells for SetD8 (right panel) and Smyd2 (left panel). Boxplots represent the 10% cells with the highest fluorescence signal as quantified from integrated intensities. Whisker show the 25th to 75th percentile and notches display interval endpoints. If notches do not overlap, they represent a significance at the 5% confidence level. Outliers are not displayed. Inhibition of Chk2 and ATM by adding 10 µM BML-277 (Chk2) and KU55933 (ATM) inhibitors at added at 4 h after irradiation shows that this sustained activity is dependent on upstream kinase activity.

8.3.5. SUPPLEMENTARY INFORMATION *CHAPTER 3.5.*

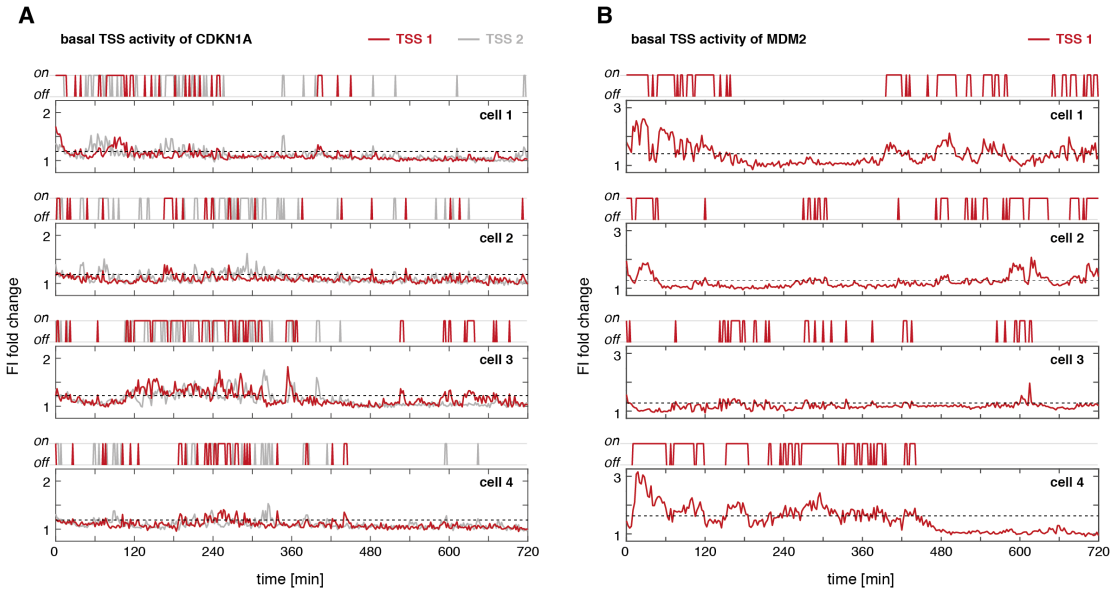

Figure 8.3.5 MS2 traces of active CDKN1A and MDM2 transcription sites.

(A) Example traces of active transcription sites of CDKN1A in MCF10A MS2 reporter cells under basal condition. The MS2 activity of two transcription start sites is displayed for four cells. Traces are 12 h, images were taken every 2 min as nine z-stacks of 300 nm distance. For analysis, images were maximum projected and TSS were tracked using the FIJI manual tracking tool. The pixel intensities were measured as maximum intensities in a range of 10 pixels. When no TSS spot was detectable, the nuclear background was measured. To correct for difference in nuclear MCP-mVenus background, TSS traces were normalized to the median FI of the 10% lowest measured intensity values per TSS and plotted as fold change. Dashed lines indicate the fold change threshold, used to identify burst activity, which was 10% above median fold change fluctuations per cell. The on/off TSS activity shows a binary representation of TSS activity below (off) or above (on) the threshold per cell.
(B) Quantification of MCF10A-MDM2-24x—MCP-mVenus TSS activity in basal state as described in A. Images were taken every 2.5 min for 12 h. Four example cells with active TSS are shown.

CHAPTER 9

ACKNOWLEDGEMENTS

The work of this thesis would not have been possible without the exceptional support of numerous people in my scientific and private life. Thank you for materials, ideas, discussions or shared moments. For contributing to the experimental part, I thank Andrea Grybowski for being my back-up system throughout two labs and sharing experience in all situations. It was an honor to work with you. Petra Snyder, for support with generating cell lines and Western Blots and helping to organize shipments between Berlin and Darmstadt. Laura Friedel, for establishing Chromatin IP's and repeating Western Blots with passion and great scientific spirit. For contributions to scientific discussions, sharing materials & rooms, setting up techniques and a wonderful time throughout my PhD I would like to thank: Jette, Andrea, Ana, Gitta, Caibin, Manu, Felix, Gregor, Christine, Marlen, Matthias, Simon, Ivan, Lotte, Aouefa, Laura B., Friedrich, Nikita, Ella, Klim, Mandy, Marwan, Zohreh, Agnieszka, Marie, Ruth, Andrew, Arik, Juliane, Florian, David, Laura F., Petra, Sabine, Diana, Dorothee, Undine, Christin. Also, all other members of the Loewer, Herrmann, Preibisch, Meller and Woehler labs. It was a great privilege to be surrounded by so many passionate scientists! I also thank the IRI and SignGene graduate schools, the coordinators Sabine, Sandra, Hanna, Stefanie and Micha, faculty and students for wonderful times and inspiring discussions across disciplines and cultural backgrounds in Germany and Israel.

My advisors and reviewers during this thesis. Markus Landthaler, for accepting to review my thesis and giving always helpful and supporting advice in my thesis advisory committee. Amit Meller, for being my co-supervisor in the SignGene program, introducing Israel culturally and scientifically and welcoming me to your lab and contributing with inspiring questions to my thesis committees and talks. Andreas Herrmann, for being my supervisor at the Humboldt University, but also for your great pragmatic and direct help and support when I needed a solid solution to keep on going with my thesis work. Thank you for helping out whenever necessary and integrating me into your group. I always enjoyed the overlaps and fruitful discussions with you and your group members. Stephan Preibisch, for adopting me as a foster lab member, sharing and discussing exciting ideas. I had the chance to see how a great team of interdisciplinary scientist can work together and got a first-hand view on what it would be to start your own lab. I really enjoyed being part of your crowd. Alex, for being on my side as a mentor in this journey and supporting all my ideas and scientific endeavors. Most importantly, I want to thank you for your trust and support in changing times, never letting me regret that I chose you as my mentor. Thank you for letting me grow as a scientist, encouraging me to thrive and discover my own paths, but also being my support-net and handing over a compass to me when necessary.

My family and friends for all trust and support, even though you wondered what has happened that I ended up staying long hours in dark rooms being overexcited about tiny things that matter so much to me. The one and only person to climb every mountain together, Daniel, for everything.

CHAPTER 10

SELBSTSTÄNDIGKEITSERKLÄRUNG

Ich erkläre hiermit, dass ich die vorliegende Arbeit mit dem Titel “Oscillatory transcription factors and stochastic gene expression” selbstständig und nur unter Verwendung der angegebenen Hilfsmittel angefertigt habe. Wurden Ergebnisse in Kooperation erzielt, ist dies an den entsprechend Stellen angegeben. Weiterhin besitze ich keinen äquivalenten Doktorgrad und habe mich nicht an anderer Stelle um einen Doktorgrad beworben. Die dem Promotionsverfahren zugrunde liegende Promotionsordnung der Lebenswissenschaftlichen Fakultät der Humboldt Universität zu Berlin ist mir bekannt.

Berlin, Dhana Friedrich

“The only person to decide what’s possible is you.“